University of New Orleans
ScholarWorks@UNO

University of New Orleans Theses and Dissertations | Dissertations and Theses

Summer 8-6-2013

An Applied Numerical Simulation of Entrained-Flow Coal Gasification with Improved Sub-models

Xijia Lu
University of New Orleans, xlv@uno.edu

Follow this and additional works at: https://scholarworks.uno.edu/td

 Part of the Applied Mechanics Commons, Computer-Aided Engineering and Design Commons, Energy Systems Commons, and the Heat Transfer, Combustion Commons

Recommended Citation

Lu, Xijia, "An Applied Numerical Simulation of Entrained-Flow Coal Gasification with Improved Sub-models" (2013). *University of New Orleans Theses and Dissertations*. 1696.
https://scholarworks.uno.edu/td/1696

This Dissertation is protected by copyright and/or related rights. It has been brought to you by ScholarWorks@UNO with permission from the rights-holder(s). You are free to use this Dissertation in any way that is permitted by the copyright and related rights legislation that applies to your use. For other uses you need to obtain permission from the rights-holder(s) directly, unless additional rights are indicated by a Creative Commons license in the record and/or on the work itself.

This Dissertation has been accepted for inclusion in University of New Orleans Theses and Dissertations by an authorized administrator of ScholarWorks@UNO. For more information, please contact scholarworks@uno.edu.

An Applied Numerical Simulation of Entrained-Flow Coal Gasification with Improved Sub-models

A Dissertation

Submitted to the Graduate Faculty of the
University of New Orleans
in partial fulfillment of the
requirements for the degree of

Doctor of Philosophy
in
Engineering and Applied Sciences

By

Xijia Lu

B.S. Hefei University of Technology, 2006
M.S. University of Science and Technology of China, 2009

August, 2013

ACKNOWLEDGEMENTS

First and the foremost, I would like to thank Dr. Ting Wang for his constant support and dedication to helping me with my research. Dr. Wang is an inspirational instructor and a dedicated mentor. I would not have been able to make it this far without his constant support, wisdom, and patience. I would like to also thank Dr. Bhaskar Kura, Dr. Kazim Akyuzlu, Dr. Linxiong Li, and Dr. Carsie Hall for serving on my dissertation committee.

I would also like to thank the Department of Energy for its financial support and to acknowledge the support from the Louisiana Governor's Energy Initiative, administered by both the Clean Power and Energy Research Consortium (CPERC) and the Louisiana Board of Regents.

I would like to thank my colleagues, Dr. Jobaidur Kahn, Dr. Lei Zhao, Dr. Armin Silaen, Mr. Henry A. Long, and all others working for UNO's Energy Conversion and Conservation Center (ECCC) for all of their help.

Finally, I would like to thank my family and friends for their supports and encouragements during the difficult times. Most of all, I would like to thank my wife, Danqian Liu, for encouraging and supporting me constantly throughout my Ph.D career.

TABLE OF CONTENTS

LIST OF FIGURES

LIST OF TABLES

NOMENCLATURE

a	local speed of sound (m/s)
c	concentration (mass/volume, moles/volume)
c_p	heat capacity at constant pressure (J/kg-K)
c_v	heat capacity at constant volume (J/kg-K)
D	mass diffusion coefficient (m^2/s)
D_H	hydraulic diameter (m)
D_{ij}	mass diffusion coefficient (m^2/s)
D_t	turbulent diffusivity (m^2/s)
E	total energy (J)
g	gravitational acceleration (m/s^2)
G	incident radiation
Gr	Grashof number ($L^3.\rho^2.g.\beta.\Delta T/\mu^2$)
H	total enthalpy (W/m^2-K)
h	species enthalpy (W/m^2-K)
J	mass flux; diffusion flux (kg/m^2-s)
k	turbulence kinetic energy (m^2/s^2)
k	thermal conductivity (W/m-K)
m	mass (kg)
M_W	molecular weight (kg/kgmol)
M	Mach number
p	pressure (atm)
Pr	Prandtl number (ν/α)
q	heat flux
q_r	radiation heat flux
R	universal gas constant
Sc	Schmidt number (ν/D)
S_f	source term due to exchange of momentum
S_h	source term due to exchange of energy
S_m	source term due to exchange of mass

t	time (s)
T	temperature (K)
U	mean velocity (m/s)
X	mole fraction (dimensionless)
Y	mass fraction (dimensionless)

Greek letter

β	coefficient of thermal expansion (K^{-1})
ε	turbulence dissipation (m^2/s^3)
ε_w	wall emissivity
κ	von Karman constant
μ	dynamics viscosity (kg/m-s)
μ_k	turbulent viscosity (kg/m-s)
ν	kinematic viscosity (m^2/s)
ν'	stoichiometric coefficient of reactant
ν''	stoichiometric coefficient of product
ρ	density (kg/m^3)
ρ_w	wall reflectivity
σ	Stefan-Boltzmann constant
σ_s	scattering coefficient
τ	stress tensor ($kg/m\text{-}s^2$)

Subscript

i	index notation
j	index notation

ABSTRACT

The United States holds the world's largest estimated reserves of coal and is also a net exporter of it. Coal gasification provides a cleaner way to utilize coal than directly burning it. Gasification is an incomplete oxidation process that converts various carbon-based feedstocks into clean synthetic gas (syngas), which can be used to produce electricity and mechanical power with significantly reduced emissions. Syngas can also be used as feedstock for making chemicals and various materials.

A Computational Fluid Dynamics (CFD) scheme has been used to simulate the gasification process for many years. However, many sub-models still need to be developed and improved. The objective of this study is to use the improved CFD modeling to understand the thermal-flow behavior and the gasification process and to provide guidance in the design of more efficient and cheaper gasifiers.

Fundamental research has been conducted to improve the gasification sub-models associated with the volatile thermal cracking, water-gas-shift (WGS) reaction, radiation effect, low-rank-coal gasification, coal to synthetic-natural-gas (SNG), and ash deposition mechanisms. The improved volatile thermal cracking model includes H_2S and COS contents. A new empirical WGS reaction model is developed by matching the result with experimental data. A new coal demoisturization model is developed for evaporating the inherent moisture inside the coal particles during low-rank-coal gasification. An ash deposition model has also been developed. Moreover, the effect of different radiation models on the simulated result has been investigated, and the appropriate models are recommended.

Some improved model tests are performed to help modify an industrial entrained-flow gasifier. A two-stage oxygen feeding scheme and a unique water quench design are investigated. For the two-stage oxygen feeding design, both experimental data and CFD predictions verify that it is feasible to reduce the peak temperature and achieve a more uniform temperature distribution in the gasifier by controlling the injection scheme without changing the composition and production rate of the syngas. Furthermore, the CFD simulation can acceptably approximate the thermal-flow and reaction behaviors in the coal gasification process, which can then be used as a preliminary screening tool for improving existing gasifiers' performance and designing new gasifiers.

Keywords: Integrated Gasification Combined Cycle (IGCC), Entrained-flow Coal Gasification, Water-Gas-Shift, Radiation Model, Water Quench, Coal-to-Synthetic Natural Gas (SNG), Ash Deposition Model.

CHAPTER ONE
INTRODUCTION

1.1 Background

Coal a combustible black or brownish-black sedimentary rock usually occurring in rock strata in layers or veins called coal beds or coal seams. The harder forms, such as anthracite coal, can be regarded as metamorphic rock because of later exposure to elevated temperature and pressure. A fossil fuel, coal forms when dead plant matter is converted into peat, which in turn is converted into lignite, then sub-bituminous coal, then bituminous coal, and lastly anthracite. This involves biological and geological processes that take place over a long period. Coal is composed primarily of carbon along with variable quantities of other elements, chiefly hydrogen, sulfur, oxygen, and nitrogen [Blander, M., 2011].

Coal is the largest source of energy for the generation of electricity worldwide, as well as one of the largest worldwide anthropogenic sources of carbon dioxide releases. EIA 2011 report shows that global carbon dioxide emissions from coal use is predicted to have the largest absolute increase, from 13.0 billion metric tons in 2008 to 19.6 billion metric tons in 2035. One quarter of the world's coal reserves are found in the United States. Energy content of those reserves exceeds the energy content of the world's known oil reserves. Coal is the United States' largest domestic energy resource, and coal generates more than 50 percents of the United States' electricity for many years until after 2012 when production of cheap shale gas reduces coal usage. At the current rates of use, United States' coal reserves are enough to last for 250 years. The dependence by the U.S. on coal as source of energy will continue as the Energy Information Administration projects a 26 percent increase in the United States' electricity demand from 2007 to 2030 with coal remaining as the main fuel source.

Unfortunately, coal is not a perfect fuel. Coal contains impurities such as nitrogen and sulfur. Burning coal will release these impurities (NO_x and SO_x) into the air, which can react with the air's water vapor and form "acid rain." In addition, as with any other carbon-based fuel, burning coal produces carbon dioxide. Carbon dioxide in the atmosphere can trap the earth's heat causing the "greenhouse effect" and changes the earth's climate.

Throughout history, coal has been a useful resource. It is primarily burned for the production of electricity and/or heat, and is also used for industrial purposes, such as refining metals. Methods of using coal can be divided into (a) combustion, (b) pyrolysis, (c) liquefaction, and (d) gasification. In combustion, coal is directly burned to produce heat. In pyrolysis, coal is decomposed through heating without oxygen, which releases volatile matter inside the coal leaving only carbon (char) and tar. In liquefaction, coal is converted into liquid fuels. In gasification, coal is converted into synthetic gas (syngas).

Gasification is a process that converts coal into primarily carbon monoxide, hydrogen and carbon dioxide. This is achieved by reacting the material at high temperatures (>700 °C), without combustion, with a controlled amount of oxygen and/or steam. The resulting gas mixture is called syngas and is itself a fuel. The clean syngas can be used as a fuel to produce electricity or valuable products such as chemicals, fertilizers, and transportation fuels. In contrast to the combustion process, which takes place in excess oxidant conditions, the gasification process takes place in sub-stoichiometric conditions. Generally, the amount of O_2 used is only 35% or less of the amount required for complete combustion. The main differences between combustion and gasification are listed in Table 1.1.

Table 1.1 Comparison between combustion and gasification.

Combustion	**Gasification**
▪ Occurs in excess-oxidant conditions ▪ Releases heat (exothermic) ▪ Produces heat	▪ Occurs in oxidant-lean conditions ▪ Absorbs heat (endothermic) ▪ Produces sygas as a fuel or feedstock for producing chemicals

A very efficient way to use the syngas as fuel for electricity generation is by employing the Integrated Gasification Combined Cycle (IGCC). A schematic of an IGCC system is presented in Figure 1.1. IGCC is a technology that uses a gasifier to turn coal and other carbon based fuels into syngas. It then removes impurities from the syngas before it is combusted. Some of these pollutants, such as sulfur, can be turned into re-usable byproducts. This results in lower emissions of sulfur dioxide, particulates, and mercury. With additional process equipment, the carbon in the syngas can be shifted to hydrogen via the water-gas shift reaction, resulting in

nearly carbon free fuel. The resulting carbon dioxide from the shift reaction can be compressed and permanently sequestered. Excess heat from the primary combustion and syngas fired generation is then passed to a steam cycle, similar to a combined cycle gas turbine. This results in improved efficiency compared to buring conventional pulverized coal in a steam power plant.

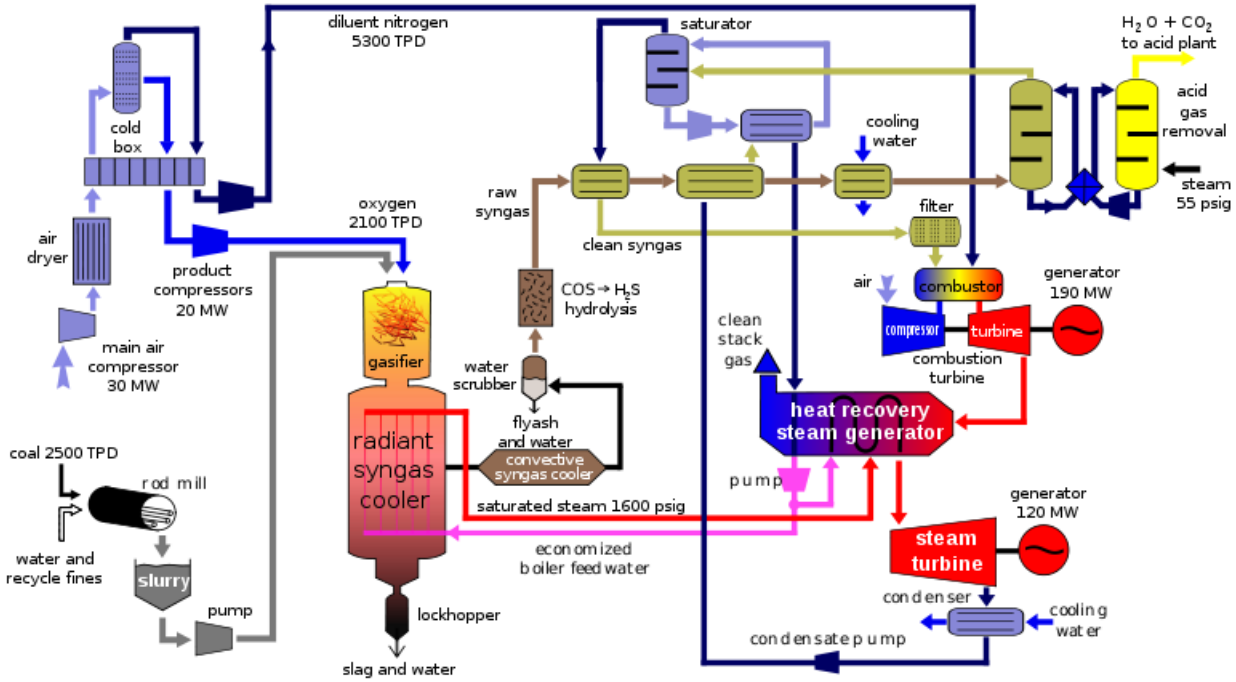

Figure 1.1 Schematic of an IGCC system (Source: Wikipedia)

The plant is called "integrated" because: firstly, the syngas produced in the gasification section is used as fuel for the gas turbine in the combined cycle; secondly, steam produced by the syngas coolers in the gasification section is used by the steam turbine in the combined cycle; and thirdly, the compressed air produced by the compressor of the gas turbine can be "integrated" with the air separation unit (ASU) to produce oxygen. In this example the syngas produced is used as fuel in a gas turbine which produces electrical power. In a normal combined cycle, so-called "waste heat" from the gas turbine exhaust is used in a Heat Recovery Steam Generator (HRSG) to make steam for the steam turbine cycle. An IGCC plant improves the overall process efficiency by adding the higher-temperature steam produced by the gasification process to the steam turbine cycle. This steam is then used in steam turbines to produce additional electrical power.

1.2 Literature Review

1.2.1 History of Gasification

Coal gasification, the chemical conversion of coal to a gaseous state, was first used to produce gas for lighting and heat in the US and UK in the early 19th century. Prior to the discovery of 'natural' gas, it was the fuel of choice, lighting cities across the US and Europe. In 1812, the first gas company was established in London to produce gas from coal to light the Westminster Bridge. The first gas plant to manufacture syngas from coal was built in the United States in 1816 to light the streets of Baltimore. Soon, more gas plants followed in Boston and New York. By 1875, manufactured gas was being widely used for home lighting. At the time natural gas was discovered it was so abundant that coal gas was quickly abandoned in the late 19th century.

The energy crisis of the 70's led to a resurgence of interest in coal gas as an energy alternative. A major effort began to commercialize the technology on a large scale for clean energy and chemical feedstock production. The abundant coal reserves of the United States and other countries posed a challenge to engineers – how to utilize this reserve of fossil fuels in a fashion that wouldnot cause the environmental harm of traditional methods of coal combustion.

Decades of research and development have resulted in a mature technology that is currently being 'scaled up' as larger and larger plants are built, allowing further improvements in the process. Recently announced projects are on the scale of large conventional PC (pulverized coal) power plants. Worldwide there are 62 operational coal gasification units and 24 in the planning stages. Generating unit construction costs are somewhat higher than PC combustion units and will likely be on a par in the near future as design costs are amortized over more units and standardized designs emerge.

1.2.2 Gasification Global Reactions

Coal gasification occurs when the coal is heated with limited oxygen and steam in a gasification reaction chamber. The main global reactions involved in a gasification process are as follows:

Heterogeneous reactions:

$$C(s) + \tfrac{1}{2} O_2 \rightarrow CO \qquad \Delta H°_R = -110.5 \text{ MJ/kmol} \qquad \text{(R1.1)}$$

$$C(s) + CO_2 \rightarrow 2CO \qquad \Delta H°_R = +172.0 \text{ MJ/kmol} \qquad \text{(R1.2)}$$

(Gasification, Boudouard reaction)

$C(s) + H_2O(g) \rightarrow CO + H_2$ $\Delta H°_R = +131.4$ MJ/kmol (R1.3)

(Gasification)

$C + 2H_2 \rightarrow CH_4$, $\Delta H°_R = -87.4$ MJ/kmol
(Direct methanation) (R1.4)

Homogeneous reactions:

$CO + ½\ O_2 \rightarrow CO_2$ $\Delta H°_R = -283.1$ MJ/kmol (R1.5)

$CO + H_2O(g) \leftrightarrow CO + H_2$ $\Delta H°_R = -41.0$ MJ/kmol (R1.6)

(Water-gas-shift)

$CH_mO_nN_oS_pCl_q \rightarrow aCO+bH_2+cCH_4+dC_2H_2+eN_2+fHCl+gH_2S+hCOS$

(Volatile cracking) (R1.7)

$CH_4 + ½\ O_2 \rightarrow CO + 2\ H_2$ $\Delta H°_R = -35.7$MJ/kmol (R1.8)

(Volatiles gasification via CH_4)

$C_2H_2 + O_2 \rightarrow 2\ CO + H_2$ $\Delta H°_R = -447.83$ MJ/kmol (R1.9)

(Volatiles gasification via C_2H_2)

$H_2 + ½\ O_2 \rightarrow H_2O$ $\Delta H°_R = -242$MJ/kmol (R1.10)

The gasification of char by CO_2 and H_2O, reactions (R1.2) and (R.1.3), respectively, are endothermic reactions. The endothermic two-step char combustion, reactions (R1.1) and (R1.5), are needed to supply the energy needed in the gasification reactions. The sythentic gas produced mainly consists of CO and H_2 as fuels with other non-reactive gases such as H_2O and CO_2. Reaction (R1.7) is the thermal cracking of the volatiles ($CH_mO_nN_oS_pCl_q$). The volatiles released from the coal particles are thermally cracked into lighter gases. The volatile species for different coals varies according to the ultimate composition of the coal.

1.2.3 Types of Gasifiers

There are four main gasifier types: (a) fluidized-bed gasifier, (b) moving/fixed-bed gasifier, (c) entrained-flow gasifier, and (d) transport gasifier. Explanations of each type and its examples are presented below. The comparison of these gasifiers is summarized in Table 1.2. Some other types of gasifiers for special applications are also presented below.

1.2.3.1 Fluidized-Bed Gasifier

In the fluidized-bed gasifier, the fuel is fluidized in oxygen and steam or air. The ash is removed dry or as heavy agglomerates that defluidize. The temperatures are relatively low in dry ash gasifiers, so the fuel must be highly reactive; low-grade coals are particularly suitable. The agglomerating gasifiers have slightly higher temperatures, and are suitable for higher rank coals. Fuel throughput is higher than for the fixed bed, but not as high as for the entrained flow gasifier. The conversion efficiency can be rather low due to elutriation of carbonaceous material. Recycle or subsequent combustion of solids can be used to increase conversion. Fluidized bed gasifiers are most useful for fuels that form highly corrosive ash that would damage the walls of slagging gasifiers. Biomass fuels generally contain high levels of corrosive ash, thus fluidized gasifiers are commonly used for biomass gasifica tion..

The operating temperature of a fluidized-bed gasifier is around 1000°C (~1800°F), which is roughly only half of the operating temperature of a coal burner. This lower temperature has several advantages:

- Lower NO_x emission; the temperature is not hot enough to break apart the nitrogen molecules and cause the nitrogen atoms to join with oxygen atoms to form NO_x.
- No slag formation; the temperature is not hot enough to melt ash. It is suitable for coals of any rank (high or low ash content).
- Lower syngas temperature; that means cheaper syngas cooling system prior to gas clean up.

Fluidized-bed gasifiers display these characteristics:

- Fuel flexibility, can gasify a wide range of feedstocks
- Moderate oxidant and steam requirements
- Has a uniform, moderately high temperature throughout the gasifier
- Extensive char recycling is required

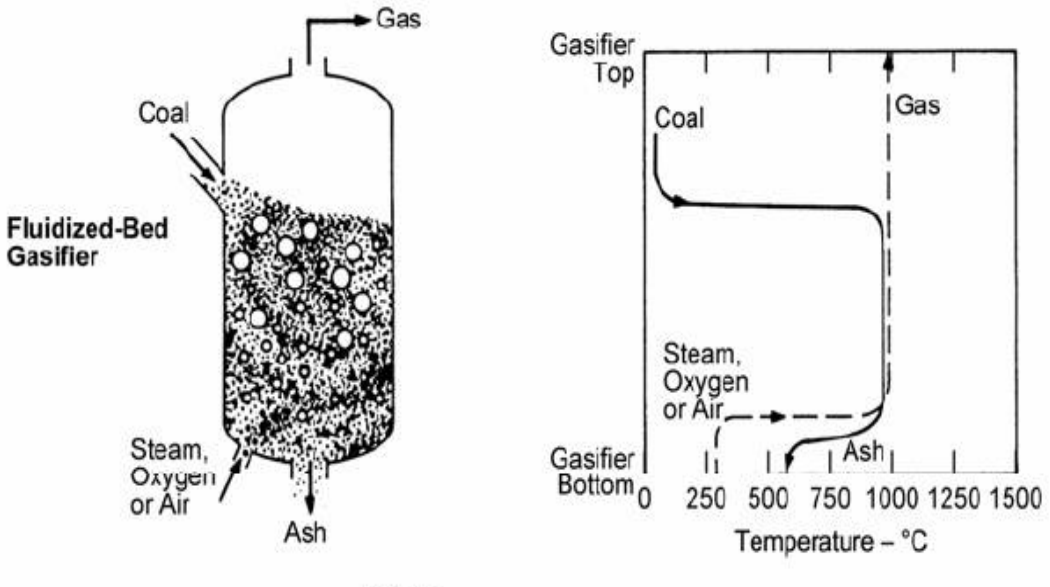

Figure 1.2 Schematic of the fluidized-bed gasifier (Holt, 2004)

Examples of commercial fluidized-bed gasifier are:

(i) Great Point Energy

Great Point Energy is commercializing a fluidized-bed, catalytic gasification process, called Bluegas™, to covert coal and other carbonaceous materials to synthetic natural gas (SNG). In contrast to the conventional coal-to-SNG process, which is based on non-catalytic coal gasification to first generate a syngas, then followed by water-gas-shift (WGS) and methanation reaction to produce methane, Catalytic Gasification offers the opportunity to combine these processes into a single step with improved thermal efficiency, i.e. a once–through catalytic gasification and methanation in one reactor.

Figure 1.3 shows an overview of the GreatPoint Energy's Bluegas™ catalytic gasification SNG process. Partially dried coal and/or other carbonaceous are mixed and catalyzed with a proprietary catalyst solution. The catalyzed coal is then dried and transported to a fluidized-bed gasifier via a lock hopper system. Steam is also added. The syngas leaving the catalytic gasifier undergoes a series of cleanup steps to remove particulates, water and acid gases followed by a separation step to recover the methane product gas. The syngas from the gasifier is not expected to contain tar, heavy oil byproducts, or volatile organic compounds (VOCs). CO_2 produced can be captured and sequestrated. The char withdrawn from the gasifier

is processed in the catalyst recovery unit, in which the catalyst is recovered and recycled to the process. Fresh makeup catalyst solution is used to supplement catalyst losses.

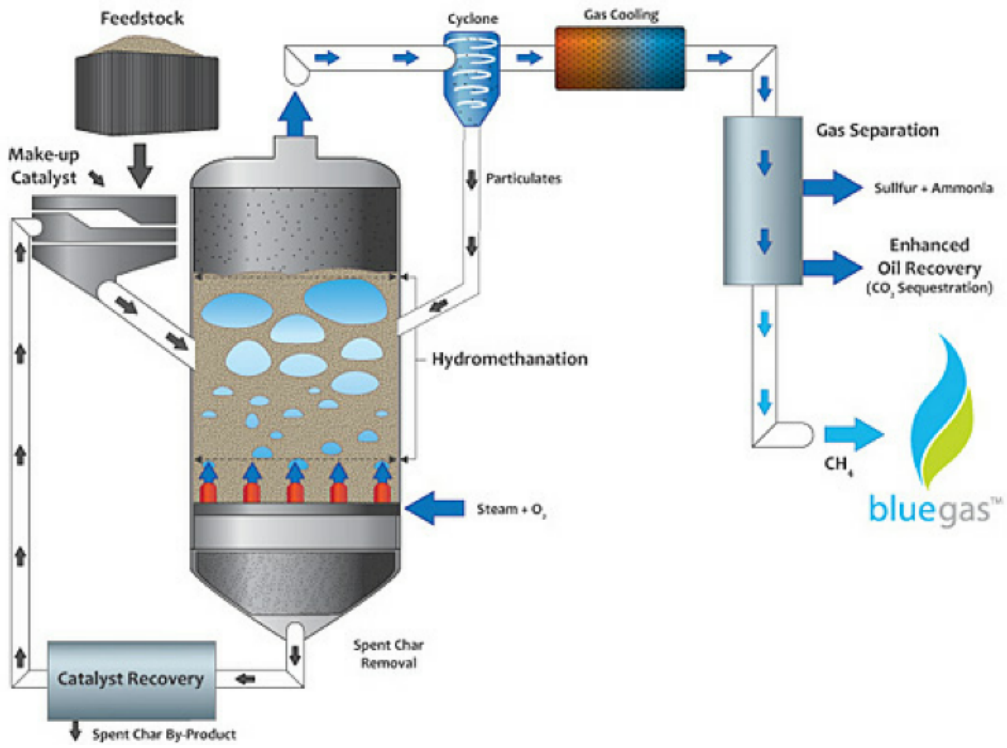

Figure 1.3 Overview of the GreatPoint Energy Bluegas™ Process – once –through catalytic gasification and methanation in one reactor. (source: Great Point Energy)

(ii) U-GAS® Gasifier

The U-GAS® gasification technology, a single stage fluidized bed gasifier developed by the Gas Technology Institute (GTI), was designed to process all ranks of coals and provide a synthesis gas (syngas) of low-to-medium heating value. The fuel flexibility of the gasifier allows for gasifying less expensive fuels, including all ranks of coals, petroleum cokes, biomass, and industrial wastes, fed either individually or in combination. Gasifier fuel flexibility allows industry to adapt to the rise and fall of fuel costs in order to maintain a cost effective operation.

The schematic U-GAS gasifier is shown in Figure 1.4. In a U-GAS® based gasification facility, a lock hopper system supplies dry fuel into the gasifier, where the fuel is reacted with

steam and air or oxygen at temperatures from 840°C to 1,100°C (1,550°F to 2,000°F). The gasifier's operating pressure depends largely on the syngas' end use, ranging anywhere from 3 to 30 bar (40 to 435 psia). After appropriate gas cleaning, the syngas can be used for heating applications, generating power, or making chemicals or fuels. When the operating temperature of the gasifier is high enough to begin melting the fuel ash (mineral content), the concentration of ash particles within the gasifier increases until a point where the ash particles cluster together, thus forming larger particles which are selectively removed from the bed. Ash is removed from the fluidized bed by gravity (when the conglomerated particle's weight becomes greater than the upward force of the fluidizing gas), and falls into a lock hopper system for depressurization and subsequent disposal. This gasifier design ensures that the larger (more dense) ash particles exiting the gasifier contain minimal amounts of carbon (less than 5%), and that 95% or more of the fuel's carbon is gasified. The introduction of the reactant gases (steam and air or oxygen) are introduced at the bottom of the gasifier, through a distribution grid, and at the ash discharge port in the center of the distribution grid.

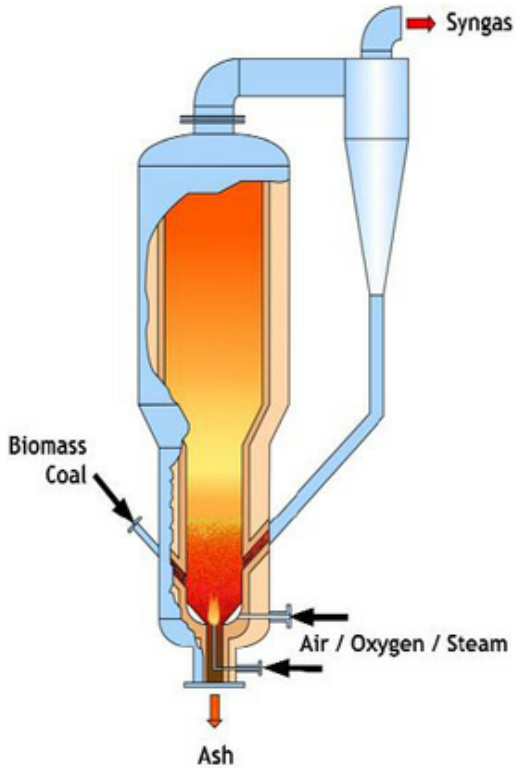

Figure 1.4 The U-GAS Gasifier Schematic (Source: Gas Technology Institute)

1.2.3.2 Moving-Bed Gasifiers

In moving-bed gasifiers, large coal particles move slowly downward through a bed while reacting with gases moving in the opposite direction going upward through the bed. Coarse particles are used in moving-bed gasifiers to ensure good bed permeability and help to avoid excess pressure drop and chemical burning. Reactions within the gasifier occur in different "zones". In the "drying zone" at the top of the gasifer, the entering coal is heated and dried, while cooling the product gas before it leaves the reactor. The coal is further heated and devolatized by the higher temperature gas as it descends through the "carbonization zone". In the next zone, the "gasification zone", the devolatized coal is gasified by reaction with steam and carbon dioxide. Near the bottom of the gasifier, in the "combustion zone", which operates at the highest temperature, oxygen reacts with the remaining char. Figure 1.5 shows schematic of a counter-current moving-bed gasifier.

Moving-bed gasifiers operate in two different modes. In the dry-ash mode of operation (e.g., Lurgi dry ash gasifier), the temperature is moderated to below the ash-slagging temperature by reaction of the char with excess steam. The ash below the combustion zone is cooled by the entering steam and oxidant (oxygen or air) and produced as a solid ash. In the slagging mode of operation (e.g., British Gas/Lurgi or BGL gasifier), much less steam is used, and as the result, a much higher temperature is achieved in the combustion zone, melting the ash and producing it in the form of a solid slag. The moisture content of the fuel is the main factor which determines the discharge gas temperature. Lignite, which has very high moisture content, produces raw gas at a temperature of around 600 °F. Lower moisture bituminous coal produces gas temperatures of over 1000 °F. Typically, the product gas leaving the gasifier is quenched by direct contact with recycle water to condense and remove tars and oils. After quench, heat can be recovered from the gas by generation of low pressure steam.

Moving-bed gasifiers share the following characteristics:

- Relatively low oxidant (oxygen or air) requirement
- Less complex feedstock preparation with the use of coarse coal particles
- Product gas at relatively low temperatures, thus no need for using expensive heat recovery equipment
- Suitable to handle coals with high reactivity and moisture
- Limited ability to handle coal fines

- Modifications of design may be needed to avoid caking coals
- Hydrocarbon liquids such as tars and oils are produced as byproducts
- High "cold-gas" thermal efficiency, when the heating value of the produced hydrocarbon liquids is accounted for
- High methane content in product gas

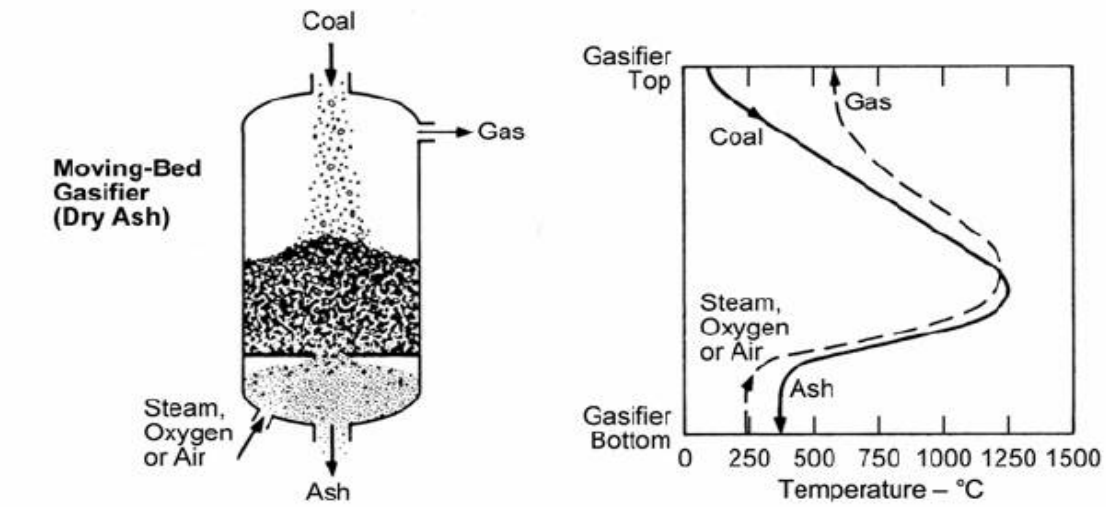

Figure 1.5 Schematic of a counter-current moving-bed gasifier (Holt, 2004)

A typical example of moving-bed gasifier is Lurgi Gasifier, shown in Figure 1.6. The Lurgi gasifier is a pressurized, dry-ash, moving bed gasifier that produces syngas from lump coal, steam, and oxygen as an oxidant. A high ratio of steam to oxygen helps moderate the temperature such that the ash does not melt, but rather is removed as dry ash. More reactive feedstocks are preferred due to the relatively low-temperature operation. Coal enters the top of the gasifier through a lock hopper and is handled by a rotary distributor as it begins its descent through the gasifier. Steam and oxygen enter from the bottom, while ash is removed at the bottom by a rotating grate and lock hopper. A top temperature of about 1,000°F and bottom temperature of about 1,800°F creates a temperature gradient in the gasifier. Exiting raw syngas at up to 1,000°F is cooled and quenched using recycle water to condense tars and oils. A water jacket cools the gasifier vessel and generates part of the steam needed by the gasifier.

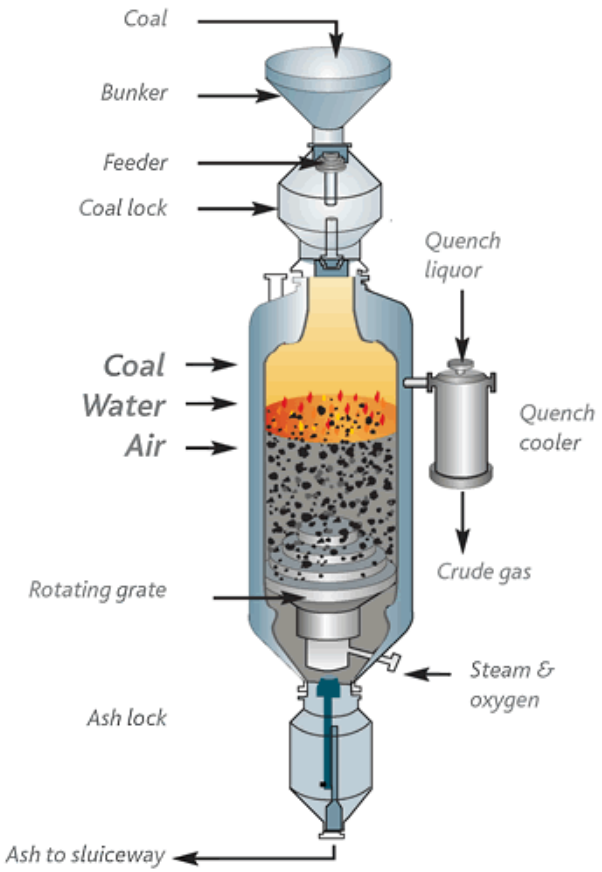

Figure 1.6 Schematic of the Lurgi moving-bed gasifier

1.2.3.3 Entrained-Flow Gasifier

In entrained-flow gasifiers, the speed of flow (air or oxygen) is fast, resulting in entraining the coal particles from the injection location to the exit. It can be designed as either upflow or down-flow system. The coal and oxidant are fed either from top or bottom of the gasifier. Gasifiers of this type typically operate at very high temperatures to melt coal ash into inert slag. The fine coal feed and high operating temperature allow the gasification reaction to occur at a very high rate (the typical residence time is on the order of few seconds), with high carbon conversion efficiencies (98-99.5%). The tar, oil, phenols, and other liquids produced from devolatization of coal inside the gasifier are decomposed into hydrogen (H_2), carbon monoxide (CO) and small amounts of light hydrocarbon gases. Entrained-flow gasifiers have the ability to handle practically any coal feedstock and produce a clean, tar-free, syngas. The fine coal feed can be fed to the gasifier in either a dry or slurry form. The former uses a lock hopper system, while

the latter relies on the use of high-pressure slurry pumps. The slurry feed is a simpler operation, but it introduces water into the reactor which needs to be evaporated. The result of this additional water is a product syngas with higher H_2 to CO ratio, but with a lower gasifier thermal efficiency. The feed preparation system is designed along with other process design alternatives, for a particular application. Figure 1.7 presents an illustration of an entrained-flow gasifier.

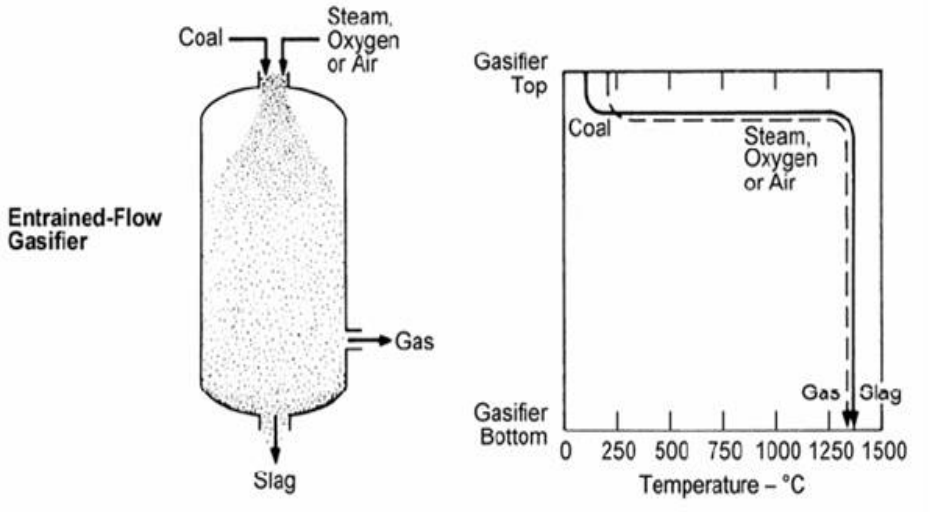

Figure 1.7 Schematic of an entrained-flow gasifier (Holt, 2004)

Entrained-flow gasifiers typically exhibit the following characteristics:

- Fuel flexibility, can accept a variety of solid feedstocks
- Large oxidant requirements
- Can either be oxygen or air blown, but most commercial plants are oxygen blown
- Uniform temperature within the reactor
- Slagging operation
- Short reactor residence time
- Higher carbon conversion, but lower coal gas efficiency
- High level of sensible heat in product gas; heat recovery is required to improve efficiency
- Environmentally most benign; produced syngas consists of mainly H_2, CO and carbon dioxide (CO_2) with trace amount of other contaminates which can be removed downstream of the reactor

Examples of entrained-flow gasifiers:

(1) Shell Coal Gasification Process (SCGP)

Shell's coal gasification technology uses a dry-feed, pressurized, entrained-flow, slagging gasifier that operates on a wide variety of feedstocks. Figure 1.8 shows the schematic of Shell gasifier. Dried, pulverized coal is fed to the gasifier through pressurized lock hoppers using a transport gas (syngas or nitrogen). Preheated 95% pure oxygen and steam (as a moderator) are mixed and fed to the injector. The coal reacts with oxygen at typical conditions of 2,700-2,900°F and 350-600 psi to produce syngas consisting of only small amounts of carbon dioxide (CO_2) and no hydrocarbon liquids or gases. Theraw syngas leaves the gasifier at a relatively high temperature (typically 2,500-2,700°F) and is sent on to a syngas cooler for heat recovery, generating high-pressure superheated steam. The syngas cooler typically consists of three sections—superheat, convection, and economizer. To protect the syngas cooler from fouling, corrosion, and erosion, the hot raw syngas leaving the gasifier is first quenched with cooler, recycled product gas to convert any entrained molten fly slag to a hardened solid material prior to entering the syngas cooler. The bulk of the fly ash contained in the raw syngas leaving the syngas cooler is removed from the gas using commercial filter equipment or cyclones. Any remaining fly ash is captured downstream with a wet scrubber. The syngas cooler is an integral part of Shell gasifier technology.

The Shell technology uses a refractory-lined reactor vessel, equipped with an inner membrane wall consisting of circulating water/steam-filled tubes. During operation, ash is converted into molten slag. The molten slag, cooled by the membrane wall, vitrifies to form a protective layer against slag erosion of the refractory. This specific reactor design contrasts most rival gasification processes, which have brick refractory walls inside the gasifier that are gradually eroded by the hot slag and must be routinely replaced. Shell's gasifier membrane wall is said to have a 20-year life. Inner reactor wall temperature is controlled by circulating water through the membrane wall, producing steam. Produced slag flows down the reactor into a water bath, where it solidifies and is removed through a lock hopper as slurry.

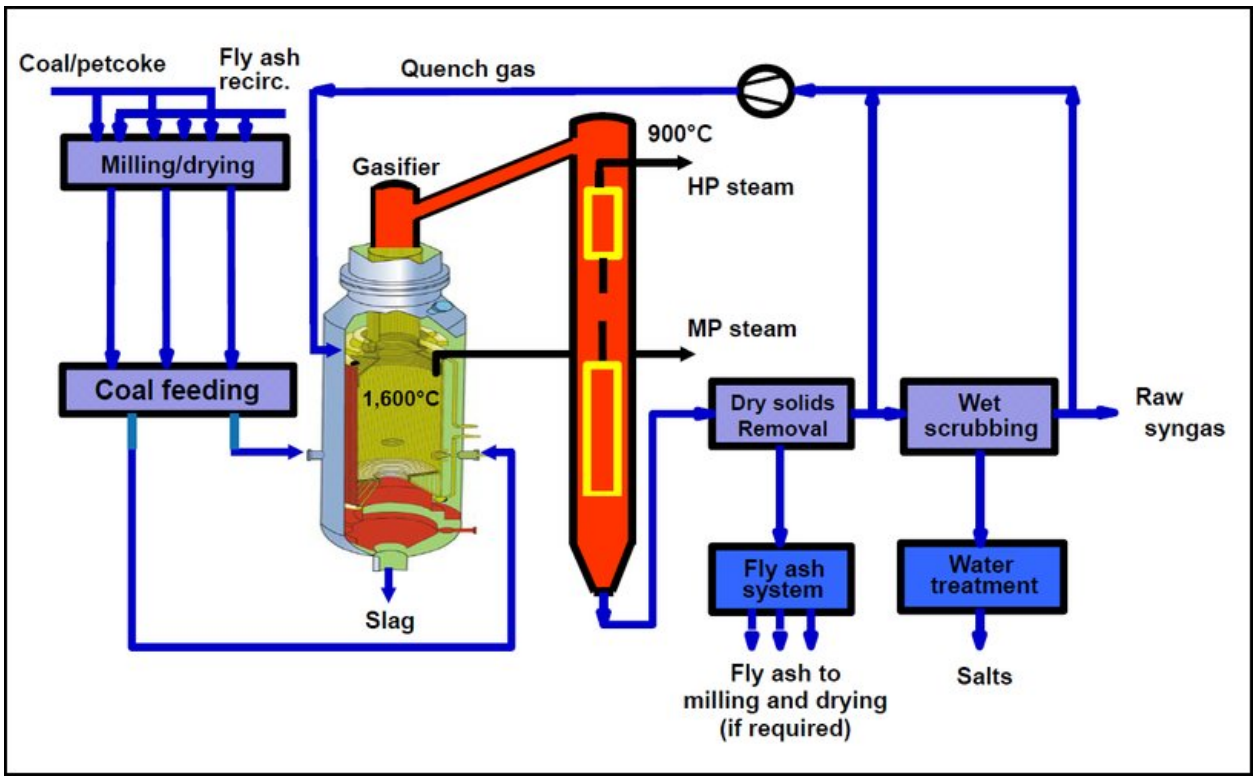

Figure 1.8 Schematic of the Shell gasifier

(2) General Electric Gasifier (Previously Texaco gasifier)

GE gasification uses a single-stage, downward-feed, entrained-flow refractory-lined reactor to produce synthesis gas (syngas) from a coal/water slurry (~ 65% in wt) and oxygen (> 95% pure). The slurried feedstock is pumped to a custom-designed injector mounted at the top of the gasifier. The coal reacts exothermically with oxygen at high temperature (~ 2,200 to 2,700°F) and pressure (>300 psi) to form syngas and slag. No hydrocarbon liquids are produced in these high temperature conditions. The syngas produced contains mostly hydrogen (H_2) and carbon monoxide (CO). The raw syngas leaving the gasifier can be cooled by a radiant and/or convective heat exchanger and/or by a direct quench system, where water or cool recycled gas is injected into the hot raw syngas. The radiant cooling design uses a soot-tolerant radiant syngas cooler that generates high-pressure steam. Slag is quenched in a water pool located at the bottom of the reactor vessel, and removed through a lock hopper. This design maximizes heat recovery as well as CO production. The syngas is further cooled after leaving the gasifier by a water scrubber to recover the fine particulate matter and char for recycle to the gasifier, before the gas is sent on to downstream processing.

A direct quench system uses an exit gas water quench. Hot gas exiting the gasifier is contacted directly with water via a quench ring; it is then immersed in water in the lower portion of the gasifier vessel. The cooled, saturated syngas is then sent to a scrubber for soot and particulate removal. The quench design is less efficient, but also less costly, and it is commonly used when a higher hydrogen to CO ratio syngas is required.

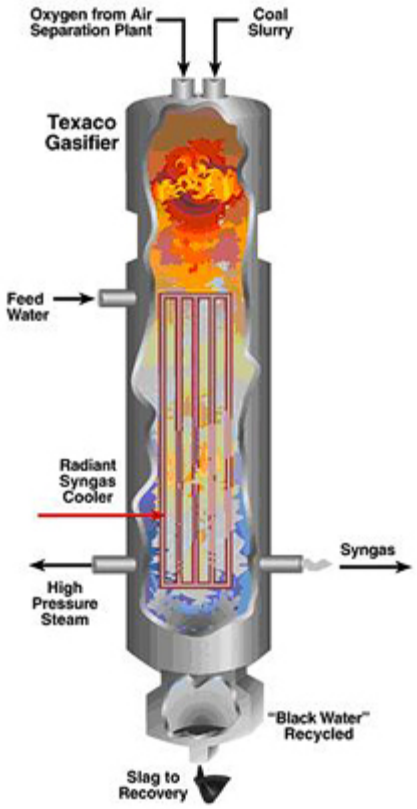

Figure 1.9 Schematic of the General Electric gasifier

(3) Conoco-Phillips (E-Gas) Gasifier

The E-Gas coal gasifier is a pressurized, upflow, slurry-feed, entrained slagging design with a unique two-stage operation. Wet crushers produce slurries from the raw feed coal. Coal slurry concentrations typically range from 50 to 70% depending on the inherent moisture and quality of the feed coal. About 75% of the total slurry feed is fed to the first (or bottom) stage of the gasifier through mixer nozzles, along with 95% pure oxygen. This stage involves highly exothermic oxidation reactions (i.e., combustion) and operates at typically 2,600°F and 400 psig. These conditions do not allow the formation of hydrocarbon gases and liquids. Ash in the coal melts and exits through a taphole at the bottom of the gasifier into a water quench, forming

an inert vitreous slag product. The hot syngas from the first stage then enters the second (top) stage where the remaining slurry feed is injected. Endothermic gasification and devolatization reactions take place at 1,900°F, resulting in the formation of some hydrocarbons in the product gas and the production of char, which are both recycled to the first stage where they are readily gasified. The product gas exits the gasifier at 1,900°F and is cooled in a fire-tube cooler to 1,100°F, generating saturated steam. Particulates and chlorides are removed from the cooled syngas in a wet scrubber and char is recycled to the gasifier. The syngas is then treated for removal of carbonyl sulfide (COS) and hydrogen sulfide (H_2S) before being used for energy conversion or other applications.

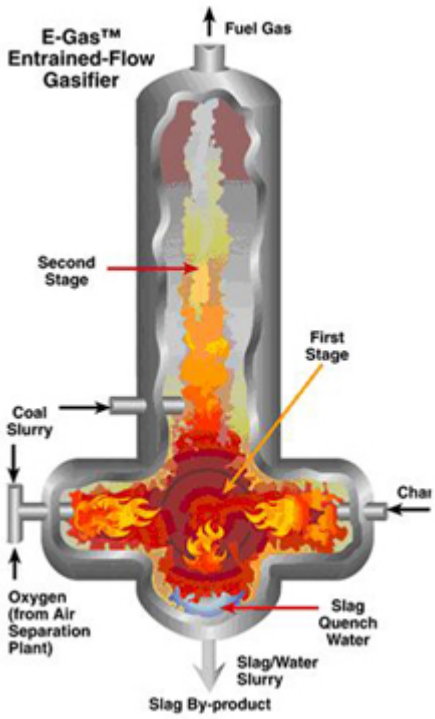

Figure 1.10 Schematic of the Conoco-Phillips (E-Gas) gasifier

(4) PRENFLO (PREssurized ENtrained-FLOw) Gasifier

PRENFLO, which operates at the pressure above 40 bar, is a further development of the Kopper-Totzek process developed in the 1940's. PRENFLO was developed by Uhde, which later merged with Krupp Koppers. PRENFLO is a one-stage, high pressure, dry-fed, oxygen-blown, slagging gasifier. The gas temperature inside a PRENFLO gasifier can exceed 2000°C

(3600°F) and uses a membrane wall. PRENFLO gasifiers are used in the world's largest solid-feedstock-based IGCC power plant in Puertolanno, Spain.

Figure 1.11 shows an illustration of a PSG (PRENFLO with Steam Generation) gasifier. Coal is injected together with oxygen and steam through several injectors in the lower part of the gasifier. Raw syngas is then sent through the waste heat boiler to cool down and produce steam. The exit gas temperature is 1350-1600°C (~2450-2900°F). In a PDQ (PRENFLOW with Direct Quench), illustrated in Figure 1.11b, coal and oxygen/steam are injected in the upper part of the gasifier. Raw syngas is quenched by water in the direct quench section in the lower part of the gasifier. The syngas is cooled down to 200-250°C (~390-480°F).

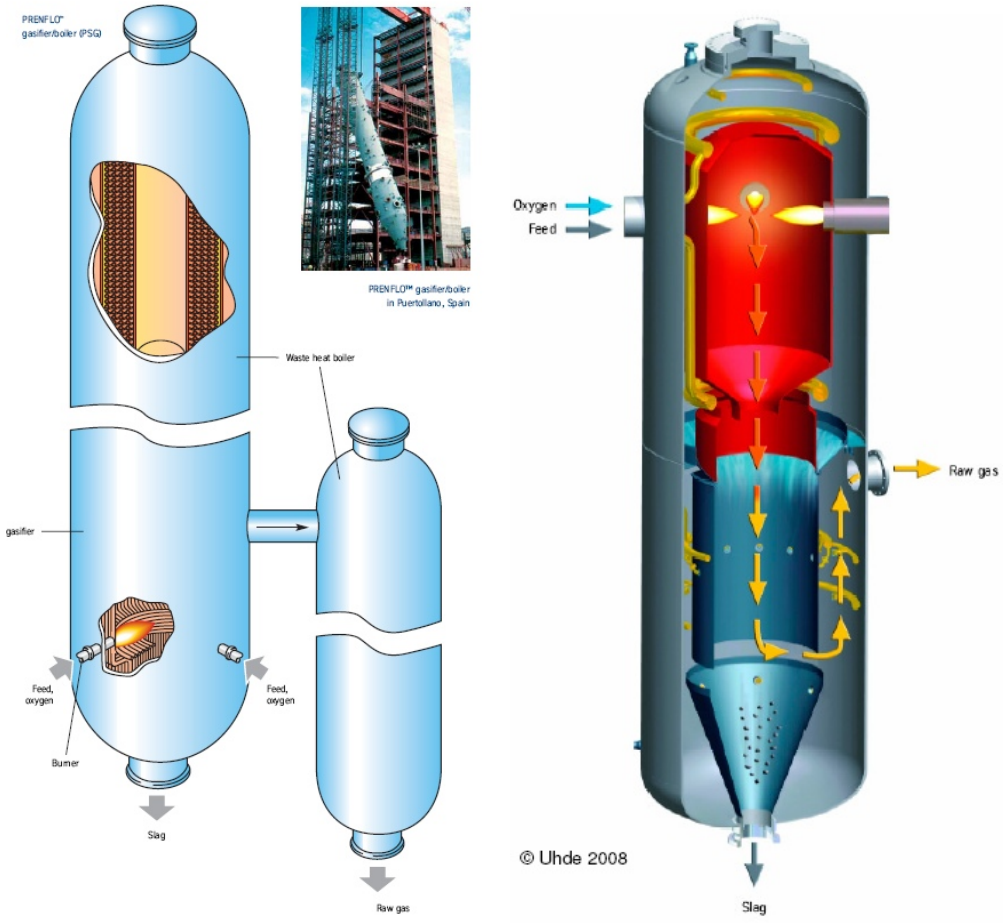

(a) PSG (b) PDQ

Figure 1.11 (a) PRENFLO with Steam Generation (PSG) and (b) PRENFLO with Direct Quench (PDQ)

(5) Siemens Gasifier

The Siemens gasifier, shown in figure 1.12, is a dry-feed, pressurized, entrained-flow reactor, which can be supplied with either a refractory lining for low ash feedstocks or with a cooling screen in the gasification section of the gasifier. The cooling screen consists of a gas-tight membrane wall structure that is studded and refractory-lined with a thin layer of silicon carbide for protection. The molten slag formed in the gasifier chamber cools and solidifies as it contacts the cooling screen, forming a compact slag layer, protecting it from further damage by the flowing slag. Once a slag layer is formed over the cooling screen, subsequent hot slag flows down the reactor chamber into the quench section of the gasifier where it solidifies upon contact with water from a ring of quench nozzles and is removed through a lock hopper. Feedstocks with an ash content of greater than two percent by weight are preferred when using the cooling screen design; in this scenario the gasifier can achieve carbon conversion rates higher than 99%. Siemens gasifier is suited for coals from anthracite to lignite, as well as biomass, petcoke, and residual oil.

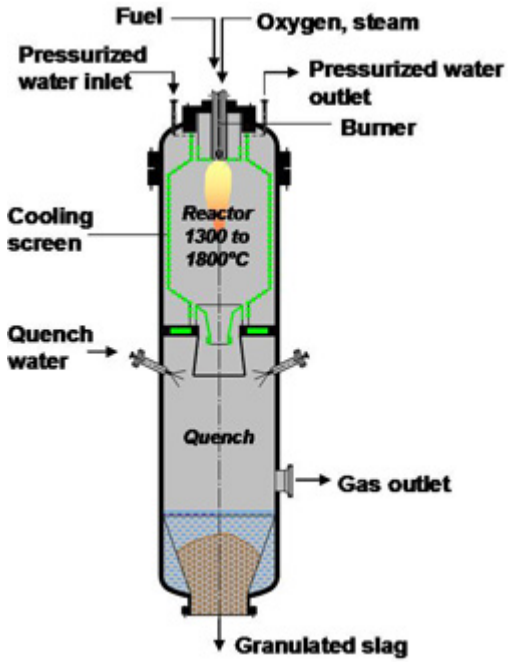

Figure 1.12 Schematic of the Siemens gasifier

(6) MHI (Mitsubishi Heavy Industries) Gasifier

The MHI gasifier is a pressurized, dry-feed, upflow, entrained-flow slagging reactor with a unique two-stage operation. The current focus of the effort is on air-blown (or enriched air blown) IGCC application. R&D activities are being carried out to develop an oxygen-blown system for coal to fuels and chemicals applications.

Figure 1.13 shows a simplified drawing of the MHI gasifier. The reactor consists of two sections (or stages): a lower combustor and an upper reductor. Dry milled coal is fed at two separate points into the gasifier with a portion being fed into the combustor together with air (or enriched air) where it is burned to produce carbon monoxide (CO) and carbon dioxide (CO2), plus water vapor. The temperature generated at the combustor is sufficiently high to melt the coal ash. The molten slag falls to the bottom of the gasifier where it is quenched in a water bath and then removed using a lock hopper system. The gas produced in the combustor rises to the reductor where the remaining coal is added, without any additional air. At the reductor stage, heat provided by the hot combustor gas is used to drive the endothermic gasification reactions. The reductor is operated at a lower temperature than the combustor. Any molten ash carried over by the upward gas is solidified. The syngas produced exits the reductor through a syngas cooler generating steam. A cyclone is used downstream of the sygnas cooler to collect the char and recycle it to the combustor section to increase the overall carbon conversion efficiency. The raw syngas leaving the reductor section of the gasifier is typically at 2,200°F, high enough in temperature that very little hydrocarbon gases and liquids are formed.

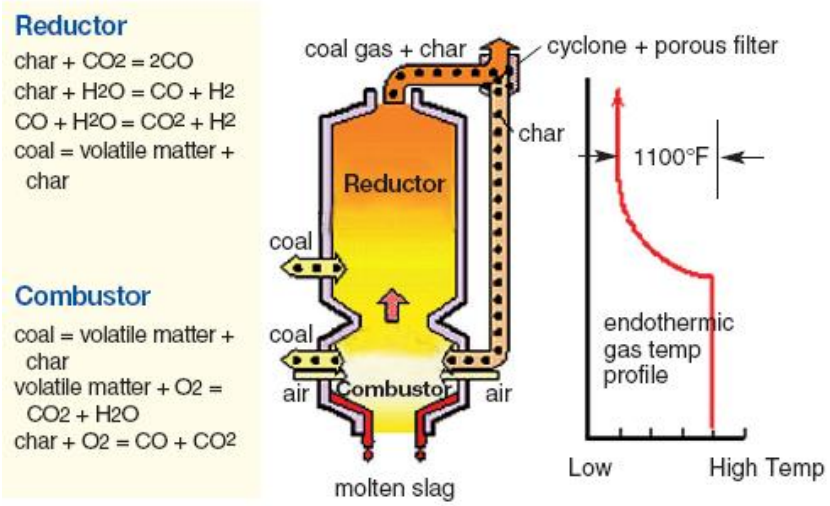

Figure 1.13 Schematic of the MHI gasifier

(7) ECUST (East China University of Science and Technology) Gasifier

In the early 1990s, the Institute of Clean Coal Technology (ICCT) at the ECUST began its development of coal gasification technology in partnership with the Yankuang Coal Mine Group. The ECUST gasifier can accommodate either coal-water slurry feeding, or dry-feeding (via N_2 or CO_2) applications. The entrained flow gasifier incorporates opposed multi-burner (OMB) technology, and a water-quench in a down-flow configuration. Operating conditions are dependent upon dry/wet feed, as well as the end product. The gasifier temperature and pressures fall in the range of 1,300 to 1,400°C, and 1 to 3 MPa. Figure 1.14 shows schematic of ECUST gasifier.

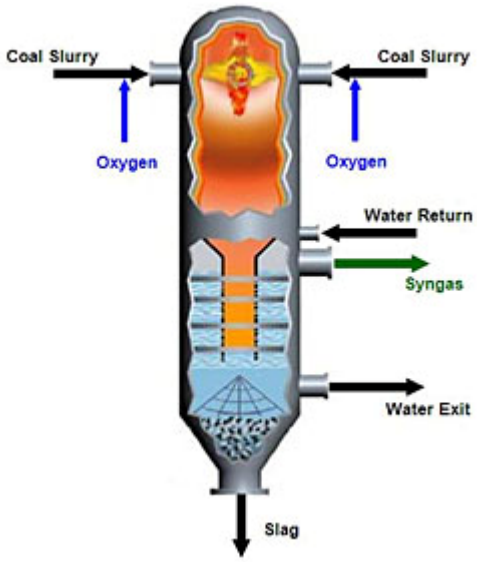

Figure 1.14 Schematic of the ECUST gasifier

(8) HCERI (Huaneng Clean Energy Research Institute) Gasifier

The Huaneng Clean Energy Research Institute (HCERI), formerly the Thermal Power Research Institute (TPRI), has developed gasification technology that is being used in numerous gasification facilities throughout China. HCERI gasification technology is a two-stage dry-feed and water-cooled gasifier, as shown in figure 1.15. The first stage of the gasifier reacts 80 to 85% of the coal feed with pure oxygen and steam. The steam and the remaining 15 to 20% of the feed coal are fed into the second stage, which operates at about 1400 to 1500°C. The temperature of the outlet syngas is decreased to 900°C due to the second stage's endothermic reaction - helping the slag particles to solidify, as well as improving the gasifier's thermal efficiency. The gasification technology can also be applied to other feedstocks, such as petcoke,

and low quality coals with high sulfur content. Commercially available sulfur capture equipment can effectively remove up to 99.9% of the sulfur from a gasification gas stream, ensuring the plant's environmental compliance.

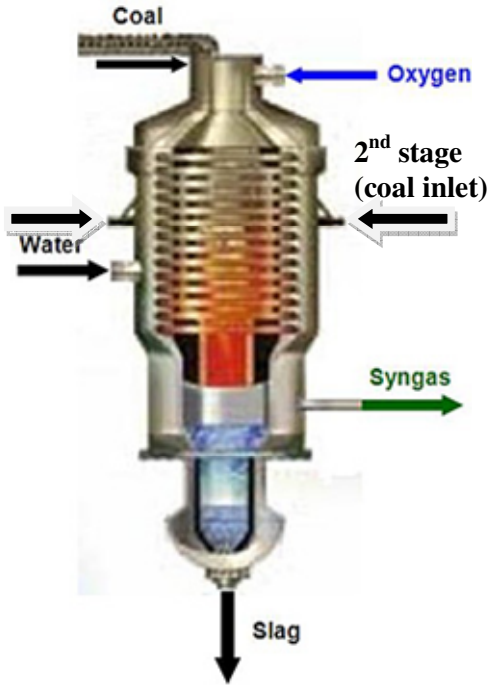

Figure 1.15 Schematic of the HCERI gasifier

(9) EAGLE (Energy Application for Gas, Liquid, and Electricity) Gasifier

EAGLE, an acronym that stands for Energy Application for Gas, Liquid, and Electricity, is a project funded by the Electric Power Development Company of Japan, in collaboration with Japan's New Energy and Industrial Technology Development Organization (NEDO). The EAGLE gasifier is a two-stage, pressurized, upflow, oxygen-blown, entrained-flow gasifier with the bottom stage operating in the slagging mode, with a second non-slagging stage on top to increase overall gasification efficiency. Figure 1.16 (a) shows a schematic of the gasifier. Being a two-stage reactor, the EAGLE gasifier is similar to the E-Gas™ gasifier and MHI's gasifier. An unique feature of the EAGLE gasifier is its tangential feed injection and burner system which allows a spiral flow pattern to be developed along the inter-reactor wall between the upper and the lower reactor stage. This flow pattern is claimed to (1) create a longer residence time for the coal particles, and thus increase the overall gasification efficiency, and (2) help facilitate slag removal as the spiral flow pattern creates a pressure differential between the wall

and the center of the gasifier which help with drawing the slag toward the bottom of the gasifier for discharge. The EAGLE gasifier uses a pneumatic system for dry coal fine feeding, using either nitrogen or recycled gas. Its reactor interior is protected by a water-cooled membrane wall; both features are similar to the Shell and Siemens designs.

Figure 1.16 (b) shows a simplified drawing of the overall EAGLE gasifier vessel, shown with a radiant cooler on top of the gasifier reactor. The gasifier operates the first (bottom) stage at high-temperature slagging conditions with only part of the coal feed, but a relatively larger amount of oxygen.The remaining coal and oxygen are added to the second (top) stage, where the hot gas drives the endothermic gasification reactions. The relative amount of coal/oxygen feed distribution into each stage depends on the nature of the coal. The distribution is optimized for high gasification efficiency versus stable slag discharge. The second stage is non-slagging. The particulate matter in the syngas contains unreacted char and dry ash. They are removed from the raw syngas downstream of the syngas cooler and recycled to the first stage. In this manner, almost all the ash in the system is removed as slag.

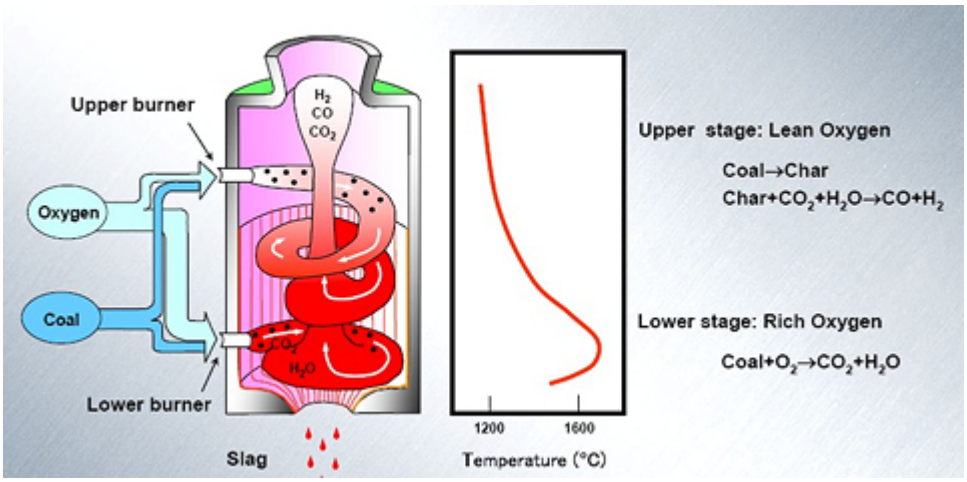

Figure 1.16 (a) Schematic of the EAGLE gasifier

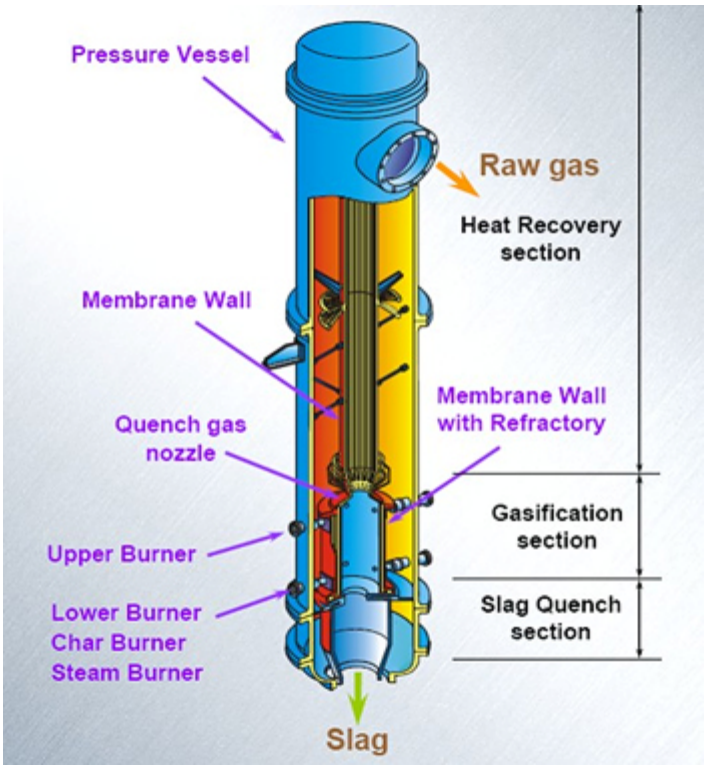

Figure 1.16 (b) Schematic of the Overall EAGLE Gasifier Vessel

1.2.3.4 Transport Gasifier

The Kellogg Brown & Root (KBR) transport gasifier, shown in Figure 1.17, is a circulating fluidized-bed reactor which operates in either air or oxygen blown modes. The design is based on fluidized catalytic cracking (FCC) technology developed for refinery gasoline production in the 1940s. The gasifier consists of a mixing zone, riser, disengager, cyclone, standpipe, loopseal, and J-leg. Steam and air/oxygen are mixed together and injected in the lower mixing zone while fuel, sorbent (for sulfur capture), and additional air or oxygen and steam are added in the upper mixing zone. The steam and air/oxygen, fuel, sorbent, and solids from the standpipe are mixed together in the upper mixing zone. The gas and solids move up the riser before entering the disengager which separates larger particles by gravity. Most of the solids flow from the disengager into the standpipe, while the remaining solids flow to the cyclone and are removed. The gas then exits the gasifier and enters the primary gas cooler and final particulate cleanup. Collected solids are recycled back to the gasifier mixing zone through the loopseal, standpipe, and J-leg. The solids circulation is maintained with recycled synthesis gas (syngas) or nitrogen as aerating gases. The gasifier operates with an internal temperature

range of 1,500 to 1,950°F, depending on the fuel. The gasifier produces coarse ash extracted from the reactor standpipe. The ash is cooled and discharged from the reactor via a lock hopper. The gasifier is constructed of refractory-lined pipe, which allows less expensive metal to be used in the reactor shell. The gasifier operates at a high solids recirculation rate which results in excellent gas-solids contact in a highly turbulent environment, with high heat and mass transfer rates. The KBR transport gasifier is particularly well suited for low-rank, high-moisture, high-ash coals due to its low temperature operation and high circulation rate. The air-blown operation may be preferable for power generation, while the oxygen-blown operation may be better suited for chemical and fuels production.

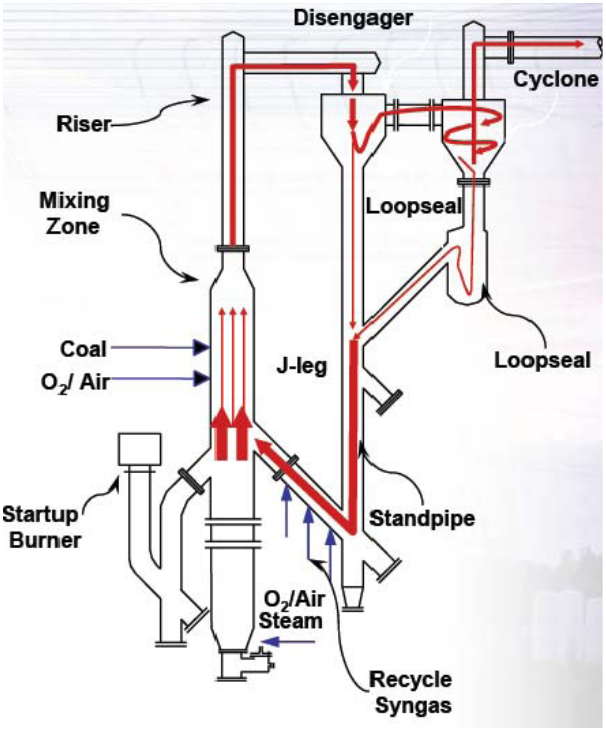

Figure 1.17 Schematic of the Kellogg Brown & Root (KBR) transport gasifier.

Table 1.2 Summary of coal gasifier comparisons.

Gasifier Type	Moving-bed	Fluidized-bed	Entrained-flow	Transport
Process Description	Coal is fed from top and moves down by gravity. Air and steam are injected from bottom.	Solid particle bed is fluidized by air and steam.	Solid particles are mixed thoroughly with air and steam and are entrained by the flow.	Circulating-bed reactor consist of mixing zone, riser, cyclones, and stand pipe
Technology Providers	BGL, Lurgi	HTW, KRW	Conoco-Phillips (E-Gas), GE, Shell, PRENFLO, Future Energy, and Siemen.	Kellogg-Brown Root (KBR)
Fuel feed:				
Size	6-50mm	6-10mm	<100 μm	< 400 μm
Caking coal	Yes	Yes	No	Yes
Coal rank	Any	Any	Dry feed -- any. Slurry feed -- high rank.	Any
Operating issues:				
Syngas temperature	Low (around 600ºC)	Moderate (1000ºC)	High (1300-1600ºC)	Moderate (1000ºC)
Oxidant demand	Low	Moderate	High	Moderate
Steam demand	High	Moderate	Low	Moderate
Throughput	Low (residence time is 30 minutes to 1 hour)	Low	High (residence time is 3-5 seconds)	High
Feed rate	Low	Low	High	High
Internal moving	Yes (needs reactor	No	No	No

1.2.4 Gasifiers for Special Applications

Although the above gasifiers work for a wide range of applications, some applications require a specialized gasifier or gasification process to be used, including:

1.2.4.1 Advanced Coal Gasifiers

Advanced coal gasifiers are compact and low-cost gasifier, with high carbon conversion and increased thermal efficiency. One typical example is the Rocketdyne Gasifier. The Rocketdyne gasifier, shown in Figure 1.18 (a), is a single-stage, pressurized, oxygen-blown, plug-flow entrained reactor, capable of achieving carbon conversions approaching 100%. The gasifier uses Rocketdyne rocket technology to enable a compact, low-cost, long-life and highly efficient gasifier design.

The gasifier includes several design features borrowed from rocket fuel engine technology. Figure 1.18 (b) shows the various components of a Rocketdyne gasifier that can be

developed by patterning after similar, but well proven, features within a rocket engine. These include a rapid mix injector design that can use multi-element injection to rapidly mix the coal feed with steam and oxygen, and disperse them across the reactor cross section. By doing so, it enables the injected coal particles to be heated rapidly to high temperature, and allows the gasification reactions to take place in a very short residence time. This rapid mixing is said to greatly minimize the mass transfer and kinetic limitations to gasification reactions. The result is a gasification system that can achieve rapid and complete carbon conversion with less oxygen required. This feed injection system is being developed in conjunction with the development of a high-pressure solids pump and a dense phase flow splitter capable of bulk feeding and distributing the pulverized coal fines to the gasifier at a high pressure.

Another engineering feature borrowed from the rocket engine experience is the gasifier cooling liner design, which allows the internal reactor wall to be cooled and protected by forming a layer of solidified slag on its inside surface. This type of ceramic matrix composite (CMC) liner helps to protect the refractory underneath, enabling an operational life much longer than the six- to 18-month life typically experienced for non-cooled refractory brick in existing gasifiers.

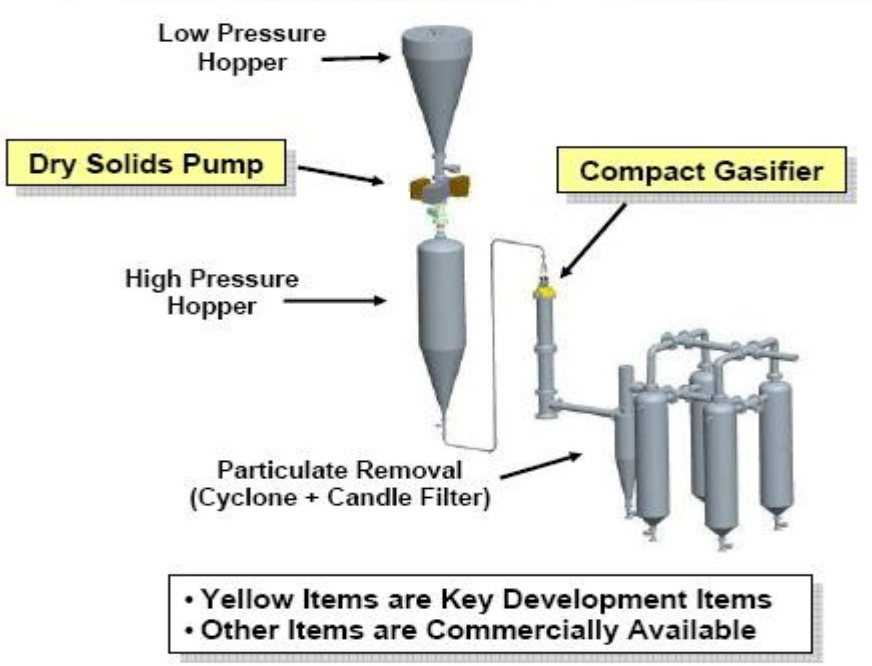

Figure 1.18 (a) A conceptual drawing of the Rocketdyne Gasification System (source: Pratt & Whitney Rocketdyne)

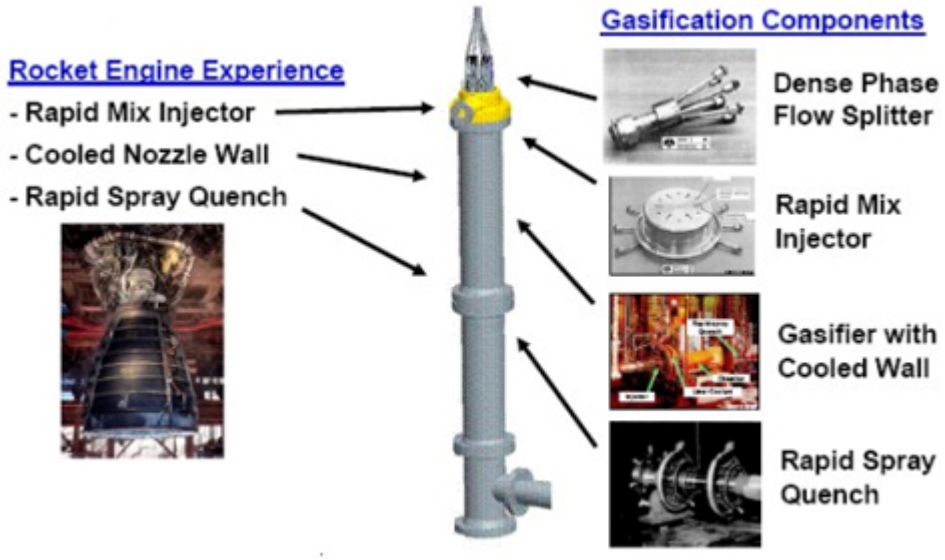

Figure 1.18 (b) Attributes of Rocketdyne Gasifier (source: Pratt & Whitney Rocketdyne)

1.2.4.2 Westinghouse Plasma Corporation (WPC) Plasma Arc Gasifier

Plasma, referred to as the "fourth state of matter," is a very high temperature, highly ionized (electrically charged) gas capable of conducting electrical current. WPC has been developing plasma gasification technology over the last decade, and recently has been investigating the application of their plasma technology to gasifiy coal. Figure 1.19 shows a schematic of the WPC plasma gasifier. The gasifier is heated by a plasma torch system located near the bottom of the reactor vessel. In the gasifier, the coal feed is charged into the vertical reactor vessel at atmospheric pressure. The gasifier is either refractory lined or water cooled on the outside, in which case the refractory is used only in the lower melting zone. A superheated blast of air, which may be enriched with oxygen, is provided to the bottom of the gasifier, at the stoichiometric amount required for gasification. The amount of air fed is such that the superficial velocity of the upward flowing gas is low, and that the pulverized feed materials can be fed directly into the reactor. Additional air and/or steam can be provided at different levels of the gasifier to assist with pyrolysis and gasification. The temperature of the syngas leaving the top of the gasifier is maintained above 1,000°C. At this temperature, tar formation is eliminated.

Gasification takes place at very high temperatures, driven by the plasma torch system, which is located at the bottom of the gasifier vessel. The high operating temperatures break down the coal and all hazardous and toxic components into their elemental constituents, and dramatically increase the kinetics of the various reactions occurring in the gasification zone,

converting all organic materials into hydrogen (H_2) and carbon monoxide (CO). Any residual materials of inorganics and heavy metals will be melted and produced as a vitrified slag which is highly resistant to leaching.

The potential benefits of WPC Plasma Arc Gasifier over a conventional gasification plant are:

- Greater feed flexibility enabling coal, coal fines, mining waste, lignite, and other opportunity fuels (e.g., biomass and MSW) to be used as fuel without the need for pulverizing
- Air blown and thus an oxygen plant is not required
- High availability (>90%)
- High conversion (>99%) organic matter to synthesis gas (syngas)
- No tar in syngas; syngas of approximately 140 Btu/scf for air-blown design suitable for syngas combustion turbine operation after gas cleanup
- No char, ash or residual carbon; only producing a glassy slag with beneficial value
- Compliant with EPA'snew source emissions standards for nitrogen oxide (NO_X), sulfur oxide (SO_X) particulates, etc.
- Higher thermal efficiency
- Lower carbon dioxide (CO_2) emissions
- Low estimated capital and operations and maintenance (O&M) costs

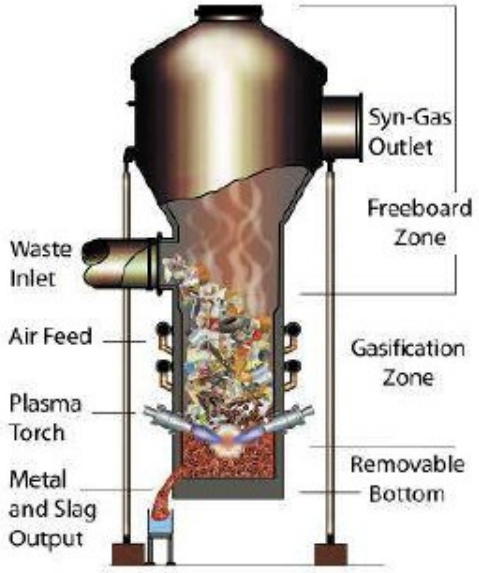

Figure 1.19 Schematic of the WPC plasma gasifier (source: Westinghouse Plasma)

1.2.4.3 Catalytic Gasifiers

Catalysts can be used to enhance the reactions involved in gasification. Many gasifiers must operate at high temperatures so that the gasification reactions will proceed at reasonable rates. Catalysts can also be used to favor or suppress the formation of certain components in the syngas product. The primary constituents of syngas are hydrogen (H_2) and CO, but other products like methane are formed in small amounts. Catalytic gasification can be used to either promote methane formation, or suppress it. Disadvantages of catalytic gasification include increased materials costs for the catalyst itself, as well as diminishing catalyst performance over time. Catalysts can be recycled, but their performance tends to diminish with age. The relative difficulty in reclaiming and recycling the catalyst can also be a disadvantage.

Exxon built and operated a process development unit (PDU) to demonstrate the performance of their catalytic coal gasification to synthetic natural gas (SNG) process at Baytown, Texas, in 1979, using bituminous Illinois No. 6 coal, shown in Figure 1.20.

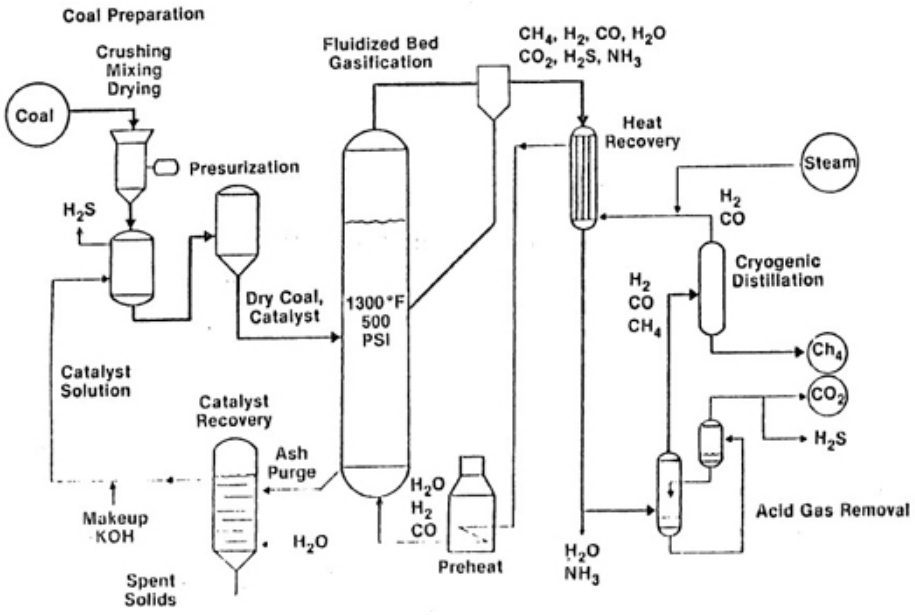

Figure 1.20 Schematic of Exxon PDU (source: Fischer-Tropsch Archive)

The PDU was fully integrated and included facilities for coal preparation, gasification, gas cleanup, methane recovery by cryogenic separation, recycled gas compression/heating, and catalyst recovery. The gasifier was operated at 1,280°F and 500 psig, using 10 to 20 wt% of

potassium salts as the catalyst system, at a nominal combined coal/catalyst feed rate of 132 lbs/hr. High pressure steam was also fed at a typical steam/coal ratio of 1.9. Demonstrated carbon conversion is at 85 to 90%, with an average methane content in the product gas of about 21%.

1.2.4.4 Underground Coal Gasification (UCG)

Underground Coal Gasification (UCG) uses a similar process to that used in surface gasification. The main difference is that in UCG the underground coal seam itself becomes the reactor, so that the gasification of the coal takes place underground instead of in a manufactured gasifier. In the UCG process, injection wells are drilled into an unmined coal seam, and either air or oxygen is injected into the seam along with water. The coal face is ignited, and the high temperatures (about 1,200°C) from the combustion and limited oxygen causes nearby coal to partially oxidize into hydrogen, carbon monoxide (CO), carbon dioxide (CO_2), and minimal amounts of methane (CH_4) and hydrogen sulfide (H_2S). These products flow to the surface through one or more production wells located ahead of the combustion zone. As the face is burned and an area depleted, the operation is moved to follow the seam. Figure 1.21 (a) illustrates the general process of UCG. The technique can be applied to resources that are otherwise not economical to extract and also offers an alternative to conventional coal mining methods for some resources. Compared to the traditional coal mining and gasification, the UCG has less environmental and social impact.

Two different methods of UCG have evolved, and both are commercially available. The first method, based on technology from the former Soviet Union, uses vertical wells and a method like reverse combustion to open up the internal pathways in the coal. The process has been used in several operating facilities and demonstration projects. The second method, tested in European and American coal seams, creates dedicated inseam boreholes, using drilling and completion technology adapted from oil and gas production. It has a moveable injection point known as controlled retraction injection point (CRIP) and generally uses oxygen or enriched air for gasification. Figure1.21 (b) shows the schematic of the CRIP method.

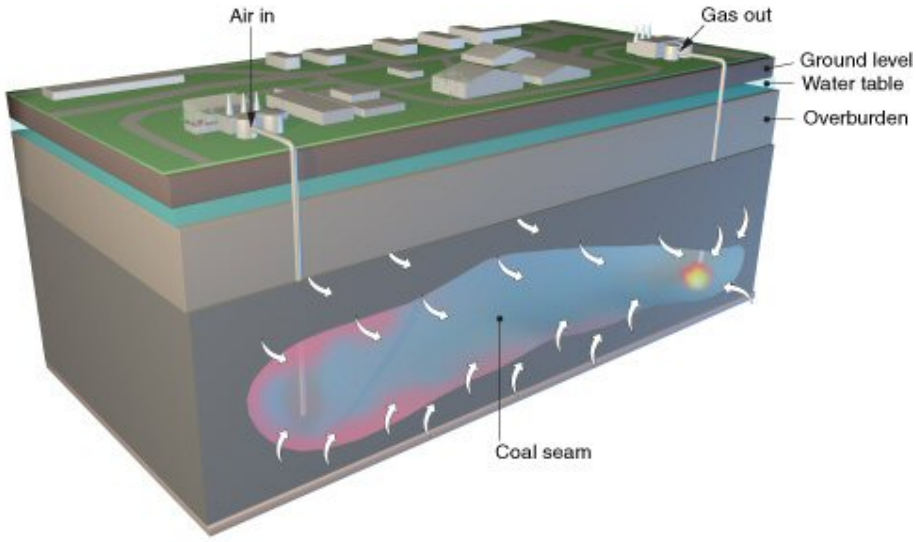

Figure 1.21 (a) The general process of UCG (source: Science & Technology Review)

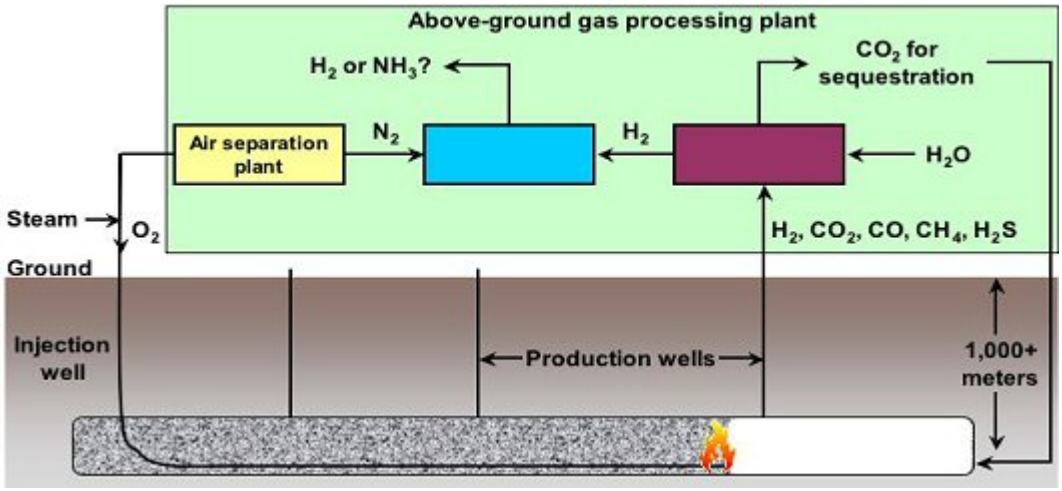

Figure 1.21 (b) Schematic of the CRIP (source: Lawrence Livermore National Laboratory)

1.2.5 Coal Combustion or Gasification

Figure 1.22 presents the typical processes undergone by coal particles in gasification. The combustion of coal particles involves two major steps: (a) thermal decomposition (pyrolysis and devolatilization) and (b) combustion of solid residue from the first step. Coal particles undergo pyrolysis when they enter the hot combustion environment. Moisture contained in the particles boils and leaves the particles once the particle temperature reaches the boiling temperature. The volatiles are then released as particle temperature continues to

increase. This volatile release process is called devolatilization. The volatiles are then thermally cracked into lighter gases, such as H_2, CO, C_2H_2, CH_4, etc. These lighter gases can react with O_2, releasing some of the heat needed for the pyrolysis. With only char and ash left, the particles undergo combustion to produce CO and CO_2, leaving only ash. The thermal decomposition occurs rapidly, while the combustion step is slow.

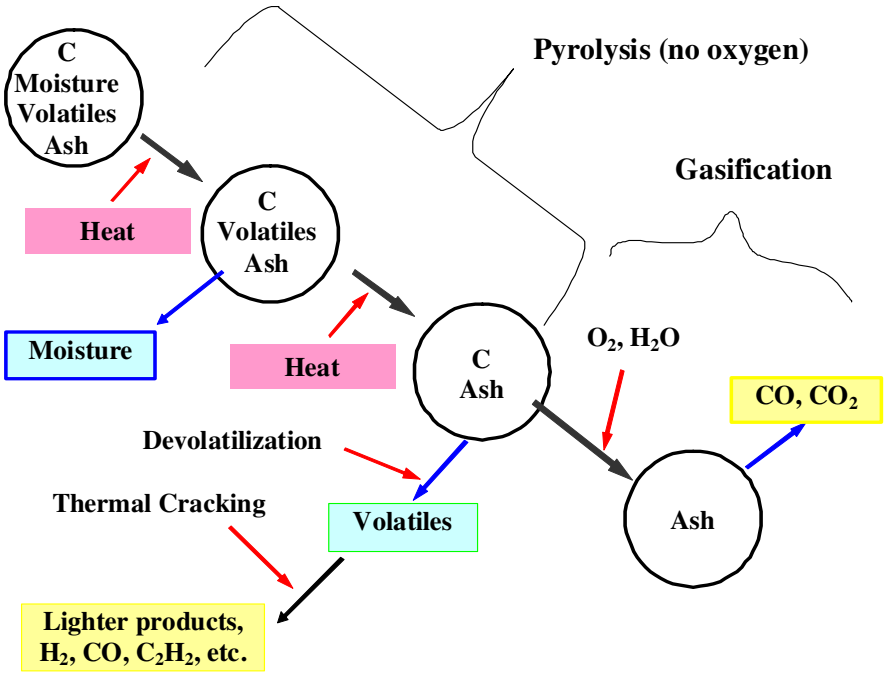

Figure 1.22 Simplified global gasification processes of coal particles (sulfur and other minerals are not included in this figure). Heat can be provided externally or internally through combustion of char, volatiles, and CO.

1.2.5.1 Coal Structure

Coal consists of (i) a large matrix of aromatic clusters connected by aliphatic bridges, (ii) aliphatic and carbonyl side chain attachments to the aromatic clusters, and (iii) some weakly bonded components sometimes referred to as the mobile phase (Smith et al., 1994 andKrevelen, 1981). The aromatic clusters consist largely of carbon, as well as heteroatoms, such as oxygen, sulfur and nitrogen. The bridges connecting to the aromatic clusters are majorlycomposed of aliphatic functional groups and atoms such as oxygen and sulfur (Spiro and Kosky, 1982 andSolomon, 1981). The bridges containing oxygen have bonds with relatively weak strengths. Some bridges consisting of a single bond between aromatic clusters, such as char links, are relatively stable. Since bridges are composed of a wide variety of functional groups, there is a

large distribution in bond strengths. The side chains are defined as the aromatic clusters that do not “bridge” to another aromatic cluster. The mobile phase consists of smaller molecular structures that are not strongly bonded to the matrix (Marzec and Schulten, 1989 and Given, 1986). Figure 1.23 is a schematic illustrating these important structural components of coal.

Coal contains approximately 1 to 2 percent nitrogen by weight, which is a weak function of the coal type (Niksa, 1995). Nitrogen in coal is presented primarily in two different heterocyclic forms: pyrrolic nitrogen and pyridinic nitrogen, as shown in Figure 1.23. The form of pyrrolic nitrogen occupies about 50% to 60% of total nitrogen in the coal, while pyridinic nitrogen accounts for 30 to 40%. Some studies have shown that the relative amounts of pyridinic and pyrrolic nitrogen increase slightly with increasing coal rank corresponding to a decrease in the relative amount of quaternary nitrogen. (Burchill and Welch, 1989;(Bartle el al., 1987;Wojtowicz et al., 1995;Kelemen et al., 1994; andWallace et al., 1989).

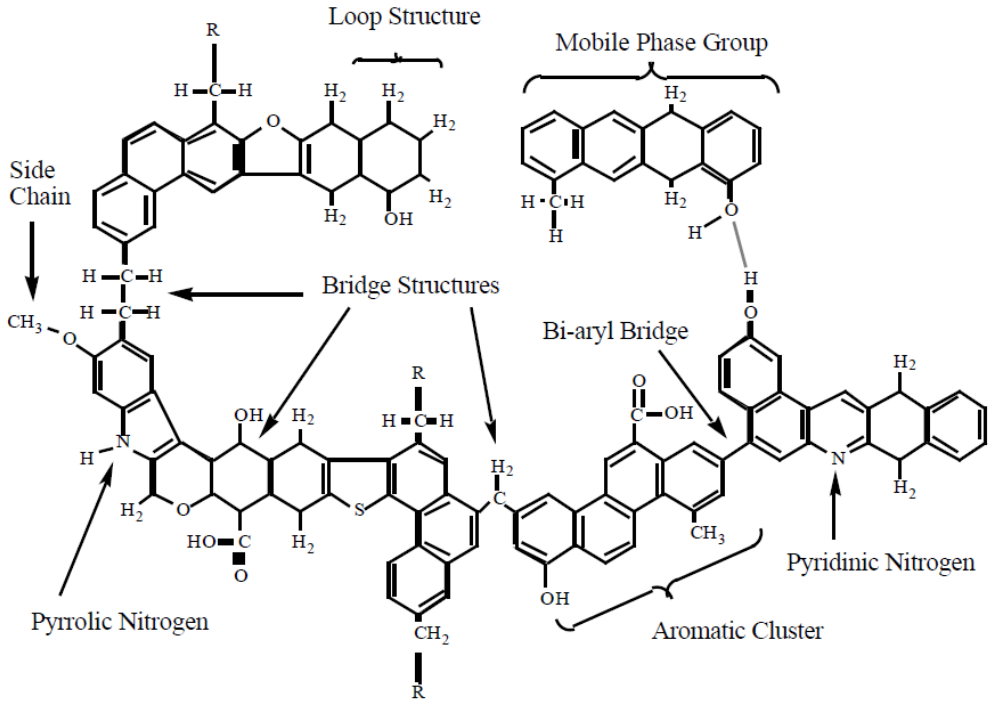

Figure 1.23 Schematic of hypothetical coal molecule. (Solomon et al., 1988)

1.2.5.2 Coal Devolatilization

Devolatilization is a decomposition process of hydrocarbon materials when they are heated. Devolatilization rates are influenced by temperature, residence time, particle size, and coal type. As the temperature of the coal increases, the bridges linking the aromatic clusters

break, resulting in finite-size fragments that are detached from the macromolecule. (Smith et al., 1994)

The bridges consist of a distribution of different types of functional groups, and the bonds with weakest strengths are broken first. The fragments are named as metaplast. The metaplast then either vaporizes and escapes the coal particle, or crosslinks back into the macromolecular structure. The metaplast which vaporizes consists mainly of the lower molecular weight fragments and becomes tar. The tar is defined as the gaseous pyrolysis products that condense at room temperature. The relationship between tar release and bridge scission is highly nonlinear. Side chains and the broken bridge material are released as light gas in the form of light hydrocarbons and oxides. The portion of the coal particle remaining after devolatilization is called char. Figure 1.24 is a schematic of a hypothetical coal pyrolysis reaction.

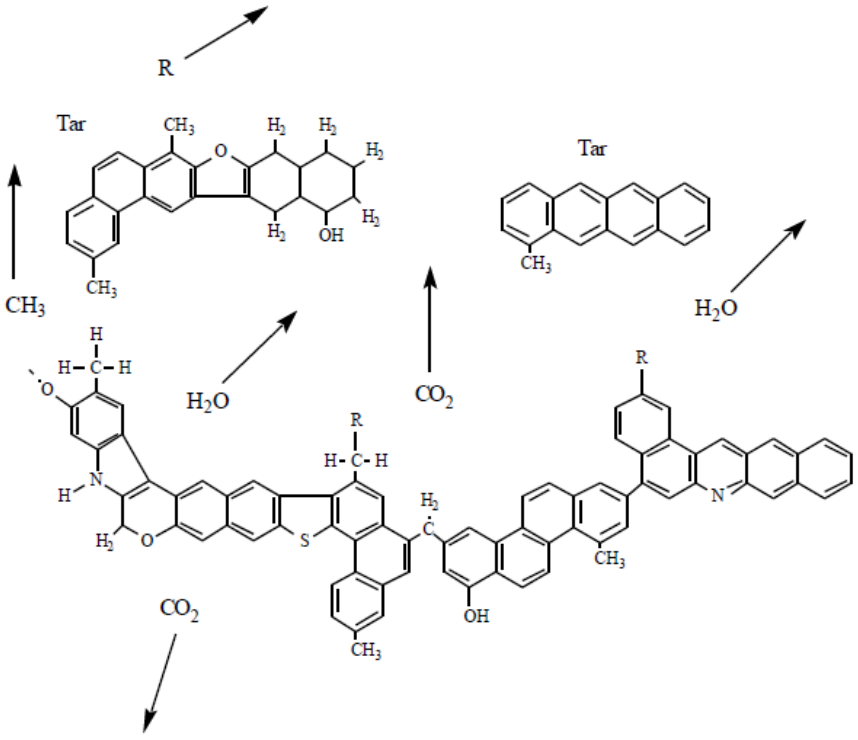

Figure 1.24 Schematic of pyrolysis reaction. (Solomon et al., 1988)

The devolatilization is affected by temperature, heating rate, pressure, particle size, and coal type among other variables (Anthony et al., 1974 andSuuberg et al., 1978). Higher mass release during devolatilization occurs at higher temperature. As temperature increases, the breaking rate of bridge and side chain increases, then more light gases are released, and more tar

is released due to higher metaplast vapor pressure. The heating rate affects devolatilization process in two different ways: (i) as heating rate increases, the temperature at volatiles release process increases; (ii) gas heating rate increases, the overall volatiles yield increases. Higher pressures lead to lower overall mass release during devolatilization because of vapor pressure considerations. (Smith et al., 1994)

Devolatilization behavior is greatly dependent on coal type. Low rank coals (lignites and subbituminous coals) release a relatively large amount of light gases and less tar. Bituminous coals release much more tar, as well as moderate amounts of light gases than lower rank coals. The highest rank coals release only small amounts of tar, and even lower amounts of light gases. Figure 1.25 illustrates these trends. Light gases released during devolatilization consist mainly of CH_4, CO_2, CO, and water vapor. Other components include low molecular weight hydrocarbons such as olefins, nitrogen species and sulfur species. Saxena (1990) studied light gas release at atmospheric pressures and low heating rates (1 K/sec). CH_4 and CO_2 are released at about 473 K. Above that temperature, condensation reactions resulted in the evolution of CO and H_2O. Between 473 K and 773 K, CH_4 and small amounts of olefins begin to come out, and nitrogen structures and organic sulfur species begin to decompose. H_2 begins to evolve at the temperature of about 673 K. At higher temperature, at the range 773K to 973K, the volumes of H_2, CO_2, and CH_4 increase compared to other hydrocarbon species. Suuberg, et al. (1978) studied the devolatilization behavior of a lignite at a heating rate of 1000 K/sec. CO_2 evolution is observed to take place at the temperature of about 723 K. The temperature between 973 K and 1173 K, H_2 and hydrocarbon gases are released. At higher temperatures the formation of additional CO_2 were observed.

The composition of the light gases released at the devolatilization process is a function of coal rank. Light gases released from lignites contain a relatively large amount of CO and CO_2, and only a small amount of methane. Light gases released from bituminous coals during the devolatilization process contain a smaller fraction of CO and CO_2, and a larger fraction of CH_4 compared to light gas released from lignites. The variations in the species distribution of light gases as a function of rank is believed to be the result of variations in the composition of the aliphatic side chains. (Solomon et al., 1990)

Several other studies on coal devolatilization process are summarized as following. Seebauer et al. (1997) investigated the effects of pressure, particle size and heating rate on coal

pyrolysis using thermogravimeteric analysis. The pressure used in the study ranged from 1 to 40 atm and the heating rate was from 0.03 to 0.1 K/s. Seebauer et al. found that the total volatile yield decreased with increasing pressure. Sun et al. (1997) studied the pyrolysis of two Chinese coals under pressure ranging from 1 to 13 atm with a heating rate as low as 0.33 K/s. It was reported that at high pressure the total volatile yield decreased with increasing pressure. The total weight loss was almost independent of the pressure at low temperatures (about less than 837 K). Fatemi et al. (1987) studied the pressure effects on devolatilization of pulverized coal up to temperature 1373 K and pressure 68 atm in an entrained-flow reactor. They indicated that the tar yield decreased significantly with increasing pressure up to 13.8 atm. Weight loss and gas yield decreased with increasing pressure up to 13.8 atm, and there was no significant effect above this pressure. Wall et al. (2002) reviewed the pressure effect on variety aspects of coal reactions reported in open literature. In general the total volatile and tar yields decrease with increasing pressure. This effect is more pronounced at high temperatures and is less pronounced at high pressures. Increasing pressure improves fluidity of the coal melt and reduces char reactivity.

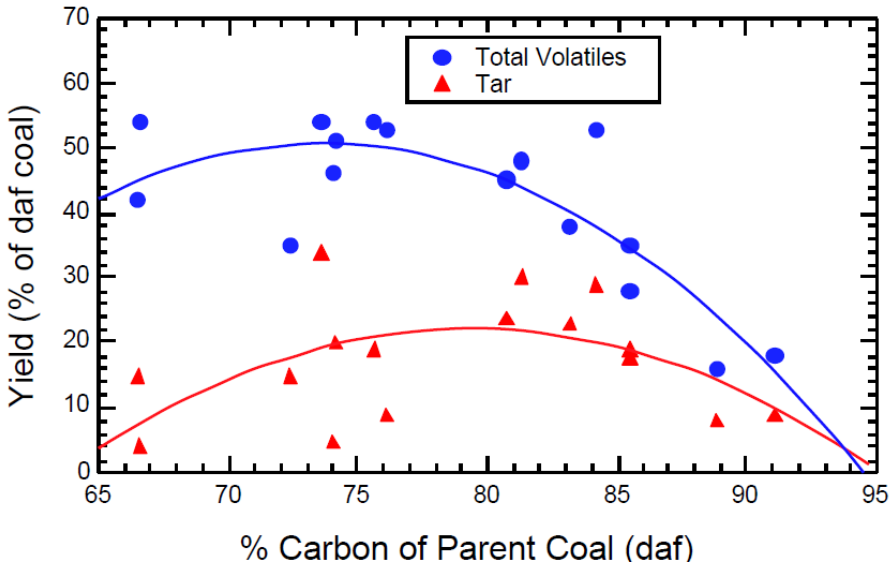

Figure 1.25 Volatiles yields from devolatilization experiments as a function of coal rank (Dominic, 1999)

1.2.5.3 Carbon Particle Combustion

The steps involved in a reaction between gas and a solid particle are as follows:

1. Transport of reactants to solid surface by convection and/or diffusion
2. Adsorption of reactant molecule on the surface

3. Reaction steps involving various combinations of adsorbed molecules, the surface condition, and the gas-phase molecules
4. Desorption of product molecules from the surface
5. Transport of product molecules away from solid surface by convection and/or diffusion

Due to the porous structure of char particles, chemical reactions between gases and the solid surface occur both on the outer and the inner surfaces of the particles. Reacting gases diffuse from the free space to the particle outer surface and then diffuse into the particle through the porous structure. As the reaction proceeds, the size of the available pores increases, which increases the inner particle surface. The particle active surface reaches a maximum at burnout of about 40%. The total active surface area is then decreasing as a result of connection of enlarging neighboring pores.

Based on the assumption made for the solid surface and gas phase chemistry, solid carbon combustion model can be divided into (a) one-film model, (b) two-film model, and (c) continuous film model.

(a) One-film model

The one-film model uses a single step reaction, $C(s) + O_2 \rightarrow CO_2$. Figure 1.26 below illustrates gas concentration and temperature distributions near the particle surface in the one-film model. O_2 diffuses inward and reacts with the surface to form CO_2 which then diffuses outward. This model ignores the intra-particle diffusion.

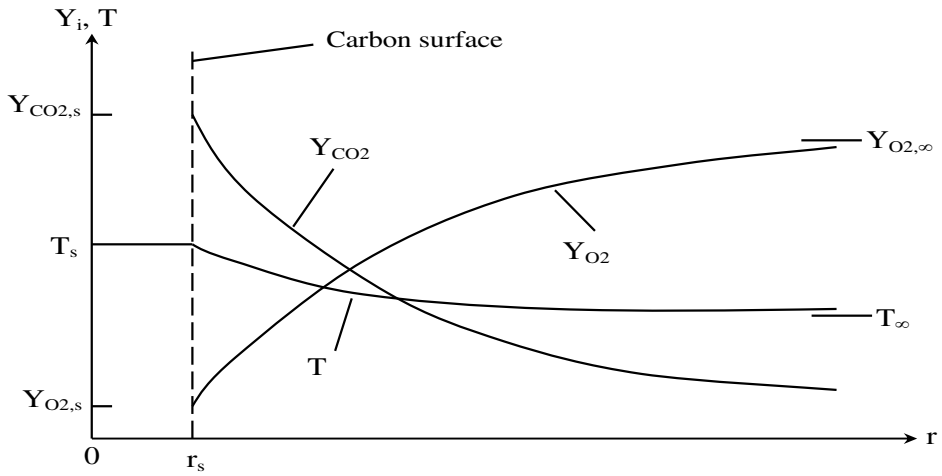

Figure 1.26 Schematic of gas concentration and temperature distributions for one-film particle combustion model (Turns, 2000)

(b) Two-film model

The two-film model involves two reactions: $C(s) + CO_2 \rightarrow 2CO$ and $CO + \frac{1}{2}O_2 \rightarrow CO_2$. Figure 1.27 illustrates the gas concentration and temperature distributions for the two-film model. CO_2 diffuses inward and attacks the particle surface. Reaction between CO_2 and the surface is $C(s) + CO_2 \rightarrow 2CO$. The CO formed then diffuses outward and is consumed at the flame sheet by O_2, which is diffusing inward according to reaction $CO + \frac{1}{2}O_2 \rightarrow CO_2$. The reaction is assumed to be infinitely fast. Thus, CO and O_2 concentrations are both zero at the flame sheet.

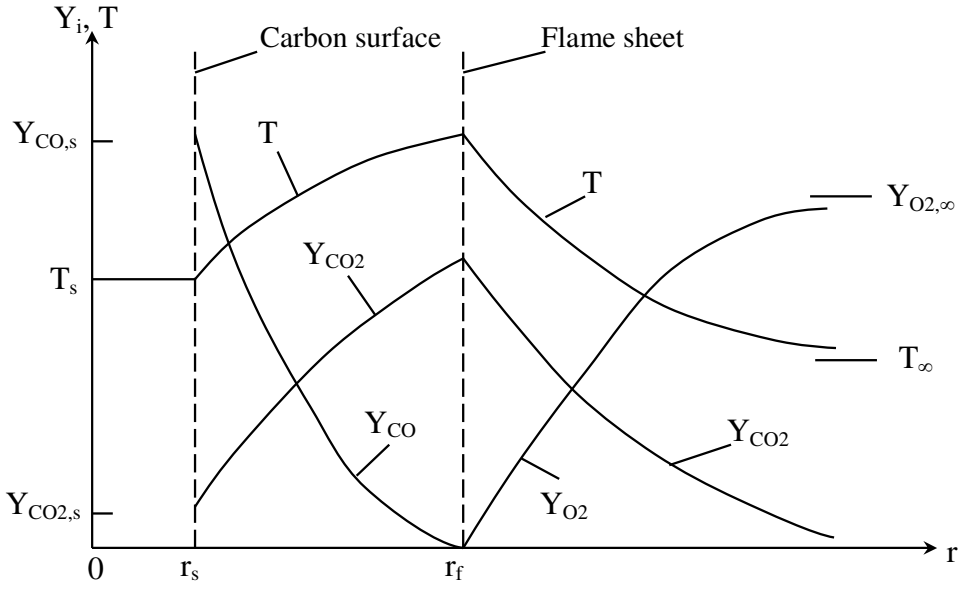

Figure 1.27 Schematic of gas concentration and temperature distributions for two-film particle combustion model (Turns, 2000)

1.2.5.4 Modeling Particle Combustion

(A) Kinetics/Diffusion Fixed-Core Model

The kinetics/diffusion fixed-core model takes into account the diffusion and kinetic rates of the combustion. The size of the particle during the combustion is assumed to be constant. The particle consumption rate is defined as follow

$$\frac{dm_p}{dt} = \frac{P_g}{\frac{1}{k_d} + \frac{1}{k_s}} A_0 \qquad (1.1)$$

where m_p is the particle mass, P_g is the partial pressure of the gas phase species, A_0 is the original particle surface area, k_d is the diffusion rate constant and k_s is the kinetics rate constant.

(B) Shrinking Core Model

The shrinking core model accounts for the reduction in the particle radius as the combustion occurs. The effect of diffusion through the ash layer surrounding the particle is also taken into account. The particle consumption rate is defined as

$$\frac{dm_p}{dt} = \frac{P_g A_0}{\frac{1}{k_d} + \frac{1}{k_s}\left(r_p / R_p\right)^2 + \frac{1}{k_{dash}}\left(\frac{R_p}{r_p} - 1\right)} \tag{1.2}$$

where m_p is the particle mass, P_g is the partial pressure of the gas phase species, k_d is the diffusion rate constant, k_s is the kinetics rate constant, and k_{dash} is the ash diffusion constant. r_p is the instantaneous radius of the particle, R_p is the initial radius of the particle, and A_0 is the initial particle surface area.

(C) Random Pore Model

The random pore model (Bhatia and Perlmutter, 1980) accounts for the evolution of the particle reactive surface during the combustion. The rate of mass change of the particle is defined as

$$\frac{dm_p}{dt} = R_k m_{po}\left(S + A_o\right) \tag{1.3}$$

where m_p is the particle mass, m_{po} is the initial particle mass, R_k is the kinetic rate, and A_0 is the initial particle surface area. S is the instantaneous internal reactive surface area, which is defined as

$$\frac{S}{S_o} = 1 - x\sqrt{1 - \psi \ln\left(1 - x\right)} \tag{1.4}$$

where S_o is the initial reactive area, x is the conversion factor, and ψ is the structure parameter for the particular char/coal type.

1.2.5.5 Carbon Combustion Reaction Rates

Field (1968) conducted an experiment to measure the rate of reaction $C(s) + ½ O_2 \rightarrow CO$. Gas temperature used by Field ranged from 1200 K to 1720 K at atmospheric pressure. Oxygen concentrations used ranged from 1% to 20%, and the particle size ranged from 20 μm to 100 μm. The measured particle temperatures ranged from 1200 K to 2000 K.

It was assumed that the product formed inside the char and on the surface of the char was carbon monoxide and that on average CO was transported to some distance from the particle before it could combine with oxygen to form carbon dioxide. The reaction rate was calculated from the weight loss of a char sample in a given transit time at a given oxygen concentration. An overall reaction rate coefficient is defined as the rate of removal of carbon per surface unit external surface area per unit atmosphere partial pressure of oxygen in the gas. Field found that the variation of the diffusional reaction rate coefficient was not strong. The experiment did not detect any effect of particle size on the reaction rate. The kinetic reaction rate was found to be $k = T(A+BT)$ where $A = -0.067$ m/(s-K) and $B = 5.26 \times 10^{-5}$ m/s-K^2.

Mayers (1934(a)) conducted an experiment to determine the rate of reaction $C(s) + CO_2 \rightarrow 2CO$, where graphite was used as the C. The experiment was conducted at atmospheric pressure. Mayers measured the reduction rate of CO_2. The effects of diffusion as the rate determining factor were eliminated by increasing the gas velocity across the particle surface, thus removing the concentration gradients.

The rate of reduction of CO_2 through the reaction appeared in two temperature ranges: (a) between 1125 K and 1225 K and (b) between 1225 K and 1575 K. Mayers found that when CO_2 reacted with carbon at low temperatures ($T < 1250$ K), CO was formed at the same rate as that at which CO_2 disappeared. This is explained by the retention of half of the oxygen of the carbon dioxide by the graphite ($C + CO_2 \rightarrow CO + C\text{-}O_{solid}$). Mayers indicated that the CO_2 reduction rate at the high temperature range might be represented by two reactions: $C + CO_2 \rightarrow CO + C\text{-}O_{solid}$ and $C\text{-}O_{solid} \rightarrow CO$, where the second reaction follows so rapidly on the first that there is no accumulation of $C\text{-}O_{solid}$. Thus the product of the CO_2 reduction is CO only. The CO_2 reduction rate is expressed in Arrhenius form $k = AT^n(-E/RT)$ where $n = 1.0$, $A = 4.4$ m/s-K, and $E = 1.62 \times 10^{+8}$ J/kmol.

Mayers (1934(b)) conducted another experiment to measure the rate of $C(s) + H_2O(g) \rightarrow CO + H_2$, where graphite was used as the source of C, at atmospheric pressure in the

temperature range of 1123-1433 K under conditions which eliminated the effects of diffusion as the rate determining process. Mayers found that the appearance of CO and CO_2 varied rather widely within the same temperature group, but their sum was found to be constant. The ratio CO/CO_2 of the products of reaction depends on the speed of the secondary reaction ($CO + H_2O \rightarrow CO_2 + H_2$) and on the time during which the mixture of gases remains in the heated zone. The rate of oxidation of carbon by steam appeared in temperature ranges 1133-1233 K and 1273-1433 K. Mayers reported that the rate of oxidation of C was of the same order of magnitude as the rate of appearance of C as CO when graphite was oxidized by CO_2. The kinetic reaction rate was found to be $k = AT^n(-E/RT)$ where $n = 1.0$, $A = 1.33$ m/s-K, and $E = 1.47 \times 10^{+8}$ J/kmol.

Hurt and Mitchell (1992) investigated coal char combustion kinetics for ten U.S. coals of various ranks. They observed that char reactivity decreased with increasing rank of the coal. Char reactivity decreases with increasing carbon content of the coal. The reactivity differences are more pronounced at low temperatures than at high temperatures. Hurt and Mitchell provided a char reactivity correlation, which is based on carbon content (coal rank) of the coal under conditions relevant to pulverized coal fired combustors.

There are other extensive studies on char combustion kinetics (Essenhigh, 1981;(Field, 1970;Smith, 1978;and Young and Smith, 1989), and a smaller but significant literature on the analysis of residual carbon in fly ash, (Beeley, et al., 1985 andHower and Roble, 1993) but few studies of kinetics have specifically addressed the complete carbon burnout process (0%-99% conversion) under conditions directly relevant in full-scale furnace environment. Most studies of kinetics have employed laboratory reactors and have focused on the main portion of the carbon conversion curve (0%-70%), where scientific measurements can most conveniently be made and interpreted. As a result, many of the kinetics models obtained are not ideally suited for the specific application of carbon burnout prediction.

A number of recent studies of kinetics have focused on the late stages of combustion. This work includes the measurement of very low reactivity for boiler fly ash carbons (Hurt and Gibbins, 1995 andHurt, et al., 1995), the analysis of reactivity loss and extinction phenomena in the late stages of combustion, and the acquisition of captive particle image sequences revealing the qualitative features of complete particle combustion lifetimes (Hurt and Davis, 1994). These later experiments reveal a slow “ash decarburization” step at the end of the burnout process that

significantly lengthens the time required to reach complete conversion. The Arrhenius rates of different coals are summarized in Table 1.3.

Table 1.3 Arrhenius rates of different coals (Smith, 1982)

Line no.	Parent coal	Pre-exponential factor (g/cm^2s $(atm)^n$)	Activation energy (kcal/mol)	Apparent order of reaction	Particle size (μm)
1	Petroleum coke	7.0	19.7	0.5	18,77,85,88
2	East Hetton, swelling bituminous coal, UK	635.8	34.0	1.0	72
3	Brodsworth, swelling bituminous coal, UK	111.3	24.1	1.0	31
4	Anthracites and semi-anthracites, UK and western Europe	20.4	19.0	1.0	78,49,22,72,42
5	Millmerran, non-swelling, sub-bituminous coal, Australia	15.6	17.5	0.5	85
6	Yallourn brown coal, Australia	9.3	16.2	0.5	89,49
7	Ferrymoor, non-swelling bituminous coal, UK	70.3	21.5	1.0	34
8	Whitwick, non-swelling bituminous coal, UK	50.4	17.7	1.0	27
9	Pittsburgh seam, swelling bituminous coal, USA	4187.0	34.0	0.17	16
10	Illinois No. 6, swelling bituminous coal, USA	6337.0	34.1	0.17	13

1.2.5.6 Numerical Simulation Models of Coal Combustion and Gasification

Numerical simulation is a very powerful tool for investigating coal combustion and gasification process. Different turbulence and chemistry models for modeling coal combustion and NO_X formation in complex turbulent flows have been proposed. However, it is most difficult to model the reacting coal particles and their effect on the gas phase. In treating the solid phase for modeling pulverized coal particles, most of the existing models are based on a Lagrangian model (Sommerfeld et al., 1993; Lockwood et al., 1988; Smoot and Smith, 1985; Papadakis and Bergeles, 1994; Coimbra et al., 1994; and Costen et al., 2000). Particle trajectory model can help to simulate the combusting coal particle history. However, in order to obtain a detailed distribution of particle velocity and concentration for comparison with experimental data, a large amount of particle trajectories are needed. Some models using the Eulerian

treatment of particle phase are based on a single-fluid model (no-slip model) (Fiveland and Wessel, 1988) and two-fluid model (Zhou, 1988). The no-slip model neglects the velocity slip between the gas phase and coal particle phase, and assumes that the temperature of the coal particle phase is equal to the temperature of the gas phase, and the temperature distribution of the gas–particle mixture can be obtained by solving the overall energy equation. The pure two-fluid (PTF) model uses a comprehensive Eulerian treatment for both gas and particle phases. Both velocity and temperature slips between coal particles and gas phase are calculated by solving the momentum equations and energy equations of the gas and particle phases. The PTF can conveniently describe all particle history effects—the particle mass change due to moisture evaporation, devolatilization and char combustion, and particle temperature change due to convection, diffusion and heat transfer between the two phases.

The numerical simulation of NO_X formation in turbulent combustion is frequently used in the optimization design of low NO_X burners and furnaces. The probability density distribution function (PDF) transport equation model (Pope, 1985), conditional moment closure (CMC) (Bilger, 1993), direct numerical simulation (DNS) (Tanahashi et al., 2000), and large-eddy simulation (LES) (Park et al., 2000) are developed in recent years, can well simulate the detailed finite-rate kinetics of NO_X formation, but these models are relatively computational intensive. For engineering NO_X formation modeling, some researchers use the EBU–Arrhenius (EA) model (Mueller and Kremer, 1995), but the EA model actually cannot take into account the finite reaction rate. Many researchers, including some commercial codes, adapt the presumed PDF-finite-reaction-rate model (DalSecco et al., 1995; Faltsi-Saravelon and Wild, 1995), using a product of several single variables PDFs instead of the joint PDF. Experimental studies point out that this model underpredicts the averaged reaction rate. Furthermore, turbulence is assumed to have no effect on the reaction rate in the model. Alternatively, the second-order moment (SOM) turbulence-chemistry models for NO_X formation, based on the idea of SOM turbulence models (Liao et al., 1996), will be more reasonable than the EA model and the presumed PDF models. In order to reduce NO_X formation during coal combustion, Li et al., (2000) designed a new type of swirl burner which is installed in a pulverized-coal concentrator in the primary-air tube. Li et al., (2003) continued their study, using a modified $k–\varepsilon–k_p$ two-phase turbulence model, a second-order moment turbulence-chemistry model to

simulation the NO_X formation, incorporating a general model of pulverized-coal devolatilization and a general model of char combustion.

1.2.5.7 Numerical Simulation Models of Coal Gasification

For coal gasification study, one-dimensional models have made a significant contribution to the research on the chemical processes of gasification, and are also the most widely published models up to date. The preliminary models derived by Thorsness and Roszd (1976), Schlich (1977) and Biba, et al. (1978), are the first attempts to describe the individual reactions and their mechanisms. These models provide an insight into the gasification process in general. Yoon, et al. (1977) derived a model that could accurately predict the operating conditions of the gasifier. Wen, et al. (1982) produced a manual for a gasifier model that could be used to study the operation of the gasifier. The model published by Adanez and Labiano (1990) and a summary of models made by Rinard and Benjamen (1985) are typical one-dimensional models at that time. One of the first comprehensive and well documented moving bed models was developed by Denn, et al. (1982). This model was first developed as a one-dimensional model and then extended to two dimensions and transients.

For gasification reactions, Desai and Wen (1978) assumed that the combustion reactions are irreversible and dominated by gas film and ash diffusion. The gasification reaction was assumed to be irreversible and dominated by a chemical reaction rate. The gasification kinetic rates and water-gas shift (WGS) equilibrium constants, which published by Hottel and Howard (1971) and Gibson and Euker (1975) were assumed to follow the Arrhenius-type dependence on temperature. In the model published by Cho and Joseph (1981), the heat of the heterogeneous reactions was assigned to the solid phase, while the heat of the water-gas shift reaction was assigned to the gas phase. The solid-gas heat transfer coefficient was determined by Gupta and Thodos (1963) with a correction factor for the reacting system. The model published by Hobbs (1990) determined the gas evolution rates by a functional group model developed by Solomon et al. (1988). The tar evolution rate was determined by a semi-empirical correlation. The model considered axially variable solid and gas flow rates as well as bed void fraction. Accounting for axially variable bed void fraction was found to be necessary in order to predict realistic axial

temperature, concentration and pressure profiles. Hobbs, et al. (1992) continued to publish a comprehensive study on the gasification model of moving bed gasifier.

For numerical analysis of entrained-flow coal gasifier, studies have been widely conducted since the early 1980's includingTyrkiel and Cudnok (1981), Lasa and Mok (1981), Rabbitts et al. (1983), Chapyak et al. (1983), Boysan et al. (1983), and Fletcher (1983). Fletcher et al. (1984) developed a computer code called PCGC-2 (Pulverized Coal Gasification or Combustion) to model coal gasification and combustion. The code was made available to the public. Celik and Chattree (1990) used PCGC-2 to study gasification of Montana Rosebud-subbituminous pulverized coal in an entrained-flow reactor and compared the results with experimental data. They found that the particle residence times significantly different from the commonly calculated gas residence times and suggested that the use of gas residence time alone as a parameter might lead to erroneous conclusions regarding char burnout.

Govind and Shah (1984) conducted a numerical study on Texaco downdraft entrained-flow which used coal liquefaction residues and coal-water slurries as feedstocks. They reported that oxygen-fuel ratio affected carbon conversion more than the steam-fuel ratio. The steam-fuel ratio significantly affected the syngas composition. The optimum oxygen-fuel ratio was between 0.8-0.9 to achieve 98-99% carbon conversion.

Chen et al. (1999) studied the flow field inside a two-stage entrained-flow gasifier. They reported that the swirl flow is sensitive to the gasifier throat diameter. To prevent sticky particles from moving toward the reductor walls, Chen et al. recommended a small swirl diameter for the lower combustor burner and an intermediate swirl diameter for the reductor burner. They reported that the Swirl number was the most important hydrodynamic scaling law for multi-stage injecting swirl flow gasifiers.

Chen et al. (2000) developed a comprehensive three-dimensional simulation model for entrained coal gasifiers which applied an extend coal gas mixture fraction model with the Multi Solids Progress Variables (MSPV) method to simulate the gasification reaction and reactant mixing process. The model employed four mixture fractions separately track the variable coal off-gas from the coal devolatilization, char-O_2, char-CO_2, and char-H_2O reactions. Chen et al. performed a series of numerical simulations for a 200 ton per day (tpd) two-stage air blown entrained flow gasifier developed for an IGCC process under various operation conditions (heterogeneous reaction rate, coal type, particle size, and air/coal partitioning to the two stages).

Chen et al.'s model predicted that coal devolatilization and char oxidation were responsible for most of the carbon conversion (up to 80%) in the two-stage air blown entrained flow gasifier. It was found that carbon conversion was independent of devolatilization rate, sensitive to the chemical kinetics of heterogeneous reactions on the char surface, and less sensitive to a change in coal particle size. They found that increasing air ratio (or reducing equivalence ratio) leads to increased CO_2 and decreased CO and H_2 concentrations. This is expected because more air input leads to more combustion and less gasification.

Chen et al. (2000) also predicted that increasing the average coal particle size decreases the carbon conversion, which results in an increase in the exit gas temperature and lower heating value. They also predicted that dry feed yielded more CO mole fraction than wet feed due to injecting less moisture into the system. Chen et al.'s model showed that an increase in the system pressure increased the average residence time due to the reduced average gas velocity which further resulted in increased particle residence time and increased carbon conversion.

Choi et al. (2001) performed numerical parametric analysis of flow field of an entrained-flow gasifier. Choi et al. changed the gas injection angle, gas inlet diameter, gas inlet velocity, extension in burner length, and gasifier geometry and found that the basic patterns of the flow field inside the gasifier were nearly the same with a parabolic distribution. They reported that the geometric parameters of the burner, such as the oxygen inlet diameter and angle, influenced the flow field at the inlet region near the burner; but the flow field was nearly the same after a certain length along the gasifier.

Bockelie et al. (2002(a)) of Reaction Engineering International (REI) developed a CFD modeling capability for entrained flow gasifiers that was focused on two gasifier configurations: single-stage down fired system and two-stage updraft system with multiple feed inlets. The model was constructed using GLACIER, an REI in-house comprehensive coal combustion and gasification tool. The basic combustion flow field was established by employing full equilibrium chemistry. Gas properties were determined through local mixing calculations and were assumed to fluctuate randomly according to a statistical probability density function (PDF) which is characteristic of the turbulence. Gas-phase reactions were assumed to be limited by mixing rates for major species as opposed to chemical kinetic rates. Gaseous reactions were calculated assuming local instantaneous equilibrium. The particle reaction processes include

coal devolatilization, char oxidation, particle energy, particle liquid vaporization and gas-particle interchange. The model also includes a flowing slag sub-model.

U.S. Department of Energy/National Energy Technology Laboratory (NETL) developed 3D CFD model of two commercial-sized coal gasifiers (Guenther and Zitney, 2005). The commercial FLUENT CFD software was used to model the first gasifier, which was a two-stage entrained-flow coal slurry-fed gasifier. The Eulerian-Lagrangian approach was applied. The second gasifier wass a scaled-up design of transport gasifier. The NETL open source MFIX (Multiphase Flow Interphase eXchanges) Eulerian-Eulerian model is used for this dense multiphase transport gasifier. NETL also developed an Advanced Process Engineering Co-Simulator (APECS) that combineed CFD models with plant-wide simulation. APECS enables NETL to couple its CFD models with steady-state process simulator, Aspen Plus.

Watanabe and Otaka (2006) developed a numerical simulation of coal gasification in an entrained-flow gasifier. They modeled CRIEPI (Central Research Institute of Electric Power Industry) 2-tons/day research scale coal gasifier. Influence of the air ratio on gasification performance, such as syngas composition, char conversion, and cold gas efficiency, was studied and compared to experimental data. The model was able to provide quite accurate results. It was reported that increasing the air ratio increased the char conversion. However, increasing the air ratio caused the atmosphere inside the gasifier to become more oxidative, and as a result it reduced the calorific value of the syngas.

Matsushita et al. (2006) conducted numerical analysis of an entrained-flow gasifier. Matsushita et al. reported that the CO mole fraction in the upper part of the combustor is higher for the smaller gasifier throat diameter. Vincente et al. (2003) used Eulerian-Eulerian concept in their numerical simulation of entrained-flow gasifier. Tominaga et al. (2000) used ash viscosity as the criteria for slagging in their numerical model and indicated that the results matched fairly well with the measured data they had.

Shi et al. (2006) described a computational fluid dynamics model of a two-stage, oxygen blown, entrained flow, coal slurry gasifier for use in advanced power plant simulations. The discrete phase method was used to simulate the coal slurry flow. The physical and chemical processing of coal slurry gasification was implemented by calculating the discrete phase trajectory using a Lagrangian formulation. Their gasification model predicted a synthesis gas composition that was very close to the values calculated by a restricted equilibrium reactor

model tuned to represent typical experimental data. The char conversions were 100 and 86% for the first stage and second stage respectively.

Ajilkumar et al. (2007) performed numerical study of gasification of Indian coal which has high ash content. They observed that as the ash content increased, the heat and mass transfer were affected and the gasification performance decreased. They suggested that this was attributed to the lower char reactivity due to thick ash layers and lower oxygen and other gas diffusion rates. They also found that increasing the temperatures of inlet air and steam reduced CO, but increasesdH_2, CO_2, and carbon conversion. Steam addition decreased the temperature but increased H_2 production at the expense of CO.

Kumar et al. (2009) used a CFD package to model the operation of a coal gasifier with the objective of assessing the impact of devolatilization and char consumption models on the accuracy of the results. They found that the random pore model with Langmuir-Hinshelwood reaction kinetics were better at predicting carbon conversion and exit syngas composition than the shrinking core model with Arrhenius kinetics. In addition, they gained qualitative and quantitative insights into the impact of the ash layer surrounding the char particle on the reaction rate.

Rehm et al. (2009) described results of the CFD modelling of a high-pressure gasification process. They discussed time scales weaknesses of the Eddy dissipation concept (EDC) scheme in reforming zones and demonstrated a possible solution of EDC model.

Wu et al. (2010) developed a comprehensive three-dimensional (3D) numerical model for simulation of entrained coal slurry gasifiers. In their model, a presumed probability density function (PDF) method was used to consider turbulent effects on gas-phase reactions in the gasifier. A realizable k−ε model was adopted to predict turbulence information. They showed that the proposed model correctly predicted the global performance of the coal gasification process with the comparison between the predictions and measured data.

Slezak et al. (2010) studied the effect of particle density and size variations on gasification performance by conducting the simulation of commercial-scale two-stage upflow and single-stage downflow entrained-flow gasifiers. They found that the density and size partitioned solution predicted nominally 10% less CO and over 5% more H_2 by volume in the product gas stream. Particle residence times and trajectories differed between these two

solutions for the larger density/size fractions. Fixed carbon conversion was 4.3% higher for the partitioned solution. Particle–wall impact velocities did not vary greatly.

Luan et al. (2011) investigated the gasification process of a pressurized, oxygen-blown, entrained-flow E-Gas like gasifier through numerical modeling by solving the 3-D, steady-state Navier–Stokes equations with the Eulerian–Lagrangian method. They showed that the increasing O2/Coal ratio resulted in a decrease of CO, but an increase of CO_2 and exit temperature. Using a modified water–gas-shift reaction rate obtained from Silaen and Wang (2010), a more reasonable trend was obtained that as the coal slurry concentration decreased, the mass flow rate of H_2, CO_2, and H_2O increased while that of CO decreased.

Zitney (2010) described recent progress toward developing an Advanced Process Engineering Co-Simulator (APECS) for the high-fidelity design, analysis, and optimization of energy plants. He also discussed ongoing co-simulation R&D activities and challenges in areas such as CFD-based reduced-order modeling, knowledge management, advanced analysis and optimization, and virtual plant co-simulation. He concluded that continued progress in co-simulation technology – through improved integration, solution, and deployment – would have profound positive impacts on the design and optimization of high-efficiency, near-zero emission fossil energy systems.

Lang et al. (2011) described the development and demonstration of a reduced order modeling (ROM) framework on gasification process. They showed how the ROMs derived from both gasification and combustion units can be integrated within an equation-oriented simulation environment for the overall optimization of an IGCC process. In addition to a systematic approach to ROM development, the approach included validation tasks for the CFD model as well as closed-loop tests for the integrated flowsheet. This approach allowed the application of equation-based nonlinear programming algorithms and leads to fast optimization of CFD-based process flowsheets.

Kumar et al. (2012) researched on the construction, validation, and application of a multi-scale model of entrained flow gasification. They presented the adaption of the moving flame front (MFF) model of char consumption to gasification computational fluid dynamics and its impact on the overall prediction. The accuracy of the integrated gasifier model was demonstrated by comparing its predictions with experimental data from pilot and research-scale

Mitsubishi Heavy Industries (MHI) gasifiers and a laboratory scale gasifier from Brigham Young University (BYU).

From 2005 to 2011, Silaen and Wang have done a series of study of entrained-flow gasification process using the commercial CFD solver, FLUENT. Silaen and Wang (2005) investigated the effects of several parameters on gasification performance, including the coal input condition (slurry or dry powder), oxidant (oxygen-blown or air-blown), wall cooling, and various coal distributions between the two stages. The simulation results provide the temperature and species distributions inside the gasifier. In 2006, they investigated the effect of flow injection directions on the gasification performance using the same generic two-stage, entrained-flow gasifier. In 2010, they did research that investigated the effects of different parameters on gasification performance, including five turbulence models, four devolatilization models, and three solid coal sizes. With several improvements in the CFD modeling, including updating the finite rates for heterogeneous reactions, adding Chemical Percolation Devolatilization (CPD) devolatilization model, and adding two-stage volatiles cracking reactions, Silaen and Wang (2012) again conducted an investigation on the effects of different operation parameters in the gasification process, including the coal input condition (dry vs. slurry,) oxidant (oxygen-blown vs. air-blown,) and different coal distributions between the two stages.

In collaboration with the research team of Industrial Technology Research Institute (ITRI), Wang and Silaen effectively employed the CFD gasification model to investigate gasification process under the influences of different part loads, two different injectors, and three different slagging tap sizes (Wang, et al., 2006, 2007, and 2010). In 2011, Wang, et al. performed the simulation on the effects of potential fuel injection techniques on gasification performance in order to help design the top-loaded fuel injection arrangement for an entrained-flow gasifier using a coal-water slurry as the input feedstock. Two specific arrangements were investigated: (a) coaxial, dual-jet impingement with the coal slurry in the center jet and oxygen in the outer jet and (b) four-jet impingement with two single coal-slurry jets and two single oxygen jets.

1.3 Objectives and Specific Goals

From the introductions of background information and literature review, it can be seen that the performance and reliability of the gasifier are extremely important factors that will affect both the overall plant performance and product cost. Therefore, *the **objective of** this study is to help improve the performance, efficiency, cost, and reliability of entrained-flow gasifiers.*

Since there are many parameters that affect the performance, efficiency, and reliability of a gasifier, a good understanding of the fundamental physics involved in the gasification process inside a gasifier is needed to help achieve the objectives. Considering the fact that there are different means to design and operate an entrained-flow gasifier, conducting experiments to investigate the many different options is a time consuming and expensive process. To help narrow down the number of experimental variables and to guide design development, an economical way to achieve this is through numerical modeling and simulations. Thus, the specific goals of this research are to:

(a) Improve the gasification model and sub-models and perform a comprehensive, numerical investigation of entrained-flow coal gasifiers via:
   - Examining and selecting appropriate reaction rates, especially the Water-Gas-Shift reaction rate and methanation reaction rate,
   - Expanding and improving the current sub-models for thermal cracking of the volatiles,
   - Incorporating a demoisturization sub-model for the inherent moisture inside the coal particles, with a special interest in low rank coals,
   - Incorporating an ash-deposition model,
   - Investigating the effects of radiation models on the gasification process.

(b) Investigate the effects of various operating conditions on gasification performance, including: dry- vs. slurry-fed, oxygen- vs. air-blown, single stage vs. two stage, low-rank coal vs. high-rank coal, and different fuel injection schemes.

(c) Investigate the coal to synthetic nature gas (SNG) process.

(d) Use the improved gasification model to help industry find ways to improve gasifier performance and reliability through a collaborative study with industry, including:
   - A two stage oxygen injection distribution strategy

CHAPTER TWO
COMPUTATIONAL MODEL

2.1 Problem Statement

This study investigates the thermal-flow and gasification process in several entrained-flow gasifiers with different designs. Figure 2.1 shows one example: an up-flow, two- stage fuel feeding, entrained flow gasifier. Four tangential fuel injectors are located in the first stage at the bottom, and four opposing fuel injectors are located in the second stage. The gas flows upward and exits the gasifier from the top. Other gasifiers will be shown in the chapters where they are studied.

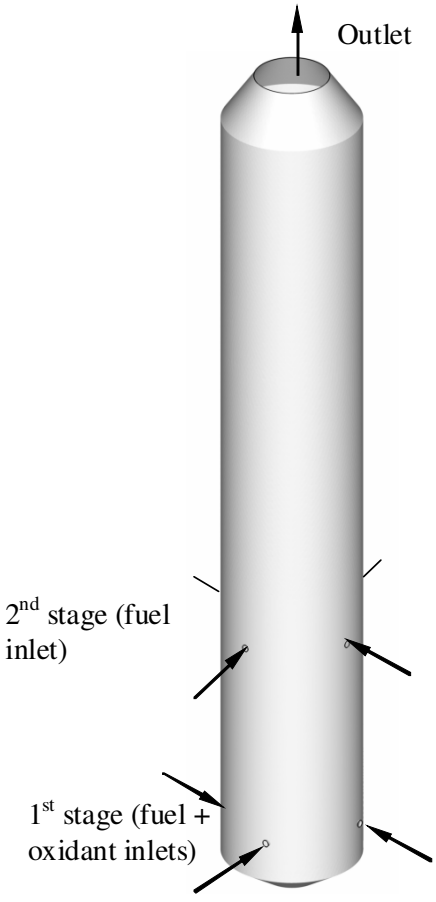

Figure 2.1 A two-stage entrained-flow gasifier studied.

Coal gasification is a multiphase reactive flow problem. It is a multiphase problem between gas and coal particles, and it is also a reactive flow which involves homogeneous reactions between gases and heterogeneous reactions between solid and gases. The Eulerian-Lagrangian method is adopted in this study. Gas phase (continuous phase) is solved using Eulerian method, while solid phase (discrete phase) is solved using Lagrangian method. The gas phase is first calculated. Once the solution for gas phase is obtained, the calculations for solid phase are performed.All of the solid particles are tracked individually. The paths taken by these particles are determined by calculating force balance on the particles based on gas flow field obtained earlier. The heterogeneous solid-gas phase reactions are also calculated. After completion of the solid phase calculations, gas phase is updated with the depletion or production of a species and the energy change due to the heterogeneous reactions. Iterations continue until both gas and solid phases reach convergence,

Using Computational Fluid Dynamics (CFD) simulation is an economical and effective tool to study coal gasification. The detailed computational models are presented below.

2.2 Governing Equations for Continuous Phase

As mentioned earlier, the Eulerian-Lagrangian method is adopted for this study. In the Eulerian method for the continuous phase, the 3-D time-averaged steady-state Navier-Stokes equations as well as the mass and energy conservation equations are solved. The governing equations for the conservations of mass, momentum and energy are given as:

$$\frac{\partial}{\partial x_i}\left(\rho u_{ij}\right) = S_m \tag{2.1}$$

$$\frac{\partial}{\partial x_i}\left(\rho u_i u_j\right) = \rho \overline{g}_j - \frac{\partial P}{\partial x_j} + \frac{\partial}{\partial x_i}\left(\tau_{ij} - \rho \overline{u_i' u_j'}\right) + S_f \tag{2.2}$$

$$\frac{\partial}{\partial x_i}\left(\rho c_p u_i T\right) = \frac{\partial}{\partial x_i}\left(\lambda \frac{\partial T}{\partial x_i} - \rho c_p \overline{u_i' T'}\right) + \mu\Phi + S_h . \tag{2.3}$$

The symmetric stress tensor, τ_{ij}, is given by

$$\tau_{ij} = \mu\left(\frac{\partial u_j}{\partial x_i} + \frac{\partial u_i}{\partial x_j} - \frac{2}{3}\delta_{ij}\frac{\partial u_k}{\partial x_k}\right). \tag{2.4}$$

Species transport model is used to model the mixing and transport of the chemical species. The equation for species transport is

$$\frac{\partial}{\partial x_i}\left(\rho u_i C_j\right) = \frac{\partial}{\partial x_i}\left(\rho D_i \frac{\partial C_j}{\partial x_i} - \rho\overline{u_i' C_j'}\right) + S_j . \tag{2.5}$$

S_j in Eq. 2.5 is the source term to accept increased or decreased chemical species resulted from the chemical reactions.

2.3 Turbulence Models

The velocity field in turbulent flows always fluctuates. As a result, the transported quantities such as momentum, energy, and species concentration fluctuate as well. The fluctuations can be small scale and high frequency, which is computationally expensive to be directly simulated. To overcome this, a modified set of equations that are computationally less expensive to solve can be obtained by replacing the instantaneous governing equations with their time-averaged, ensemble-averaged, or otherwise manipulated to remove the small time scales. However, the modifications of the instantaneous governing equations introduce new unknown variables. Many turbulence models have been developed to determine these new unknown variables (such as Reynolds stresses or higher order terms) in terms of known variables. Two of the turbulence models are explained below.

2.3.1 Standard k-ε Model

The standard k-ε model defines the Reynolds stresses as

$$-\rho\overline{u_i' u_j'} = \mu_t\left(\frac{\partial u_i}{\partial x_j} + \frac{\partial u_j}{\partial x_i}\right) - \frac{2}{3}\rho k \delta_{ij} \tag{2.6}$$

where k is the turbulence kinetic energy, and μ_t is the turbulence viscosity given by

$$\mu_t = \rho C_\mu k^2 / \varepsilon \tag{2.7}$$

where C_μ is a constant and ε is the turbulence dissipation rate. The equations for the turbulence kinetic energy (k) and dissipation rate (ε) are

$$\frac{\partial}{\partial x_i}\left(\rho u_i k\right) = \frac{\partial}{\partial x_i}\left[\left(\mu + \frac{\mu_t}{\sigma_k}\right)\frac{\partial k}{\partial x_i}\right] + G_k - \rho\varepsilon \tag{2.8}$$

$$\frac{\partial}{\partial x_i}\left(\rho u_i \varepsilon\right) = \frac{\partial}{\partial x_i}\left[\left(\mu + \frac{\mu_t}{\sigma_\varepsilon}\right)\frac{\partial \varepsilon}{\partial x_i}\right] + C_{1\varepsilon} G_k \frac{\varepsilon}{k} - C_{2\varepsilon} G_k \rho \frac{\varepsilon^2}{k}. \tag{2.9}$$

G_k is the generation of turbulence kinetic energy due to the mean velocity gradients. The turbulent heat flux and mass flux can be modeled with the turbulent heat conductivity (λ_t) and the turbulent diffusion coefficient (D_t), respectively.

$$\rho c_p \overline{u'_i T'} = -\lambda_t \frac{\partial T}{\partial x_i} = -c_p \frac{\mu_t}{Pr_t}\frac{\partial T}{\partial x_i}. \tag{2.10}$$

$$\rho \overline{u'_i C'} = -\rho D_t \frac{\partial C}{\partial x_i} = -\frac{\mu_t}{Sc_t}\frac{\partial C}{\partial x_i}. \tag{2.11}$$

The constants $C_{1\varepsilon}$, $C_{2\varepsilon}$, C_μ, σ_k, and σ_ε used are: $C_{1\varepsilon} = 1.92$, $C_{2\varepsilon} = 0.09$, $C_\mu = 1.0$, $\sigma_k = 1.3$ (Launder and Spalding, 1972). The turbulence Prandtl number, Pr_t, is set to 0.85, and the turbulence Schmidt number, Sc_t, is set to 0.7.

The turbulence models are valid for the turbulent core flows, i.e. the flow in the regions somewhat far from walls. The flow very near the walls is affected by the presence of the walls. Viscous damping reduces the tangential velocity fluctuations and the kinematic blocking reduces the normal fluctuations. The solution in the near-wall region can be very important because the solution variables have large gradients in this region.

However, the solution in the boundary layer is not important in this study. Therefore, the viscous sublayer, where the solution variables change most rapidly, does not need to be solved. Instead, the wall functions, which are a collection of semi-empirical formulas and functions, are employed to connect the viscosity-affected region between the wall and the fully-turbulent region. The wall functions consist of:

- the laws-of-the-wall for mean velocity and temperature (or other scalars)
- the formulas for near-wall turbulent quantities.

There are three types of wall function: (a) standard wall function, (b) non-equilibrium wall function, and (c) enhanced wall function.

Standard Wall Function – The momentum is expressed as

$$U^+ = \frac{1}{\kappa}\ln\left(Ey^+\right) \tag{2.12}$$

where

$$U^+ \equiv \frac{U_P C_\mu^{1/4} k_P^{1/2}}{\tau_w / \rho} \tag{2.13}$$

$$y^+ \equiv \frac{\rho C_\mu^{1/4} k_P^{1/2} y_P}{\mu} \tag{2.14}$$

and

κ = von Karman constant (= 0.42)

E = empirical constant (= 9.793)

U_P = mean velocity of fluid at point P

k_P = turbulence kinetic energy at point P

y_P = distance from point P to the wall

μ = dynamic viscosity of the fluid.

The wall function for the temperature is given as

$$T^+ \equiv \frac{(T_w - T_P)\rho c_p C_\mu^{1/4} k_P^{1/2}}{\dot{q}} = \begin{cases} \Pr y^+, y^+ \langle y_T^+ \\ \Pr_t \left[\frac{1}{\kappa} \ln(E y^+) + P \right], y^+ \rangle y_T^+ \end{cases} \tag{2.15}$$

where P is given as

$$P = 9.24 \left[\left(\frac{\Pr}{\Pr_T} \right)^{3/4} - 1 \right] \left[1 + 0.28 e^{-.007 \Pr / \Pr_T} \right] \tag{2.16}$$

and

r = density of the fluid

c_p = specific heat of fluid

q = wall heat flux

T_P = temperature at cell adjacent to the wall

T_W = temperature at the wall

Pr = molecular Prandtl number

Pr_t = turbulent Prandtl number (0.85 at the wall)

A = 26 (Van Driest constant)

κ = 0.4187 (von Karman constant)

E = 9.793 (wall function constant)

U_c = mean velocity magnitude at $y^+ = y^+_T$

y^+_T = non-dimensional thermal sublayer thickness.

The species transport is assumed to behave analogously to the heat transfer. The equation is expressed as

$$Y^+ \equiv \frac{\left(Y_{i,w} - Y_i\right)\rho c_p C_\mu^{1/4} k_P^{1/2}}{J_{i,w}} = \begin{cases} Scy^+, y^+ < y_c^+ \\ Sc_t\left[\frac{1}{\kappa}\ln\left(Ey^+\right) + P_c\right], y^+ > y_c^+ \end{cases} \tag{2.17}$$

where Y_i is the local mass fraction of species i, Sc and Sc_t are the molecular and turbulence Schmidt numbers respectively, and $J_{i,w}$ is the diffusion flux of species i at the wall. The molecular Schmidt number, Sc, is given as $\mu/\rho D$, where μ is the viscosity and D is the diffusivity. The P_c and y^+_c are calculated in a similar way as P and y^+_T, with the difference being that the Prandtl numbers are replaced by the corresponding Schmidt numbers.

In the k-ε model, the k-equation is solved in the whole domain, including the wall-adjacent cells. The boundary condition for k imposed at the wall is

$$\frac{\partial k}{\partial n} = 0 \tag{2.18}$$

where n is the local coordinate normal to the wall. The production of kinetic energy, G_k, and its dissipation rate, ε, at the wall-adjacent cells, which are the source terms in the k-equation, are computed on the basis of equilibrium hypothesis with the assumption that the production of k and its dissipation rate assumed to be equal in the wall-adjacent control volume. The production s of k and ε are computed as

$$G_k \approx \tau_w \frac{\partial U}{\partial y} = \tau_w \frac{\tau_w}{\kappa\rho C_\mu^{1/4} k_p^{1/4} y_P} \tag{2.19}$$

and

$$\varepsilon_P = \tau_w \frac{C_\mu^{3/4} k_p^{3/2}}{k y_P}. \tag{2.20}$$

Notice that in the wall-adjacent control volume when the equilibrium hypothesis is employed, the k-transport Eq. 2.8 is solved, while the ε-transport Eq. 2.9 is not solved but is replaced by Eq. 2.20.

Enhanced Wall Function – The k-ε model is mainly valid for high Reynolds number fully turbulent flow. A special treatment is needed in the region close to the wall. The enhanced wall function is one of several methods that model the near-wall flow. In the enhanced wall treatment, the two-layer model is combined with the wall functions. The whole domain is separated into a viscosity-affected region and a fully turbulent region by defining a turbulent Reynolds number, Re_y,

$$Re_y = yk^{1/2} / \nu \tag{2.21}$$

where k is the turbulence kinetic energy and y is the distance from the wall. The standard k-ε model is used in the fully turbulent region where $Re_y > 200$, and the one-equation model of Wolfstein (1969) is used in the viscosity-affected region with $Re_y < 200$. The turbulent viscosities calculated from these two regions are blended with a blending function (θ) to smoothen the transition.

$$\mu_{t,enhanced} = \theta\mu_t + (1-\theta)\mu_{t,l} \tag{2.22}$$

where μ_t is the turbulence viscosity from the k-ε model of high Reynolds number, and $\mu_{t,l}$ is the viscosity from the near-wall one-equation model. The blending function is defined so it is equal to 0 at the wall and 1 in the fully turbulent region. The linear (laminar) and logarithmic (turbulent) laws of the wall are also blended to make the wall functions applicable throughout the entire near-wall region. A similar thermal wall function equation is employed for the temperature calculation.

2.3.2 Reynolds Stress Model

The Reynolds stress model (RSM), a second-moment closure, is considered in this study. The Reynolds stress transport equation can be given as

$$\frac{\partial}{\partial x_k}\left(\rho u_k \overline{u'_i u'_j}\right) = -\frac{\partial}{\partial x_k}\left[\rho u_k \overline{u'_i u'_j u'_k} + \overline{P(\delta_{kj}u'_i + \delta_{ik}u'_j)} + \mu\frac{\partial}{\partial x_k}\left(\overline{u'_i u'_j}\right)\right]$$
$$-\rho\left(\overline{u'_i u'_k}\frac{\partial u_j}{\partial x_k} + \overline{u'_j u'_k}\frac{\partial u_i}{\partial x_k}\right) + \overline{P\left(\frac{\partial u'_i}{\partial x_j} + \frac{\partial u'_j}{\partial x_i}\right)} - 2\mu\overline{\frac{\partial u'_i}{\partial x_k}\frac{\partial u'_j}{\partial x_k}} \tag{2.23}$$

The diffusive term on the right-hand side can be modeled as

$$-\frac{\partial}{\partial x_k}\left[\rho u_k \overline{u'_i u'_j u'_k} + \overline{P(\delta_{kj}u'_i + \delta_{ik}u'_j)} + \mu\frac{\partial}{\partial x_k}\left(\overline{u'_i u'_j}\right)\right] = \frac{\partial}{\partial x_k}\left(\frac{\mu_t}{\sigma_k}\frac{\partial}{\partial x_k}\left(\overline{u'_i u'_j}\right)\right) \qquad (2.24)$$

The second term on the right-hand side of Eq. 2.23 is the production term, and it is notated as G_{ij}

$$G_{ij} = -\rho\left(\overline{u'_i u'_k}\frac{\partial u_j}{\partial x_k} + \overline{u'_j u'_k}\frac{\partial u_i}{\partial x_k}\right) \qquad (2.25)$$

The third term is the pressure-strain term, which can be modeled as

$$\overline{P\left(\frac{\partial u'_i}{\partial x_j} + \frac{\partial u'_j}{\partial x_i}\right)} = C_1\rho\frac{\varepsilon}{k}\left(\overline{u'_i u'_j} - \frac{2}{3}\delta_{ij}k\right) - C_2\left[A_{ij} - \frac{1}{3}\delta_{ij}A_{kk}\right] \qquad (2.26)$$

where $A_{ij} = G_{ij} - \frac{\partial}{\partial x_k}\left(\rho u_k \overline{u'_i u'_j}\right)$. The constants C_1 and C_2 are 1.8 and 0.6, respectively. The last term in Eq. 2.23 can be approximated by

$$2\mu\overline{\frac{\partial u'_i}{\partial x_k}\frac{\partial u'_j}{\partial x_k}} = \frac{2}{3}\delta_{ij}\rho\varepsilon \qquad (2.27)$$

with the assumption that the dissipation isisotropic.

Modeling of the turbulent heat flux and mass flux are similar as in the k-ε model. The turbulent kinetic energy and its dissipation rate can be calculated from the Reynolds stresses.

2.3.3 Other Models

Ignoring details here, the turbulent models adopted in this study also include the RNG k-ε model, k-ω model, and the shear-stress transport (SST) k-ω model. RNG k-ε model was derived using renormalization group theory (Choudhury, 1993). It has an additional term in the ε-equation to improve the accuracy for rapidly strained flows. It uses the effective viscosity to account for the low-Reynolds-number effects. Theoretically, this model is more accurate and reliable than the standard k-ε model. The standard k-ω model is an empirical model based on transport equations for the turbulence kinetic energy (k) and the specific dissipation rate (ω), which can also be considered as the ratio of ε to k (Wilcox, 1998). The low-Reynolds-number effect is accounted for in the k-ω model. The SST model is a mixture of the k-ω model and the

k-ε model: close to the wall it becomes the k-ω model while in the far field the k-ε model is applied (Menter, 1993).

2.4 Radiation Model

Five different radiation models to coal gasification process have been investigated in this study, including Discrete Transfer Radiation Model (DTRM), P-1 Radiation Model, Rosseland Radiation Model, Surface-to-Surface (S2S) Radiation Model, and Discrete Ordinates (DO) Radiation Model. The detail descriptions of each model are presented in Chapter 5. The P-1 radiation model is used to calculate the flux of the radiation at the inside walls of the gasifier in this study. The general descriptions of P-1 model are stated as below.

The P-1 radiation model is the simplest case of the more general P-N radiation model that is based on the expansion of the radiation intensity I. The P-1 model requires only a little CPU demand and can easily be applied to various complicated geometries. It is suitable for applications where the optical thickness **a**L is large where "**a**" is the absorption coefficient and L is the length scale of the domain.

The heat sources or sinks due to radiation is calculated using the equation

$$-\nabla . q_r = \mathbf{a}G - 4\mathbf{a}\sigma T^4 \tag{2.28}$$

where

$$q_r = -\frac{1}{3(a+\sigma_s)-C\sigma_s}\nabla G \tag{2.29}$$

and q_r is the radiation heat flux, **a** is the absorption coefficient, σ_s is the scattering coefficient, G is the incident radiation, C is the linear-anisotropic phase function coefficient, and σ is the Stefan-Boltzmann constant. The gases are assumed to be the participating media. However, when the effect of particles is included in the radiation model, the heat sources or sinks due to radiation become,

$$-\nabla \cdot q_r = -4\pi\left(a\frac{\sigma T^4}{\pi}+\varepsilon_p\right)+(a+a_p)\nabla G \tag{2.30}$$

where ε_p and a_p are the equivalent emissivity and equivalent absorption of the particle, respectively.

The flux of the radiation, $q_{r,w}$, at walls caused by incident radiation G_w is given as

$$q_{r,w} = -\frac{4\pi\varepsilon_w \frac{\sigma T_w^4}{\pi} - (1-\rho_w)G_w}{2(1+\rho_w)} \tag{2.31}$$

where ε_w is the emissivity and is defined as

$$\varepsilon_w = 1 - \rho_w \tag{2.32}$$

and ρ_w is the wall reflectivity.

2.5 Discrete Phases (Solid Particles or Liquid Particles)

Discrete phases include coal particles and liquid particles. The Lagrangian method to track each particle is adopted in this study. The discrete phase is justified in entrained-flow gasification process because the particle concentration is lower than 10%. Particles in the airflow can encounter inertia and hydrodynamic drags. Because of the forces experienced by the particles in a flow field, the particles can be either accelerated or decelerated. The velocity change is determined by the force balance of the particle, which can be formulated by

$$m_p dv_p/dt = F_d + F_g + F_o \tag{2.33}$$

where F_d is the drag force of the fluid on the particle and F_g is the gravity. F_o represents the other body forces, typically include the "virtual mass" force, thermophoretic force, Brownian force, Saffman's lift force, etc. In this study, Saffman's lift force reaches about 30% of Fg, so it is included in this study.

The drag force, F_d, is calculated as

$$F_D = \frac{18\mu}{\rho_p d_p^2}\frac{C_D Re}{24}(v - v_p)m_p \tag{2.34}$$

and the gravity force, F_g, is calculated using the following equation

$$F_g = \frac{g(\rho_p - \rho)}{\rho_p} m_p \tag{2.35}$$

where m_p is particle mass, d_p is particle diameter, v is the fluid phase velocity, v_p is the particle velocity, ρ is the fluid phase density, ρ_p is the particle density, g is gravity, μ is the fluid phase molecular viscosity, and C_D is the drag coefficient. The relative Reynolds number, Re, is defined as

$$Re = \frac{\rho d_p |v_p - v|}{\mu} \tag{2.36}$$

2.5.1 Coal particles

Gasification or combustion of coal particles undergoes the following global processes: (i) evaporation of moisture, (ii) devolatilization, (iii) gasification to CO and (iv) combustion of volatiles, CO, and char. (See Figure 1.12)

2.5.1.1 Devolatilization Models

After all the moisture contained in the coal particle has evaporated, the particle undergoes devolatilization. Four different devolatilization models widely used are the Kobayashi model, single rate model, constant rate model, and CPD (Chemical Percolation Devolatilization) model.

(a) Kobayashi model --- The Kobayashi model (Kobayashi, 1976) with two-competing devolatilization rates are expressed as a weighted function of two competing rates, R_1 and R_2, as shown below,

$$\frac{m_v(t)}{(1-f_{w,0})m_{p,0}-m_a} = \int_0^t (\alpha_1 R_1 + \alpha_2 R_2)\exp\left(-\int_0^t (R_1+R_2)dt\right)dt \qquad (2.37)$$

where α_1 and α_2 are yield factors, f_w is mass fraction of moisture, m_p is mass of particle, m_a is mass of ash, and R_1 and R_2 are given as,

$$R_1 = A_1 e^{-(E_1/RT_p)} \qquad (2.38)$$

and,

$$R_2 = A_2 e^{-(E_2/RT_p)}. \qquad (2.39)$$

The value of the constants are $A_1 = 2\text{x}10^5$, $A_2 = 1.3\text{x}10^7$, $E_1 = 1.046\text{x}10^8$ J/kgmol, and $E_2 = 1.67\text{x}10^8$ J/kgmol.

(b) Single rate model --- The devolatilization rate is dependent on the amount of volatiles remaining in the particle (Badzioch and Hawsley, 1970). The devolatilization kinetic rate is defined in Arrhenius form below

$$k = Ae^{-(E/RT)} \qquad (2.40)$$

where the pre-exponential factor, A, used in this study is $4.92\text{x}10^5$ and the activation energy, E, is $7.4\text{x}10^7$ J/kgmol.

(c) Constant rate model --- This model assumes that volatiles are released at a constant rate (Baum and Street, 1971). The rate used in this study is 12/s (Pillai, 1981).

(d) Chemical Percolation Devolatilization (CPD) model --- The CPD model considers the chemical transformation of the coal structure during devolatilization. It models the coal structure transformation as a transformation of chemical bridge network which result in release of light gas, char, and tar (Fletcher and Kerstein (1992), Fletcher et al. (1990), and Grant et al. (1989)). The initial fraction of the bridges in the coal lattice is 1, and the initial fraction of char is 0. The lattice coordination number is 5. The cluster molecular weight is 400 and the side chain molecular weight is 50.

Volatiles released by coal particles contain a large amount of various lighter gases. When simulating coal gasification, decision has to be made as to what lighter gases are released during the devolatilization.

Silaen and Wang (2010) compared the effect of these four different devolatilization models on the gasification process respectively. The analysis concluded that the rate calculated by the Kobayashi two-competing rates devolatilization model [H. Kobayashi et al. (1976)] is very slow, while that of the CPD model gives a more reasonable result. Therefore, the Chemical Percolation Devolatilization (CPD) model was chosen for this study.

The study by Chen et al. (2000) modeled that hydrogen, oxygen, nitrogen, and sulfur in the coal particles to be released as a volatile species. The volatile species then reacts with oxygen according to Eq. 2.41 below for oxygen-rich conditions and Eq. 2.42 for oxygen-lean conditions.

For oxygen-rich conditions,

$$\begin{aligned} C_{m1}H_{m2}O_{m3}N_{m4}S_{m5}mois_{m6} + \left(m_1 + \frac{m_2}{4} - \frac{m_3}{2} + m_5\right)O_2 \rightarrow m_1CO_2 \\ + \left(m_7 + \frac{m_2}{4}\right)H_2O + m_5SO_2 + \frac{m_4}{2}N_2 \end{aligned} \quad . \tag{2.41}$$

For oxygen-lean conditions $\left(\varphi < \left(m_1 + \frac{m_2}{4} - \frac{m_3}{2} + m_5\right)\right)$,

$$\begin{aligned} C_{m1}H_{m2}O_{m3}N_{m4}S_{m5} + \varphi O_2 \rightarrow \alpha_1 CO_2 + \alpha_2 CO + m_1(1-\alpha_1-\alpha_2)CO_2 \\ + \left[\frac{(1-\alpha_1)}{2}(m_2 - 2m_5) - 2(1-\alpha_1-\alpha_2)\right]H_2 \\ + \frac{\alpha_1(m_2-2m_5)}{2}H_2O + \frac{\alpha_1(m_2-2m_5)}{2}H_2O + m_5H_2S + \frac{m_4}{2}N_2 \end{aligned} \quad . \tag{2.42}$$

The values of m_1 through m_6, which determine the composition of the volatile, in Eqs. 2.41 and 2.42 above are calculated from the proximate and ultimate analyses of the coal. The coefficient φ is the criteria for which the condition is considered oxygen-lean.

Kumar et al. (2009) modeled that volatiles are broken up as follow,

$$\text{Volatiles} \rightarrow \alpha_1 CO + \alpha_2 H_2O + \alpha_3 CO_2 + \alpha_4 H_2 + \alpha_5 CH_x + \alpha_6 N_2 \quad (2.43)$$

where the stoichiometric coefficients α_i's and value of x in CH_x are determined by the proximate and ultimate analyses of the coal. In this study, the volatile matters contained in the coal are assumed to be composed of CO, H_2, N_2, CH_4, and C_6H_6 (Tomeczek, 1994) or C_2H_2. However, the devolatilization model used can only model the release of one volatile gas. Thus, the devolatilization model is divided into two steps:

(i) Release of a volatile gas modeled using the devolatilization model. All of the volatile matters are lumped into one intermediate gas species ($C_xH_yO_z$), whose release rate is given by the devolatilization model.

(ii) Thermal cracking of the volatile gas into several different gases. Once this intermediate is released, it is decomposed into the volatile gases – CO, H_2, and CH_4 – through chemical reaction: $C_xH_yO_z \rightarrow aCO + bH_2 + cCH_4$

To model part (i), the chemical formula of the intermediate gas species ($C_xH_yO_z$) has to be known. However, coal composition does not provide the volatiles' chemical formula. Thus, the chemical formula needs to be found out. Based on the proximate and ultimate analyses, the elemental composition of the volatiles is calculated. The enthalpy of the volatiles is calculated from the coal heating value. The detailed calculation is presented in Appendix A.

2.5.2 Liquid droplets

Theoretically, evaporation occurs at two stages: (a) when temperature is higher than the saturation temperature (based on local water vapor concentration), water evaporates from the particle's surface, and the evaporation is controlled by the water vapor partial pressure until 100% relative humidity is achieved; (b) when the boiling temperature (determined by the air-water mixture pressure) is reached, water continues to evaporate even though the relative humidity reaches 100%. After the moisture is evaporated due to either high temperature or low moisture partial pressure, the vapor diffuses into the main flow and is transported away. The

rate of vaporization is governed by concentration difference between surface and gas stream, and the corresponding mass change rate of the particle can be given by,

$$\frac{dm_p}{dt} = \pi d^2 k_c (C_s - C_\infty) \tag{2.44}$$

where k_c is the mass transfer coefficient and C_s is the concentration of the vapor at the particle's surface, which is evaluated by assuming that the flow over the surface is saturated. C_∞ is the vapor concentration of the bulk flow, obtained by solving the transport equations. The values of k_c can be calculated from empirical correlations by (Ranz and Marshall, 1955):

$$Sh_d = \frac{k_c d}{D} = 2.0 + 0.6 Re_d^{0.5} Sc^{0.33}. \tag{2.45}$$

where Sh is the Sherwood number, Sc is the Schmidt number (defined as ν/D), D is the diffusion coefficient of vapor in the bulk flow. Re_d is the particle slip Reynolds number, defined as $u\nu/d$, where u is the particle slip velocity relative to the gas flow.

When the droplet temperature reaches the boiling point, the following equation can be used to evaluate its evaporation rate (Kuo, 1986):

$$\frac{dm_p}{dt} = \pi d^2 \left(\frac{\lambda}{d}\right)(2.0 + 0.46 Re_d^{0.5}) \ln\left(1 + c_p (T_\infty - T)/h_{fg}\right)/c_p \tag{2.46}$$

where λ is the heat conductivity of the gas/air, h_{fg} is the droplet latent heat, and c_p is the specific heat of the bulk flow.

The droplet temperature can also be changed due to heat transfer between droplets and the continuous phase. The droplet's sensible heat change of the droplet is shown in the following equation

$$m_p c_p \frac{dT}{dt} = A_p h(T_\infty - T) + \frac{dm_p}{dt} h_{fg} + f_h \frac{dm_p}{dt} H_{reac} + A_p \varepsilon_p \sigma\left(\theta_R{}^4 - T^4\right) \tag{2.47}$$

where θ_R is the radiation temperature. The convective heat transfer coefficient (h) can be obtained with a similar empirical correlation to equation (2.35):

$$Nu_d = \frac{hd}{\lambda} = 2.0 + 0.6 Re_d^{0.5} Pr^{0.33} \tag{2.48}$$

where Nu is the Nusselt number, and Pr is the Prandtl number.

2.5.3 Stochastic Tracking

The various turbulence models are based on the time-averaged equations. Using this flow velocity to trace the droplet will result in an averaged trajectory. In the real flow, the instantaneous velocity fluctuation would make the droplet dance around this average track. However, the instantaneous velocity is not calculated in the current approach as the time averaged Navier-Stokes equations are solved. One way to simulate the effect of instantaneous turbulence on droplets dispersion is to use the stochastic tracking scheme (Fluent, 2012). Basically, the droplet trajectories are calculated by using the instantaneous flow velocity ($\overline{u} + u'$) rather than the average velocity ($\overline{u}$). The velocity fluctuation is then given as:

$$u' = \zeta\left(\overline{u'^2}\right)^{0.5} = \zeta(2k/3)^{0.5} \tag{2.49}$$

where ζ is a normally distributed random number. This velocity will apply during a characteristic lifetime of the eddy (t_e), given from the turbulence kinetic energy and dissipation rate. After this time period, the instantaneous velocity will be updated with a new ζ value until a full trajectory is obtained. When the stochastic tracking is applied, the basic interaction between droplets and continuous phase keeps the same, accounted by the source terms in the conservation equations. The source terms are not directly but rather indirectly affected by the stochastic method. For example, the drag force between droplets and the airflow depends on the slip velocity calculated by the averaged Navier-Stokes equations if without the stochastic tracking. With the stochastic tracking a random velocity fluctuation is imposed at an instant of time, and the drag force and additional convective heat transfer will be calculated based on this instantaneous slip velocity. The source terms associated with this instantaneous drag force and convective heat transfer enter the momentum and energy equations without any additional formulation. For a steady-state calculation, the "instant of time" means "each iteration step." Therefore, the averaged momentum equation will not be affected by the stochastic tracking scheme; rather the trajectory of the droplet will reflect the effect of the imposed instantaneous perturbation.

2.6 Reaction Models

2.6.1 Particle Reactions

The reaction of particle occurs after the devolatilization process has finished. The rate of depletion of solid due to a surface reaction is expressed as (Smith, 1982),

$$\overline{R} = A\eta YR \tag{2.50}$$

$$R = k\left(p_n - \frac{R}{D} \right)^N \tag{2.51}$$

where

$\overline{R}$ = rate of particle surface species depletion (kg/s)

A = particle surface area (m^2)

Y = mass fraction of surface the solid species in the particle

η = effectiveness factor (dimensionless)

R = rate of particle surface species reaction per unit area (kg/m^2-s)

p_n = bulk concentration of the gas phase species (kg/m^3)

D = diffusion rate coefficient for reaction

k = kinetic reaction rate constant (units vary)

N = apparent order of reaction.

The kinetic rate of reaction is usually defined in an Arrhenius form as

$$k = AT^n e^{-(E/RT)} \ . \tag{2.52}$$

For reaction order N = 1, the rate of particle surface species depletion is given by

$$\overline{R} = A\eta Y p_n \frac{kD}{D+k} \ . \tag{2.53}$$

For reaction order N = 0,

$$\overline{R} = A\eta Y k \ . \tag{2.54}$$

For reaction order N = 0, the unit for the kinetic reaction rate constant, k, is kg/m^2-s.

The reaction order of the particle reaction is assigned 0. Thus, Eq. 2.50 is used to calculate rate of depletion of the solid, $\overline{R}$ (kg/s). The kinetic reaction rate constant, k (kg/m^2-s), is to be supplied by the user.

The kinetic reaction rate constants, k, for the solid-gas char reactions are determined by kinetic reaction rate constants adopted from published literatures as presented in Table 2.1.

These rate constants are taken from Chen et al. (2000(a)). These kinetic reaction rate constants have to be carefully checked and adjusted if necessary so that their units are consistent with the unit of k (kg/m^2-s) in Eq. 2.54. The sources of these kinetic reaction rate constants are introduced and discussed below.

Table 2.1 Kinetic reaction rate constants for solid-gas reactions. (Chen et al., 2000)

Reaction	***Rate Constant***	***Parameters***
$C(s) + ½O_2 \rightarrow CO$ (Combustion)	$k = AT^n \exp(-E/RT)$ (kg/m^2-s-$Pa^{0.5}$)	n = 0 A = 0.052 kg/m^2-s-$Pa^{0.5}$ E = $6.1x10^7$ J/kmol
$C(s) + CO_2 \rightarrow 2CO$ (Gasification, Boudouard reaction)	$k = AT^n \exp(-E/RT)$ (kg/m^2-s-$Pa^{0.5}$)	n = 0 A = 0.0732 kg/m^2-s-$Pa^{0.5}$ E = $1.125x10^8$ J/kmol
$C(s) + H_2O(g) \rightarrow CO + H_2$ (Gasification)	$k = AT^n \exp(-E/RT)$ (kg/m^2-s-$Pa^{0.5}$)	n = 0 A = 0.0782 kg/m^2-s-$Pa^{0.5}$ E = $1.15x10^8$ J/kmol

2.6.2 Gas Phase (Homogeneous) Reactions

Three approaches are adopted to solve homogenenous gas- phase reactions: (a) eddy-dissipation model, (b) global equilibrium model, and (c) finite-rate kinetic model.

(a) Eddy-dissipation model takes into account the turbulent mixing of the gases. It assumes that the chemical reaction is faster than the time scale of the turbulence eddies. Thus, the reaction rate is determined by the turbulence mixing of the species. The net rate of production of species i due to reaction r, $R_{i,r}$ is given by the smaller of the two expression below:

$$R_{i,r} = \nu'_{i,r} M_{w,i} A\rho \frac{\varepsilon}{k} \min_R \left(\frac{Y_R}{\nu'_{R,r} M_{w,R}} \right) \tag{2.55}$$

$$R_{i,r} = \nu'_{i,r} M_{w,i} AB\rho \frac{\varepsilon}{k} \left(\frac{\sum_P Y_P}{\sum_j^N \nu''_{j,r} M_{w,j}} \right) \tag{2.56}$$

where $\nu'_{i,r}$ is the stoichiometric coefficient of the reactant i in reaction r, and $\nu''_{j,r}$ is the stoichiometric coefficient of the product j in reaction r. Y_P is the mass fraction of any product species P, and Y_R is the mass fraction of a particular reactant R. A is an empirical constant equal

to 4.0, and B is an empirical constant equal to 0.5. The smaller of the two expressions is used because it is the limiting value that determines the reaction rate.

(b) Global equilibrium model.

(c) The finite-rate kinetic model calculates the reaction rate using an expression that takes into account temperature, but does not take into account the turbulent mixing of the species. For non-reversible reaction, the net source of chemical species i due to reaction is computed as the sum of the Arrhenius reaction sources over N_R reactions that the species participate in:

$$R_i = M_{w,i} \sum_{r=1}^{N_R} \Gamma(\nu''_{i,r} - \nu'_{i,r})(k_{f,r} \prod_{j=1}^{N} [C_{j,r}]^{(\eta'_{j,r} + \eta''_{j,r})}) \quad (2.57)$$

where,

$M_{w,i}$ = molecular weight of species i (kg/kmol)

$\nu'_{i,r}$ = stoichiometric coefficient of reactant i in reaction r

$\nu''_{i,r}$ = stoichiometric coefficient of product i in reaction r

$k_{f,r}$ = forward kinetic reaction rate constant for reaction r (s^{-1})

$[C_{j,r}]$ = molar concentration of species j in reaction r ($kmol/m^3$)

$\eta'_{j,r}$ = rate exponent of reactant species j in reaction r

$\eta''_{j,r}$= rate exponent of product species j in reaction r

Reaction rate constant, k, is usually expressed in an Arrhenius form, $k = AT^n \exp(-E/RT)$. The unit of k is s^{-1}. (Note that this is different from the unit in Eq. 2.54 because it is the reaction rate constant for homogenous gas phase reaction while the k in Eq. 2.54 is based on surface rate for the heterogeneous gas-solid reaction)

For each gas-phase homogeneous reaction in this study, the reaction rates based on both the eddy-dissipation and finite-rate kinetic rate are calculated. The smaller of the two is used as the reaction rate. The summary of the kinetic reaction rate constants for the gas-phase homogeneous reactions are presented in Table 2.2. The reaction rate constant for the reaction $CO + ½\ O_2 \rightarrow CO_2$ is taken from Westbrook and Dryer (1981). The reaction rate constant for the water-gas-shift (WGS)reaction ($CO + H_2O_{(g)} \rightarrow CO_2 + H_2$) listed in the table has been reduced from the original value by Jones and Lindstedt (1988). Jones and Lindstedt obtained the reaction rate constant through experiment where catalyst was used. Since catalyst is not used in this study, the reaction rate constant would not be correct. The original reaction rate

constant by Jones and Lindstedt was used in the preliminary study. It was found that the syngas contained no H_2O with very low CO and very high H_2 and CO_2. This indicates that the water-shift reaction was dominant. The reaction rate constant for the water-shift was then purposely slowed down to make the syngas composition consistent with that in the actual similar commercial entrained-flow gasifier with coal-slurry feed from bottom operated by Wabash River Energy Ltd. (Wabash River Energy Ltd., 2000). More detailed discussions and a special investigation of WGS rate are conducted in Chapter 4.

Table 2.2 Kinetic reaction rate constants for finite-rate gas phase reactions.

Reaction	**Rate Constant**	**Parameters**
$CO + ½\ O_2 \rightarrow CO_2$	$k = AT^n \exp(-E/RT)$ (s^{-1})	n = 0 $A = 2.2x10^{12}$ $E = 1.67x10^8$ J/kmol
$CO + H_2O(g) \rightarrow CO_2 + H_2$ (Watershift)	$k = AT^n \exp(-E/RT)$ (s^{-1})	n = 0 $A = 2.75x10^2$ $E = 8.38x10^7$ J/kmol
$C_2H_2 + O_2 \rightarrow 2CO + H_2$	Eddy-dissipation only	

2.7 Gasification Models

There are two gasification models used in this study: (a) finite-rate gasification model and (b) the instantaneous gasification model.

2.7.1 Finite-Rate Model

In the finite-rate model, the flow (continuous phase) is solved in Eulerian form as a continuum while the particles (dispersed-phase) are solved in Lagrangian form as a discrete phase. Stochastic model is employed to model the effects of turbulence on the particles. The continuous phase and discrete phase are communicated through drag forces, lift forces, heat transfer, mass transfer, and species transfer. The finite-rate combustion model is used for the heterogeneous reactions. Both the finite-rate and eddy-dissipation models are used for the homogeneous reactions, and the smaller of the two is used as the reaction rate. The finite-rate model calculates the reaction rates based on the kinetics, while the eddy-dissipation model calculates based on the turbulent mixing rate of the flow. Gasification or combustion of coal

particles undergoes the following global processes: (i) evaporation of moisture, (ii) devolatilization, (iii) gasification to CO and (iv) combustion of volatiles, CO, and char.

For solid particles, the rate of depletion of the solid due to a surface reaction is expressed as a function of kinetic rate, solid species mass fraction on the surface, and particle surface area as described in Section 2.6.1 earlier. The reaction rates are all global net rates, i.e., the backward reaction, calculated by equilibrium constants, are included in the global rate. The water evaporation for the liquid droplets is calculated as described in Section 2.5.2.

2.7.2 Instantaneous Gasification Model

The interphase exchange rates of mass, momentum and energy are assumed to be infinitely fast. Carbon particles are made to gasify instantaneously, thus the solid-gas reaction process can be modeled as homogeneous gas combustion reactions. This approach is based on the locally-homogeneous flow (LHF) model proposed by Faeth (1987), implying infinitely-fast interphase transport rates. The instantaneous gasification model can effectively reveal the overall reaction process and results without dealing with the details of the otherwise complicated heterogeneous particle surface reactions, heat transfer, species transport, and particle tracking in turbulent reacting flow. The eddy-dissipation model is used to model the chemical reactions. This model can significantly reduce the computational time but can only provide a qualitative trend of gasification process. Although the instantaneous gasification model is crude, it catches the effect of thermal-fluid field (including turbulence structure) on chemical reactions, which are not readily available from the global equilibrium method. The instantaneous gasification model is only used for preliminary studies to exam if the boundary conditions are adequately assigned, if the thermo-flow field can achieve convergence, if the homogeneous reactions can take place, and if the computational grid is of good quality. After the initial examination of all the computational parameters and preliminary results, the computational scheme is switched to the finite-rate model.

CHAPTER THREE
COMPUTATIONAL METHOD

3.1 Computational Scheme

The major steps in the CFD simulation are divided into three: (a) preprocessing, (b) processing, and (c) postprocessing.

3.1.1 Preprocessing

Preprocessing refers to the geometry generation, geometry mesh, model specifications and boundary specifications. Before any calculation can be done, computational domain has to be created. The commercial preprocessing software GAMBIT is used to generate and then mesh geometries (computational domains) in this study. Once a computational domain geometry has been meshed in GAMBIT, it is imported into the commercial CFD code FLUENT (Version 14.1) from ANSYS, Inc. Then, the appropriate models and boundary conditions are set.

3.1.2 Processing

In the processing step, calculations are performed to obtain the solution for the governing equations. As indicated earlier, ANSYS/FLUENT is used in this study. ANSYS/FLUENT is a finite-volume based CFD solver. Solution is obtained through iteration until convergence criteria, which are set by the user, are satisfied. Residuals are used as means to determine the convergence. Residuals are the imbalanced errors in the governing equations over all the cells in the computational domain.

3.1.3 Postprocessing

Postprocessing involves analyzing and interpreting solution obtained. Charts and various visualization schemes can be employed to aid in understanding the physics of the solution.

3.2 Numerical Procedures

The segregated solution method is employed in solving the governing equations. The segregated solution method means that the governing equations of continuity, momentum, energy, and species transport are solved sequentially (segregated from one another). The non-linear governing equations are implicitly linearized, which means that each unknown value is computed using a relation that includes both existing and unknown values from the neighboring cells. As a result, each unknown will appear in more than one equation in the linear system produced. Thus, these equations must be solved simultaneously in order to obtain the unknown quantities.

The governing equations are discretized spatially to yield discrete algebraic equations for each control volume. The second order scheme is used as the discretization scheme. The SIMPLE algorithm (Patankar, 1980) is used to couple the pressure and velocity.

There are three types of boundary conditions used:

a. Mass flow rate inlet – All the inlet surfaces are defined as mass flow rate inlets. Mass flow rate, temperature of the gas mixture, and mass fractions of all species are specified.
b. Pressure outlet – The outlet surface is assigned as a pressure outlet boundary. Pressure, temperature, and species mass fractions of the gas mixture just downstream of the outlet (outside of the domain) are specified. This information does not affect the calculations inside the computational domain but will be used if the backflow occurs at the outlet.
c. Walls – The outside surfaces are defined as the wall boundary. The walls are stationary with no-slip condition imposed (zero-velocity) on the surface. The heat flux on the walls is set to 0 (adiabatic walls).

The dispersed phase enters the computational domain through the injection points. In this study, the "surface" injections are used. The surface where an injection is located is specified. A stream will then be placed at the center of each cell face on that particular surface. The total mass flow rate for the injection is specified, and is equally divided among the streams. For "surface" injections, velocity, size, and temperature of the particles at these injection points are specified.

As mentioned in Chapter 2, the Eulerian-Lagrangian method is adopted to solve the multiphase problem. Eulerian method is used for the continuous phase, and the Lagrangian method for the disperse phase. The iterations are conducted alternatively between the

continuous and the dispersed phases. The continuous phase is updated in the next iteration based on the dispersed phase calculation results, and the process is repeated.

The detailed steps of the calculation process are given below. Figure 3.1 depicts the flow chart of these steps.

1. Fluid properties are updated based on the current solution or the initialized condition.
2. The momentum equations are solved using the current values of pressure and face mass fluxes to get the updated velocity field.
3. The equation for the pressure correction is calculated from the continuity equation and the linearized momentum equations since the velocity field obtained in step (2) may not satisfy the continuity equation.
4. The pressure correction equations obtained from step (3) are solved to correct the pressure and velocity fields, and face mass such that the continuity equation is satisfied.
5. The equations for turbulence are solved using the updated values of the other variables.
6. The homogeneous gas phase reactions are solved. Production and consumptions of each species are calculated.
7. Enthalpy change due to reaction is calculated.
8. The species transport equations are solved. Changes in the species mass fraction due to reactions in steps 6 and 12 appear as source or sink terms in the species transport equation.
9. The energy equation is solved. This includes source or sink terms due to reactions in steps 6 and 7.
10. Particles (dispersed phase) are tracked one by one. Forces on the particles (drag, lift) are calculated.
11. Particle heat transfer is calculated.
12. Heterogeneous reactions (gas-solid) are calculated. Production and consumptions of each species are calculated.
13. Enthalpy changes due to reaction are calculated.

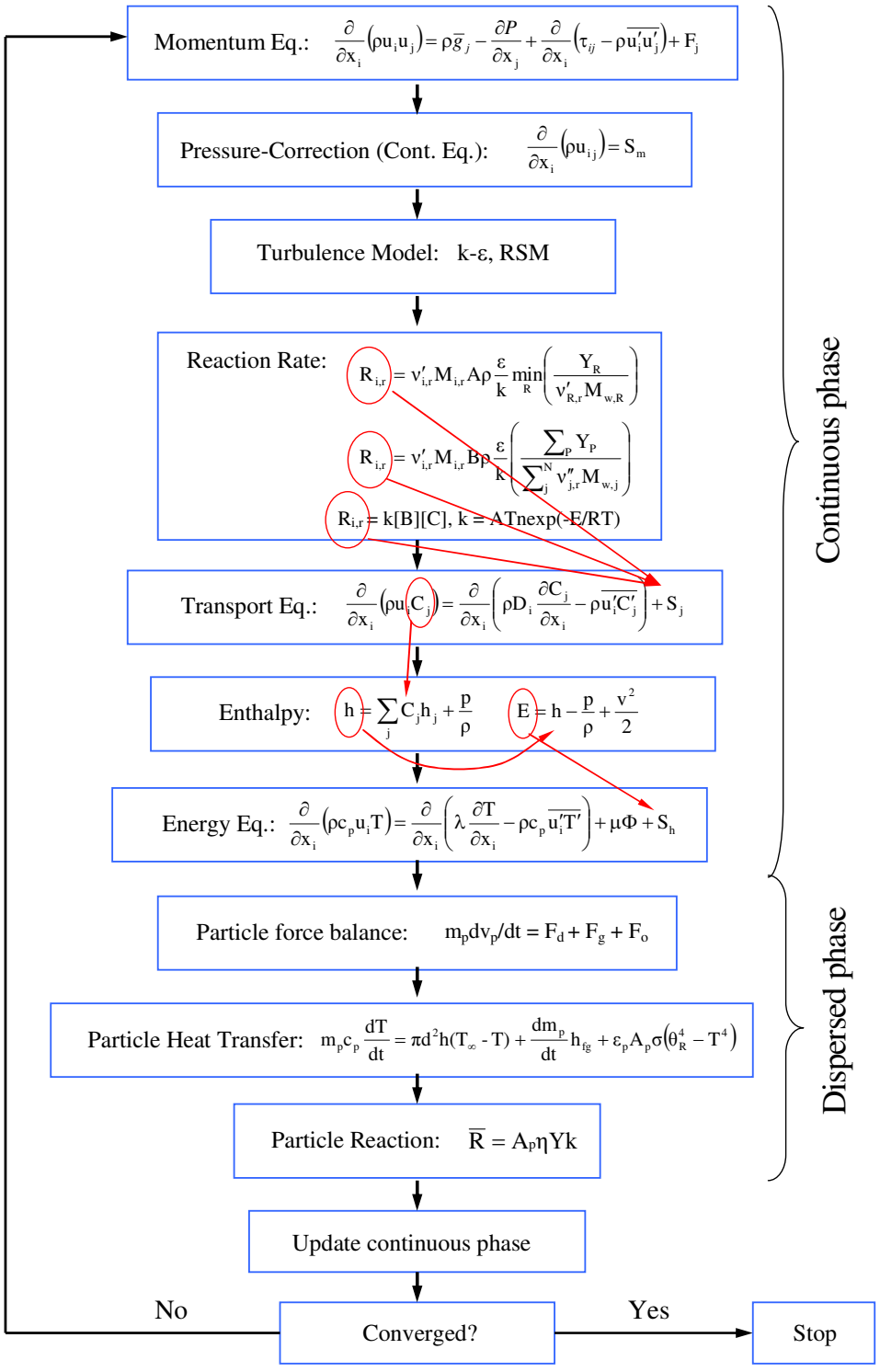

Figure 3.1 Outline of numerical procedures.

14. The species transport equations are solved. Changes in the species mass fraction due to reactions in step 12 appear as source or sink terms in the species transport equation.
15. Momentum equations are updated with drag forces and solved again.
16. The energy equation is solved. This includes source or sink terms due to particle heat transfer and reactions in steps 11 and 13.
17. Continuous phase properties are updated based on the dispersed phase.
18. The equation is checked for convergence.
19. If convergence criteria are met, the process is stopped. Otherwise, the process is repeated from step 1.

Converged results are obtained when the residuals satisfy mass residual of 10^{-3}, energy residual of 10^{-5}, momentum and turbulence kinetic energy residuals of 10^{-4}. These residuals are the summation of the imbalance in each cell, scaled by a representative for the flow rate. Figure 3.2 shows a graph of typical variable residuals. The fluctuations shown in Fig. 3.2 are a normal display of calculation alternating between continuous and dispersed phases.

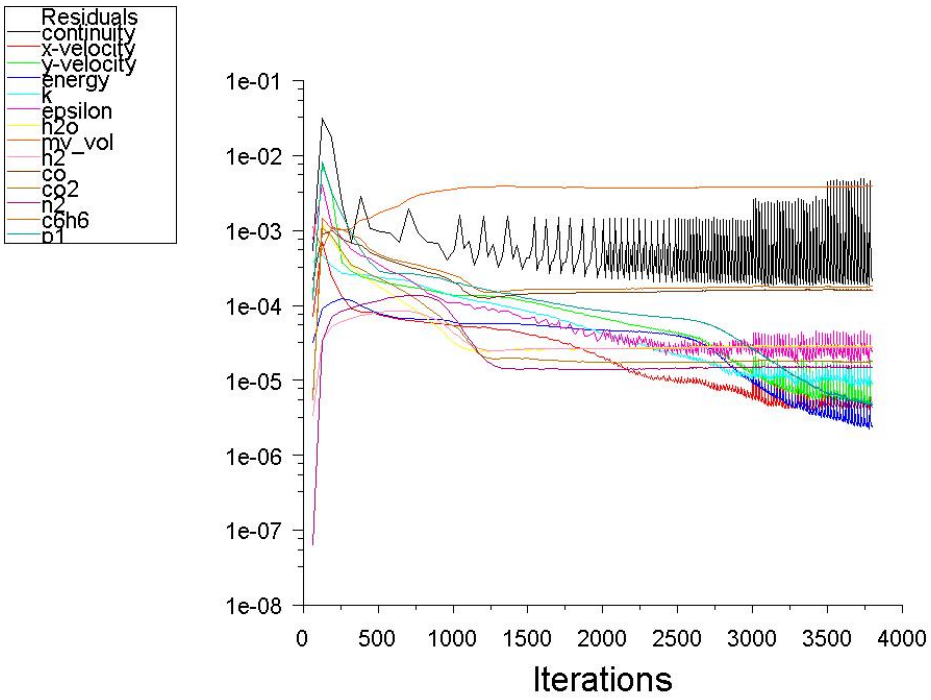

Figure 3.2 Typical variable residuals during calculation.

Material properties:

Variable properties for enthalpy, specific heat and conductivity are used for each species. The specific heat is calculated using piecewise-polynomial relation as a function of temperature defined as

$$\text{For } T_{min1} < T < T_{max1},\ F(T) = A_1T + A_2T^2 + A_3T^3 + ...$$
$$\text{For } T_{min2} < T < T_{max2},\ F(T) = B_1T + B_2T^2 + B_3T^3 + ... \quad (3.1)$$

The specific heat of the whole continuous phase, which is a mixture of species, is also a variable and is calculated as a mass fraction average of the pure species heat capacities defined as

$$F = \sum_i Y_i F_{,i} \quad (3.2)$$

Where F is the property (enthalpy, specific heat, or conductivity), Y_i is the mass fraction of species i and F_i is the property of species i.

Simulation procedures:

As mentioned earlier, the calculations for the continuous phase and the dispersed phase are performed alternately. The pathlines of the particles are calculated based on the continuous phase flow field. Thus, a good continuous phase flow field is needed. This can be a problem in the beginning of the simulation where usually the flow field has not yet been established. As a remedy, only the equations for the continuous phase are solved in the beginning of a simulation while the equations for the dispersed phase and chemical reactions are not solved. The purpose is to obtain a good initial isothermal flow field before incorporating the dispersed phase. Usually 300 iterations are performed to let the continuous phase flow field develop. After this, the dispersed phase equations and chemical reactions equations are solved.

Patching temperature:

The initial gas temperature in the gasifier is set the same as the gas temperature at inlets, which is 420 K in this study. Gasification will not occur at this temperature. The energy at this temperature is below the level necessary to overcome the activation energy of the reactions, thus the reactions will not occur. A high temperature is needed to start (or ignite) the reactions. Thus, the domain needs to be patched with a high temperature. This process is akin to using a lighter to ignite combustion inside a combustor. This temperature patching is done by setting the temperature of the cells near the injections to 1500 K, which is high enough to start the

reactions. After the temperature patching, one dispersed phase iteration step is performed, followed by one continuous phase iteration.

Dispersed phase and continuous phase iterations:

As shown in Figure 4.1, the continuous phase is updated after each iteration in dispersed phase. The dispersed phase affects the continuous phase through source terms in the momentum, species transport, and energy equations. These changes in the continuous phase equations will affect the convergence. Normally, twenty continuous phase iterations are performed before changing to the dispersed phase iteration. This allows the continuous phase to settle down before the next dispersed phase iteration and can help the simulation converge faster.

However, it was found during preliminary study, that the practice of performing 20 continuous phase iterations per iteration in dispersed phase in the beginning can sometimes cause the flame to die out. Theoretically, once the char combustion occurs, the energy released should be enough to maintain the flame. However, this is not the case in the simulation.

The reason the flame dies out during initial simulation is explained below. During the dispersed phase calculation, char particles are tracked and the heterogeneous reaction ($C + ½ O_2 \rightarrow CO$) is calculated. The heterogeneous reaction produces CO and releases energy. In the next continuous phase iteration, the homogeneous reaction is calculated where CO produced by the heterogeneous reaction is combusted. This continuous phase iteration is repeated 20 times without performing any dispersed phase iteration at all. In each continuous phase iteration, CO is combusted but no CO is being produced by the heterogeneous reaction. As a result, CO in cells near the injector will be totally consumed. Once CO in a particular cell is totally consumed, no reaction will happen and the temperature in that cell will decrease as gasification reactions (endothermic) take place. If the temperature decreases below the minimum temperature required for char combustion, char will not react in the next dispersed phase iteration.

As the iterations continue in the continuous phase, it can be seen that hot temperature region near the injections/inlets is slowly convected downstream and is replaced by the cold gas from the inlets. Thus, the particles will not react near the injector but instead further downstream. The location where the char combustion starts to occur slowly moves downstream toward the

outlet until it finally moves out of the computational domain. At this stage, all the flames die out and no reaction will occur any more inside the computational domain.

To avoid the flame from dying out, the number of continuous phase iterations per dispersed phase iteration needs to start more frequent in the beginning with one dispersed phase iteration being performed immediately followed by one continuous phase iteration. Then one dispersed phase iteration is done followed by five (5) continuous phase iterations until the flame is stabilized. Typically this would take about 200 steps. Then, ten (10) continuous phase iteration per dispersed phase iteration is done for a total of 200 steps. Finally, it is increased to 20 continuous phase iterations per discrete phase iteration until convergence is achieved. In an extreme case, one continuous phase iteration per single dispersed phase iteration is performed as long as is needed to ensure the flame stabilizes.

Under-relaxation factor:

The under-relaxation factor for variables can help stabilize convergence behavior of the variables. Equation 3.3 defines how the under-relaxation factor, α, affects the value of the variable.

$$\phi = \phi_{old} + \alpha \, \Delta\phi \tag{3.3}$$

ϕ is the variable and $\Delta\phi$ is the change in the variable. The value of under-relaxation factor, α, ranges from 0 to 1. The smaller the under-relaxation factor is, the smaller the change in the variable during the iteration. It can help stabilize the convergence but requires more iteration steps to reach convergence.

The under-relaxation factors are set to 0.3 for the pressure, 0.7 for the momentum, 0.1 for the dispersed phase, and 0.8 for the species, k and ε. The under-relaxation factor for the energy is set to 0.4 in the early stage of the simulation to aid in ensuring the flame or char combustion does not die out (as explained earlier). The under-relaxation factor is then increased to 0.7 once the reactions have stabilized to speed up the computation.

Temperature Limits:

During the preliminary study, it was found that the temperature during iterations could sometimes go as low as 1 K and as high as 5000 K. It is known that the gas temperature in a real gasifier will never reach 1 K or 5000 K. Thus, these extremely low temperature (1 K) and

extremely high temperature (5000 K) are not realistic. To avoid these non-realistic temperatures, the lower and the upper temperature limits are set to 273 K and 3500 K, respectively. It is obvious that the gas temperature inside gasifier will never go below 273 K. The upper limit 3500 K is well above the typical adiabatic flame temperature of coal (2500 K). These upper and lower temperature limits give the CFD solver a good temperature range of where the solution should be bounded. It will prevent the CFD solver from going astray and getting the wrong or unrealistic solutions.

CHAPTER FOUR

TOPIC 1: WATER-GAS SHIFT MODELING IN COAL GASIFICATION IN AN ENTRAINED-FLOW GASIFIER

4.1 Introduction

Gasification is an incomplete oxidation process of converting various carbon-based feedstocks into clean synthetic gas (syngas), which is primarily a mixture of hydrogen (H_2) and carbon monoxide (CO), with minor amounts of methane (CH_4) and inert nitrogen gas (N_2). Syngas coming out of a gasifier is usually very hot. Cooling is necessary to allow this syngas to be transported without damaging downstream piping or equipment. Furthermore, the existing cold syngas cleaning technology also requires that the syngas temperature to be reduced below 600^{o}F. The syngas cooling process would significantly reduce the thermal efficiency of the system if care is not taken to employ the energy cascading scheme to properly maintain the grade (or quality) of the energy during the heat transfer process by applying cooling at different temperature ranges with an optimum pinch point for each cooling stage in a sequentially descending order. Radiant syngas coolers have been usually employed to achieve the highest thermal efficiency. However, a radiant syngas cooler is large, bulky, and expensive, so the direct syngas quenching process has also been adopted for the benefits of reduced space, cost, and maintenance, although it is accompanied by reduced thermal efficiency. A rule of thumb is that a gasification system using a radiant syngas cooler will have approximately 2-3 percentage points higher thermal efficiency than a unit employing the quenching scheme. Recently, as carbon capture and sequestration (CCS) has become an important approach to curb global warming, the syngas quenching approach has become more popular in the gasification process because CCS typically employs the water-shift process (WGS) ($CO + H_2O \Leftrightarrow CO_2 + H_2$) to convert steam and CO to CO_2 and H_2, and, in this process, relatively low-temperature steam (below 600^{o}C, see Table 4.1) is required to allow the reaction to move in forward direction towards products. Since a large amount of relatively low-temperature steam is required, it might as well just directly employ quench cooling. This will allow preliminary water-shifting to occur and also provides the possibility of utilizing the quench chamber to serve as the first-stage shift reactor, thus removing the cost of installing an actual first-stage shift reactor. In addition to

providing cooling and driving the WGS reaction, a water quench can also help clean out ash and other particulate matter. These additional benefits unfortunately are accompanied with another disadvantage: the unburned chars can also be washed away, causing a downgrade in the carbon conversion efficiency.

Table 4.1 Water-gas shift (WGS) reaction equilibrium balance constant

T(^{o}C)	600	800	1000	1200	1400
logK_p	1.396	0.553	0.076	-0.222	-0.424

The WGS reaction rate has been discovered to play an important role in affecting the accurate prediction of the syngas composition during simulations of the gasification process. The earliest data recording the WGS reaction dates back to 1888, and its prominence came with the Haber ammonia synthesis process and catalyst development by Bosch and Wilde in 1912. Most of the reaction rates for the WGS reaction were obtained from experiments with specific catalysts under laboratory conditions of relatively narrow ranges of pressure and temperature. A few of the reaction rates without using catalysts were obtained under various supercritical (water) conditions because a large excess of water solvent could possibly drive the reaction to produce hydrogen without a catalyst. However, the pressure under a supercritical condition is much higher than that in an operating gasifier. In either case, it is not clear how the published reaction rates can be trustfully used to predict the actual WGS reaction rate in a gasifier without the presence of catalysts and under different temperature and pressure conditions than those used in the laboratory. Due to the unavailability of appropriate WGS reaction rates for broad operating conditions in actual gasifiers, the objective of this study is to obtain an appropriate representative WGS global reaction rate under non-catalytic conditions by calibrating the WGS rate against the experimental data from water quench section of an experimental gaisifer, then apply the calibrated WGS reaction rate to CFD simulation of fully gasification process.

4.1.1 Review of WGS Reaction Rates

4.1.1.1 WGS Catalytic Reactions

Chen et al. (2008) investigated the characteristics of carbon monoxide conversion and hydrogen generation from the WGS reaction experimentally using a high-temperature catalyst

and a low-temperature catalyst. The important parameters, including the catalyst type, residence time of the reactants in the catalyst bed, reaction temperature, and CO/steam ratio, were addressed as the influential factors that affected the performance of the WGS reaction. The experimental results showed that when the residence time was as long as 0.09s, the WGS developed well no matter which catalyst was used. It also revealed that the WGS reactions with the high-temperature catalyst and the low-temperature catalyst were governed by chemical kinetics and thermodynamic equilibrium.

It is difficult to narrow down the expression for the WGS reaction with a catalyst because the rate of the reaction is dependent on various parameters, including the composition of the catalyst, the active surface area and structure of the catalyst, the size of the catalyst, age of the catalyst, the operating temperature and pressure, and the composition of the gases. Smith, et al. (2010) made a comprehensive review of research on the WGS reaction rate and the developments in modeling approaches for designing WGS reactors. They consolidated a listing of the various important kinetic expressions published for both the high temperature and the low temperature water-gas shift reactions along with the details of the make-up of the catalysts and the operating conditions at which the kinetics were obtained. Selected studies from Smith et al.'s review are shown in Table 4.2-4.4.

Table 4.2 WGS Reaction Rate with Noble Metal Catalysts (Smith et al., 2010)

Catalyst	Opertating Conditions	Arrhenius Parameters		Reference
		A	E (kJ/mol)	
Ru	300°C-1000°C 0.008 to 0.05 contact time Coated on alumina support 5wt% loading	1.6×10^7 (1/s)	80	Wheeler et al. (2004)
Ru/Ceria		5.0×10^7 (1/s)	80	
Ni		8.0×10^7 (1/s)	85	
Ni/Ceria		1.7×10^8(1/s)	85	
Pd		4.0×10^6(1/s)	100	
Pd/Ceria		4.0×10^7(1/s)	100	
Pt		1.0×10^6(1/s)	80	
Pt/Ceria		2.5×10^7(1/s)	80	
Rh/SiO_2	350°C	3.23×10^6 (molecules/s/site)	22.8±2.5 (kcal/mole)	Grenoble et al. (1981)
Pt/Al_2O_3	270°C	1.9×10^6 (molecules/s/site)	19.6±2.5 (kcal/mole)	
Pt/SiO_2	340°C	1.9×10^6 (molecules/s/site)	19.1±0.8 (kcal/mole)	
Pt/C	340°C	3.84×10^6 (molecules/s/site)	25.5±1.4 (kcal/mole)	
$CuO.1CeO.8O_{2-y}$ (Cu ceria)	200°C - 350°C	1.8×10^3 (1/s)	61	Kusar et al. (2006)
$CuO.1CeO.8O_{2-y}$ (Cu ceria)	300°C - 350°C	4.0×10^3 (1/s)	78	

Table 4.3 WGS Reaction Rate with High-Temperature Catalysts (310°C-450°C) (Smith et al., 2010)

Catalyst	Operating Conditions	Arrhenius Parameters		Reference
		A	E (kJ/mol)	
Power plant data	1/4" × 3/8",2.20g/cm^3	9.4 × 10^7 (1/s)	21.4(kCal/gmol)	Rase (1977)
Fe_3O_4/Cr_2O_3	3-5bar, 573°C-633°C	ln A = 26.1	95	Keiski et al.(1996)
Fe_3O_4/Cr_2O_3 8wt% Cr_2O_3	1atm, 350°C-440°C	ln A = 11.5	112	Rhodes et al. (2003)
Fe_3O_4/Cr_2O_3	1bar, 380°C-450°C	ln A = 10.1±0.2	118±1	
Fe_3O_4/Cr_2O_3	6bar, 380°C-450°C	ln A = 12.0±0.2	124±1	
Fe_3O_4/Cr_2O_3	27bar, 350°C-450°C	ln A = 7.4±0.1	111±1	
80-95% Fe_3O_4, 5-10% Cr_2O_3, 1-5%CuO	1atm, 450°C	10$^{0.659}$(mol/gcat-s)	88	San et al. (2009)

Table 4.4 WGS Reaction Rate with Low-Temperature Catalysts (200°C-250°C) (Smith et al., 2010)

Catalyst	Opertating Conditions	Arrhenius Parameters		Reference
		A	E (kJ/mol)	
ICI 52-1 (Copper based catalyst) density=5.83g/cm^3	1atm, 200°C	K = 5.37 × 10^{-7} (mol/m^{2}s)/atm^{1+m}		Salmi et al. (1989)
Cu-ZnO-Al_2O_3 (EX-2248)Sud Chemie	200-250µm, 120-250°C	lnA = 12.6	47.4	Choi et al. (2003)
42% CuO-ZnO-Al_2O_3	123°C-175°C CO/H_2O=1/3	4.9 × 10^6 (S^{-1})	71	Henrik et al. (2006)
CuO-ZnO-Al_2O_3	1atm, 200°C	-	79	Koryabkina et al. (2003)

4.1.1.2 WGS non-catalytic reactions

The above studies reviewed by Smith, et al. (2010) are all involved with catalysts, whereas those studies without using catalysts were all conducted under supercritical (water) conditions. Watanabe et al. (2001) did the research on the partial oxidation of *n*-hexadecane at 673K in supercritical water and found that when a carbon to oxygen ratio of 3:1 was used, the CO concentration in the products could reach almost 40%. So, it is possible to use partial oxidation of hydrocarbons to produce CO via the WGS reaction. In other words, it is possible to develop a non-catalytic way of reforming hydrocarbons without using high temperatures (1073-1273K).

Hirth and Franck (1993) reported the equilibrium constant K_a of WGS reaction at 773-873K and 40MPa. It is also mentioned that K_a is largely different from that in the ideal gas state and the equilibrium shifted to the reactants' side with increasing pressure. Holgate et al. (1992) proposed a global rate expression of the WGS reaction by conducting experiments in non-catalytic, supercritical conditions at 712-866K at 24.6MPa, $R_{WGS} = 10^{2.6\pm1.2} \exp[(-67\pm11)/RT](CO)^{0.81\pm0.19}$.

Sato et al. (2004) studied the kinetics of the WGS reaction under non-catalytic, supercritical conditions (653-713K and 10-30MPa) with an initial CO/H_2O ratio of 0.03 in a flow-type reactor. By analyzing the rate constants obtained by their study and those reported previously, a global reaction model for the WGS reaction under supercritical conditions was proposed as $k = 10^{5.58\pm1.38} \exp(-1.16 \pm 0.19 \times 10^5/RT)$ /s at 10-59.6 MPa and 653-866K. Wade et al. (2008) conducted experiments on the WGS reaction non-catalytically in the temperature range of 770 to 1050 K with an operating pressure of 24 MPa. They obtained the rate constants of $A = 2.512 \times 10^5$ and $E = 1.325 \times 10^5$ J/mol.

NETL (2004) evaluated the reverse WGS reaction rate in an empty quartz reactor at elevated-temperature (1148-1198K), low-pressure (0.1MPa) conditions in the absence of a diluent gas. The rate they proposed is $A = 1.09 \times 10^7$ $L^{0.5}mole^{-0.5}s^{-1}$ and E = 222 kJ/mol. Meanwhile, experiment at high temperature, high pressure conditions (up to 1.6 MPa) was also conducted in a pressure-equilibrated quartz reactor, the results yielded $A = 5.99 \times 10^8$ $L^{0.5}mole^{-0.5}s^{-1}$ and E = 218kJ/mol. For forward WGS reaction rate, NETL (2005) studied under conditions of high temperature (1070-1134K) and both low (0.1MPa) and high pressure (1.6MPa). The forward rate they got is $A = 4.7 \times 10^8$ $L^{0.5}mole^{-0.5}s^{-1}$ and E = 288.3 kJ/mol.

Further, they also proposed that the effect of the high pressure condition on the forward reaction rate was negligible.

Siemens (2011) experimental investigated thermodynamic equilibrium of WGS reaction under water quench process. They proposed that thermodynamic equilibrium of the WGS reaction cannot be achieved for realistic residence times due to kinetic limitations for temperature below 1223K. Nevertheless, catalytic effects caused by gasification ash or slag may enhance CO conversion within water quench section under the condition of atmospheric pressure and the temperature between 773 and 1273K.

4.1.1.3 WGS reaction rates used in CFD modeling

Usually, there are two approaches to modeling the WGS reaction rate in CFD. The first approach is to use the detailed kinetics with both forward and backward elementary reactions. In this approach, the rates of the elementary reactions are usually too many to be calculated in the CFD model, so the reaction rates are calculated separately in another software package, like Chemkin, at each iteration as the local temperature and pressure change. The advantage of this approach is that it provides the most appropriate vehicle to model the correct kinetics for the reaction rates, while the disadvantages are that the elementary kinetics may not be adequately known and that it could be difficult to achieve convergence in CFD computation. The second approach is to use Global Reaction Rates that are obtained by experiments. Since the rates are global, the rates usually reflect the net rate between the difference of the forward and backward rates. The advantages are that the global rates simplify the complex CFD modeling and conserve the computational power, while the disadvantages are that (a) the experimental data are usually obtained in relatively narrow temperature and pressure ranges, (b) the rates are usually obtained when the products are lean and the presence of other species commonly in a gasifier is nonexistent, and (c) there is still a lack of sufficient data covering the entire span of the temperature range for the gasification process.

Watanabe and Otaka (2006) performed a numerical simulation with the coal gasification model on the Japanese 2 tons/day, research scale coal gasifier supported by the Central Research Institute of Electric Power Industry (CRIEPI). The rate constants of the WGS reaction that they used is $A = 2.75 \times 10^{10}$ and $E = 8.37 \times 10^{7}$ J/kmol for the forward reaction rate and $A = 2.65 \times 10^{-2}$ and $E = 3.96 \times 10^{3}$ J/kmol for the backward reaction rate. The influence of the air

ratio on gasification performance, gas temperature distribution, and product gas composition were presented and discussed in their paper. The numerically simulated results were compared favorably with the experimental data, and most features of the gasification process were claimed to have been captured adequately. Ajilkumar et al. (2008) used the same WGS finite rate constant as employed by Watanabe and Otaka to simulate the same coal gasification process in the CRIEPI gasifier, but their computational domain was a small section of a simplified, axisymmetric cylinder (i.e. this was essentially a 2-D computation.) It was not clear how the inlet conditions and fuel injection were scaled down from 3D to 2D; however, they claimed that the predicted results showed good agreement with the experimental data of the CRIEPI gasifier. If Ajikumar et al.'s claim were correct, it implies that the gasfier's geometry and injection locations would not be critical for designing a gasifier. Further studies are needed to verify this implication.

Silaen and Wang (2011) used Jones and Lindstedt's rate (1998, abbreviated as Jones's rate later) and compared their CFD-simulated syngas results with that from the actual production of a commercial, slurry-fed, entrained-flow coal gasifier fed from the bottom. Perhaps due to the fact that Jones's rate was obtained under catalytic conditions, they found that Jones's rate was too fast and they had to purposely reduce the reaction rate constant to A= 2.75 x 10^2 to match the operating data. In this study, in addition to the modified Jones rate, the other two WGS reaction rates (Sato's and Wade's rates) obtained under non-catalytic conditions are to be employed for comparison as shown in Table 4.5.

Table 4.5 WGS Reaction Rates used in this study

Sources of the WGS rate	Catalyst	$k = AT^n \exp(-E/RT)$ with n=0
Jones and Lindstedt, 1998	Yes	$A = 2.75 \times 10^{10}$ s^{-1}, $E = 8.38 \times 10^7$ J/kmol
Wade et al., 2008	No	$A = 2.512 \times 10^5$ s^{-1}, $E = 1.325 \times 10^5$ J/mol
Sato, et al. 2004	No	$A = 10^{5.58 \pm 1.38}$ s^{-1}, $E = 1.16 \times 10^5$ J/mol

4.1.2 The Strategy for Generating Experimental Data for WGS Reaction Rate Calibration

For any calibration process, a set of clean experimental data is of the utmost importance. Unfortunately, a clean set of data needed for this study is not available in public domains. The syngas data typically published are usually taken after the gas clean-up process (scrubbing and

desulfurization) with very different syngas compositions (H_2, CO, CO_2, and H_2O) from the raw syngas right at the exit of a gasifier. Fortunately, the authors were able to collaborate with the Industrial Technology Research Institute (ITRI) in Taiwan to obtain a relatively clean data set by specifically measuring the raw syngas information before and after the quench section. Since the reaction in the quench section is mainly WGS without involving other complex reactions and since the experiment was conducted in an industrial environment instead of in a lab test cell, this data set is thought to be very valuable and unique for the intended calibration process. A description of the ITRI's gasifier and quench section follows below.

The Industrial Technology Research Institute (ITRI) has installed and operated a small, experimental, oxygen-blown, entrained-flow coal gasifier in Taiwan for six years. In previous operations, dry, pulverized coal was pneumatically transported via nitrogen to the gasifier and injected from the bottom of the gasifier. This gasifier has been modified with a new design which requires that the feedstock be mixed with water to form coal slurry and be injected with oxygen from top of the gasifier, while the syngas exits near bottom of the gasifier (see Fig4.1a). The syngas is usually very hot (1400-1700K or 2200-2600^{o}F for oxygen-blown gasification) and needs to be cooled for two purposes: (a) so that it may be transported without damaging downstream piping materials or other equipment and (b) to satisfy the lower-temperature requirement of the desulfurization and other cleaning processes. Direct water quench scheme is used for ITRI gaisifer. The schematic of the quench section is presented in Fig4.1b. The syngas flow enters the main chamber in the center of the quench section, impinges on the water bath surface, and deflects radially outward through eight openings to an annular outflow peripheral section that surrounds the main central chamber and is separated from the main chamber by a wall. The flow then moves upward and leaves the quench section through two outlets. The temperature and pressure of the incoming flow are 954 K and 3 atm, respectively. There are two injection locations: the primary one is located near the entrance of the quench section in the main flow chamber and another set of eight injectors serve as the secondary sprays. The primary injection provides the main water spray cooling with two pairs of opposing jets, separated 90^o apart. The secondary sprays are located in the annular duct and spray water downward against the up-flowing gas. This set of secondary injectors is used to aid in fine-tuning the temperature and syngas composition. The syngas composition is taken immediately before it enters and

exits the quench section. Hence, the computational domain simulation is conducted by only taking the quench section of the gasifier.

The experiment data taken in the gasifier before the syngas cooling section is very limited, typically no information on the water vapor concentration is available. Lack of adequate "raw data" has made calibration of the gasification model and the WGS reaction rate uncertain and difficult. For example, the data of syngas composition published from the Wabash River Coal Gasification Repowering Project (2000) didn't show the mole fraction of water vapor at the exit of the gasifier, although the water vapor information was shown for syngas composition after desulfurization. The experimental data provided by the Tampa Electric Polk Power Station IGCC Project (2002) was the cleaned syngas composition, which was taken after the syngas cooler and gas cleanup processes. Hughes et al. (2010) provided the syngas data from a two-tonne per day (slurry feed rate) pilot-scale gasifier, and, similarly, no water vapor mole fraction was given. Wained and Whitty (2010) performed tests in a 1 ton/day pressurized, slurry-fed, oxygen-blown, entrained-flow coal gasifier. The experimental data also lacked information for the water vapor content at the exit. So far, to the authors' knowledge, the only published experimental syngas data obtained before syngas cooling with water vapor content information is from the CRIEPI research scale coal gasifier presented in the paper by Watanabe and Otaka (2006). Therefore, the CRIEPI data is used for calibrating the WGS reaction rate in fully gasification process in this chapter.

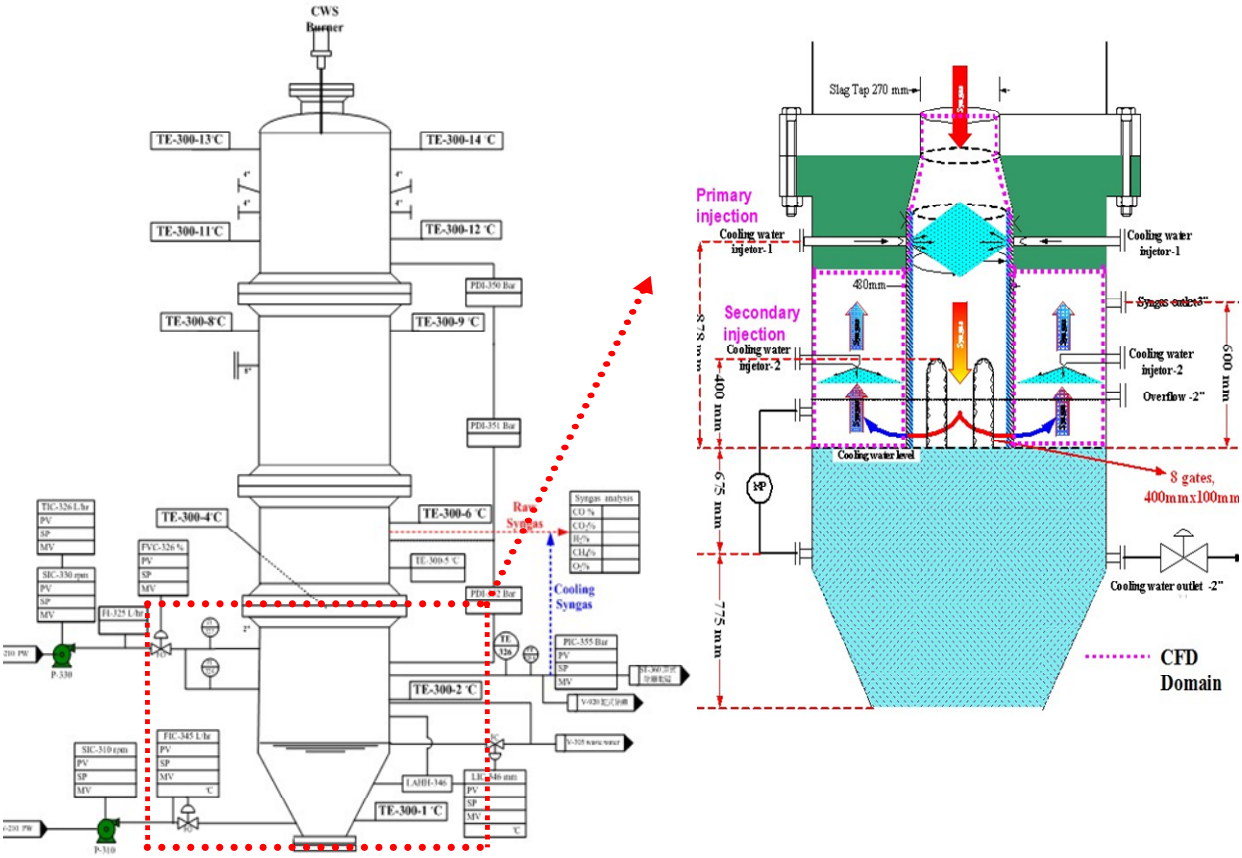

Fig. 4.1 (a) Schematic diagram of ITRI downdraft coal slurry-fed gasifier (b) gasifier's quench section showing locations of water injections: primary at the inlet and secondary in the outer annular

4.2 Global Gasification Chemical Reactions

This study deals with the global chemical reactions of coal gasification that can be generalized in reactions (R1.1) through (R1.10) in Table 4.6. WGS reaction rates used in this study are presented in Table 4.5.

Table 4.6 Summary of reaction rate constants used in this study

Reactions		Reaction Type	Reaction heat, $\Delta H°_R$ (MJ/kmol)	$k = AT^n exp(-E/RT)$ (n=0)		Reference
				A	E(J/kmol)	
Heterogeneous Reactions						
R 1	$C(s) + ½ O_2 \rightarrow CO$	Partial combustion	-110.5	0.052	6.1×10^7	Chen et al.(2000)
R 2	$C(s) + CO_2 \rightarrow 2CO$	Gasification, Boudouard reaction	+172.0	0.0732	1.125×10^8	
R 3	$C(s) + H_2O \rightarrow CO + H_2$	Gasification	+131.4	0.0782	1.15×10^8	
Homogeneous Reactions						
R 4	$CO + ½ O_2 \rightarrow CO_2$	Combustion	-283.1	2.2×10^{12}	1.67×10^8	Westbrook and Dryer (1981)
R 5	**$CO+H_2O(g)\leftrightarrow CO_2+H_2$**	**Water Gas shift**	**-41.0**	**2.75×10^{10}**	**8.38×10^7**	**Jones and Lindstedt (1998)**
R 6	$CO + 3H_2 \leftrightarrow CH_4 + H_2O$	Methanation	-205.7	$k_f = 4.4\times10^{11}$	1.68×10^8	
				$k_b = 5.12\times10^{-14}$	2.73×10^4	Benyon P.(2002)
R 7	$CH_{2.2538}O_{0.3015} \rightarrow 0.3015CO + 0.3025H_2 + 0.3168CH_4 + 0.1908C_2H_2$	Two-step Volatiles Cracking	+12.088	Eddy dissipation		N/A
R 8	$CH_4 + ½O_2 \rightarrow CO+2H_2$	Volatiles gasification via CH_4	-35.71			
R 9	$C_2H_2 + O_2 \rightarrow 2CO + H_2$	Volatiles gasification via C_2H_2	-447.83			
R10	$H_2 + ½ O_2 \rightarrow H_2O$	Oxidation	-242	$6.8x10^{15}$	$1.68x10^8$	Jones and Lindstedt (1998)
1) All $\Delta H°_R$ at 298K and 1 atm. 2) "+" Endothermic (absorbing heat), "-" Exothermic (releasing heat)						

In this study, the methanation reactions are not considered since the production of methane is negligible under the studied operating conditions. The volatiles are modeled to go through a two-step thermal cracking process (R1.7) and gasification processes (R1.8 and R1.9) with CH_4 and C_2H_2 as the intermediate products. The coal used in this study is Japanese Black

Coal, whose compositions are given in Table 4.7. The compositions of volatiles are derived from the coal's heating value, proximate analysis, and ultimate analysis. The oxidant is considered to be a continuous flow and the coal particles are considered to be discrete. The discrete phase only includes the fixed carbon and liquid water droplets from the moisture content of coal (5.3% wt). Other components of the coal, such as N, H, S, O, and ash, are injected as gas, together with the oxidant in the continuous flow. N is treated as N_2, H as H_2, and O as O_2. S and ash are not modeled and their masses are lumped into N_2.

Table 4.7 Compositions of Japanese Black Coal

Proximate Analysis (MF), wt%		**Ultimate Analysis (MF), wt%**	
Volatile	46.8	C	68.2
Fixed Carbon	35.8	H	5.71
Moisture	5.3	O	12.26
Ash	12.1	N	0.99
	100	S	0.19
HHV (kJ/kg)	2.74×10^4	Ash	12.65
			100.00

4.3 Computational Model

The governing equations, turbulence models, radiation model, discrete phase model, devolatilization model, and reaction model have been stated in Chapter 1 explicitly, so they are not repeated here, but briefly summarized below. The time-averaged steady-state Navier-Stokes equations as well as the mass and energy conservation equations are solved. Species transport equations are solved for all gas species involved. The standard k-ε turbulence model is used to provide closure. The P1 model is used as the radiation model. CPD model is used as devolatilization model. The flow (continuous phase) is solved in Eulerian form as a continuum while the particles (dispersed phase) are solved in Lagrangian form as a discrete phase. Stochastic tracking scheme is employed to model the effects of turbulence on the particles. The continuous phase and discrete phase are communicated through drag forces, lift forces, heat transfer, mass transfer, and species transfer.

4.4 Boundary and Inlet Conditions

4.4.1 Boundary and Inlet Conditions for the ITRI Water Quench Simulation

The computational domain of the quench section of the ITRI gasifier is shown in Fig. 4.2. The computational domain contains roughly 300,000 elements. FLUENT 12.0.16 is used as the CFD solver. The simulation uses the segregated solver, which employs an implicit pressure-correction scheme and decouples the momentum and energy equations. The SIMPLE algorithm is used to couple the pressure and velocity. The second-order upwind scheme is selected for spatial discretization of the convective terms and species. The computation is conducted for the continuous phase first. After obtaining an approximate, converged flow field of the syngas the droplet trajectories are calculated. At the same time, the drag, heat transfer, and mass transfer between the droplets and the syngas are calculated.

Based on the experimental data, the mass flow rate of 0.04 kg/s for raw syngas is assigned as the inlet conditions at the top of the quench section. The entrance of the quench section connects to the bottom of the gasifer (Fig. 4.1). The temperature and pressure of the incoming flow are 954 K and 3 atm, respectively. The locations of the primary and secondary injectors are shown in Fig.4.3.

The walls are all set as adiabatic and with no slip (ie. velocity is zero), but the thermal boundary condition of the shell wall of the main chamber (i.e., the wall between the primary injection and secondary injection) is set as "coupled," which means the heat fluxes on both sides of the wall will be calculated and matched to obtain the heat flux through the wall. The particles are assigned to reflect if they hit any wall. The operating pressure inside the gasifier is set at 3 atm. The outlet is set as a constant pressure condition at 1 atm. The syngas is considered to be a continuous flow, and the water from the spray is considered to be a discrete particle flow. The water droplets are all considered to be perfectly spherical with a uniform, arithmetic diameter of 10 μm. Although the actual size distribution of the atomized water droplets will be non-uniform, simulation using a uniform droplet size distribution provides a more convenient way to track the droplet evaporation process than a non-uniform droplet size distribution.

Water droplets are injected from the center of each primary injectors and secondary injectors. Stochastic tracking method is used to simulate the effect of instantaneous turbulence on water droplets dispersion. Each injector has ten different tracks, the time scale constant is set

as 0.015. The number of continuous phase iterations per dispersed phase iteration is set as 10, which means 10 iterations are down in the continuous phases before it is switched to the discrete phase. Converged results are obtained after the residuals satisfy a mass residual of 10^{-4}, an energy residual of 10^{-6}, and momentum and turbulence kinetic energy residuals of 10^{-5}. These residuals are the summation of the imbalance for each cell, scaled by a representative of the flow rate. Also, the simulations are proceeded until the mass fractions of various species are stabilized. A typical number of iterations of about 3000 is required for reaching the steady state.

Grid sensitivity study is conducted by comparing the results syngas temperature and composition from the models with 0.3, 0.6 and 0.9 million mesh size. The difference between the results of each case is within 2%. The model with 0.3 million mesh size is chosen in this study in order to save computational time.

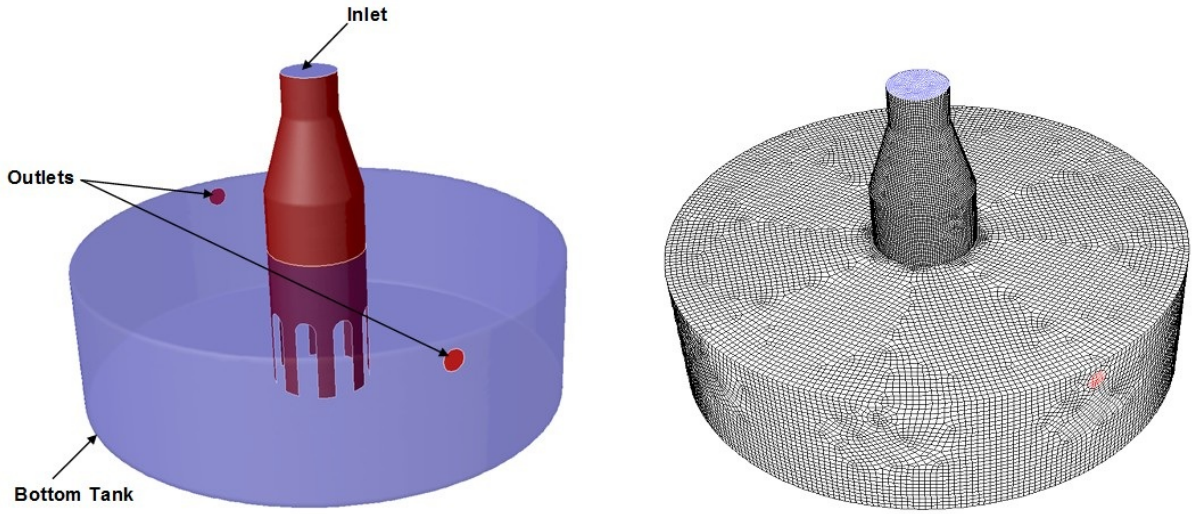

Fig. 4.2 Geometry, boundary conditions and meshed computational domain of the quench section of the ITRI Gasifier

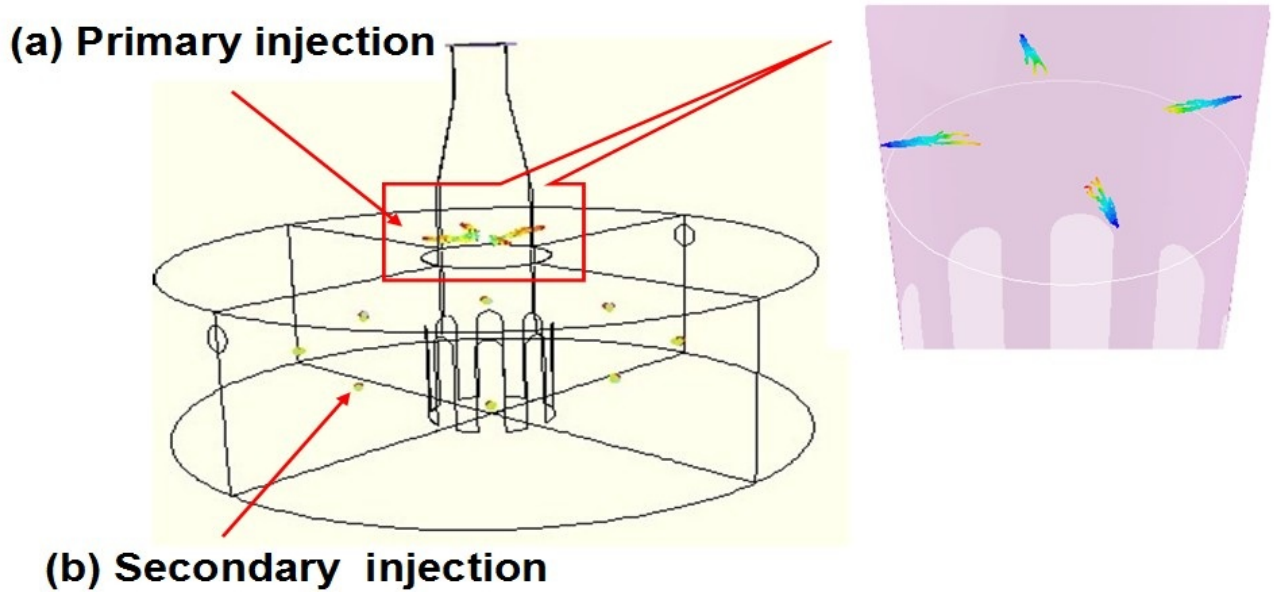

Fig. 4.3 Locations of water injections: (a) the primary injection consisting of two pairs of opposing jets and (b) the secondary injection consisting of eight injectors spraying downward against the up moving flow.

4.4.2 Boundary and Inlet Conditions for the Simulation of Gasification in the Japanese CRIEPI Gasifier

The geometry of the CRIEPI gasifier described by Watanabe and Otaka (2006) is shown in Fig 4.4. A simplified geometry shown in Figure 4.5 is employed in this present study without including the contraction section connecting the oxidation and reduction sections. The coal (fuel) injection design follows that of CRIEPI, consisting of a two-stage injection method with four tangential injections at the first stage and two opposite injections at the second stage. The residence time is around 3-4 seconds. The recycled char is injected from two opposite char injection locations at the first stage in the CFD model. The grid consists of 1,106,588 unstructured tetrahedral cells. In the simulations, the buoyancy force is considered, varying fluid properties are calculated for each species and the gas mixture, and the walls are assumed impermeable and adiabatic.

Japanese Black coal is used as the feedstock in this study; its composition is given in Table 4.8. The CRIEPI gasifier is an air-blown, dry-fed gasifier and is operated at 20 atm. The inlet, boundary, and operating conditions for the baseline case are shown in Figure 4.5. At the

first stage, coal is injected tangentially with a mass flow rate of 0.00695 kg/s at each injection location. The recycled char is injected oppositely with a mass flow rate of 0.0045 kg/s at each injector. The total mass flow rate of air is distributed into four injectors equally at 0.095 kg/s. At the second stage, coal is injected through a pair of opposite injectors with a mass flow rate 0.00725 kg/s at each injection location. The total mass flow rate of air is 0.0172 kg/s. All of the parameters stated above are the same as the experiment data.

The walls are all set to be adiabatic and with the no-slip condition (i.e. zero velocity). The boundary condition of the discrete phase at the walls is assigned as "reflect", which means the discrete phase elastically rebounds off once reaching the wall. The operating pressure inside the gasifier is set at 2MPa. The outlet is set at a constant pressure of 1 bar. The syngas is considered to be a continuous flow, and the coal and char from the injection locations are considered to be discrete particles. The particle size is uniformly given as spherical droplets with a uniform arithmetic diameter of 40 μm. Although the actual size distribution of the coal particles will be non-uniform, a simulation using uniform particle size provides a more convenient way to track the devolatilization process of coal particles than a non-uniform size distribution.

Same as the simulation of ITRI water quench process, the simulation of the Japanese CRIEPI gasification process is steady-state and uses the pressure-based solver, which employs an implicit pressure-correction scheme and decouples the momentum and energy equations. SIMPLE algorithm is used to couple the pressure and velocity. The second-order upwind scheme is selected for spatial discretization of the convective terms. For the finite rate model, where the Eulerian-Lagrangian approach is used, the iterations are conducted by alternating between the continuous and the discrete phases. Initially, one iteration in the continuous phase is conducted followed by one iteration in the discrete phase to avoid having the flame die out. The iteration number in the continuous phase gradually increases as the flame becomes more stable. Once the flame is stably established, fifteen iterations are performed in the continuous phase followed by one iteration in the discrete phase. The drag, particle surface reaction, and mass transfer between the discrete and the continuous phases are calculated. Based on the discrete phase calculation results, the continuous phase is updated in the next iteration, and the process is repeated. Converged results are obtained when the residuals satisfy a mass residual of 10^{-3}, an energy residual of 10^{-5}, and momentum and turbulence kinetic energy/dissipation

residuals of 10^{-4}. These residuals are the summation of the imbalance in each cell, scaled by a representative for the flow rate.

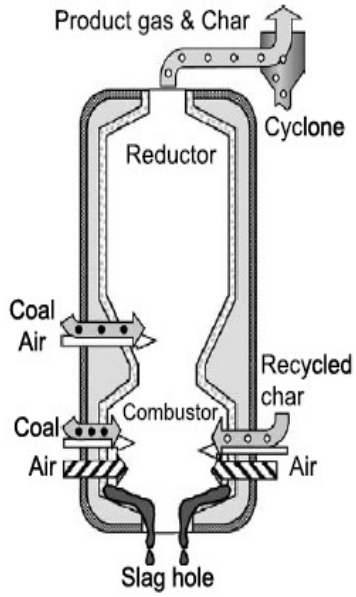

Fig. 4.4 CRIEPI research scale coal gasifier

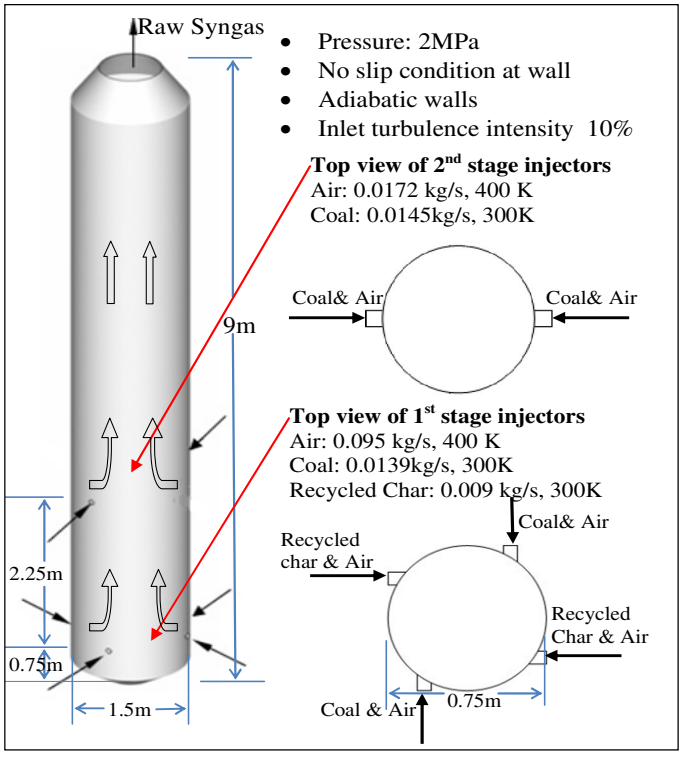

Fig. 4.5 Boundary conditions of the simulated gasifier

4.5 Results and Discussions

4.5.1 Results and Discussions for ITRI Water Quench Process

In this paper, investigation of syngas as the inlet flow is carried out with a syngas mass flow rate of 0.04 kg/s, a temperature of 954 K, and a pressure of 3 atm. The syngas compositions and inlet conditions are taken from the ITRI experimental data and shown in Table 4.8.

Table 4.8 Syngas inlet composition

	Mole fraction
CO	0.31
H_2	0.24
CO_2	0.19
H_2O	0.25
CH_4	0.01
Temp (K)	954

4.5.1.1 Calibration of WGS Rates with Experimental Data of ITRI Water Quench Experiment

As mentioned before, most of the reaction rates for the water-gas shift (WGS) reaction were obtained from experiments under simplified laboratory conditions with specific catalysts. A few of the reaction rates without using catalysts were obtained under supercritical (water) conditions, with the pressure much higher than those in a typical gasifier. In either case, it is not clear how the published reaction rates can be trustfully used to predict the actual WGS reaction rate in a gasifier without the presence of a catalyst and under different temperature and pressure conditions than those in the laboratory. This study focuses first on reviewing the published WGS reaction rates with and without the presence of catalysts, followed by calibrating the WGS reaction rate to match the experimental data taken from Industrial Technology Research Institute (ITRI) gasifier, as well as the CFD thermodynamic equilibrium results.

Due to the uncertainty of the WGS reaction rate, three different reaction rates (Jones's rate under catalytic condition and Wade's and Sato's rates under non-catalytic conditions) are used with water spraying at the primary injection location with a flow rate of 0.0052 kg/s. The result in Table 4.9 shows that all the three reaction rates are too fast because most of CO has been converted to H_2 and CO_2, since the computed mole fractions of H_2 and CO_2 are higher than the experimental data while that of CO is lower. Also, because the reaction rates are too fast, the

exit syngas reaches equilibrium and the results of all three rates are essentially identical. The CO conversion rate in Table 4.9 is defined as $(CO_{in} - CO_{out})/CO_{in}$, where CO_{in} is the mass flow rate of CO at inlet and CO_{out} is the mass flow rate of CO at outlet. Furthermore, the exit syngas temperature is approximately 173 K higher than the experimental data, indicating more heat is released from the WGS reaction. These discrepancies could be caused by the fact that this study employs the rates at different operating pressure and temperature ranges than those in the laboratory conditions under which the published rates themselves were derived.

To calibrate the reaction rates, the exponential constant, A, of each reaction rate is then progressively adjusted to lower values until the syngas composition matches the experimental data. An example of this process is shown in Table 4.10 by adjusting the A value of Wade's rate from 2.512×10^5 to 2.512×10^{-5}. There is a large change of syngas composition from the case with $A = 2.512 \times 10^5$ to the case with $A = 2.512 \times 10^{-3}$, but no notable further change is seen after Compared with the experimental data, the result of the CFD simulated case with $A = 2.512 \times 10^{-1}$ fairs best. The progressive change of syngas composition is shown in Fig. 4.6 which clearly shows that a faster rate produces more H_2 and CO_2, lower CO, and a higher exit temperature. The similar calibration process is applied to both Jones's and Sato's rates and all their results are listed in Table 11 for comparison. It appears that all of the original rates can be adjusted to a slower rate that can match the experimental gas composition data well. Without much preference between Sato's and Wade's rate, Wade's rate was chosen for the calibration with $A = 2.512 \times 10^{-1}$ and $E = 1.325 \times 10^5$ J/mol under a non-catalytic condition. However, even though the experimental gas composition data have been matched well by the calibrated WGS reaction rate, the computed gas exit temperature is still about 170K higher than the experimental data. This temperature difference could be contributed by two possible reasons: (a) The heat loses through the real wall, which can't be perfectly insulated as assumed in the simulation model; (b) The additional gas cooling due to gas stream penetrating into the water bath is not included in the simulation model either.

Note that the experimental data doesn't have the water vapor composition because a large part of the water vapor has condensed during the transportation of the sampled syngas to the gas analyzer. Therefore, the water vapor amount is not included in the comparison and the syngas composition of the simulated CFD results are renormalized by taking off the water vapor component.

Table 4.9 CFD simulated syngas composition using three original published WGS reaction rates (Note, experimental water vapor data is not available for comparison.)

Primary injection	Experiment data	$A=2.75\times10^{10}$ $E=8.38\times10^{7}$ J/kmol Jones et al. (1998)	$A=10^{5.58\pm1.38}$ $E=1.16\times10^{5}$ J/mol Sato et al. (2004)	$A=2.512\times10^{5}$ $E=1.325\times10^{5}$ J/mol Wade et al. (2008)
Syngas composition	Exit Mole Fraction			
H_2	0.36	0.50	0.49	0.49
CO_2	0.29	0.46	0.45	0.45
CO	0.34	0.03	0.05	0.05
CH_4	0.01	0.01	0.01	0.01
CO conversion (%)		88	80	80
Temperature (K)	673	948	944	946

Table 4.10 Effect of WGS rate constants on quenched syngas composition by changing A value of Wade's rate (Note, experimental water vapor data is not available for comparison)

Primary injection	Exper. data	$A=2.512\times10^{5}$ $E=1.325\times10^{5}$ J/mol	$A=2.512\times10^{0}$ $E=1.325\times10^{5}$ J/mol	$A=2.512\times10^{-1}$ $E=1.325\times10^{5}$ J/mol	$A=2.512\times10^{-3}$ $E=1.325\times10^{5}$ J/mol	$A=2.512\times10^{-5}$ $E=1.325\times10^{5}$ J/mol
Syngas composition	Exit mole fraction					
H_2	0.36	0.49	0.46	0.37	0.31	0.31
CO_2	0.29	0.45	0.41	0.30	0.25	0.25
CO	0.34	0.05	0.12	0.32	0.42	0.42
CH_4	0.01	0.01	0.01	0.01	0.02	0.02
CO conversion (%)		80	62	16	2	2
Temperature (K)	673	946	864	875	857	848

Table 4.11 CFD simulated syngas composition using three calibrated WGS reaction rates (Note, experimental water vapor data is not available for comparison)

Primary injection	Experiment data	A=2.75x10^{3} E=8.38x10^{7}J/kmol	A=10^{-1} E=1.16x10^{5}J/mol	A=2.512x10^{-1} E=1.325x10^{5}J/mol
Syngas Composition	Exit mole fraction			
H_2	0.36	0.36	0.34	0.37
CO_2	0.29	0.28	0.29	0.30
CO	0.34	0.38	0.36	0.32
CH_4	0.01	0.01	0.01	0.01
CO conversion (%)		8	10	16
Temperature (K)	673	842	864	875

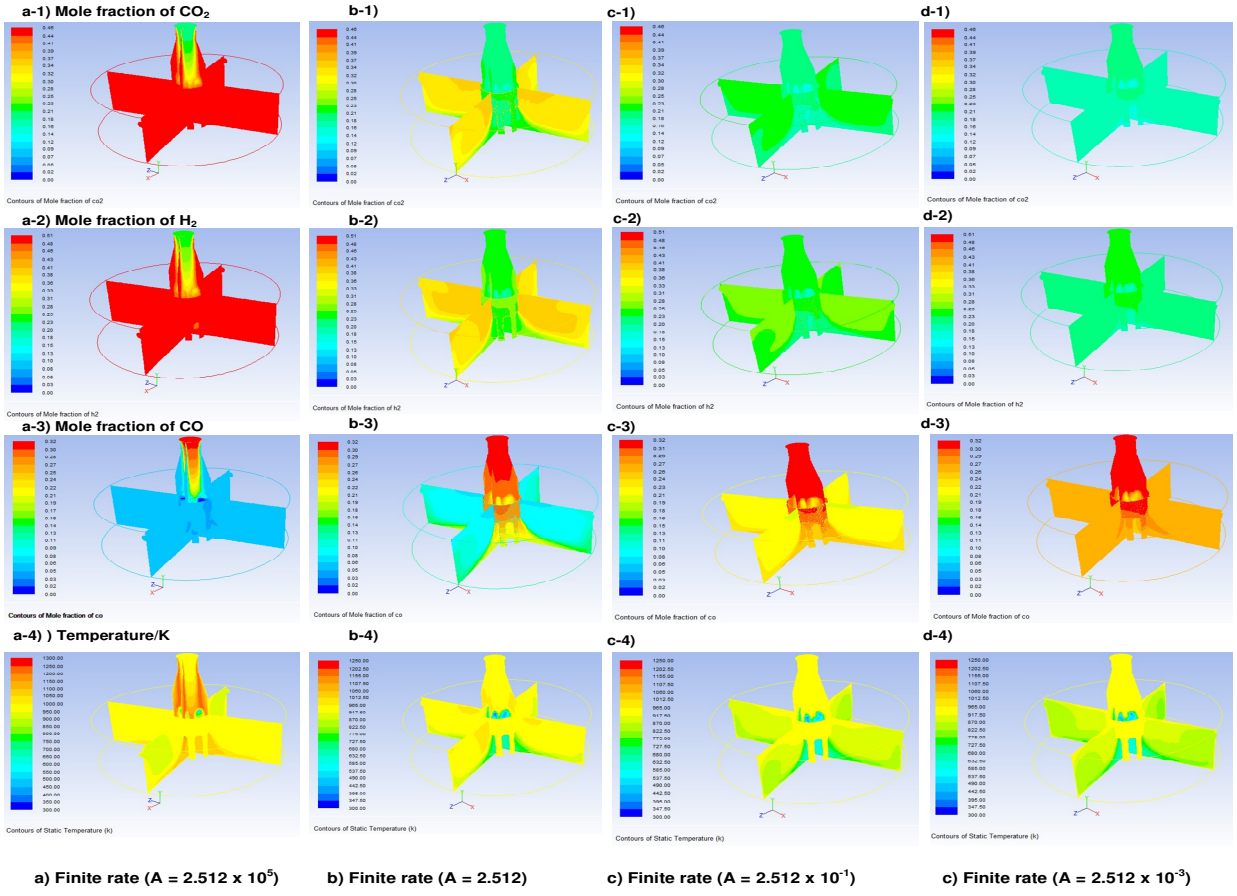

Fig. 4.6 Variation of Temperature and syngas composition by changing the A value of Wade's rate with the primary water injection

4.5.1.2 Calibration of WGS Rates including backward WGS Reactions

The WGS reaction rates employed so far are the net global rates, which means that they are the net results of forward and backward reactions. In order to see if adding a backward reaction rate would change the results, two different approaches are. The first approach is adding a backward WGS reaction ($CO_2 + H_2 \rightarrow CO + H_2$) as a separate equation with Jones's backward WGS reaction rate ($A = 2.65 \times 10^{-2}$ and $E = 3.96 \times 10^3$ J/kmol). The result shows that adding this backward WGS reaction equation only increases the computational time for achieving convergence, but it doesn't change the gas composition and temperature at the gasifier exit as the data without adding the backward WGS reaction in Table 4.9 does. The backward WGS reaction equation is, therefore, not added to the rest of the cases.

The WGS forward and backward reaction rates from NETL (2005) are also employed for water quench simulation. The result is very similar to that of Jones' rate: the forward rate dominates the process (i.e., too fast), and the computed mole fractions of H_2 and CO_2 are higher than the experimental data while that of CO is lower. This exercise further implies that the WGS reaction rates need be carefully calibrated before it is applied to the simulation of water quench process because each WGS rate only works for a specific temperature and pressure range.

The second approach is to calculate the backward reaction rate through *chemical equilibrium*. In this approach, the laminar finite rate model is chosen. The backward rate constant for reaction r, $k_{b,r}$, is computed from the forward rate constant using the following relation:

$$k_{b,r} = \frac{k_{f,r}}{K_r} \tag{4.1}$$

Where $k_{f,r}$ is the forward rate, Kr is the equilibrium constant for the r^{th} reaction, computed from

$$K_r = \exp\left(\frac{\Delta S_r^0}{R} - \frac{\Delta H_r^0}{RT}\right)\left(\frac{p_{atm}}{RT}\right)^{\sum_{i=1}^{N}\left(\nu''_{i,r} - \nu'_{i,r}\right)} \tag{4.2}$$

where p_{atm} denotes atmospheric pressure (101,325 Pa). The term within the exponential function represents the change in Gibbs free energy, and its components are computed as follows:

$$\frac{\Delta S_r^0}{R} = \sum_{i=1}^{N}\left(\nu''_{i,r} - \nu'_{i,r}\right)\frac{S_i^0}{R} \tag{4.3}$$

$$\frac{\Delta H_r^0}{RT} = \sum_{i=1}^{N} \left(\nu''_{i,r} - \nu'_{i,r}\right) \frac{h_i^0}{RT} \tag{4.4}$$

where S_i^0 and h_i^0 are the standard-state entropy and standard-state enthalpy (heat of formation). In this study, $\Delta S°_r$= -41929J/kmol-K, $\Delta H°_r$= -4.12 x10^{-7}J/kmol.

Table 4.12 shows the experimental data, results of original Wade's rate, calibrated Wade's rate, as well as the thermodynamic equilibrium state of Wade's rate. The thermodynamic equilibrium results also consolidate our justification that original Wade's rate is too fast, based on the CO conversion percentage comparison, 80% for Original rate vs 38% for thermodynamic equilibrium. However, thermodynamic equilibrium results show faster forward rate compared to the calibrated rate since CO conversion for Calibrated rate is only 16%. There are two possible reasons. Firstly, syngas residence time inside of the domain is too short that WGS reaction cannot reach to thermodynamic equilibrium state. Secondly, Wade's rate is experimental taken with an operating pressure of 24 MPa, while the operating condition of ITRI water quench section is only 3 MPa. The huge pressure difference will affect WGS reaction rate drastically as mentioned in the introduction part.

Table 4.12 CFD simulated syngas composition using original Wade's rate, calibrated Wade's rate (A=2.512x10^{-1} E=1.325x10^5J/mol) and thermodynamic equilibrium method (Note, experimental water vapor data is not available for comparison.)

Primary injection	Experiment data	Original Wade's rate	Calibrated Wade's rate	Thermodynamic equilibrium
Syngas Composition	Exit mole fraction			
H_2	0.36	0.49	0.37	0.40
CO_2	0.29	0.45	0.30	0.34
CO	0.34	0.05	0.32	0.25
CH_4	0.01	0.01	0.01	0.01
CO conversion (%)		80	16	38
Temperature (K)	673	946	875	890

4.5.2 Results and Discussions for Japanese CRIEPI gasification Process

4.5.2.1 Results of Using Three Original Experimental WGS Reaction Rates

The three original experimental WGS reaction rates shown in Table 4.7 are used first for comparison. In Watanabe and Otaka's paper, the sum of the mole fractions of CO, CO_2, H_2O, and H_2 in the syngas composition is only 45%. The other 55% of the gases are not stated, although the major component is N_2. For the convenience of comparison between the experimental data and the CFD results, the mole fractions of CO, CO_2, H_2O, and H_2 are renormalized to 100% as shown in Table 4.13. The CFD results show that all three of the originally published rates are too fast, as can be seen by the much higher mole fraction of H_2 (product) and much lower mole fraction of remaining CO (reactant). Due to the exothermic character of the WGS reaction, the rapid WGS reaction rate results in the exit temperatures of all three cases being 100 – 130 K higher than the experimental data. This phenomenon further supports the conclusion derived from the results of water quench part—the original rates cannot work well in the simulation of gasification process due to different operating range in temperature and pressure. Since the adopted approach, keeping the activation energy intact and subsequently reducing the pre-exponential constant value (A), has been examined and proved by comparing results with experimental results and thermodynamic equilibrium results of water quench part, the same approach has been used here. For Jones's rate, which was obtained under a catalytic condition, it could be explained that the WGS reaction rate is low because no catalyst is used in the gasifier. For Wade's rate and Sato's rate, there are two reasons that might partially contribute to the faster experimental reaction rates: (a) the experiments were conducted in an environment deprived of concentrations of products (H_2 and CO_2) and other gases, so the forward experimental reaction rates could be faster. (b) The experimental pressure and temperature conditions are different from those in the gasifier. In the gasifier, the temperature is higher than in the experimental conditions, thus the WGS reaction rate could be lower in the gasifier than in the experimental test condition. The temperature and species distributions in the gasifier are show in Fig. 4.7.

Table 4.13 Comparison of exit temperature and syngas composition between the experimental data and the simulated cases using the 3 original WGS rates

Mole fraction	**Experimental Data**	**Jones's Rate $A=2.75\times10^{10}$ $E=8.38\times10^{7}$ J/kmol**	**Wade's Rate $A=2.512\times10^{5}$ $E=1.325\times10^{5}$ J/mol**	**Sato's Rate $A=10^{5.58\pm1.38}$ $E=1.16\times10^{5}$ J/mol**
T	1250K	1356K	1382K	1378K
H_2	0.20	0.48	0.48	0.48
CO	0.42	0.27	0.26	0.27
CO_2	0.20	0.25	0.26	0.25
H_2O	0.18	< 0.01	< 0.01	< 0.01

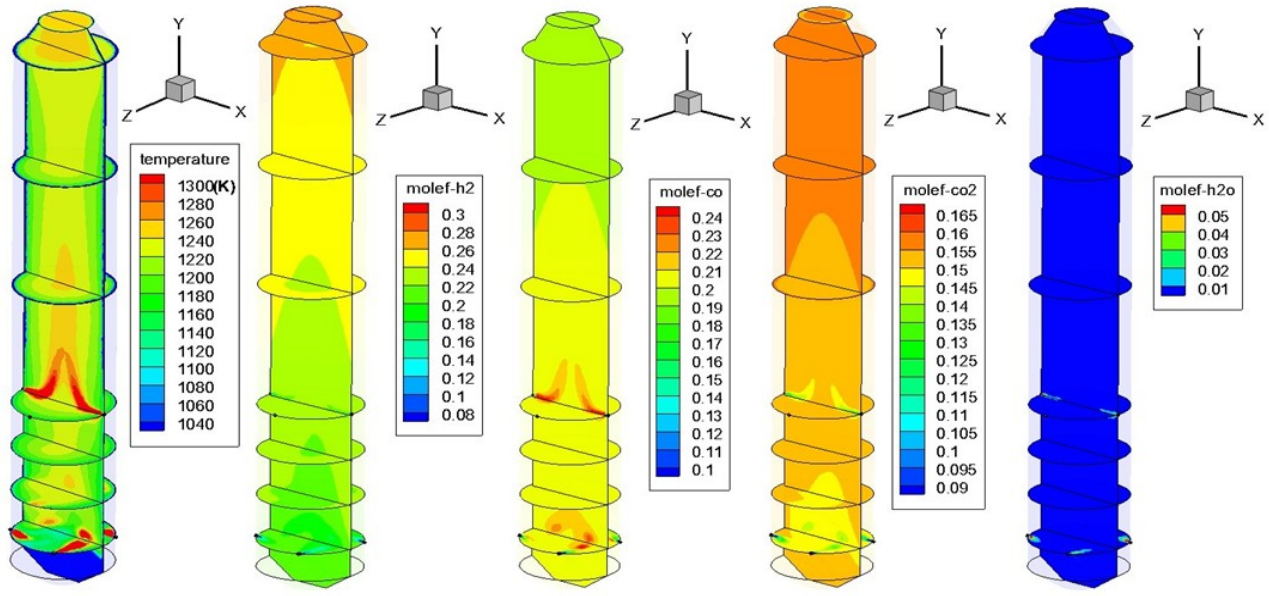

Fig. 4.7 Gas temperature and species mole fraction distributions for using the Jones's rate ($A=2.75\times10^{10}$ $E=8.38\times10^{7}$ J/kmol) (Note: the mole fractions in this figure are based on all gases and are not the same as those shown in Table 4.13)

4.5.2.2 Calibration of the Catalytic WGS Rates (Jones's) Against the Experimental Data

The purpose of this study is calibrating WGS reaction rate by matching experimental data of real entrained flow gasification process. The approach, adjusting pre-exponential rate constant and keep activation energy value, is discussed and proved above. Therefore, the same calibration approach against the experimental data of Japanese CRIEPI gasification is performed by consecutively changing the pre-exponential rate constant, A, from 2.75 $x10^{10}$ in Jones's rate to 2.75 x 10^{-2}, while the activation energy is kept the same as the original value (E = 8.38$x10^{7}$ J/kmol). The calibration of non-catalytic WGS rates (Wade's and Sato's) is stated in section 4.3. The CFD results of seven cases are shown in Table 4.14 together with the experimental data. The result clearly shows the gradual change of syngas composition and temperature at the exit when the A value is reduced from 2.75 x 10^{10} to 2.75 x 10^{-2}. There is little change in syngas composition and temperature at the exit when the rate constant A is reduced from 2.75 x 10^{10} to 2.75 x 10^{4} because the water vapor content is almost completely consumed in both cases. It demonstrates that the rate A = 2.75 x 10^{4} is still too fast compared to the experimental data. There is a relatively big change of the gas composition when the rate constant A is reduced from 2.75 x 10^{2} to 2.75. When the A-value is reduced below 2.75, the result appears stabilized and fluctuates slightly. The case with **A=2.75** seems to result in the best match with the experimental data. Figure 4.8 shows the comparison of syngas composition at exit with the experimental data, original Jones' rate, and calibrated Jones' rate. This calibrated pre-exponential rate constant, A=2.75, has one three order of magnitude difference compared to the calibrated rate derived from Part 1, A=2750. This deviation is mainly caused by two different types of experiments. For the WGS rate which calibrated by the water quench experimental data, is only involved WGS reaction, the operating pressure is 3atm, the temperature range inside of domain is around 700K-1000K. For the real entrained flow gasification process, it is involved nine reactions, include devolatilization, combustion and gasification process. More species and reactions make the case become much more complicated than water quench process. Furthermore, the operating pressure of the gasification process is 20 atm, the temperature range is approximate 1000K-1700K. All these factors could affect the WGS reaction rate in different reaction processes.

Figures 4.9 and 4.10 shows the contours and mass weighted average of gas temperature and species mole fraction distributions for the Case with A=2.75 and E=8.38$x10^{7}$ J/kmol

respectively. The gas temperature is higher in the region above the second stage injection location than it is in the region between the first and second stages. The maximum gas temperature in the first stage reaches 1650K near the fuel injection locations, and, in the second stage, it reaches 1570K. This phenomenon is different from the well-known E-gas gasifier in which no oxygen is provided at the second stage, so the temperature after the second-stage injection is much lower than in the first stage because the endothermic Char-CO_2 (R2) and Char-steam (R3) gasification processes are very active after the second stage injection. In this gasifier, it is very interesting to see that the highest production of CO_2 occurs near the first stage injection locations and the lowest production occurs near the second stage. The CO_2 mole fraction is low in most parts of the production until the syngas reaches the top quarter of the gasifier where the CO_2 mole fraction increases again. This history of the CO_2 mole fraction changes indicates that complete char combustion (R4) occurs near the first-stage injection, but CO_2 is effectively consumed via Char-CO_2 gasification in most parts of the gasifier to produce H_2 and CO, as also is evidenced by increasing H_2 and CO mole fractions. The WGS seems to become more active in the upper quarter of the gasifier as the temperature increases due to the exothermic effect of the WGS process. In this upper quarter region, the active WGS reaction can be evidenced by the increased H_2 and CO_2 and decreased CO.

Furthermore, similar to water quench part, we also employed the WGS forward and backward reaction rates from NETL (2005) for gasification simulation. The result is very similar to that of water quench part: the forward rate dominates the process and the computed mole fraction of H_2 is 2.5 times higher than the experimental data while that of CO is lower. It further supports the necessity of calibrating the WGS reaction rates before it is applied to the simulation of both water quench and gasification process.

Table 4.14 Comparison of the temperature and syngas composition at exit with the experimental data by consecutively reducing the pre-exponential value, A, of the Jones' rate

Exit	Exp. Data	$2.75x10^{10}$	$2.75x10^{4}$	$2.75x10^{2}$	$2.75x10^{1}$	**2.75**	$2.75x10^{-1}$	$2.75x10^{-2}$
T	1250K	1356K	1296K	1282K	1278K	**1267K**	1246K	1236K
H_2	0.20	0.48	0.44	0.41	0.31	**0.27**	0.29	0.27
CO	0.42	0.27	0.31	0.32	0.41	**0.45**	0.44	0.45
CO_2	0.20	0.25	0.25	0.23	0.14	**0.12**	0.12	0.12
H_2O	0.18	< 0.01	< 0.01	0.05	0.14	**0.16**	0.15	0.16

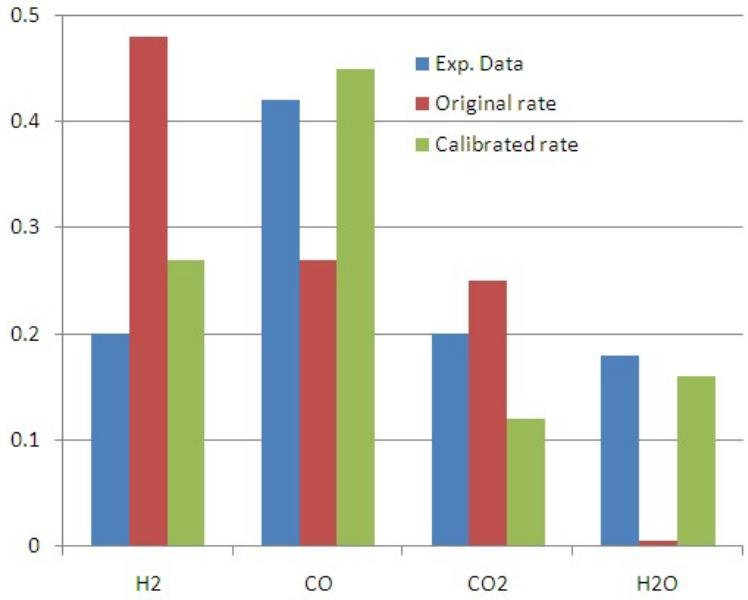

Fig. 4.8 Comparison of syngas composition at exit with the experimental data, original Jones' rate, calibrated Jones' rate (A=2.75 and $E=8.38x10^{7}$ J/kmol)

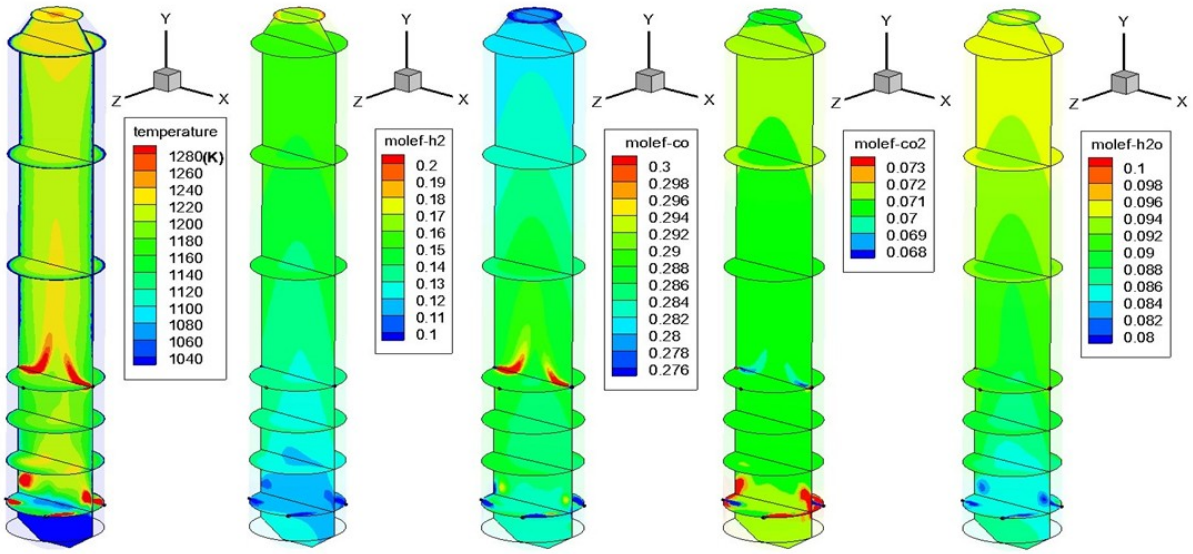

Fig. 4.9 Gas temperature and species mole fraction distributions for the Case with modified Jones's rate (A=2.75 and E=8.38x10^7 J/kmol). (Note: the mole fractions in this figure are based on all gases and are not the same as those shown in Table 4.14)

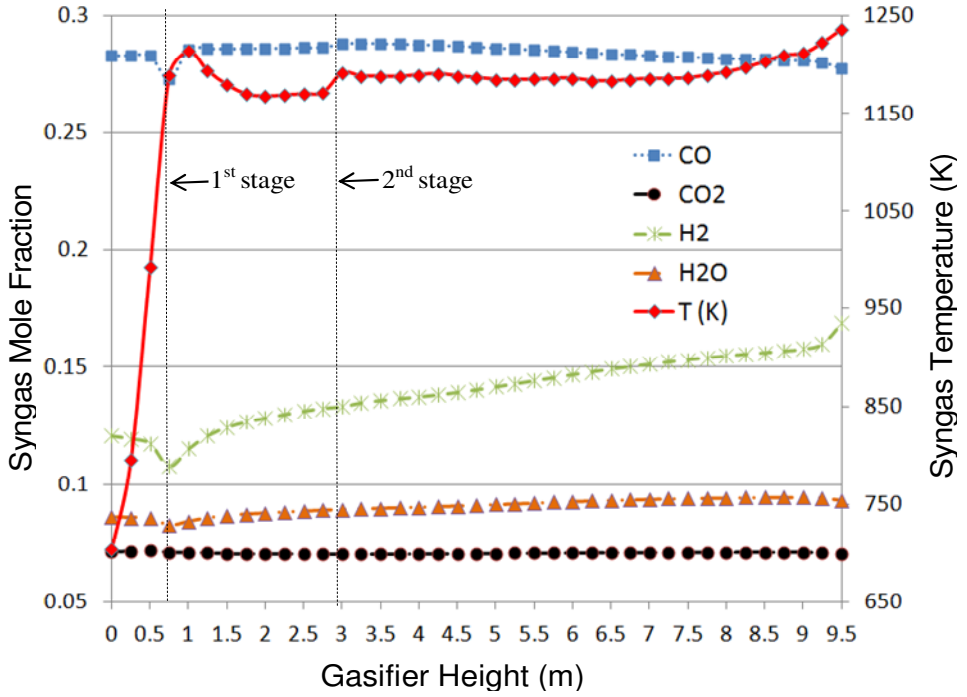

Fig. 4.10 Mass-weighted averages of gas temperature and species mole fraction distributions along gasifier height for the Case with modified Jones's rate (A=2.75 and E=8.38x10^7 J/kmol)

4.5.2.3 Calibration of the Non-catalytic WGS Rates (Wade's and Sato's) Against the Experimental Data

The same calibration process is performed for Wade's and Sato's rates, which were obtained without using catalysts, but in the supercritical range. Without showing all the incremental cases, only three selected cases are shown in Table 4.15. The results of A = 2.512 x 10^{-3} for Wade's rate and A = 1 x 10^{-3} for Sato's rate show the best matches with the experimental data. Both rates are slower than those obtained from quench-only process.

In summary, all three WGS reaction rates can be modified to match the experimental data reasonably well by reducing the value of the pre-exponential rate constant, A. The exit temperature can be matched within 2% (20K) of the experimental value. The mole fractions of CO and H_2O can be matched fairly well within 4 percentage points (or 10%); however, the simulated H_2 mole fractions are always 7-9 percentage points (or about 40%) higher than the experimental data.

Table 4.15 Temperature and syngas composition at exit for six cases and experiment data based on Wade's rate and Sato's rate

MF		A-value of Wades' Rate (E=1.325x10^5J/mol)			A-value of Sato's Rate (E=1.16x10^5 J/mol)		
(%)	Exp. Data	2.512x10^5	2.512x10^{-1}	**2.512x10^{-3}**	$10^{5.58\pm1.38}$	1x10^{-1}	**1x10^{-3}**
T	1250K	1382K	1280K	**1273K**	1378K	1276K	**1238K**
H_2	0.20	0.48	0.43	**0.29**	0.48	0.40	**0.28**
CO	0.42	0.26	0.29	**0.43**	0.27	0.33	**0.46**
CO_2	0.20	0.26	0.24	**0.12**	0.25	0.21	**0.11**
H_2O	0.18	0	0.04	**0.16**	0	0.06	**0.15**

4.6 Conclusions

The WGS reaction rate has been discovered to affect notably the result of CFD modeling of coal gasification processes in a gasifier. Almost all of the published WGS rates were conducted with catalysts under limited temperature ranges and at a certain fixed pressure condition. Only a few WGS rates were obtained without involving catalysts, but they were

performed under supercritical (water) conditions. Therefore, employing any of the published WGS reaction rates to simulate the coal gasification process in a gasifier, which usually doesn't use catalysts and doesn't operate at the same temperature or pressure conditions as in the laboratory conditions, is likely to result in misleading or uncertain results. To help calibrate the global WGS reaction rates, three published WGS reaction rates are used in this study. They are Jones's rate ($A = 2.75 \times 10^{10}$, $E = 8.38 \times 10^{7}$ J/kmol,) Wade's rate ($A = 2.512 \times 10^{5}$, $E = 1.325 \times 10^{5}$J/mol,) and Sato's rate ($A = 105.58 \pm 1.38$, $E = 1.16 \times 10^{5}$ J/mol.) The study is focused on both water quench section of ITRI gasifier, which only involves WGS reaction, and fully gasification process in the Japanese CRIEPI gasifier. Calibrated WGS rates are derived from comparing CFD results the experimental data, as well as with thermodynamic equilibrium results. The conclusions are:

(1) All of the originally published rates cannot work well in the simulation of both water quench process and coal gasification process due to different temperature and pressure range. Adding the backward WGS reaction rate (Jones' rate) as a separate reaction equation results in the same gas composition and temperature at the gasifier exit as the case without adding the backward WGS reaction rate.

(2) For water quench part, the result of employing the forward and backward rates from NETL is very similar to that of Jones' rate—the forward rate dominates the process (too fast) and the computed mole fractions of H_2 and CO_2 are higher than the experimental data while that of CO is lower.

(3) Applying the chemical equilibrium approach further verifies that original WGS rates are too fast in applying in the range of water quench operation parameters.

(4) Each of the three rates are slowed down by consecutively reducing the pre-exponential rate constant, A, while the activation energy is kept the same as the original value. The results show that all three WGS reaction rates can match the experimental data well by reducing the value of the pre-exponential rate constant, A. For the results of gasification process, the exit temperature can be matched within 2% (20K). The mole fractions of CO and H_2O can be matched fairly well within 4 percentage points (or 10%); however, the simulated H_2 mole fractions are always 7-9 percentage points (or about 40%) higher than the experimental data.

(5) The calibrated global WGS reaction rates that best match the experimental data of ITRI water quench process are:

- Modified Jones's rate: A = 2.75, E = 8.38×10^7 J/kmol
- Modified Wade's rate: A = 2.512×10^{-3}, E = 1.325×10^5 J/mol and
- Modified Sato's rate: A = 1×10^{-3}, E = 1.16×10^5 J/mol

(6) The calibrated global WGS reaction rates that best match the experimental data of Japanese CRIEPI coal gasification process are:

- Modified Jones's rate: A = 2.75, E = 8.38×10^7 J/kmol
- Modified Wade's rate: A = 2.512×10^{-3}, E = 1.325×10^5 J/mol and
- Modified Sato's rate: A = 1×10^{-3}, E = 1.16×10^5 J/mol

(7) There is a two orders of magnitude difference of the pre-exponential rate constant, A, between the calibrated WGS reaction rates derived from these two different simulations. This deviation is mainly caused by two different types of experiments. For the WGS rate which calibrated by the water quench experimental data, is only involved WGS reaction, the operating pressure is 3atm, the temperature range inside of domain is around 700K-1000K. For the real entrained flow gasification process, it is involved nine reactions, include devolatilization, combustion and gasification process. More species and reactions make the case become much more complicated than water quench process. Furthermore, the operating pressure of the gasification process is 20 atm, the temperature range is approximate 1000K-1700K. All these factors could affect the WGS reaction rate in different reaction processes.

It needs to be emphasized that the modified reaction rates are obtained under air-blown and dry-fed operating conditions. These modified rates may not be applicable to slurry-fed or oxygen-blown gasifiers because the higher water vapor concentration in slurry-fed gasifiers and higher operating temperatures in oxygen-blown gasifiers may affect the global WGS rate. More studies, as well as more adequate experimental data, are needed in the future. The adequate data are those data taken immediately at the end of gasification section but right before the syngas cooling section in the gasifier, and it is important that the water vapor concentration must be included. An alternative approach is to include the kinetics of elementary reactions instead of taking a global data match on the condition that the adequate elementary reactions are known.

CHAPTER FIVE
TOPIC 2: EFFECT OF RADIATION MODELS ON COAL GASIFICATION SIMULATION

5.1 Introduction

In the majority of industrial combustion devices, thermal radiation plays a significant role for an important energy transfer. Even though the coal gasification process undergoes a partial combustion process, thermal radiation may still play a very important role in heat and energy transfer between different gas species, coal particles, as well as the wall of gasifier. Furthermore, in order to extend the lifetime of the refractory bricks and to reduce the maintenance cost, keeping the process temperature relatively low, but still effective in performing the gasification process and cracking the volatiles, is one of the important goals for gasification research. Therefore, an accurate and computationally efficient thermal radiation model is needed to predict flame shape and temperature distributions of syngas at the wall of gasifier. In this study, five radiation models are applied into gasification simulation: Discrete Transfer Radiation Model (DTRM), P-1 Radiation Model, Rosseland Radiation Model, Surface-to-Surface (S2S) Radiation Model, and Discrete Ordinates (DO) Radiation Model. The objectives are to identify the pros and cons of each model's applicability to gasification process and determine which radiation model is most suitable for simulating gasification process in entrained-flow gasifiers with a consideration of the gasifier's geometry, radiative properties of participating medium (mainly CO, CO_2, H_2 and water vapor), and coal particles interactions.

5.1.1 Literature Review of Radiation Models Implemented in Gasification Simulation

Chen et al. (2000) developed a three-dimensional simulation model for entrained-flow coal gasifiers, which applied an extended coal-gas mixture fraction model with the Multi Solids Progress Variables (MSPV) method. The model employed four mixture fractions separately track the variable coal off-gases from the coal devolatilization, char-O2, char-CO2, and char-H2O reactions. Chen et al. performed a series of numerical simulations for a 200 ton per day (tpd) two-stage air blown entrained flow gasifier developed for an IGCC process under various operation conditions (heterogeneous reaction rate, coal type, particle size, and air/coal

partitioning to the two stages). In these computational models, the discrete transfer method (DTRM) based on the solution of the fundamental radiative transfer equation within discrete solid angles was used.

Bockelie et al. (2002) developed a comprehensive CFD modeling tool (GLACIER) to simulate entrained-flow gasifiers, including a single-stage, down-fired system and a two-stage system with multiple feed inlets. They used DO radiation model which included the heat transfer for absorbing-emitting, anisotropically scattering, turbulent, and sooting media. The radiative intensity field was solved based on properties of the surfaces and participating media, and the resulting local flux divergence appeared as a source term in the gas phase energy equation.

The U.S. Department of Energy/National Energy Technology Laboratory (NETL) developed a 3D CFD model of two commercial-sized coal gasifiers (Guenther and Zitney, 2005). The commercial CFD software, FLUENT, was used to model the first gasifier, which was a two-stage, entrained-flow, slurry-fed coal gasifier. The Eulerian-Lagrangian method was used in conjunction with the discrete phase model to simulate the entrained-flow gasification process. The second gasifier was a scaled-up design of a transport gasifier. The NETL open source MFIX (Multiphase Flow Interphase Exchanges) Eulerian-Eulerian model was used for this dense multiphase transport gasifier. MFIX is a general-purpose hydrodynamic model that describes chemical reactions and heat transfer in dense or dilute fluid-solids flows, typically occurring in energy conversion and chemical processing reactors. The radiative heat transfer is not considered in this model. NETL has also developed an Advanced Process Engineering Co-Simulator (APECS) that combines CFD models and plant-wide simulation. APECS enables NETL to couple its CFD models with the steady-state process simulator, Aspen Plus.

Chodankar et al. (2009) developed a steady state model to estimate the gas production from Underground Coal Gasification (UCG) Process. This model featured surface reactions of coal char with gasification medium to produce combustible gaseous product, and predicts gas composition, temperature and gross calorific value of product gas across the gasification channel. P1 radiation model was used in their study. Ajilkumar (2009) performed a numerical simulation on a steam-assisted tubular coal gasification process. The syngas temperature, carbon conversion, heating value of the exit gas, and cold gas efficiency were predicted and compared with the experimental data. P1 model was chosen as the radiation model in their simulation

model study. Wu et al. (2010) used 3D CFD model for the simulation of an entrained coal slurry gasification process. The effect of particle size on coal conversion, as well as the effect of the coal slurry concentration and molar ratio of oxygen/carbon on the gasifier performance, was investigated. The P1 radiation model was also used in their study. Chen (2010) used a 3-D simulation model to investigate the effect of oxygen/carbon ratio and water/coal ratio on the entrained flow coal gasification process.. P1 model was selected as the radiation model in his study.

From 2005 to 2011, Silaen and Wang (2005, 2006, 2011) have conducted a series of study of entrained-flow gasification process using the commercial CFD solver, FLUENT. In these studies, they investigated the effects of several parameters on gasification performance, including the coal input condition (slurry or dry powder), oxidant (oxygen-blown or air-blown), wall cooling, flow injection angles, and various coal distributions between the two stages. They also investigated the effects of various turbulence models and devolatilization models on the result of gasification simulations (Silaen and Wang, 2010). Furthermore, they compared the effect of instantaneous, equilibrium and finite rate gasification models on the entrained flow coal gasification process (Silaen and Wang, 2009). Lu and Wang (2011) investigated the effect of Water-Gas-Shift (WGS) reaction rate on gasification process. They found that most of the published WGS reaction rates, both under catalytic and non-catalytic conditions, are too fast in gasification simulation process. By adjusting the pre-exponential rate constant value (A) against experimental data, calibrated WGS reaction rate were obtained. In all of the above studies, only the P1 radiation model was used.

In collaboration with the research team of Industrial Technology Research Institute (ITRI), Wang and Silaen effectively employed the CFD gasification model to investigate gasification process under the influences of different part loads, two different injectors, and three different slagging tap sizes (Wang and Silaen, 2006, 2007, 2010). In 2011, Wang, et al. (2011) performed the simulation on the effects of potential fuel injection techniques on gasification performance in order to help design the top-loaded fuel injection arrangement for an entrained-flow gasifier using a coal-water slurry as the input feedstock. Two specific arrangements were investigated: (a) coaxial, dual-jet impingement with the coal slurry in the center jet and oxygen in the outer jet and (b) four-jet impingement with two single coal-slurry jets and two single oxygen jets. Wang and Lu (2011) investigated the performance of a syngas

quench cooling design in the ITRI downdraft entrained flow gasifier. Numerical simulation was performed to investigate the effect of different injection stage of cooling water, and water gap level on syngas composition, higher heating value and temperature at exit of gasifier. Again, only the P1 radiation model was used.

Based on the above literature review, only the P1 model has been widely used in gasification simulation. Although Chen et al.(2000) and Bockelie et al. (2002) used DTRM and DO radiation models respectively, to the authors' knowledge, no study has been published in the public domain to compare the results obtained from different radiation models. The lack of information on the uncertainty of simulated results resulting from employment of different radiation models has motivated the investigation conducted in this study.

5.1.2 Review of Radiation Models

5.1.2.1 Radiation of Participating Media (Gas Phase)

In coal gasification process, CO, H_2, CO_2, and water vapor are produced and participate in radiant heat transfer by the virtue of interaction of infrared radiation with vibrational and rotational modes of energy absorption by gaseous molecules.

Two aspects of radiation heat transfer in participating media need to be modeled: one is the radiant energy transfer in the participating media, described by the radiative transfer equation, the other is the absorption, emission, and scattering of radiation by the participating media itself.

For the first aspect, the transfer equation alone with a number of representative rays could be solved by discrete transfer method described by Lockwood and Shah (1981) as well as by the discrete ordinate method described by Chandrasekhar (1950). The accuracy of the solution is the function of numerical errors that could be reduced to any required level by solving enough number of rays or directions.

For the second aspect, several models for participating media have been introduced in conjunction with the flow field by simultaneously solving the fluid flow equations such as the mixed grey gas models introduced by Hottel and Sarofim (1967). Grosshandler (1980) introduced the total transmittance non-homogeneous model, which is a simplified model, using total transmittance data to predict the radiance emanating from non-isothermal, variable concentration carbon dioxide and water-vapor mixtures. Computational times using this model

are two-orders of magnitude less than that required by the Goody statistical narrow-band model with Curtis-Godson approximation, but with a sacrifice in accuracy of less than 10%.

Edwards and Balakrishnan (1973) introduced exponential wide band model and presented the generalized expressions for the calculation of the emissivity, absorptivity, and other relevant radiation properties of molecular gases. Cumber et al. (1998) adapted a spectral version of the exponential-wide band for implementation within a computational fluid dynamic framework. They also showed that the spectral wide band approach is in a reasonable agreement with experimental data and achieves accuracy comparable to that of the narrow band model in total quantities while requiring almost one order of magnitude less of computational time.

5.1.2.2 Radiation of Combustion Particles (Solid Phase)

During the coal gasification process, radiation of solid particles also plays an important role in heat transfer since the coal particles will go through preheating, devolatilization, ignition, and partial combustion process at the beginning stage of the gasification process. For the field of radiation heat transfer of solid particles, most of the studies have been carried out in coal combustion system. Sarofim and Hottel (1978) gave a detailed review of the importance of radiative heat transfer in combustion systems. All combustion processes are very complicated. There are intermediate chemical reactions in sequence or parallel, intermittent generation of a variety of intermediate species, generation of soot, agglomeration of soot particles, and partial burning of the soot sequentially. Since thermal radiation contributes greatly to the heat and energy transfer mechanism of combustion, fundamental understanding and appropriate modeling of the processes of radiation of combustion particles need to be addressed and implemented for gasification process, which involves partial combustion and several other reactions.

5.1.2.2.1 Coal Particles and Fly Ash Dispersions

To calculate the radiative properties of arbitrary size distributions of coal particles, their complex index of refraction as a function of wavelength and temperature must be investigated. Foster and Howarth (1968) have employed a Fresnel reflectance technique to measure the complex refractive index of coals at different ranks. Brewster and Kunitomo (1984) questioned the validity of the reflectance technique applied to the coal. They measured the absorption index

of some Australian coals to be less than 0.05 in the infrared by using a transmission technique for small coal particles.

Viskanta et al. (1981) summarized the representative values for the complex index of refraction in the near infrared for different coals and ashes, such as carbon, anthracite, bituminous, lignite, and fly ash. They also found that variations with particle distribution functions are relatively minor, and the different index of refraction made a difference only for mid-sized particles. Buckius and Hwang (1980) analyzed the extinction and absorption coefficients, as well as the asymmetry factor for polydispersions of absorbing spherical particles. By showing that dimensionless spectral radiation properties are independent of the explicit size distribution of the particle, they indicated the usefulness of the dimensionless and mean properties for defining the optical properties of coal particles which are wavelength dependent.

5.1.2.2.2 Char

In the radiation heat transfer process of coal gasification, optical constants of char are considered to be more important than that of coal since the coal devolatilization time is generally insignificant compared with the char burning and char gasification time. Grosshandler and Monteiro (1982) investigated the absorption and scattering of thermal radiation within a dilute cloud of pulverized coal and char. They proposed an empirical equation of the form $\alpha\lambda = 0.78 + 0.18/\lambda^{1/2}$ for all coals and chars within 5 percent in the spectral region of $\lambda = 1.2–5.3$ μm. They also recommended a single total hemispherical absorptivity of 0.89 for heat transfer calculation in pulverized coal and char clouds, if the particles can be assumed to act as Mie scatters and if the volume fraction of ash and soot particles is small. Brewster and Kunitomo (1984) determined the extinction efficiency from transmissivity measurements on micron-sized char suspensions by a particle extinction technique using compressed KBr tablets. IM and Ahluwalia (1992) conducted a dispersion analysis of the transmissivity measurement by Brewster and Kunitomo on char particles dispersed in infrared transmissive KBr pellets. They introduced some question as to the uniqueness of the optical constants inferred purely from the extinction measurement. In order to properly resolve the contributions of absorption and scattering to extinction efficiency, they recognized that it is necessary to measure a second independent variable.

5.1.2.2.3 Soot

Soot particles are produced in fuel-rich flames, or fuel-rich parts of flames, as a result of incomplete combustion of hydrocarbon fuels. In coal gasification process, soot production coincides with the stage of volatile matters being driven from the coal. Since soot particles are very small and are generally at the same temperature as the flame, they strongly emit thermal radiation in a continuous spectrum over the infrared region. Experiments have shown that soot emission often is considerably stronger than combustion gases' emission. Foster and Howarth (1968) were first to report experimental measurements for the complex index of refraction of hydrocarbon soot based on various carbon black powders. Lee and Tien (1981) used the dispersion theory applied to a two bound and one free-electron oscillator model to analyze the optical constants of soot. Their results show that the infrared optical properties of soot are relatively independent of the ratio of fuel hydrogen to carbon and the molecular structure of soot. Thus their dispersion constants can be treated as some mean values applicable to many fuels. Since the soot effect on gasification process is very complicated, it is not investigated in the current study.

5.2 Global Gasification Chemical Reactions

This study deals with the global chemical reactions of coal gasification (Smoot and Smith, 1985) that can be generalized in reactions (R1) through (R1) in Table 5.1.

In this study, the methanation reactions are not considered since the production of methane is negligible under the studied operating conditions. The volatiles are modeled to go through a two-step thermal cracking process (R7) and gasification processes (R8) with CH_4 as the intermediate products. The finite rate of water gas shift reaction has been reduced to A = 2.75, E = 8.38×10^7 based on the investigation carried out by Lu and Wang (2011).

The coal used in the study is sub-bituminous from Indonesia, whose compositions are given in Table 5.2a. It has a moisture content of 8.25%. Its moisture-free (MF) proximate and ultimate analyses compositions are listed in Table 5.2b. The compositions of volatiles in R7 are derived from the coal heating value, proximate analysis, and ultimate analysis.

Table 5.1 Summary of reaction rate constants used in this study

Reactions		Reaction Type	Reaction heat, ΔH°_R (MJ/kmol)	$k = AT^n exp(-E/RT)$ (n=0)		Reference
				A	E(J/kmol)	
Heterogeneous Reactions						
R 1	$C(s) + ½ O_2 \rightarrow CO$	Partial combustion	-110.5	0.052	6.1×10^7	Chen et al.(2000)
R 2	$C(s) + CO_2 \rightarrow 2CO$	Gasification, Boudouard reaction	+172.0	0.0732	1.125×10^8	
R 3	$C(s) + H_2O \rightarrow CO + H_2$	Gasification	+131.4	0.0782	1.15×10^8	
Homogeneous Reactions						
R 4	$CO + ½ O_2 \rightarrow CO_2$	Combustion	-283.1	2.2×10^{12}	1.67×10^8	Westbrook & Dryer (1981)
R 5	$CO+H_2O(g)\leftrightarrow CO_2+H_2$	Water Gas Shift	-41.0	2.75×10^{10}	8.38×10^7	Jones and Lindstedt (1998)
R 6	$CO + 3H_2 \leftrightarrow CH_4 + H_2O$	Methanation	-205.7	$k_f = 4.4\times10^{11}$	1.68×10^8	
				$k_{b\,14} = 5.12\times10^{-}$	2.73×10^4	Benyon P.(2002)
R 7	$CH_{2.121}O_{0.5855} \rightarrow 0.5855CO + 0.2315H_2 + 0.4145CH_4$	Two-step Volatiles Cracking	+12.088	Eddy dissipation		N/A
R 8	$CH_4 + ½O_2 \rightarrow CO+2H_2$	Volatile gasification via CH_4	-35.71			
R 9	$H_2 + ½ O_2 \rightarrow H_2O$	Oxidation	-242	$6.8x10^{15}$	$1.68x10^8$	Jones and Lindstedt (1998)

1) All ΔH°_R at 298K and 1 atm. 2) "+" Endothermic (absorbing heat), "-" Exothermic (releasing heat)

Table 5.2a Compositions of Indonesian sub-bituminous coal

	Weight %
Volatile	38.31%
H_2O	8.25%
ash	3.90%
C	37.95%
H	2.68%
N	0.69%
S	0.31%
O	7.91%
Total, wt %	100.00%
HHV, kcal/kg	5690

Table 5.2b Moisture-free (MF) compositions of Indonesian sub-bituminous coal

Proximate Analysis (MF), wt%		***Ultimate Analysis (MF), wt%***	
Volatile	51.29	C	73.32
Fixed Carbon (FC)	47.54	H	4.56
Ash	1.17	O	20.12
	100.00	N	0.72
		S	0.11
		Ash	1.17
			100.00

5.3 Computational Model

The governing equations, turbulence models, radiation model, discrete phase model, devolatilization model, and reaction model have been stated in Chapter 1 explicitly, so they are not repeated here. The five detailed radiation models are described as following.

5.3.1 Radiation Model

Five radiation models which allow you to include radiation into simulation process: Discrete Transfer Radiation Model (DTRM), P-1 Radiation Model, Rosseland Radiation Model, Surface-to-Surface Radiation Model, and Discrete Ordinates (DO) Radiation Model. The theories of these five radiation models are briefly summarized below. The detailed theories can

be found in any radiation textbook such as Hottel (1967), Siegel and Howell (1980) and Modest (2003).

5.3.2 Radiative transfer equation

The radiative transfer equation for an absorbing, emitting and scattering medium at position $\vec{r}$ in the direction $\vec{s}$ is

$$\frac{dI(\vec{r},\vec{s})}{ds} + (a+\sigma_s)I(\vec{r},\vec{s}) = an^2\frac{\sigma T^4}{\pi} + \frac{\sigma_S}{4\pi}\int_0^{4\pi} I(\vec{r},\vec{s}')\phi(\vec{s}\cdot\vec{s}')d\Omega' \qquad (5.1)$$

where $\vec{r}$ = position vector

$\vec{s}$ = direction vector

$\vec{s}'$ = scattering direction vector

s = path length

a = absorption coefficient

n = refractive index

σ_s = scattering coefficient

σ = Stefan-Boltzmann constant (5.672×10^{-8} W/m^2-K^4)

I = radiative intensity, which depends on position ($\vec{r}$) and direction ($\vec{s}$)

T = local temperature

ϕ = phase function

Ω' = solid angle

The sum of ($\mathbf{a}+\sigma_s$) is the extinction coefficient K. Integration of K along a distance "s" in the participating medium gives the optical thickness or opacity, $\kappa(s) = \int_0^s K(s)ds$. For a uniform gas medium with constant **a** and **σ**, the optical thickness can be simplified as $(a+\sigma_s)\times s$. The refractive index n is important when considering radiation in semi-transparent media. Absorption coefficient "**a**" and scattering coefficient σ_s are functions of local concentrations of H_2O and CO_2, path length, temperature and total pressure. In this study, absorption coefficient and scattering coefficient are calculated by piecewise polynomial approximation.

5.3.3 P-1 Radiation Model

For a gray medium (or on a spectral basis) with a known temperature distribution, the general problem of radiative transfer entails determining the radiative intensity from an integro-differential equation in five independent variables, including three space coordinates and two direction coordinates. The method of spherical harmonics provides a vehicle to obtain an approximate solution of arbitrarily high order, by transforming the equation of transfer into a series of simultaneous partial differential equations. To simplify the problem, an approximation is made by truncating the series of equations after very few terms. The highest value N, gives the method its order and its name, *P-N approximation*. It is known from neutron transport theory that approximations of odd order are more accurate than even ones of net highest order, so that P-2 approximation is never used.

The P-1 radiation model is the simplest case of the more general P-N radiation model. The P-1 model requires relatively little CPU demand and can easily be applied to various complicated geometries. This model includes the effect of scattering It is suitable for applications where the optical thickness **a**L is large, where "**a**" is the absorption coefficient and L is the length scale of the domain. In a gasifier, the optical thickness is thick due to the presence of various gases, coal particles, soot, and ashes. There are some limitations for this model. First, P-1 model assumes all surfaces are diffuse, which means the reflection of incident radiation at the surface is isotropic with respect to the solid angle. Second, the implementation of P-1 model assumes gray radiation. Third, when optical thickness is small, P-1 model may loss some accuracy, depending on the complexity of the geometry. Meanwhile, P-1 model tends to overpredict the radiative flux from localized heat sources or sinks.

The heat sources or sinks due to radiation are calculated using the equation:

$$-\nabla q_r = aG - 4aG\sigma a^4 \tag{5.2}$$

where

$$q_r = -\frac{1}{3(a+\sigma_s)-C\sigma_s}\nabla G \tag{5.3}$$

and q_r is the radiation heat flux, σ_s is the scattering coefficient, G is the incident radiation, C is the linear-anisotropic phase function coefficient, and σ is the Stefan-Boltzmann constant. The flux of the radiation, $q_{r,w}$, at the walls, caused by the incident radiation, G_w, is given as

$$q_{r,w} = -\frac{4\pi\pi_w \frac{\sigma T_w^4}{\pi} - (1-\rho_w)G_w}{2(1+\rho_w)} \tag{5.4}$$

where ε_w is the wall emissivity and is defined as $\varepsilon_w = 1 - \rho_w$ and ρ_w is the wall reflectivity.

When the model includes a dispersed second phase of particles the effect of particles can be included in the P-1 radiation model. Note that when particles are present, scattering in the gas phase is ignored. For a gray, absorbing, emitting, and scattering medium containing absorbing, emitting, and scatting particles, the transport equation for the incident radiation can be written as

$$\nabla \cdot (\Gamma \nabla G) + 4\pi\left(a\frac{\sigma T^4}{\pi} + E_P\right) - (a + a_p)G = 0 \tag{5.5}$$

where E_p is the equivalent emission of the particles and a_p is the equivalent absorption coefficient. These are defined as follow:

$$E_P = \lim_{V\to 0}\sum_{n=1}^{N} \varepsilon_{pn} A_{pn} \frac{\sigma T_{pn}^4}{\pi V} \tag{5.6}$$

$$a_P = \lim_{V\to 0}\sum_{n=1}^{N} \varepsilon_{pn} \frac{A_{pn}}{V} \tag{5.7}$$

In Equations 5.6 and 5.7, ε_{pn}, A_{pn}, and T_{pn} are the emissivity, projected area, and temperature of particle n. The summation is over N particles in volume V. These quantities are computed during particle tracking.

The projected area A_{pn} of particle n is defined as

$$A_{pn} = \frac{\pi d_{pn}^2}{4} \tag{5.8}$$

where d_{pn} is the diameter of the nth particle.

The quantity Γ in Equation 5.5 is defined as

$$\Gamma = \frac{1}{3(a + a_p + \sigma_{p)}} \tag{5.9}$$

where the equivalent particle scattering factor is defined as

$$\sigma_p = \lim_{V \to 0} \sum_{n=1}^{N} (1 - f_{pn})(1 - \varepsilon_{pn}) \frac{A_{pn}}{V} \tag{5.10}$$

and is compute during particle tracking. In equation 5.10, f_{pn} is the scattering factor associated with the n-th particle. Heat sources (sinks) due to particle radiation are included in the energy equation as follows:

$$-\nabla \cdot q_r = -4\pi \left(a \frac{\sigma T^4}{\pi} + E_P \right) + (a + a_p) G \tag{5.11}$$

5.3.4 Rosseland Radiation Model

The Rosseland model is valid when the medium is optically thick, $((a+\sigma_s)L \gg 1)$. Usually this model can be used when the optical thickness is greater than 3. The Rosseland model can be derived from the P-1 model, with some approximations. The difference between the P-1 model and the Rosseland model is the incident radiation G. Rosseland model assumes the intensity is the blackbody intensity at the gas temperature, while P-1 model calculates a transport equation for incident radiation G. Thus for Rosseland model, $G = 4\sigma n^2 T^4$, where n is the refractive index. The radiation flux is obtained by

$$q_r = -16\sigma \Gamma n^2 T^3 \nabla T \tag{5.12}$$

where $\Gamma = \frac{1}{(3(a+\sigma_s) - C\sigma_s)}$ and C is the linear-anisotropic phase function coefficient. By simplification, Rosseland model has two advantages over P-1 model. Rosseland model can be calculated faster than P-1 model and requires less memory since it does not solve an extra transport equation for the incident radiation, while P-1 model does.

5.3.5 Discrete Transfer Radiation Model (DTRM)

The main assumption of the DTRM model is that the radiation leaving the surface element in a certain range of solid angles can be approximated by a single ray. This "ray tracing" technique could provide a prediction of radiation heat transfer between surfaces without conducting explicit view factor calculations. Thus, the accuracy of this model really depends on the number of rays traced and the computational gird.

The equation for change of radiant intensity, *dI,* along a path, *ds,* can be presented by

$$\frac{dI}{ds} + aI = \frac{a\sigma T^4}{\pi} \tag{5.13}$$

Here, the refractive index is assumed to be unity. DTRM model integrates Equation (5.13) along a series of rays emanating from boundary faces. Thus in DTRM model, I(s) can be represented as

$$I(s) = \frac{\sigma T^4}{\pi}(1 - e^{-as}) + I_0 e^{-as} \tag{5.14}$$

where I_0 is radiant intensity at the start of the incremental path, which is determined by the appropriate boundary condition. The energy source in fluid due to radiation is calculated by summing the change in intensity along the path of each ray that is traced though the fluid control volume.

DTRM model is a relatively simple model, and the accuracy of this model can be increased by increasing the number of rays. Nevertheless, DTRM can be computationally expensive if there are too many surfaces to trace rays from and too many volumes being crossed by rays. There are some limitations for DTRM model. DTRM model assumes gray radiation: all surfaces are diffuse. Meanwhile, the effect of scattering is not included in the DTRM model.

5.3.6 Discrete Ordinates (DO) Radiation Model

The DO model solves the radiative transfer equation for a finite number of discrete solid angles, each associated with a vector direction $\vec{s}$ fixed in the global Cartesian system (x, y, z). Different from DTRM model which performs ray tracing, DO model transforms the radiative transfer equation (5.1) into a transport equation for radiation intensity in the spatial coordinates (x, y, z). The DO model solves for as many transport equations as there are directions $\vec{s}$. It can be implemented by two approaches: energy uncoupled or energy coupled. The uncoupled implementation is sequential in nature and uses a conservative variant of DO model called the finite-volume scheme. The equations for the energy and radiation intensities are solved one by one, assuming prevailing values for other variables in uncoupled implementation. On the contrary, the discrete energy and intensity equations are solved simultaneously in the energy coupled method. The advantage of the coupled approach is that it can speed up applications involving high optical thicknesses and high scattering coefficients. Typically, energy coupled DO model is used when optically thickness is greater than 10. This is typically encountered in

glass-melting applications. The energy coupling DO model sometimes will lead to slower convergence when there is weak coupling between energy and directional radiation intensities.

The DO model considers the radiative transfer equation (RTE) in the direction $\vec{s}$ as a field equation. Also, DO model allows the modeling of non-gray radiation by using a gray-band model. Thus, the RTE for the spectral $I_\lambda(\vec{r},\vec{s})$ can be written as:

$$\nabla\cdot(I_\lambda(\vec{r},\vec{s})\vec{s})+(a_\lambda+\sigma_s)I_\lambda(\vec{r},\vec{s})=a_\lambda n^2 I_{b\lambda}+\frac{\sigma_S}{4\pi}\int_0^{4\pi} I_\lambda(\vec{r},\vec{s}')\phi(\vec{s}\cdot\vec{s}')d\Omega' \tag{5.15}$$

Here λ is the wavelength, a_λ is the spectral absorption coefficient, and $I_{b\lambda}$ is the black body intensity given by the Planck function. The scattering coefficient, the scattering phase function, as well as the refractive index n are assumed independent of wavelength. The total intensity $I(\vec{r},\vec{s})$ in each direction $\vec{s}$ at position $\vec{r}$ is computed by

$$I(\vec{r},\vec{s})=\sum_k I_{\lambda_k}(\vec{r},\vec{s})\Delta\lambda_k \tag{5.16}$$

where the summation is over the wavelength bands.

Compared with other radiation models, DO model can fit for the entire range of optical thickness. Moreover, scattering effect, exchange of radiation between gas and particulates, and non-gray radiation have been considered in this model. It also allows considerations of the radiation at a semi-transparent wall, a specular wall, and a partially-specular wall. The disadvantage of DO model is that solving a problem with a fine angular discretization is computationally expensive.

5.3.7 Surface-to-Surface (S2S) Radiation Model

The main assumption of the S2S model is that any absorption, emission, or scattering of radiation can be ignored. Therefore, S2S model can be used to account for the radiation exchange in an enclosure of gray-diffuse surfaces. The energy exchange between two surfaces depends only on "view factor."

The energy flux leaving a given surface is composed of directly emitted and reflected energy, which is

$$J_k=\varepsilon_k\sigma T_k^4+\rho_k\sum_{j=1}^{N}F_{kj}J_j \tag{5.17}$$

where J_k represents the energy that is given off (or radiosity) of surface k, ρ_k is reflectivity of surface k. The view factor F_{jk} is the fraction of energy leaving surface k that is incident on surface j, which is given by:

$$F_{ij} = \frac{1}{A_i}\int_{A_i}\int_{A_j}\frac{\cos\theta_i \cos\theta_j}{\pi r^2}\delta_{ij}\,dA_i\,dA_j \tag{5.18}$$

where δ_{ij} is determined by visibility of dA_j to dA_i. δ_{ij} = 1 if dA_j is visible to dA_i and 0 otherwise.

S2S model is good for modeling the enclosure radiative heat transfer without participating media. Compared with DTRM and DO models, S2S model has a much faster computation time per iteration, although the view factor calculation itself is CPU-intensive. Since S2S model doesn't include participating media, it serves as a reference case for comparing the effect of participating media on gasification process.

5.3.8 Physical Characteristics of the Model and Assumptions

This study investigates a two-stage entrained flow coal gasifier as shown in Fig. 5.1. The gasifier capacity is around 1700 ton/day for coal input, and the energy output rate is around 190MW. The grid consists of 1,106,588 unstructured tetrahedral cells. In the simulations, the buoyancy force is considered, varying fluid properties are calculated for each species and the gas mixture, and the walls are assumed impermeable and adiabatic. Since each species' properties, such as density, Cp value, thermal conductivity, absorption coefficient, et al. are functions of temperature and pressure, their local values are calculated by using *piecewise polynomial approximation* method. The mixture properties are calculated by mass weighted average method. The flow is steady and no-slip condition (zero velocity) is imposed on the wall surfaces.

For gas phase, each species' properties, such as density, Cp value, thermal conductivity, absorption coefficient, et al. are functions of temperature and pressure. To reflect this relationship, the local value of each property is calculated by using piecewise polynomial approximation method. The absorption coefficient of each species at different temperature and pressure range is based on Hottel chart (1967) and Zhang's chart (2001). For particulate effect, only the P-1 and DO models account for exchange of radiation between gas and particulates.

The particulates' equivalent absorption coefficient a_p and equivalent particle scattering factor σ_p are defined below as:

$$a_p = \lim_{V \to 0} \sum_{n=1}^{N} \varepsilon_{pn} \frac{A_{pn}}{V} \tag{5.19}$$

$$\sigma_p = \lim_{V \to 0} \sum_{n=1}^{N} (1 - f_{pn})(1 - \varepsilon_{pn}) \frac{A_{pn}}{V} \tag{5.20}$$

where ε_{pn}, A_{pn}, T_{pn}, f_{pn} are the emissivity, projected area, temperature and scattering factor of particle n. They are computed during the particle tracking.

5.4 Boundary and Inlet Conditions

The total mass flow rates of the coal slurry and the oxidant are 19.86 kg/s and 14.50 kg/s, respectively (Case 1, 3). The total mass flow rate of the dry coal case (Case 2) is 19.86 kg/s. The difference in fuel mass flow rates is caused by water added for making coal slurry. The inherent moisture in the coal is included in both the slurry and the dry feed cases. The coal/water weight ratio of the coal slurry is 60%-40%. Oxidant/coal slurry feed rate gives O_2/C stoichiometric ratio of 0.5. The stoichiometric ratio is defined as the percentage of oxidant provided over the stoichiometric amount for complete combustion of carbon. For the dry coal case, N_2 (25% of total weight of Oxidant) has been injected with O_2 to transport the coal power into the gasifier.

The oxidant is considered as a continuous flow and the coal slurry is considered as a discrete flow. The discrete phase only includes the fixed carbon and water from the inherent moisture content of coal (8.25% wt.) and water added to make the slurry. The slurry coal is treated as particles containing both coal and liquid water. Other components of the coal, such as N, H, S, O, and ash, are injected as gas together with the oxidant in the continuous flow. N is treated as N_2, H as H_2, and O as O_2. S and ash are not modeled, and their masses are lumped into N_2.

The walls are all set to be adiabatic and imposed with the no-slip condition (i.e., zero velocity). The internal emissivity of inlet, exit and wall is set as 0.8. The gasifier's wall is set as opaque and the internal emissivity is also 0.8. The boundary condition of the discrete phase at the walls is assigned as "reflect," which means the discrete phase elastically rebounds off once reaching the wall. The operating pressure inside the gasifier is set at 24 atm. The exit pressure

is the same as operating pressure, 24 atm. The syngas is considered to be a continuous flow, and the coal and char from the injection locations are considered to be discrete particles. The particle size is uniformly given as spherical droplets with a uniform arithmetic diameter of 40 μm. Although the actual size distribution of the coal particles is non-uniform, a simulation using uniform particle size provides a more convenient way to track the devolatilization process of coal particles than a non-uniform size distribution.

The computation is performed using the finite-volume-based commercial CFD software, FLUENT 12.0, from ANSYS, Inc. The simulation is steady-state and uses the pressure-based solver, which employs an implicit pressure-correction scheme and decouples the momentum and energy equations. SIMPLE algorithm is used to couple the pressure and velocity. The second-order upwind scheme is selected for spatial discretization of the convective terms. For the gas/particle phase coupling, where the Eulerian-Lagrangian approach is used, the iterations are conducted by alternating between the continuous and the discrete phases. Initially, one iteration in the continuous phase is conducted followed by one iteration in the discrete phase to avoid having the flame die out. The iteration number in the continuous phase gradually increases as the flame becomes more stable. Once the flame is stably established, fifteen iterations are performed in the continuous phase followed by one iteration in the discrete phase. The drag, particle surface reaction, and mass transfer between the discrete and the continuous phases are calculated. Based on the discrete phase calculation results, the continuous phase is updated in the next iteration, and the process is repeated.

Converged results are obtained when the residuals satisfy a mass residual of 10^{-3}, an energy residual of 10^{-5}, and momentum and turbulence kinetic energy residuals of 10^{-4}. These residuals are the summation of the imbalance in each cell. The computation is performed in a PC-cluster of 20 nodes.

The following three cases are studied. Each case is performed without radiation model, with DTRM model, P-1 model, Rosseland Model and DO radiation models, respectively. S2S radiation model is investigated in the baseline case only.

Case 1: Baseline case, oxygen-blown, coal slurry, fuel stream: 100% in 1 stage

Case 2: Oxygen-blown, dry coal, fuel stream: 100% in 1 stage

Case 3: Oxygen-blown, coal slurry, fuel stream: 50%-50% distribution in 2 stages

The summary of the studied cases are listed in Table 3. In the baseline (Case 1) of this study, dry-coal-fed and two-stage configuration is used with fuel distribution of 100%-0% between the first and the second stages.

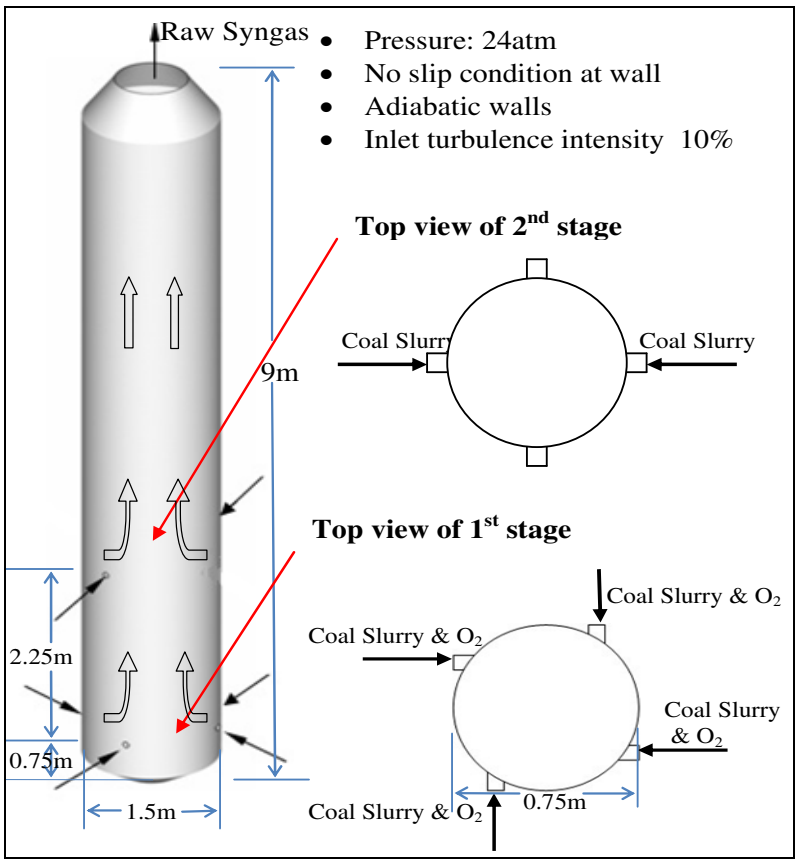

Figure 5.1: Schematic of the two-stage entrained-flow gasifier

5.5 Results and Discussions

5.5.1 Baseline Case (Case 1, coal slurry)

The baseline case (Case 1) is the two-stage oxygen-blown operation with coal slurry distribution of 100%-0% between the first and the second stages, which means all the fuel is injected from the first stage. Syngas temperature and species mole fraction distributions at exit for different sub-cases are shown in Table 5.3. It is observed that the syngas compositions at exit for the cases without radiation model, with P1 model, and with DO model have very similar

results, while DTRM model, S2S model and Rosseland model yield slightly lower mole fractions of CO_2 and H_2. The reason for this phenomenon is that the Water-Gas-Shift (WGS) reaction $CO+H_2O \leftrightarrow CO_2+H_2$ proceeds in the forward direction and yields more CO_2 and H_2 for the cases of P1 and DO models. The syngas temperature for the cases of P1 and DO models are higher (200K-300K) than the rest of the three models, since an exothermic WGS reaction releases more reaction heat. By comparing the average value and standard deviation, the P1 model has the result most close to the mean.

Based on the energy balance, higher syngas temperature should yield lower syngas Higher Heating Value (HHV) since the "total HHV" of the syngas consists mainly of the sensible heat (evaluated at the gasifier's exit temperature) and the heating value (evaluated at 298K). When the gas temperature is high, it implies that more heating value in the fuel has been converted to the syngas's sensible heat, so the HHV of syngas tends to be low. This is verified as the total HHV (kJ/kg) values (syngas heating value + sensible heat) in Table 3 —the total HHV (kJ/kg) value of syngas in each case is similar. The minor difference may be caused by the different kinetic energy at gasifier exit of each case or by the fact that syngas composition is normalized by excluding the minor species, N_2, CH_4, and O_2,, resulting in a minor difference in the real syngas molecular weight.

The syngas and inner wall temperature distributions for the different sub-cases are shown in Figs 5.2 and 5.3. It is surprising to see the large variations of syngas and wall temperatures predicted by different radiation models. For syngas temperature distribution, it can be observed that the results are separated into two groups with the none radiation model, the P1 model, and the DO model forming the first group producing higher syngas temperature, while the results for cases with the S2S model, the Rosseland model, and the DTRM model form the second group, producing syngas temperatures approximately 300K lower than the first group. This large variation of predicted syngas temperature could be caused by the reason that both the S2S model and DTRM model do not consider exchange of radiation between gas and particulates, nor are the mechanisms of scattering and emissivity considered. Therefore, the syngas temperature at second stage drops more in DTRM model and S2S model because the syngas at the second stage cannot receive the radiation energy coming from the syngas at the first stage which is at a higher temperature. Nonetheless, the predicted temperatures in the

combustion zone (near the first stage injection location) from all the models converge at around 2050K. This indicates that it is more consistent in predicting combustion temperatures with different radiation models, but it is very uncertain and challenging by applying an appropriate radiation model in simulating the gasification process.

The result of the Rosseland model seems unreasonable because it shows that mass-weighted average temperature maintains almost at a constant value along the gasifier. Hence, the Rosseland model is not suitable for radiation modeling of Case 1. This unreasonable result may be caused by the fact that the Rosseland model only works for optically very thick media and that it assumes the intensity to be the black-body intensity at gas temperature. This is different from the P1 model that actually calculates the radiation intensity through solving a transport equation.

For the inner wall temperature shown in Fig. 5.3, the variation span (about 500K near the exit) is wider than the variation of syngas temperature. The non-radiation case has the highest value, whereas the P1 model case has the lowest wall temperature. The difference of wall temperature between these two cases is about 300K-500K. In the second stage, the S2S model gives a relatively uniform inner wall temperature when compared to other models. It appears that, when the radiation effect is included, both the syngas and wall temperatures decrease under the slurry coal gasification condition.

Table 5.3 also shows the average CPU time per iteration for each case. It can be clearly seen that DO and DTRM model take about twice more CPU time than other models. Due to an extreme computational time required for using the gray band method, only the total gray radiation approach is employed in this paper. For angular discretization in the DO model, the Theta Divisions and Phi Divisions are both set as 3 to obtain reliable results. The pixelation of 1×1 is used because it is sufficient for modeling gray-diffuse radiation.

5.5.2 Case 2 (dry coal, 100%-0% for two stage injection)

Case 2 is the two-stage oxygen-blown operation with dry coal distribution of 100%-0% between the first and the second stages. Syngas temperature and species mole fraction distributions at exit for different sub-cases are shown in Table 5.4. Similar to Case 1 (1 stage coal slurry), it is shown that the sub-cases with the none radiation, the P1 and the DO models

have very similar results of syngas composition and temperature at the exit, while the results of the DTRM model and the Rosseland model yield noticeably different syngas compositions and produce very high exit syngas temperatures (400K-700K higher). Different from Case 1 with coal slurry, in the dry coal study of Case 2, the lower syngas exit temperatures predicted by the DO and P1 model could be caused by the slower forward WGS reaction rate than in the cases with Rosseland and DTRM models. Since water content in dry coal is much less than in the coal slurry, steam has not been sufficiently provided to promote forward WGS reaction to produce more H_2 and CO_2, so the results of syngas composition for P1 and DO models in Case 2 with more CO and less H_2 are thought to be more reasonable than the sub-cases with DTRM and Rosseland models.

Figures 5.4 and 5.5 provide contour and mass-weighted temperature distributions for both syngas and inner wall temperatures. It is interesting to see that the syngas temperature distributions predicted by none radiation model, the P1 model, and the DO model are very consistent, while the DTRM model gives a higher syngas temperature (about 400K higher at the exit). The result of syngas temperature distribution for the Rosseland model is apparently not reasonable because it yields a very large and unrealistic swing of both syngas and wall temperatures along the gasifier.

For the inner wall temperature, the case with the DO model yields a similar result with the case without employing any radiation model. The wall temperature for P1 model is around 400K lower than it for DO model, while the temperature for DTRM model is about 300K higher than DO model. Note that in both the slurry coal and dry coal cases, P1 model predicts the lowest wall temperature.

5.5.3 Case 3 (coal slurry, 50%-50% for two stage injection)

Case 3 is the two-stage oxygen-blown operation with dry coal distribution of 50%-50% between the first and the second stages. Syngas temperature and species mole fraction distributions at exit for different sub-cases are shown in Table 5.5. Syngas temperature and inner wall temperature distribution are shown in Figures 5.6 and 5.7. Similar to Case 1, the Rosseland model gives uniform syngas temperature distribution, so this model does not work for gasification simulation. DO model, P1 model, DTRM model, and none radiation model have the same syngas temperature distribution with different levels. The combustion process is the

main reaction at the first stage. The DO model yields the highest syngas temperature, while the P1 model continues to give the lowest syngas temperature; the maximum temperature difference between DO and P1 models is about 1000K between the first and second stage at around 2.5 m. Because 50% coal slurry is injected from second stage injection without oxygen, the gasification process dominates in the second stage; and, consequently, the syngas temperature drops drastically near the second stage injection location, as shown in Figure 6. The syngas temperature slightly increases at the second stage all the way to the exit of gasifier. This temperature increase may be caused by the exothermic process from the WGS reaction in the second stage after coal slurry has been consumed completely.

At the second stage, the maximum wall temperature difference between the DO model and P1 model is about 300K. Different from the syngas temperature distribution, the inner wall temperature decreases from the first stage injection location (combustion area) all the way to the exit of gasifier. The case with the DTRM model predicts the highest inner wall temperature, while the P1 model continues to predict the lowest one. The biggest temperature difference between these two models reaches an uncomfortably large value of approximately 1000K.

5.6 CONCLUSION

Five different radiation models have been tested through three different operating conditions of gasification process. The results of syngas composition, syngas temperature, as well as the inner wall temperature in each case have been compared. The conclusions are the following:

a. Rosseland model does not yield reasonable and realistic results for gasification process. It either predicts an uncharacteristic nearly-constant syngas and wall temperature distributions along the gasifer for the slurry coal cases or a unreasonably large swing of temperature from very high to very low and back to very high value along the gasifier for the dry-coal feed case.
b. Inner wall temperature is more uniform in the case of S2S model than any other radiation models, since S2S model only considers the enclosure radiation transfer without including participating media.

c. The effect of radiation is much more significant in predicting the inner wall temperature than syngas temperature distribution.
d. The P1 model always predicts the lowest inner wall temperature in all the cases.
e. The DTRM model predicts very high syngas and wall temperatures in the dry coal feed case. In the one-stage coal slurry case, DTRM result is close to the S2S result.
f. DO and DTRM model take about twice more CPU time than the other models.

In this study, the various radiation models yield uncomfortably large uncertainties in predicting syngas composition (18%), syngas temperatrure (21%), and wall temperature (28%). No solid conclusion can be derived from this study without a comparison with detailed experimental data consisting of local syngas composition and temperature information, as well as of the inner wall temperature distribution of the gasifier. However, it is fair to note that the Rosseland model does not seem to work reasonably well for simulating the gasification process. The P1 method seems to behave stably and is robust in predicting the syngas temperature and composition, but it seems to underpredict the gasifier's inner wall temperature.

Table 5.3 Syngas composition and temperature at exit for case 1 (1 stage slurry) with different radiation models (Syngas composition is normalized by $CO + H_2O + CO_2 + H_2 = 1$.)

Radiation Model	None	DTRM	P1	Rosseland	DO	S2S	Average	Standard Deviation
CO_2 (Vol)	0.10	0.07	0.09	0.08	0.10	0.08	0.087	0.012
CO (Vol)	0.31	0.33	0.32	0.34	0.31	0.32	0.322	0.012
H_2O (Vol)	0.39	0.42	0.40	0.39	0.39	0.42	0.402	0.015
H_2 (Vol)	0.20	0.18	0.19	0.19	0.20	0.18	0.190	0.009
T_{exit} (K)	1756	1415	1665	1500	1721	1480	1590	142.24
Carbon Conversion Rate (CCR)	99%	97%	98%	99%	98%	98%	98%	0.008
HHV(kJ/kmol)	160,746	161,906	161,123	166,105	160,746	159,076	159,284	6544
Total HHV (kJ/kmol)	215,783	202,507	215,571	210,071	215,153	202,589	207,946	8466
Total HHV (kJ/kg)	10,526	10,005	10,334	10,277	10,495	10,029	10,278	223
Average CPU time per iteration (s)	10.1	21.4	11.3	10.9	20.5	13.4	14.5	5.1

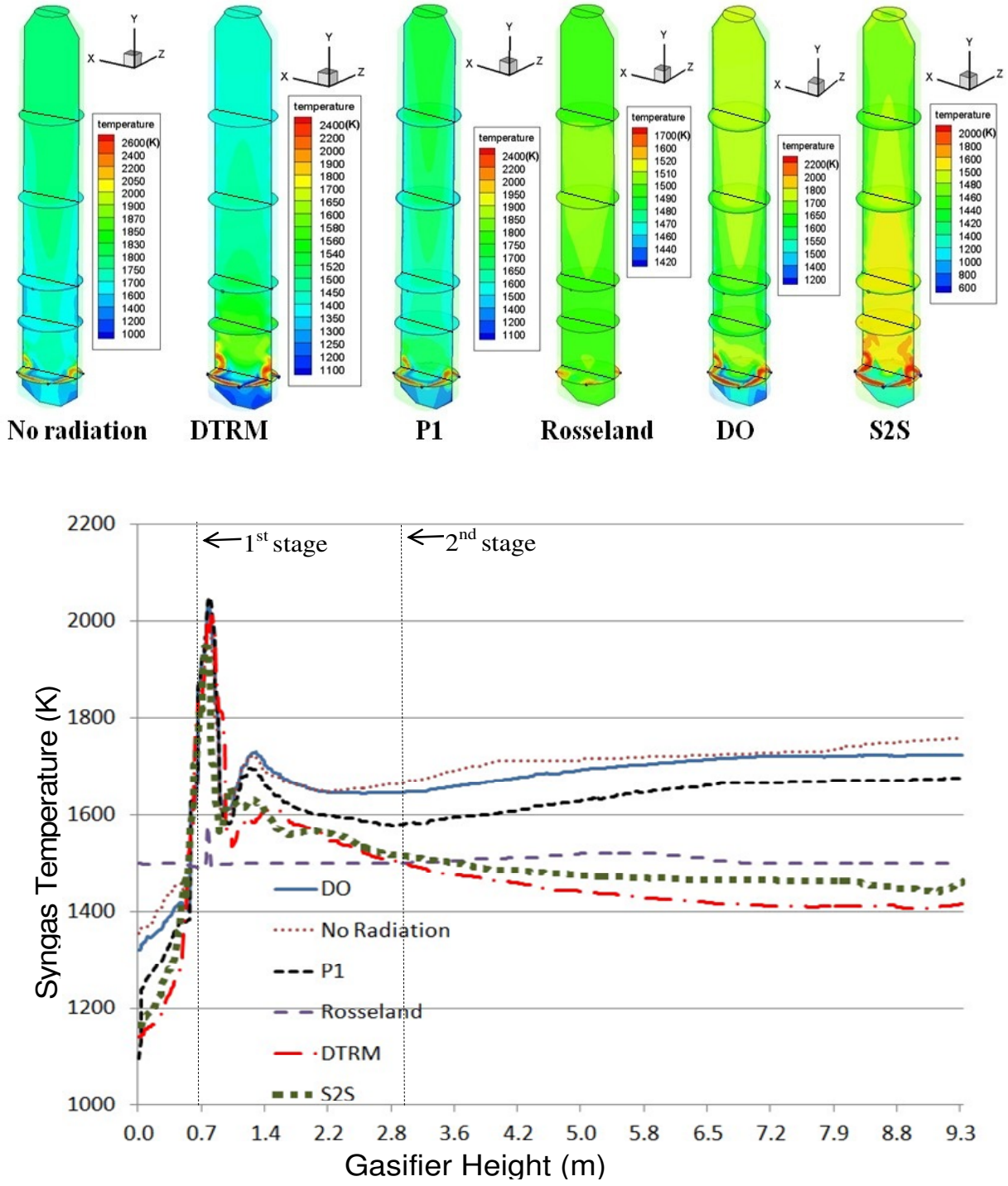

Figure 5.2 Mid-plane syngas temperature contour and mass-weighted average of syngas temperature distribution along the gasifier for Cases 1 (coal slurry)

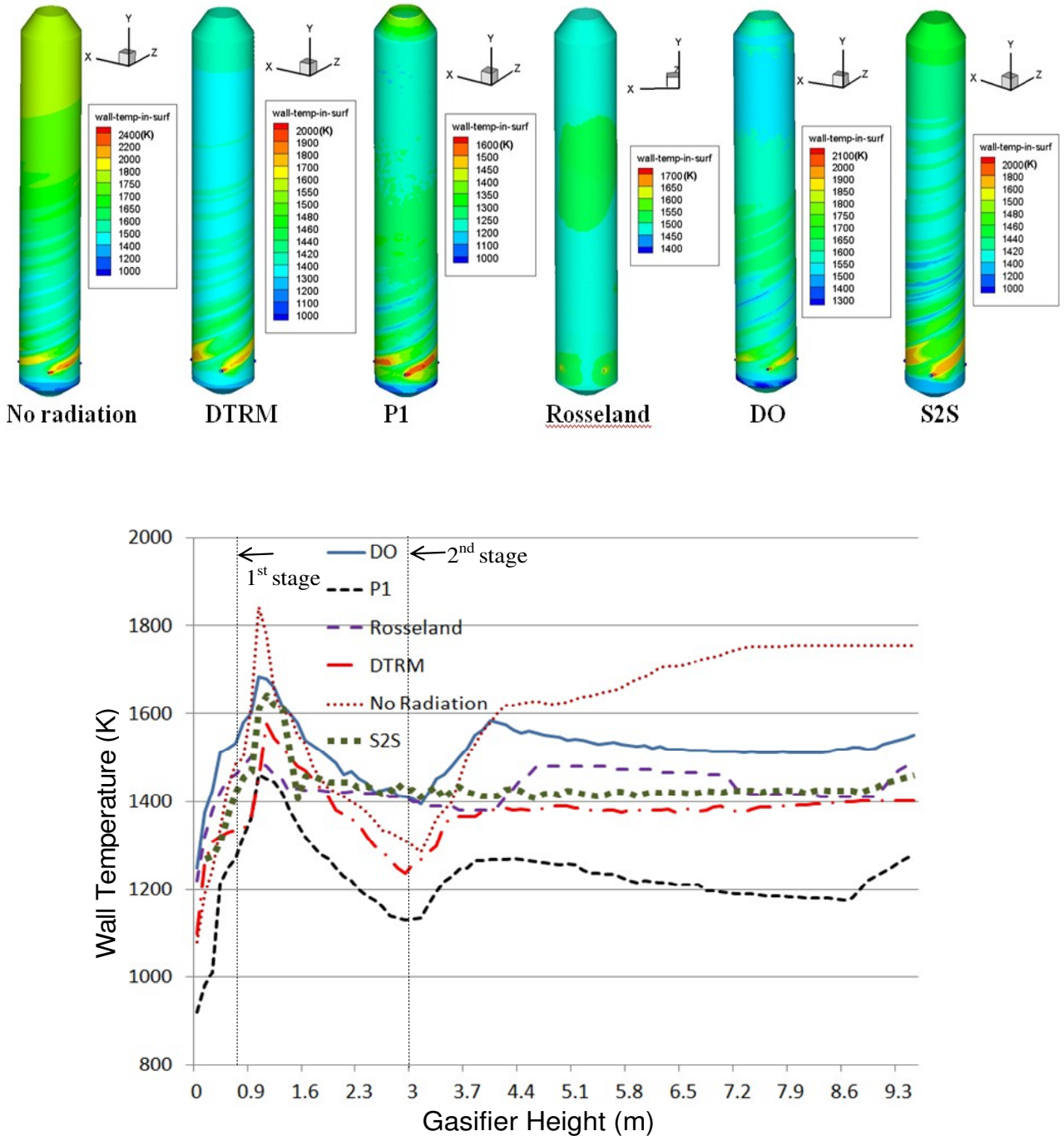

Figure 5.3 Wall temperature contour and circumferential average of gasfier inner wall temperature distribution along the gasifier for Cases 1 (coal slurry)

Table 5.4 Syngas composition and temperature at exit for Case 2 (dry coal, 100%-0%) with different radiation models (Syngas composition is normalized by $CO + H_2O + CO_2 + H_2 = 1$.)

Radiation Model	None	DTRM	P1	Rosseland	DO	Average	Standard Deviation
CO_2 (Vol)	0.06	0.10	0.05	0.10	0.07	0.076	0.023
CO (Vol)	0.53	0.51	0.53	0.48	0.52	0.514	0.021
H_2O (Vol)	0.18	0.14	0.17	0.17	0.18	0.168	0.016
H_2 (Vol)	0.23	0.25	0.23	0.26	0.23	0.24	0.014
T_{exit} (K)	1733	2145	1747	2476	1770	1974	328.81
CCR	99%	97%	97%	99%	98%	98%	0.01
HHV(kJ/kmol)	223,042	221,472	222,635	217,060	220,212	220,884	2405
Total HHV(kJ/kmol)	267,605	288,503	270,533	299,184	270,446	279,254	13893

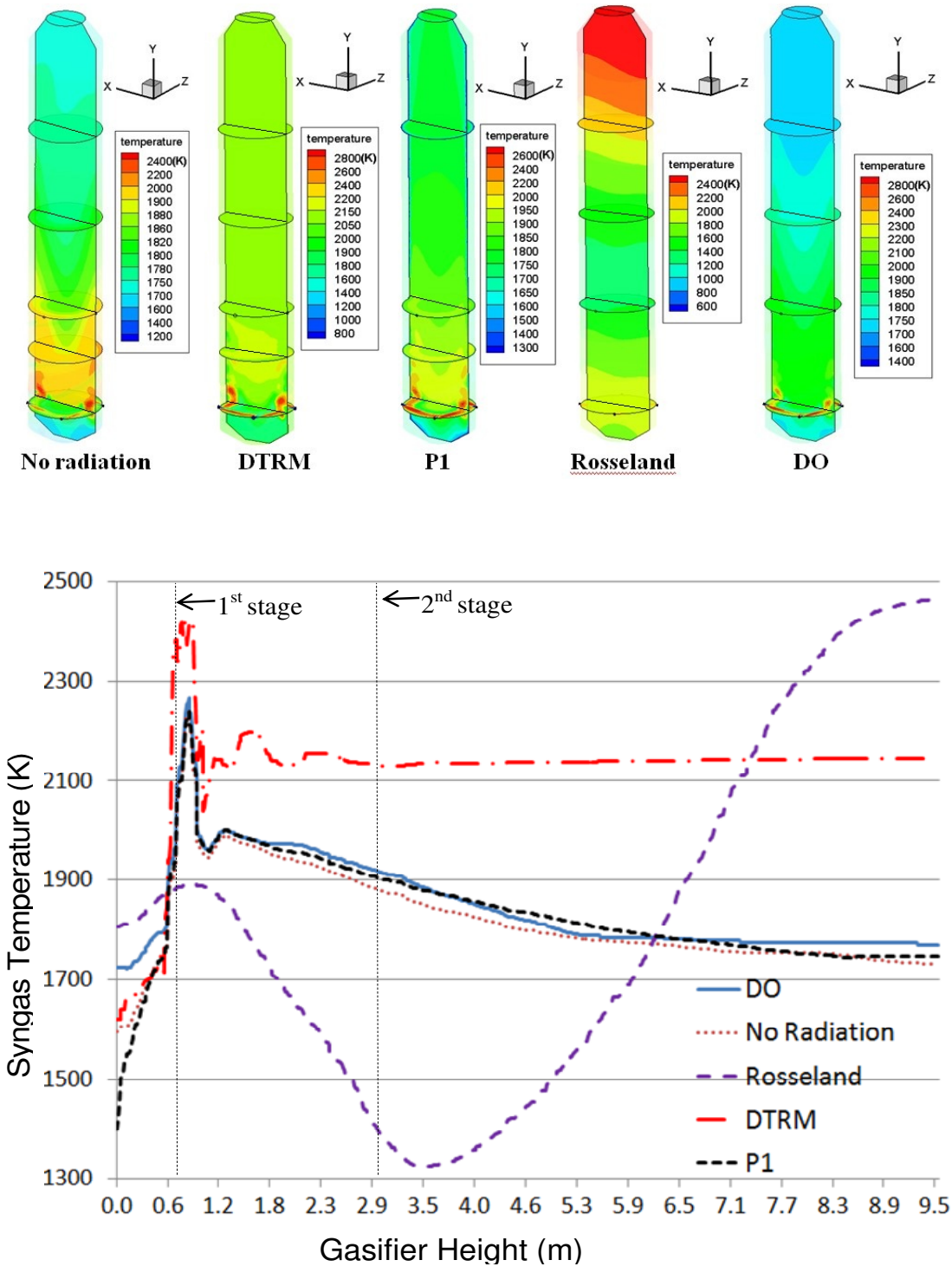

Figure 5.4: Mid-plane syngas temperature contour and mass-weighted average of syngas temperature distribution along the gasifier for Cases 2 (dry coal)

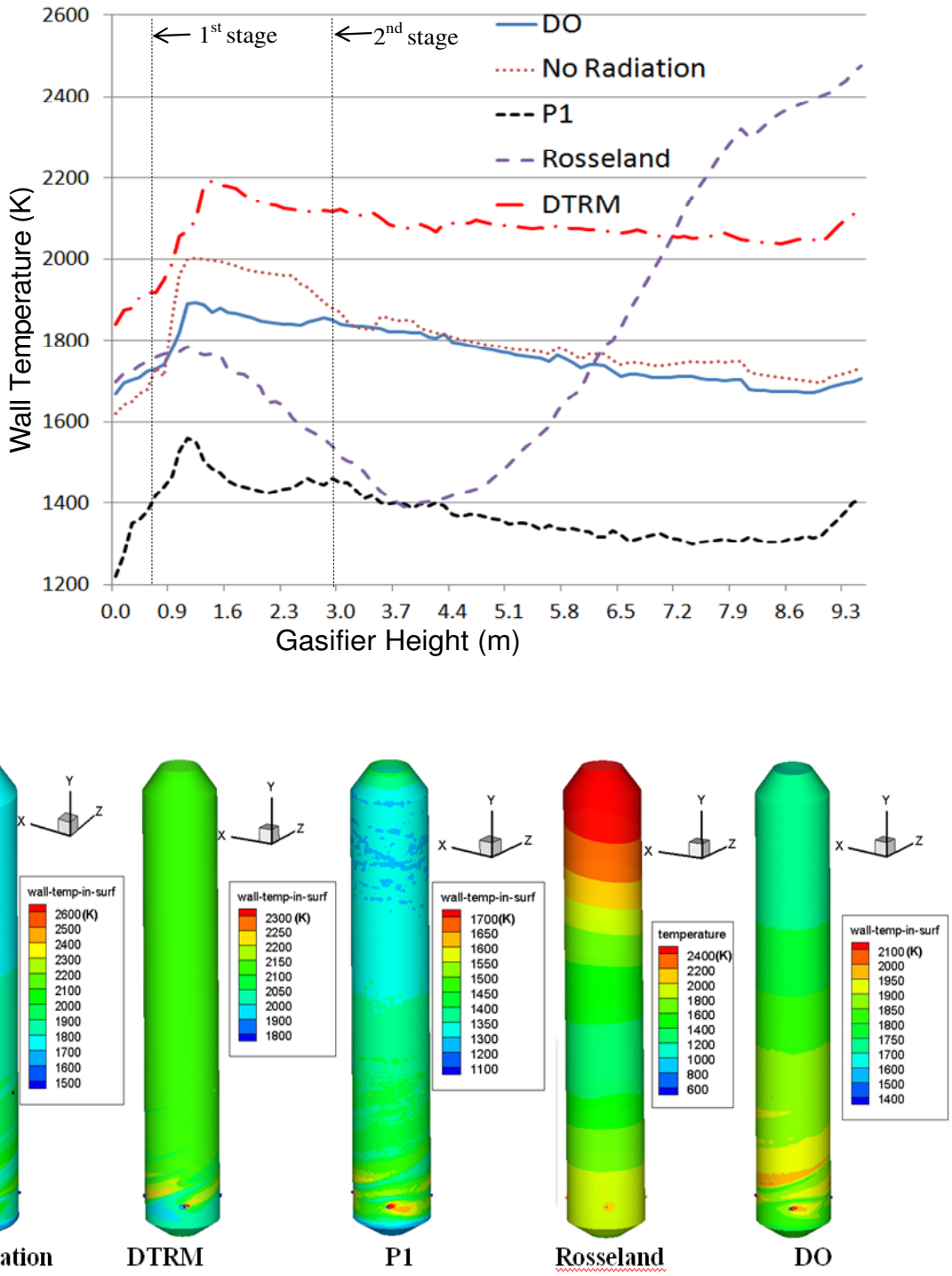

Figure 5.5 Wall temperature contour and circumferential average of wall temperature distribution along the gasifier for Cases 2 (dry coal)

Table 5.5 Syngas composition and temperature at exit for case 3 (2 stage slurry) with different radiation models (Syngas composition is normalized by $CO + H_2O + CO_2 + H_2 = 1$)

Radiation Model	None	DTRM	P1	Rosseland	DO	Row Average	Standard Deviation
CO_2 (Vol)	0.09	0.08	0.12	0.05	0.12	0.092	0.029
CO (Vol)	0.30	0.32	0.26	0.28	0.28	0.288	0.023
H_2O (Vol)	0.41	0.39	0.44	0.41	0.41	0.412	0.018
H_2 (Vol)	0.20	0.21	0.18	0.26	0.19	0.208	0.031
T_{exit} (K)	1551	1216	1312	1498	1414	1398	136.184
CCR	98%	99%	97%	99%	98%	98.2%	0.008
HHV(kJ/kmol)	158,727	166,440	142,910	170,217	150,209	157,701	11280
Total HHV(kJ/kmol)	205,613	198,642	181,381	208,106	175,493	193,847	14637

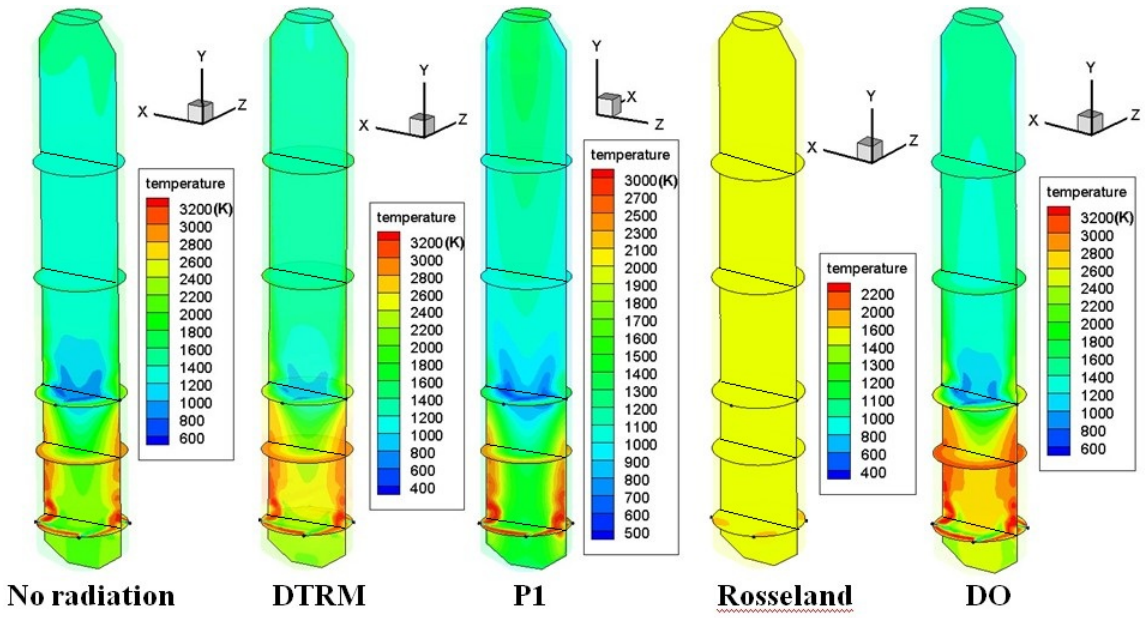

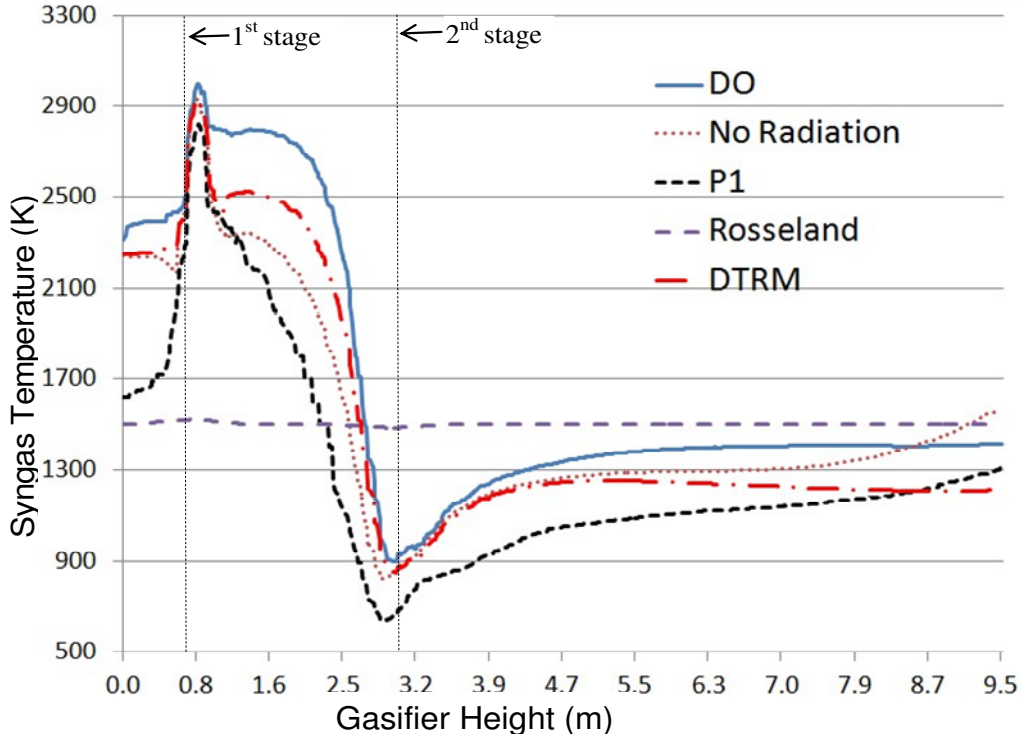

Figure 5.6 Mid-plane syngas temperature contour and mass-weighted average of syngas temperature along the gasifier for Cases 3 (Coal slurry, 50%-50%)

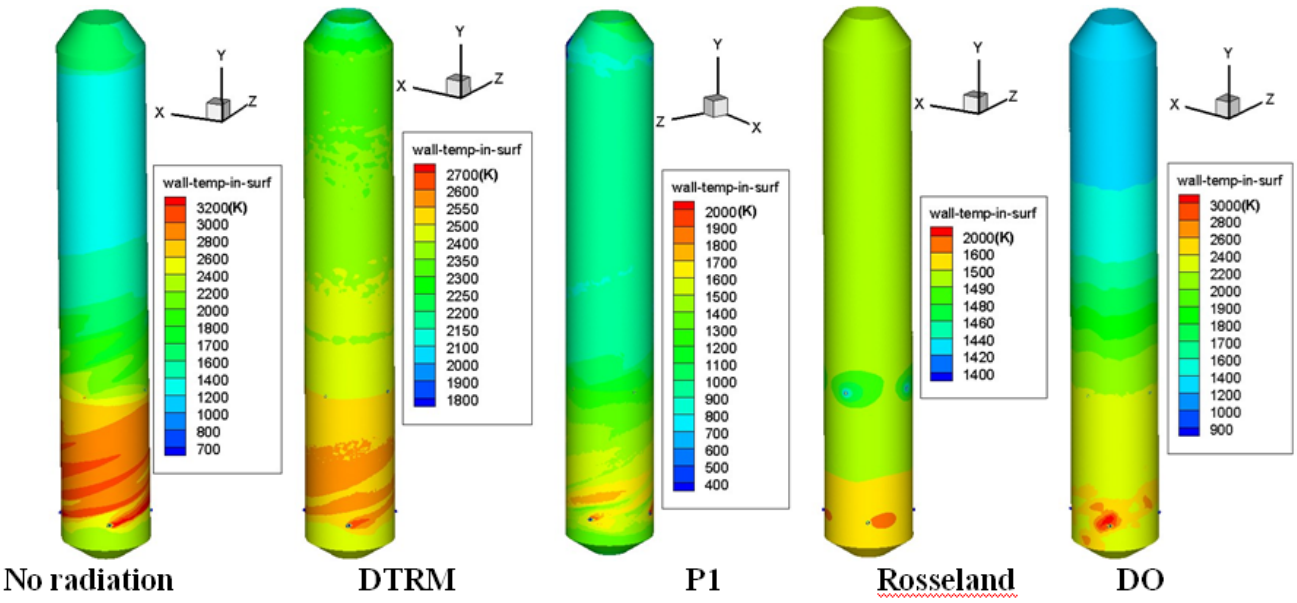

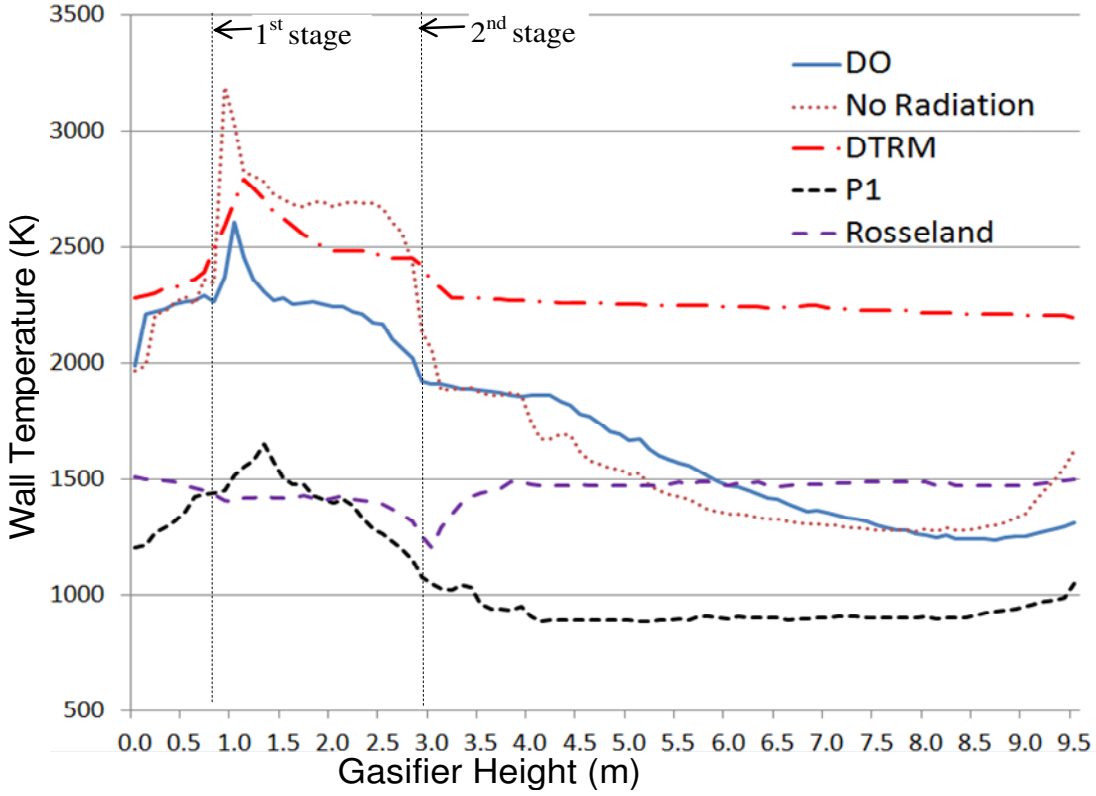

Figure 5.7 Wall temperature contour and circumpherential average of inner wall temperature distribution along the gasifier for Cases 3 (Coal slurry, 50%-50%)

CHAPTER SIX
TOPIC 3: STUDY OF LOW RANK COAL GASIFICATION

6.1 Introduction

Most studies of coal gasification performance are conducted for bituminous coals. However, approximately 47% of the global coal reserves consists of low-rank coals, including lignite and sub-bituminous coals. Low-rank coals present unique challenges as well as opportunities for coal gasification techniques, since they typically contain more volatiles (on the dry or equal moisture base), more inherent moisture, more alkali metal content (Na, K, Ca), and higher oxygen content than high-rank coals, but contain lower sulfur and cost less. Furthermore, low-rank coals have higher reactivity compared to high-rank coals (bituminous coals). The increased reactivity of low-rank coals is caused by higher concentrations of active sites, higher porosity as well as a more uniform dispersion of alkali impurities that act as inherent catalysts (Johnson, 1976; Linares-Solano et al. 1979; Philip et al. 1983).

The low-rank coals' characteristics of higher moisture content, greater tendency to combust spontaneously, higher degree of weathering, and a more adverse dusting nature have restricted their widespread use. The high moisture content leads to high transportation and pretreatment costs and parasitic energy consumption, resulting in reduced thermal efficiency for power generation either through the traditional pulverized coal (PC) combustion process or through the gasification process via an Integrated Gasification Combined Cycle (IGCC) system (Karthikeyan et al 2009). Reduction in coal moisture content is an additional but necessary feedstock pretreatment process in the utilization of low-rank coals, accompanied by increased equipment and O & M (operating and maintenance) costs. The benefits of using low rank coals are derived from their low cost and abundant supply.

Coal moisture consists of surface moisture and inherent moisture. Low-rank coals have higher inherent moisture content and total moisture compared to high-rank coals. Depending on the size of the coal particles fed to the gasifier, it may be necessary to reduce most, if not all, of the surface moisture for the coal to be transported to the gasifier properly (NETL report 2011). Based on the criterion of using Shell gasification technology, for the dry-fed, entrained-flow gasifiers, sub-bituminous coal is dried until 6 percent of the moisture remains, while lignite is

dried until 12 percent of the moisture remains before either coal is injected into the gasifier. It should be noted that the heating value of low-rank coals will increase after the drying process.

Since there are many different parameters that need to be investigated in the study of entrained-flow gasification with low-rank coals, conducting experiments is a time consuming and expensive process. To help narrow down the number of experimental variables and to guide preliminary design development, the objective of this study is to employ a Computational Fluid Dynamics (CFD) scheme to investigate the low-rank coal gasification process. Both a high-rank coal (Illinois No.6 bituminous coal) and a low-rank coal (South Hallsville Texas (SHT) Lignite) are used for comparison. Both single- and two-stage fuel feeding schemes are investigated in a downdraft, entrained-flow, refractory-lined reactor.

One of the questions typically asked is "does the high inherent moisture in the low-rank coals reduce the amount of water required for making coal slurry?" The answer is "Yes, it can help somewhat, but not much, because, to make the coal slurry transportable through pipes, a certain required amount of surface water is needed to reduce the slurry viscosity, but, other than that, the slurry isn't affected much by the inherent moisture." Considering that the inherently high moisture content in low-rank coals doesn't reduce the required amount of surface water needed for making a coal slurry, pre-drying of coal is considered in this study. A third condition of using low-rank coals without a pre-drying process is also studied. Although this condition is not common in real applications, its result could provide a reference for demonstrating the influence of high inherent moisture in coal on the thermal-flow behavior during the gasification process.

6.2 Global Gasification Chemical Reactions

This study deals with the global chemical reactions of coal gasification that can be generalized in reactions (R1) through (R11) in Table 6.1.

In this study, the methanation reactions are not considered since the production of methane is negligible under the studied operating conditions. The volatiles are modeled to go through a two-step thermal cracking process (R7 for low-rank coal, R8 for high-rank coal) and gasification processes with CH_4 (R9) and C_2H_2 (R10) as the intermediate products. Since the thermal cracking process is endothermic, it is important to check that the enthalpy of reaction is positive in both R7 and R8 to ensure that the assumed thermal cracking model doesn't violate

fundamental thermodynamic and chemical principles. The low-rank coal used in this study is SHT Lignite, whose composition is given in Table 6.2. The high-rank coal used in this study is Illinois No.6 bituminous coal, whose composition is given in Table 6.3. The compositions of the volatiles are derived from the coal's heating value, proximate analysis, and ultimate analysis. The oxidant is considered to be a continuous flow, and the coal particles are considered to be the discrete phase. The discrete phase includes the fixed carbon and liquid water droplets from the moisture content of coal. Other components of the coal, such as N, H, S, O, and ash, are injected as gas together with the oxidant in the continuous flow. N is treated as N_2, H as H_2, and O as O_2. S and ash are not modeled, and their masses are lumped into N_2.

For the reaction rate of the water-gas shift reaction (R5), Lu and Wang (2013) modified the rate constant from Jones's rate to A=2.75 to match the experimental data from the quench section of a down-draft entrained flow gasifier. Consequently, the WGS reaction rate is modified as A=2.75, E=8.38×10^7 in this study, as was used in Lu and Wang's paper (2013).

Table 6.1 Summary of reaction rate constants used in this study

Reactions		Reaction Type	Reaction heat, ΔH°_R (MJ/kmol)	$k = AT^n \exp(-E/RT)$ (n=0)		Reference
				A	E(J/kmol)	
Heterogeneous Reactions						
R 1	$C(s) + ½ O_2 \rightarrow CO$	Partial combustion	-110.5	0.052	6.1×10^7	Chen et al.(2000)
R 2	$C(s) + CO_2 \rightarrow 2CO$	Gasification, Boudouard reaction	+172.0	0.0732	1.125×10^8	
R 3	$C(s) + H_2O \rightarrow CO + H_2$	Gasification	+131.4	0.0782	1.15×10^8	
Homogeneous Reactions						
R 4	$CO + ½ O_2 \rightarrow CO_2$	Combustion	-283.1	2.2×10^{12}	1.67×10^8	Westbrook and Dryer (1981)
R 5	**$CO+H_2O(g)\leftrightarrow CO_2+H_2$**	**Water Gas shift**	**-41.0**	**2.75×10^{10}**	**8.38×10^7**	**Jones and Lindstedt(1998)**
R 6	$CO + 3H_2 \leftrightarrow CH_4 + H_2O$	Methanation	-205.7	$k_f = 4.4\times10^{11}$	1.68×10^8	
				$k_b = 5.12\times10^{-14}$	2.73×10^4	Benyon P.(2002)
R 7	$CH_{2.694}O_{0.5581} \rightarrow 0.5581CO + 0.7632H_2 + 0.2419CH_4 + 0.1C_2H_2$	Volatiles Cracking (Low-rank coals)	+68.575	Eddy dissipation		N/A
R 8	$CH_{2.761}O_{0.264} \rightarrow 0.264CO + 0.5085H_2 + 0.336CH_4 + 0.2C_2H_2$	Volatiles Cracking (High-rank coals)	+6.263			
R 9	$CH_4 + ½O_2 \rightarrow CO+2H_2$	Volatiles gasification via CH_4	-35.71			
R10	$C_2H_2 + O_2 \rightarrow 2CO + H_2$	Volatiles gasification via C_2H_2	-447.83			
R11	$H_2 + ½ O_2 \rightarrow H_2O$	Oxidation	-242	6.8×10^{15}	1.68×10^8	Jones and Lindstedt (1998)
1) All ΔH°_R at 298K and 1 atm. 2) "+" = Endothermic (absorbing heat), "-" = Exothermic (releasing heat)						

Table 6.2 The proximate and ultimate analyses of SHT Lignite

Coal	SHT Lignite	
Proximate Analysis, (wt %)		
	Before pre-drying	**After pre-drying**
Moisture	37.7	12
VM	28.16	40
Ash	6.48	9
Fixed Carbon	27.66	39
Heating value (MJ/kg)	16.5	23.2

Ultimate Analysis (wt %)		
	Before pre-drying	**After pre-drying**
Moisture	37.7	12
Ash	6.48	9.15
C	41.3	58.34
H	3.05	4.31
N	0.63	0.89
S	0.75	1.06
O	10.09	14.25

Table 6.3 The proximate and ultimate analyses of Illinois No.6 bituminous coal

Coal	Illinois No.6
Proximate Analysis (wt %)	
Moisture	11.12
VM	34.99
Ash	9.7
Fixed Carbon	44.19
Heating value (MJ/kg)	27.1

Ultimate Analysis(wt %)	
Moisture	11.12
Ash	9.7
C	63.75
H	4.5
N	1.25
S	2.51
O	6.88
Cl	0.29

6.3 Computational Model

The governing equations, turbulence models, radiation model, discrete phase model, devolatilization model, and reaction model have been stated in Chapter 1 explicitly, so they are not repeated here, but briefly summarized below. The time-averaged, steady-state Navier-Stokes equations as well as the mass and energy conservation equations are solved. Species transport equations are solved for all gas species involved. The standard k-ε turbulence model is used to provide closure. The P1 model is used for both gas and particle radiation. The CPD model is used for the devolatilization process. The flow (continuous phase) is solved in Eulerian form as a continuum while the particle motion (dispersed phase) is solved in Lagrangian form as a discrete phase. A stochastic tracking scheme is employed to model the effects of turbulence on the particles. The continuous phase and discrete phase are communicated through drag forces, lift forces, heat transfer, mass transfer, and species transfer.

6.3.1 Computational Models and Assumptions

The computational domain and elements on the gasifier wall are shown in Figure 6.1. The gasifier's capacity is around 800 tons/day for coal input, producing syngas with an equivalent power of around 100MW. The computational domain contains about 1.2 million elements. FLUENT 12.0.16 from ANSYS, Inc. is used as the CFD solver. The simulation is conducted under steady-state conditions. The segregated solver is selected, which decouples the momentum and energy equations. The SIMPLE algorithm is used to couple the pressure and velocity with an implicit pressure correction scheme. The second order upwind scheme is selected for spatial discretization of the convective terms and species. For the finite rate model, where the Eulerian-Lagrangian approach is used, the iterations are conducted by alternating between the continuous and the dispersed phases. Initially, two iterations in the continuous phase are conducted, followed by one iteration in the discrete phase to avoid the flame from dying out. Once the flame is stably established, five iterations are performed in the continuous phase followed by one iteration in the dispersed phase. The drag, particle surface reactions, and mass transfer between the dispersed and the continuous phases are calculated. Based on the calculation results in the dispersed phase, the continuous phase is updated in the next iteration, and the process is repeated. Converged results are obtained when the residuals satisfy a mass residual of 10^{-3}, an energy residual of 10^{-5}, and momentum and turbulence kinetic energy

residuals of 10^{-4}. These residuals are the summation of the imbalance in each cell, scaled by a representative for the flow rate.

In the simulations, the buoyancy force is considered, varying fluid properties are calculated for each species and the gas mixture, and the walls are assumed impermeable and adiabatic. Since each species's properties, such as density, C_p value, thermal conductivity, absorption coefficient, etc. are functions of temperature and pressure, their local values are calculated by using a piecewise polynomial approximation method. The mixture properties are calculated using a mass-weighted average method. The flow is steady, and the no-slip condition (zero velocity) is imposed on the wall surfaces.

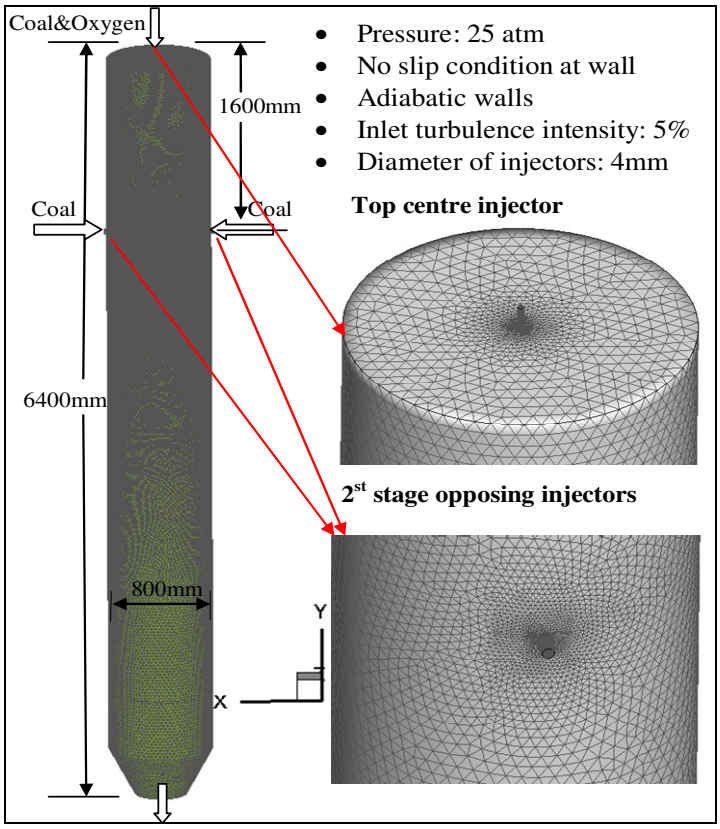

Figure 6.1 Meshed computational domain of the two-stage entrained-flow gasifier

6.3.2 Boundary and Inlet Conditions

The summary of the studied cases is listed in Table 6.4. In Case 1 (baseline case), SHT Lignite is used for a dry-fed, single-stage fuel feeding scheme. Based on a DOE/NETL report (2011), the lignite must be dried to 12 percent moisture before being injected into the gasifier. After the pre-drying process, the higher heating value (HHV) of the SHT Lignite is increased from 14.9 MJ/kg to 20.9 MJ/kg. It should be noted that the energy spent on pre-drying the lignite is about 659 kJ/kg. The mass flow rate of the dry coal is 2.625 kg/s and the mass flow rate of the oxidant is 1.7 kg/s. The oxidant/dry coal feed rate gives the O_2/C stoichiometric ratio of 0.3. The stoichiometric ratio is defined as the percentage of oxidant provided over the stoichiometric amount required for the complete combustion of carbon. N_2 (5% of the total weight of the oxidant) has been injected with O_2 to transport the coal powder into the gasifier. The operating pressure is 25atm.

In Case 2, a two-stage fuel feeding scheme is employed using SHT Lignite, with 25%-75% coal distribution between the top (first) and the bottom (second) injection stages. The oxygen is injected entirely from the top injector. Case 3 is identical to Case 1 using single-stage fuel feeding scheme, except for the fact that Illinois No.6 bituminous coal is used. With the purpose of investigating the effects of the inherent moisture of the low-rank coals on the gasification process, Case 4 is conducted using single-stage gasification and SHT Lignite without pre-drying. By keeping the same amount of char and volatiles inside of the coal particles, the only difference in lignite's composition with and without the pre-drying process is the amount of moisture. Case 5 is a single-stage coal feeding configuration using SHT Lignite with water injection at the second stage without preheating. The mass ratio between coal and total water including inherent moisture and slurry water is 60% to 40%.. The inherent moisture is treated as a part of the coal, different from the water added to make the slurry. The slurry water is injected as droplets. Both the coal and water particle sizes are uniformly given as 50μm for the purpose of conveniently tracking the change of particle sizes, even though it is understood that the actual particle size distribution is not uniform.

The walls are assigned as adiabatic with an internal surface emissivity of 0.8. The boundary condition of the discrete phase at the walls is assigned as “reflect,” which means that the discrete phase elastically rebounds off once reaching the wall. At the outlet, the discrete

phase simply escapes/exits the computational domain. An area near the coal injection locations is initially patched with a temperature of 1500K to simulate the ignition process of a real operation. The limit of the highest temperature is assigned to be 3500K, and the limit of the lowest temperature is assigned to be 400K. This will remove potential runaway conditions caused by erratic, unreasonably high, or low temperatures during the iteration process.

Table 6.4 Parameter and operating conditions of the studied cases

Parameters	Case 1	Cases 2	Cases 3	Case 4	Case 5
Coal Type	Low-rank (Dry)	Low-rank (Dry)	High-rank (Dry)	Low-rank (No pre-drying)	Low-rank (Coal slurry)
Injection Stage	1 - 2	1 - 2	1 - 2	1 - 2	1 - 2
Coal distribution	100%-0%	25%-75%	100%-0%	100%-0%	100%-0%
Total Coal (kg/s)	2.625	2.625	2.625	3.816	2.625
Oxygen (kg/s)	1.7	1.7	1.91	1.7	1.7
Water droplet (kg/s)	0	0	0	0	1.225

6.4 Results and Discussions

6.4.1 Comparison between low-rank coal and high-rank coal (Case 1 vs. Case 3)

Cases 1 and 3 use a single-stage, oxygen-blown, downdraft mode of operation with SHT Lignite and Illinois No.6 bituminous coal, respectively. They both have the same dry coal mass flow rate, which is 2.625 kg/s, and the same O_2/C stoichiometric ratio of 0.3, so the mass flow rate of injected oxygen is 1.7 kg/s in Case 1 and 1.91kg/s in Case 3, respectively. Dry coal in this study means that no additional steam or water is added during fuel injection, although inherent moisture after pre-drying is still included in the coal. The syngas temperature and species mole fraction distributions on the horizontal and selected vertical mid-planes in the gasifier for Case 1 are shown in Figure 6.2. Since all of the fuel and oxidant are injected from the top for the single-stage injection cases, the gas temperature is higher in the top injection

region than it is at the second stage location. The maximum gas temperature in the top injection stage is 2300K. The dominant reaction in the top injection stage consists mainly of the intense char combustion ($C + ½ O_2 \rightarrow CO$ and $CO + ½ O_2 \rightarrow CO_2$) in the first stage and gasification reactions (mainly $C + ½ CO_2 \rightarrow CO$, $C + H_2O \rightarrow CO + H_2$) in the second stage. Due to the exothermic nature of the combustion process and the endothermic nature of the gasification reactions, the temperature drops gradually from the top injection to the exit of the gasifier. Oxygen is completely depleted through the char combustion in the top injection region. CO_2 can be seen quickly produced near the top in Figure 6.2, but it is consumed by the gasification process $C + ½ CO_2 \rightarrow CO$ in the rest of the gasifier.

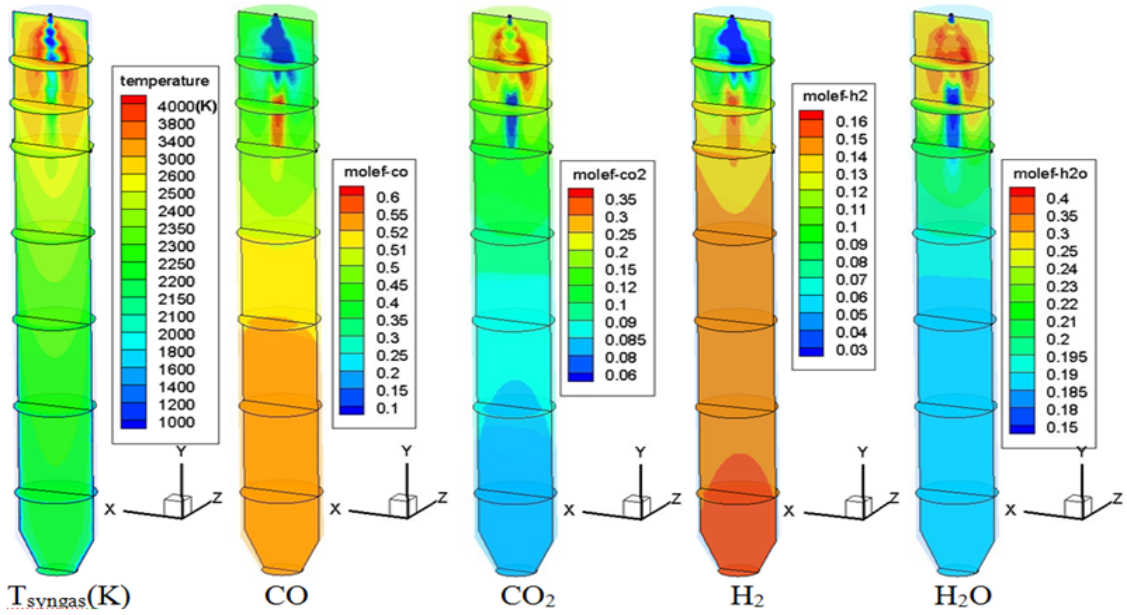

Figure 6.2 Syngas temperature and species mole fraction distributions of Case 1

Table 6.5 shows the temperature and syngas compositions at the exit for Cases 1 and 3. It can be observed that the syngas temperature at the exit from low-rank coal gasification (Case 1) is 538 K (21%) lower than it is for high-rank coal gasification (Case 3). In the meantime, the syngas HHV of Case 1 is 18% (30,222 kJ/kmol) greater than that of Case 3 due to the higher volume fraction of CO and H_2. It should be noted that the HHV in this study is calculated at 25°C, including the sensible and latent heat of the water vapor in the syngas's composition as part of the fuel—this is not the same sensible or latent heat to be released from the water vapor

in the product after syngas is burned. It is shown in Tables 6.2 and 6.3 that the volatile content (40%) is higher than the fixed carbon (39%) after the pre-drying process of the SHT Lignite. On the contrary, for the high-rank coal, the fixed carbon content is 26% higher than that of the volatiles (44.19% vs. 34.99%). Therefore, keeping the same fuel mass flow rates, more oxygen needs to be injected in order for the high-rank coal to go through the partial combustion process with the same O/C stoichiometric ratio. The gasification process is more productive in the SHT Lignite gasification process since more volatiles could go though the volatile cracking-gasification process (R7 ~ R10) to produce more syngas with a relatively lower exit temperature. Based on this result, low-rank coals could be a very competitive fuel for coal gasification.

Table 6.5 Comparison of the results of syngas temperature, composition, HHV at exit between Case 1 (Lignite) and Case 3 (Illinois #6) (The sensible heat of water vapor in the syngas is counted for HHV.)

Syngas composition	Case 1	Case 3
CO (Vol)	52%	45%
CO_2 (Vol)	8%	15%
H_2 (Vol)	15%	11%
H_2O (Vol)	19%	22%
$CH_4 + C_2H_2 + N_2$ (Vol)	6%	7%
Temperature (K)	2170	2738
HHV (kJ/kmol)	197,951	167,729

6.4.2 Comparison between single-stage and two-stage fuel feeding schemes (Case 1 vs. Case 2)

Among the existing commercial coal gasifiers, the two-stage fuel feeding scheme has been employed only in updraft gasifiers, such as the E-GAS gasifier and the Mitsubishi Heavy Industries gasifier. In this study, the two-stage fuel feeding scheme is investigated in a downdraft, entrained-flow, refractory-lined reactor. The two-stage coal feeding gasification

process injects all of the oxygen in the first stage and provides a certain amount of coal without oxygen in the second stage. The endothermic gasification processes downstream of the second stage could keep the gasifier at a lower temperature. Hence, the life of the refractory bricks can be extended, and the associated maintenance costs can be reduced. However, this benefit gained at the second stage is obtained at the cost of a higher peak combustion temperature in the first stage compared to a typical one-stage gasifier. Since the combustion temperature of low-rank coal is lower than that of high rank coal, it is hypothesized that low-rank coals can help reduce the peak temperature in the first stage. Therefore, hypothetically, it seems that it is more advantageous to utilize low-rank coals in a two-stage coal gasification process. In this study, two-stage fuel feeding is simulated in Case 2 using SHT Lignite with a 25%-75% coal distribution between the top and the second injection stages. The oxygen is injected entirely through the top injector, i.e. no oxygen is injected at the second stage. The total mass flow rates of coal and oxygen are the same as those in Case 1.

Figure 6.3 shows the syngas temperature distribution of Case 2. It can be observed clearly that combustion reactions dominate throughout the first stage, with a peak syngas temperature of approximately 3500K. Since 75% of the coal is injected at the second stage, active gasification reactions take place and dominate from the second stage onwards. The syngas temperature decreases gradually from near the first injection location to 1850K at the exit. Table 6.6 compares the syngas temperature, composition, and HHV at the exit between Cases 1 and 2. Compared to the single-stage injection scheme (Case 1), the two-stage fuel feeding scheme (Case 2) effectively reduces the syngas temperature by 15 % (320K) and increases the syngas HHV by 1% (1,468 kJ/kmol). Furthermore, Figs 6.4 and 6.5 show that, compared to the single-stage scheme, the two-stage fuel feeding scheme also reduces the wall temperature by about 100 K at the lower 60% of the gasifier, but it results in higher peak wall temperature (about 100 K) near the second stage.. Figure 6.5 shows that the peak syngas temperatures appear at the first stage in both cases due to the strong presence of coal combustion reactions. The syngas temperature drops more sharply in Case 2 because of the strong endothermic gasification reactions between the syngas and coal particles at the second injection stage. It is interesting to discover that the peak wall temperature does not appear at the first stage, but appears at the location which is about 0.3 meters lower than the second injection location. In order to find the reason, a contour plot of the syngas velocity field in the XY mid-

plane cutting through the injection holes and a contour plot of the syngas temperature in the YZ mid-plane (perpendicular to the second injection direction) are shown in Figure 6.4. It is clearly shown here that the opposing jets in the XY-mid-plane issued at the second injection location squeeze the mainstream of hot syngas from the center to the side of gasifier, touching the wall in the YZ-mid-plane. Consequently, the inner wall is heated in the region intercepting this compressed hot plane, resulting in the peak wall temperature located a little bit lower than the second injection location (since the main stream is going downwards).

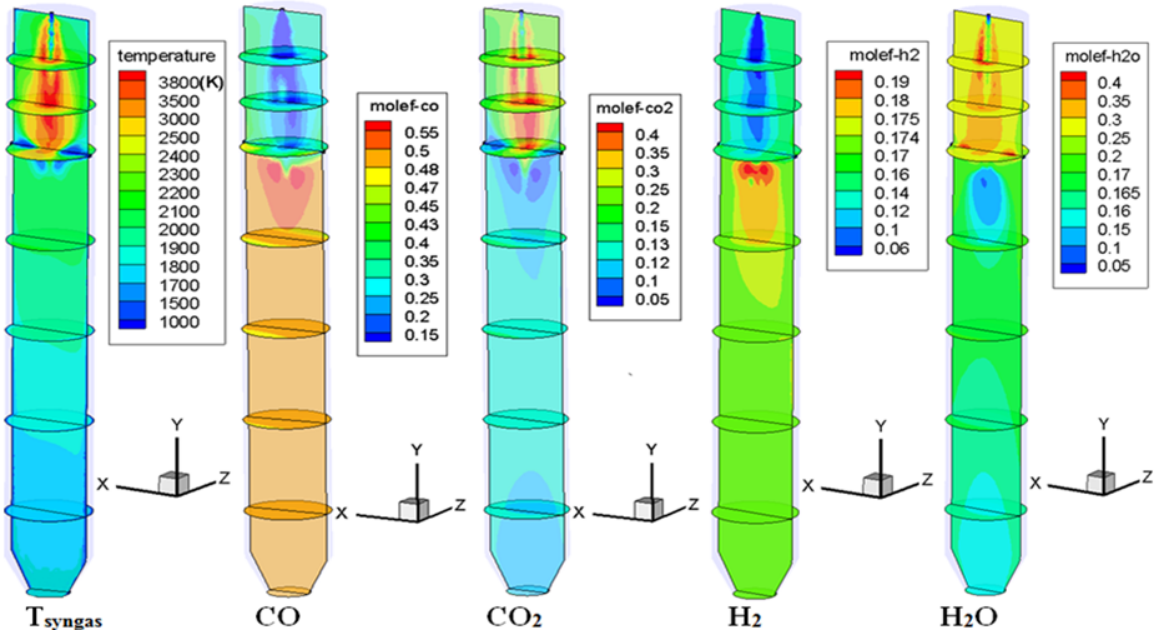

Figure 6.3 Syngas temperature and species mole fraction distributions of Case 2

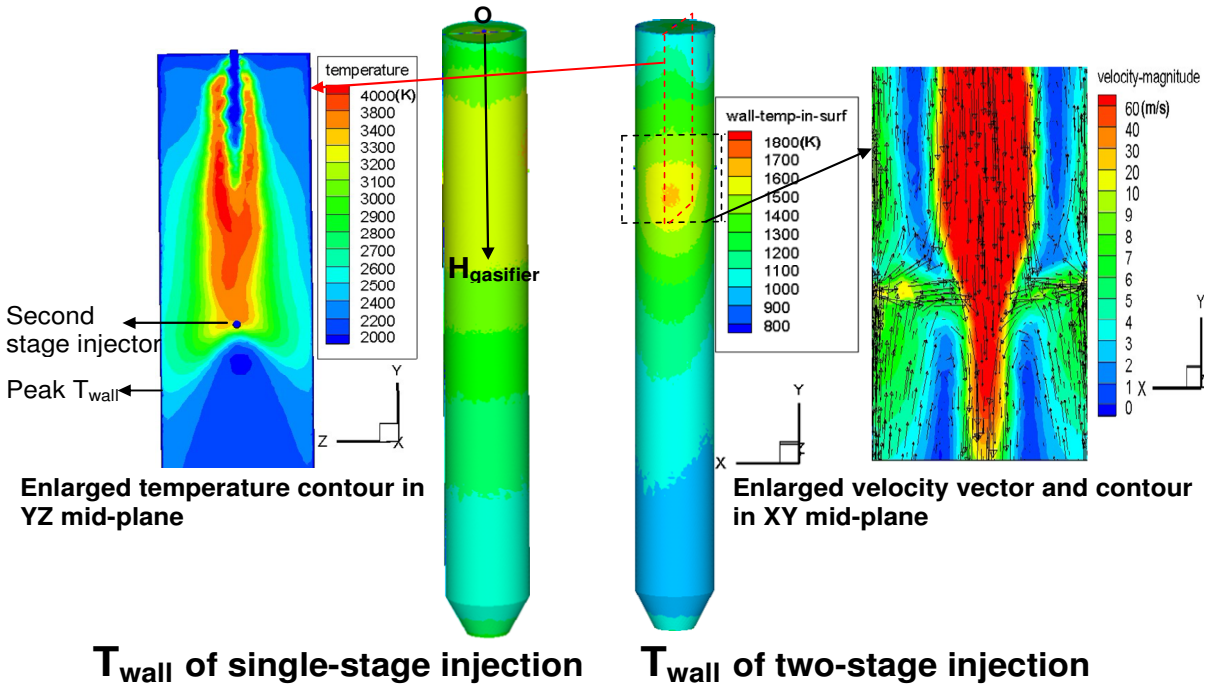

Figure 6.4 Contours of inner wall temperature distributions of Case 1 and 2

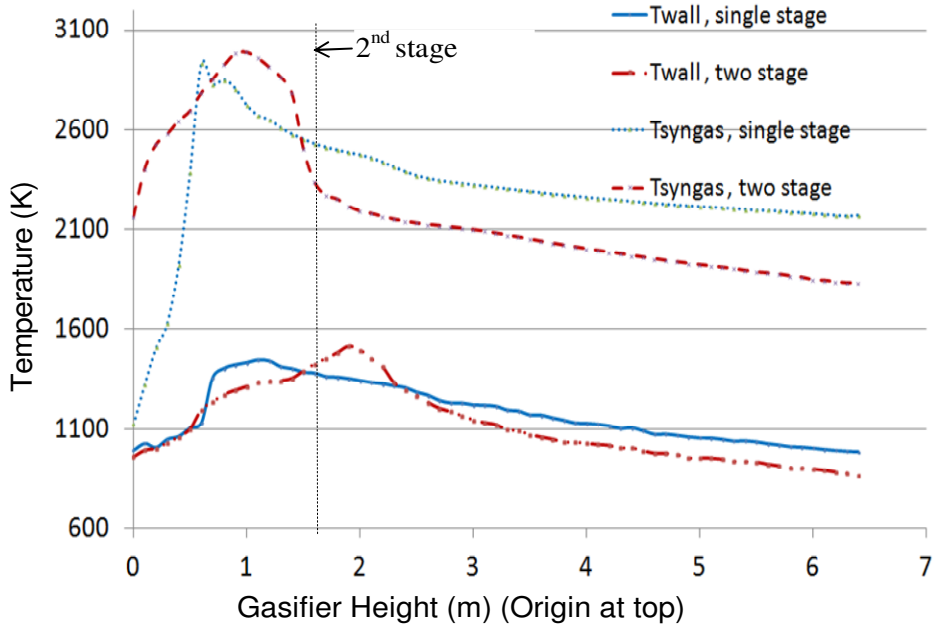

Figure 6.5 Circumferentially averaged inner wall temperature distribution along the gasifier of Case 1 and Case 2

Table 6.6 Comparison of the results of syngas temperature, composition, HHV at the gasifier exit between Case 1 and Case 2

Syngas composition	Case 1	Case 2
CO (Vol)	52%	51%
CO_2 (Vol)	8%	11%
H_2 (Vol)	15%	17%
H_2O (Vol)	19%	16%
$CH_4 + C_2H_2 + N_2$ (Vol)	6%	5%
Temperature (K)	2170	1850
HHV (kJ/kmol)	197,951	199,419

6.4.3 Comparison of lignite gasification performance with and without pre-drying process (Case 1 vs. Case 4)

As explained in the introduction, considering the fact that the high moisture content of low-rank coals leads to high transportation costs and the low thermal efficiency of the gasification process, most of moisture needs be removed before the low-rank coal is either injected into a dry-fed gasifier or mixed with water and injected as slurry. In this study, SHT Lignite is dried to 12 percent of moisture. Table 6.2 shows the lignite's proximate analysis, ultimate analysis, and HHV before and after the pre-drying process. After the pre-drying process, the lignite's HHV increases by 41%. It should be noted that the energy spent on pre-drying the lignite is about 659 kJ/kg, which is calculated as 2258 kJ/kg (latent heat at 1bar) × 0.292 (amount of vaporized water per 1kg coal). Since it is more difficult to vaporize the abundant inherent moisture in low-rank coals, more energy and residence time will be required for the "demoisturization" process. It is interesting to investigate how the "demoisturization" process would affect the effectiveness of the gasification process without first pre-drying the coal. In order to include the resistance of driving the inherent moisture out of the pores of low-rank coals, a simple model is applied by increasing the standard latent heat of water by 20%. This case, without pre-drying, is assigned to be Case 4. Table 6.7 compares the results of syngas temperature, composition, and HHV for Cases 4 and 1. Without pre-drying (Case 4), the syngas HHV decreases by 27%, both the H_2

and CO concentrations decrease by 33% (vol), and the water vapor concentration increases by 121% (vol). This is not a surprising result because the delivered lignite, before pre-drying, only contains 78% of the HHV present after pre-drying, and a significant amount of the high-grade combustion energy is used to vaporize the large amount of inherent moisture in the fuel. Figure 6.6 shows the contour plots of syngas temperature and species mole fraction distributions of Case 4. In comparison with Case 1 in fig. 6.2, the influence of the large amount of inherent moisture can be seen from following three observations:

(a) The high H_2O mole fraction values exist in a larger region in Case 4 (Fig. 6.6) compared to in Case 1.

(b) The presence of this high H_2O mole fraction does not effectively react with C to produce H_2 via the steam-gasification process ($C+H_2O \rightarrow H_2 + CO$), perhaps due to the fact that the water vapor is newly formed via demoisturization, and it will take time to react with char. This minimal steam-gasification process leads to low H_2 and CO mole fractions near the upper 20% of the gasifier.

(c) The temperature near the top injector region in Case 4 is about 1500K cooler than it is in Case 1.

To further understand the physics, the reaction rates of the three heterogeneous reactions: the combustion reaction, water-gas shift reaction, and thermal cracking reaction are calculated and compared between Case 1 and Case 4 as shown in Fig. 6.7. It is clearly shown that all of the reactions actively take place in the region near the top fuel injection area in Case 1, while, in Case 4, all of the reactions are delayed until after the first third of the gasifier's height.. With the exceptions of reactions 3 and 5, which involve H_2O, during the peak reactions, all of the reactions in Case 1 have much higher reaction rates (5-10 times) than those in Case 4. These phenomena illustrate the influence that the large inherent moisture content has on delaying the gasification process. Therefore, it is beneficial to pre-dry low-rank coals to below 12% total moisture content before injecting them into the gasifier.

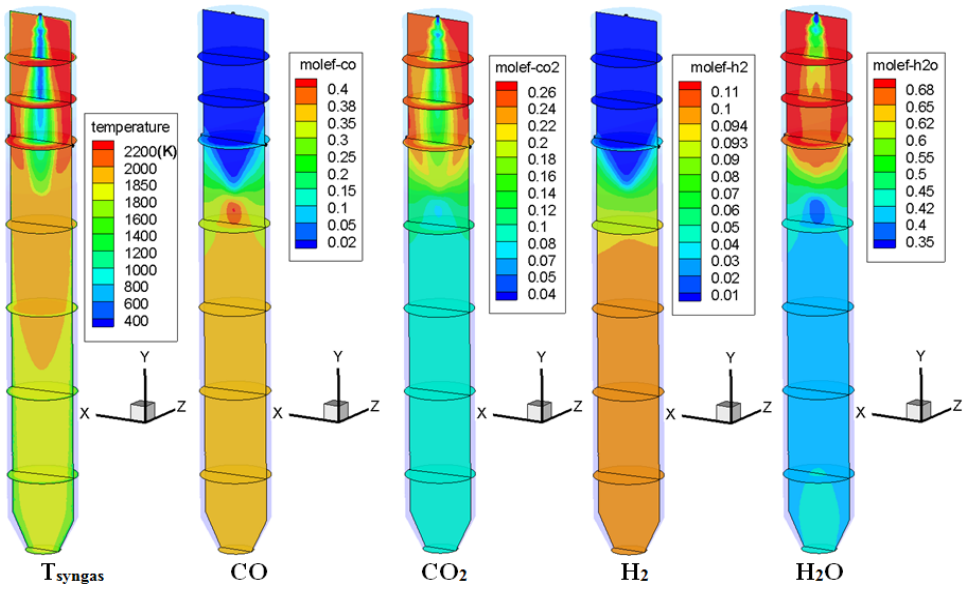

Figure 6.6 Syngas temperature and species mole fraction distributions of Case 4 (no pre-drying)

(a) Reaction Rates (kgmol/m^3-s) of Case 1 (coal with pre-drying process):

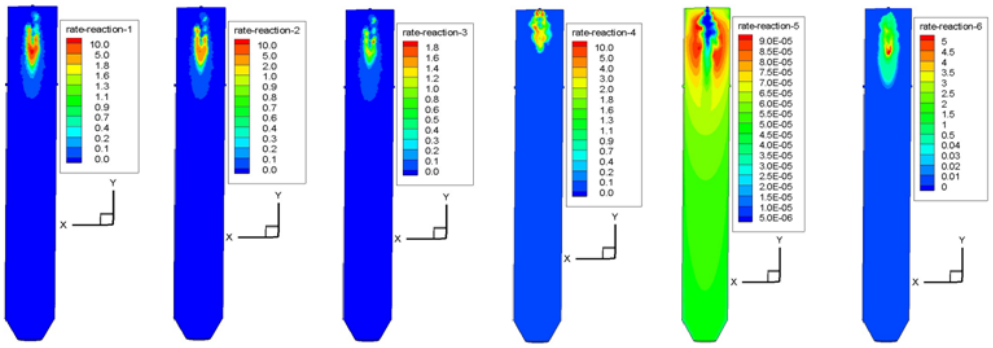

(b) Reaction Rates (kgmol/m^3-s) of Case 4 (coal without pre-drying process):

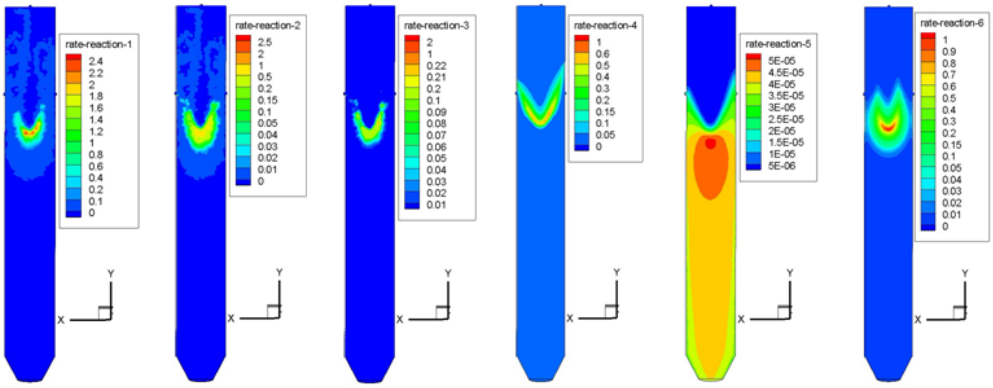

$C(s) + \frac{1}{2} O_2 \rightarrow CO$ $C(s) + CO_2 \rightarrow 2CO$ $C(s) + H_2O \rightarrow CO + H_2$ $CO + \frac{1}{2} O_2 \rightarrow CO_2$ $CO + H_2O\ (g) \leftrightarrow CO_2 + H_2$ $CH_{2.694}O_{0.5581} \rightarrow 0.5581CO + 0.7632H_2 + 0.2419CH_4 + 0.1C_2H_2$

Figure 6.7 Comparison of reaction rates of Case 1 vs. Case 4

Table 6.7 Comparison of temperature, composition, HHV of syngas at exit between Case 1 and Case 4

Syngas composition	Case 1	Case 4
CO (Vol)	52%	35%
CO_2 (Vol)	8%	9%
H_2 (Vol)	15%	10%
H_2O (Vol)	19%	42%
$CH_4 + C_2H_2 + N_2$ (Vol)	6%	4%
Temperature (K)	2170	1788
HHV (kJ/kmol)	197,951	144,700

6.4.4 Comparison of dry coal gasification with coal slurry gasification using SHT Lignite (Case 1 vs. Case 5)

For a slurry-fed gasifier, coal is mixed with a certain amount of water before it is injected into the gasifier. It should be noted that the water used for mixing with the coal is treated as surface moisture, which is different from the inherent moisture embedded in the coal structure. In order to more accurately simulate the coal slurry gasification process by differentiating between these two different types of moisture, the surface moisture is modeled by injecting water with standard latent heat, while the inherent moisture is modeled inside of the coal as a part of its composition. The demoisturization process of the inherent moisture is modeled by adding more energy to drive the moisture out through the lattice or pores inside the coal structures. This additional energy is accounted for by increasing the standard latent heat of water by 20%. Case 5 is a single-stage, slurry-fed configuration using pre-dried SHT Lignite with a total-water-to-dry-coal mass flow ratio of 40% - 60%. The total water includes the 12% inherent moisture and 28% added water (surface moisture). The added water is injected alongside the coal as 50μm water droplets from the top of gasifier. Table 6.8 shows the comparison of syngas composition, temperature, and HHV at the exit between Cases 1 and 5. When the coal slurry is injected into the gasifier in Case 5, the exit syngas temperature decreases by 15% (323 K) compared to Case 1. The syngas HHV in Case 5 decreases by 39% (77,951kJ/kmol) as well, since H_2O now occupies 37% (volume fraction) of the total gas mixture at the exit, which is 1.9 times that of the syngas result for Case 1. Based on this result,

a conclusion can be drawn that the syngas temperature and HHV will decrease significantly when a coal slurry is used as the feedstock. The syngas HHV includes the latent heat of water vapor in the fuel as well as in the product.

Table 6.8 Comparison of syngas temperature, composition, and HHV at the exit between Cases 1 and 5

Syngas composition	Case 1	Case 5
CO (Vol)	52%	37%
CO_2 (Vol)	8%	10%
H_2 (Vol)	15%	11%
H_2O (Vol)	19%	37%
$CH_4 + C_2H_2 + N_2$ (Vol)	6%	5%
Temperature (K)	2170	1847
HHV (kJ/kmol)	197,951	120,000

6.5 Conclusion of Chapter six

This study focuses on a low-rank coal gasification study. SHT Lignite was used as the low-rank coal and Illinois No.6 bituminous coal was used as the high-rank coal in this study. Several comparisons have been conducted on the same operating conditions: 1) low-rank coal vs. high-rank coal; 2) one-stage injection vs. two-stage injection; 3) low-rank coal with pre-drying vs. without pre-drying; and 4) dry coal feeding without steam injection vs. with steam injection at the second stage. Several conclusions are drawn as follows:

1) Syngas produced from lignite has 21% (538 K) lower exit temperature and 18% (30,222 kJ/kmol) greater HHV than syngas produced from Illinois #6 (high-rank coal). Based only on this result of HHV value, it follows that low-rank coal could be a better alternative fuel for coal gasification.

2) The one-stage and two-stage fuel injection schemes have similar syngas compositions and Higher Heating Values at the exit. However, the two-stage fuel feeding scheme results in a lower wall temperature (around 100 K) in the lower half of the gasifier than the single-stage injection scheme. The introduction of the second injection with a pair of opposing jets produces

a flattened plane stretching from the hot reaction zone laterally towards the wall, resulting in a peak wall temperature about 0.3 meters downstream of the second injection location.

3) Without pre-drying, the high inherent moisture content in the lignite causes the syngas HHV to decrease by 27% and the mole fractions of both H_2 and CO to decrease by 33%, while the water vapor content increases by 121% (by volume). The low-rank coal, without pre-drying, will take longer to finish the demoisturization and devolatilization processes, resulting in delayed combustion and gasification processes.

4) When the coal slurry with the mass ratio of total water (inherent moisture + surface moisture) to dry coal of 40% - 60%, is injected into the gasifier at the second stage for the pre-dried lignite, the exit syngas temperature decreases by 15% (323 K) compared Case 1. Also compared with Case 1, the syngas HHV in Case 5 also decreases by 39% (77,951 kJ/kmol).

CHAPTER SEVEN
TOPIC 4: INDUSTRIAL APPLICATIONS

A collaborative study has been conducted with the Industrial Technology Research Institute (ITRI) of Taiwan to help with its design and modifications of a demonstration coal gasifier. In return, ITRI's experimental data and operating experience are shared with University of New Orleans. The Energy and Resources Laboratories of the Industrial Technology Research Institute constructed a demonstration gasifier (Hsu et al., 2003) in the Southern Taiwan city of Kaohsiung. The gasifier, shown in Figure 7.1, is designed for a maximum load of two tons of coal per day. The gasifier is operated with oxygen-blown scheme. Coal powder is transported by nitrogen and feeds from the bottom. The hot gas flows upwards and exits from the top. A water spray device is installed on the top of the gasifier to cool the syngas temperature and adjust the H_2 or CO content of the syngas. If necessary, a water spray device is also used to control the exit gas temperature. Slag that forms on the inside wall flows to the bottom through a slag tap throat and is quenched in a water bath.

This facility is designed to convert pulverized coal and petroleum cokes into syngas at a pressure below 15 bars. The designed coal gasification efficiency under full-load operation is approximately 75% and carbon conversion exceeds 90%. The experimental system includes the following major sections: solids handling, solids feeding, gas feeding, gasification, syngas cooling, slag discharge, fines removal.

The solid feed materials include pulverized coal, petroleum cokes, and fluxing agents such as limestone. The feed materials are pulverized to a size distribution of greater than 70% by weight by passing through 200 mesh. The feed solids are discharged by the hoppers via rotary feeders and a screw conveyor, and are then transferred to the three feed injection vessels. The feed solids are discharged from the injection vessels by variable speed metering screws located at the bottom of the injection vessels. These screws are used to control the rate of the solids that are fed into the pipes of gasifier. The feed solids are mixed with oxygen and steam and are injected into the gasifier through three feed nozzles by a dense-phase pneumatic conveying system using high-pressure nitrogen.

Figure 7.1 Actual IRTI gasifier

The gasifier consists of a gasification section and a slag quench section. The gasification section is a single- stage, refractory-lined, entrained-flow reactor where the feed solids react with oxidants and steam to be converted into syngas. The molten slag generated from the gasification section flows down through slag tap opening located at the bottom of the gasification section and falls into the slag quench section for water quenching. The designed slag tap opening size is 33% of the gasifier inner diameter. Two projects have been conducted.

- Investigation of Two-Stage Oxygen/Coal Slurry Feeding Scheme
- Investigation of a Syngas Quench Cooling Design

7.1 Investigation of Two-Stage Oxygen/Coal Slurry Feeding Scheme

7.1.1 Introduction

7.1.1.1 Brief Review of Fuel Feeding Scheme of Entrained Coal Gasification

Gasification is an incomplete oxidation process converting various carbon-based feedstocks into clean synthetic gas (syngas), which is primarily a mixture of hydrogen (H_2) and carbon monoxide (CO) with minor amounts of methane (CH_4) and inert nitrogen gas (N_2). There are four main classes of gasifiers: fixed bed gasifier, fluidized bed gasifier, entrained flow gasifier, and transport gasifier. The fixed bed gasifier and fluidized bed gasifier have low (425-650°C) and moderate (900-1050°C) outlet gas temperatures, respectively. Entrained flow gasifiers have high outlet temperatures (1250-1600°C) and operate in the slagging range (the ash is fully liquid with low viscosity). The main benefits of entrained flow gasifiers can be summarized as the ability to handle practically any coal as feed, syngas is free of oils and tars, high carbon conversion, suitable for synthesis gas products, and high throughput because of high reaction rates at elevated temperature.

According to the direction of the main flow inside the gasifiers, the entrained flow gasifiers can be classified as up-flow design such as the Shell SCGP and E-gas processes, and down-flow design such as the GE and Simmens gasifiers. For down-flow coal gasifier (GE gasifier), coal slurry and oxidant are introduced from the top of the gasifier. The hot raw gas produced during the gasification process flows toward the bottom of the gasifier. The ash forming components melt in the gasifier, flow down the walls of the reactor, and finally leave the reactor as a liquid slag.

Based on the fuel injection scheme, the entrained flow gasifiers can be categorized as single-stage injection and two-stage injection. The E-Gas process of ConocoPhillips features a two-stage up-flow gasifier design consisting of a horizontal cylindrical vessel as the first stage and a vertical cylindrical vessel as the second stage. Approximately 78% of the coal slurry and 100% of the oxygen are fed in the first stage. Additional coal-water slurry without oxygen is injected into this hot syngas in the second gasifier stage. Endothermic gasification reactions occur between the hot syngas and the second stage coal feed. This lowers the temperature of the syngas and increases the cold gas efficiency of the process. One of the most important advantages of this 2-stage practice is to keep the gasifier temperature low downstream from the

2nd stage and thus extends the life of the refractory bricks, decreases gasifier shut-down frequency for scheduled maintenance, and reduces maintenance costs.

7.1.1.2 Motivation, Hypothesis, and Objectives

Contrast to the traditional concept of two-stage coal feeding practices of injecting coal slurry into two different stages, it is hypothesized that splitting oxygen between two stages, while feeding all the coal in the first stage, i.e., a distributed oxygen injection scheme, can distribute heat release into a larger gasifier's volume and hence reduces the peak temperature and make temperature distribution more uniform in the gasifier. In this approach, the increased life expectancy and reduced maintenance of the refractory can prevail in the entire gasifier—not just downstream from the second stage as in the traditional two-stage coal slurry fed system. To verify this hypothesis, both experiments and computational simulations are conducted. Since conducting experiments are expensive, time consuming, and usually performed with limited cases, it would be more effective and meaningful to establish a computational model to simulate effects of varying operating conditions to help obtain a preliminary understanding of the fundamental thermal-flow physics inside the gasifier. To obtain a trustful computational model, the experimental data is used to calibrate the computational model. The calibrated computational model is utilized later to perform detailed thermal-flow and chemical reaction simulation for more parametric studies that have not been performed by experiments. To this end, the objectives of this study are:

1. Calibrate the CFD model with the baseline experimental data, including syngas temperature, syngas compositions, carbon conversion rate, and gasification efficiency before the water quench section.
2. Use two different material balance methods to cross-check the experimental data.
3. Use the calibrated CFD model to simulate experimental cases with different oxygen split fed from 100% to 40% under the condition of 2.5 bars and 0.6 stoichiometric O_2.
4. Investigate computationally the effect of distributed oxygen fed on gasification performance and temperature distribution under a higher operating pressure (25 bars) and 0.4 stoichiometric O_2.

7.1.1.3 Experimental Facility

The ITRI dry-fed, updraft entrained-flow gasifier into a top-injected coal slurry fed, downdraft entrained-flow gasifer is shown in Fig.7.2. The height of the gasification section above the quench section is 4831 mm, the inner diameter is 270 mm, and the thickness of the refractory is 350 mm.

A series of experiments have been conducted to studying coal-slurry mixing and feeding at two different stages. The slurry coal and oxidants are transported by two options: externally premixed and internal premixed method. "External" or "internal" means outside or inside the fuel injector, respectively. In the externally premixed method, the coal powder is first mixed with water at a mass ratio of approximately 43% (coal) /57% (water). The slurry coal is then pre-mixed with pressurized oxygen (O_2) in an external mixing tank (Fig. 7.3). The amount of pre-mixed oxygen requires at least 10Nm^3/ hr, which is approximately 25-28% of the oxygen used in the gasifier. The externally premixed coal slurry/oxygen mixture is then injected into the gasifier through the center tube of the injector with cooling water circulating through an outer water jacket that wraps around the oxygen tube. For the internal premixing method, only the coal slurry is transported through the center tube. All the oxygen is fed through the outer concentric annular pipe and is mixed with the slurry coal before injection (Fig. 7.4) in the desulfurization process. In this study, the internal premixing method is chosen for coal slurry mixing and feeding.

The coal powder is first mixed with water at a mass ratio of approximately 43% (coal)/57% (water). All the oxygen is fed through the outer concentric annular pipe and is mixed with the slurry coal before injection. The total oxygen fed to the gasifier is about 60% of the stochiometric amount needed for complete coal combustion. The injector is water cooled through an annular water jacket wrapping around the fuel and oxygen passages. The blunt injector tip with multiple holes is derived from a previous study which studied the performance and life expectancy of two injector's designs (Wang et al., 2010). It was discovered that the injector with a blunt tip geometry and multiple injection holes was able to reduce temperature gradient along the injector and significantly increase the life of the fuel injector more than the injector with the conical tip. The gas temperatures are sampled with thermocouples being placed in cavities recessing one-inch in the wall. The gasification process occurs in a down-drafted mode with the syngas exiting near the bottom of the gasifier and continuously entering the

quenching section. The syngas are sampled upstream (before) and downstream (after) the quench section. A detailed discussion about the quench section has been documented in Wang et al. (2011).

With the purpose of finding an optimum oxygen feeding ratio between injections from the top and a second location about 1/3 from the top of the gasifer, a series of experiments were conducted. The experiment is first conducted with 100% oxygen injected from the top, but it is discovered that the temperature is too high on the top and too cold in the middle section of the gasifier. Moreover, the carbon conversion rate is poor, at around 72%. To improve the temperature distribution and carbon conversion rate, part of the oxygen up to 60% (Fig. 7.1), is diverted from the top injector to the side injectors in the middle section. This is done to hopefully provide more effective oxidation and hence more energy for feeding the gasification process in the middle section. The results are encouraging and show that the previous low temperatures in the middle and lower sections of the gasifier increased while the high temperature on the top reduced, resulting in a more uniform temperature distribution along the entire gasifier. More detailed analysis of the experimental results will be presented together with the computational results later.

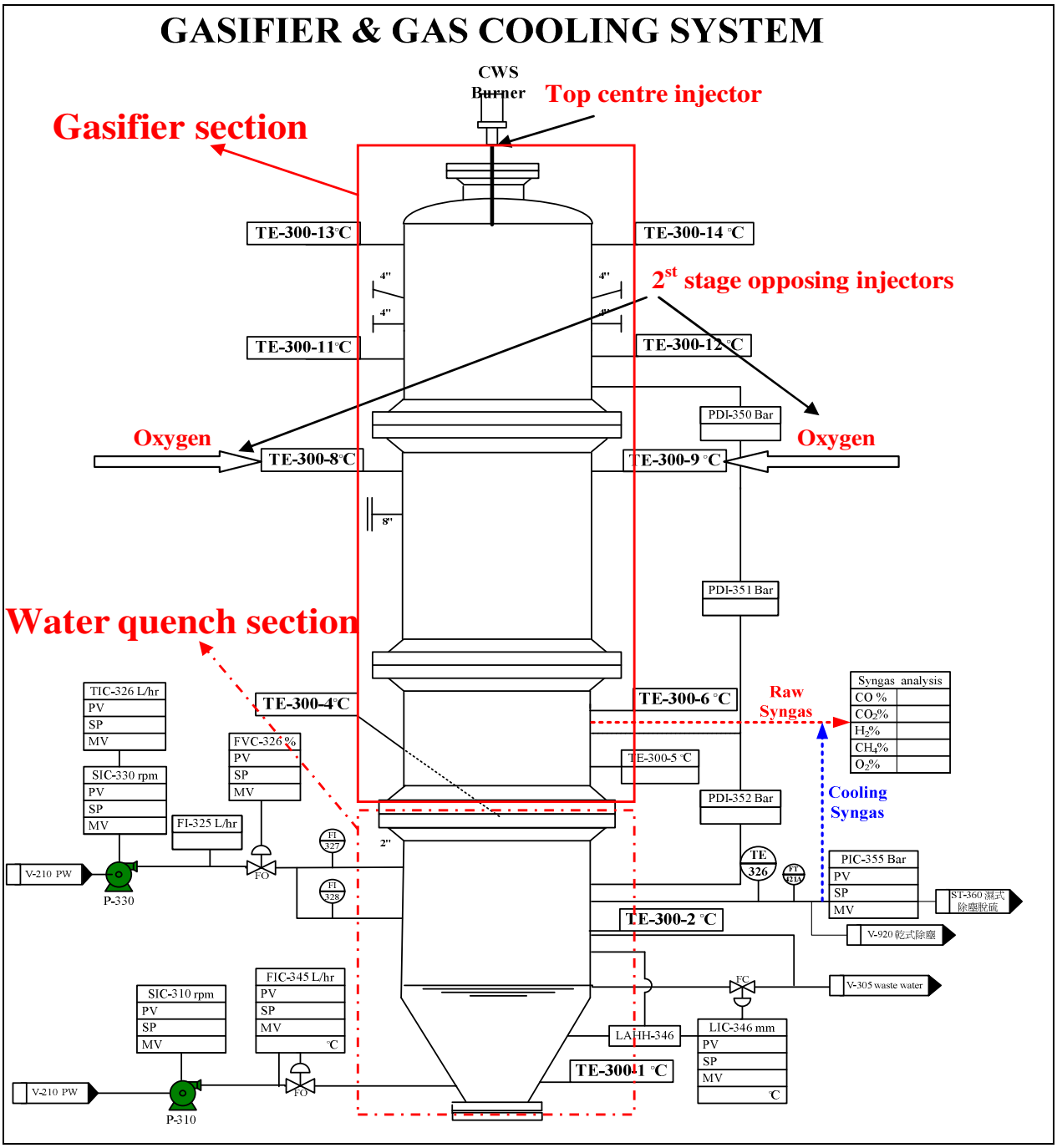

Figure 7.2 ITRI coal-slurry fed, oxygen blown, downdraft entrained-flow gasifier. The outline of the gasifier is based on the outside diameter of the refractory.

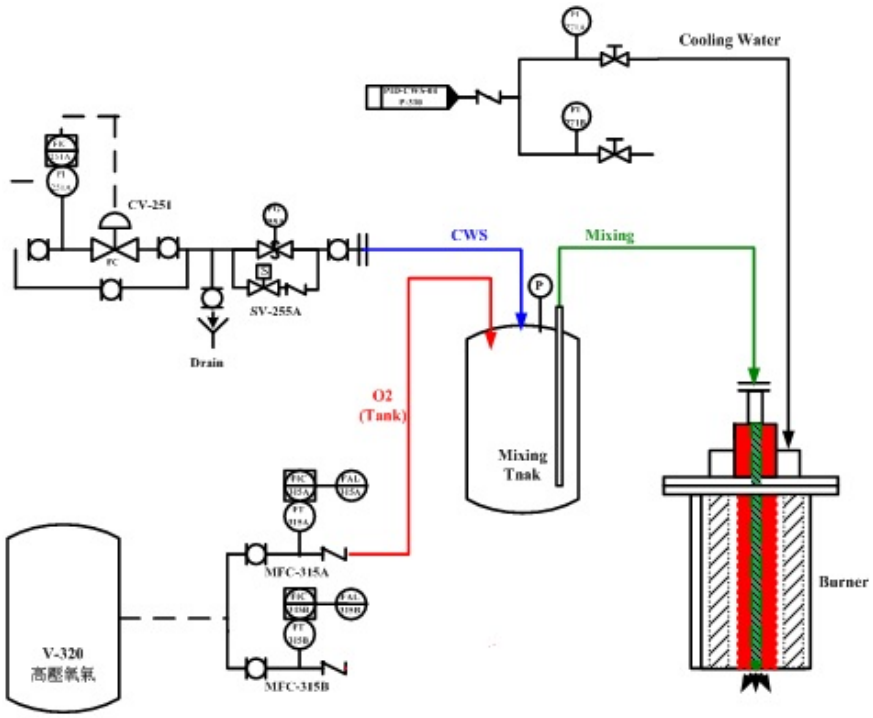

Figure 7.3 Externally pre-mixed coal slurry/oxygen feeding system

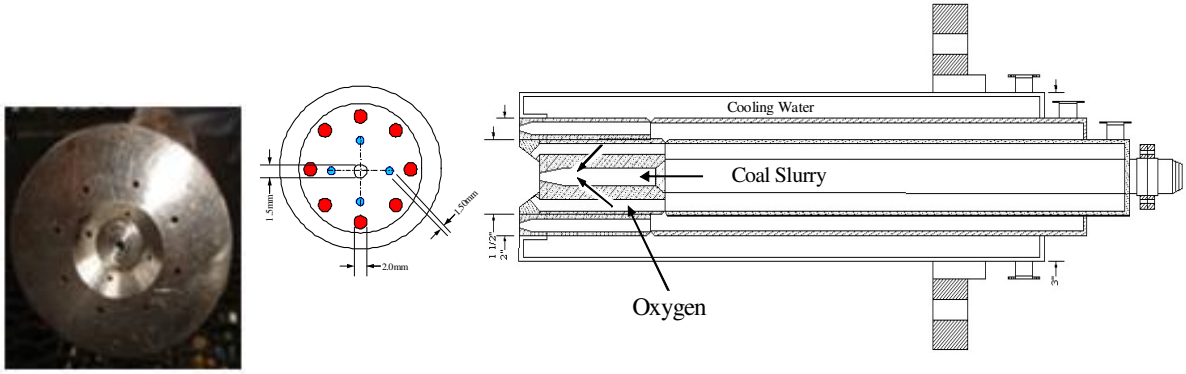

Figure 7.4 The internally premixed slurry-coal/oxygen injector with the coal-slurry fed in the center with oxygen fed through the co-centric outer annular pipe.

7.1.2 Global Gasification Chemical Reactions

This study deals with the global chemical reactions of coal gasification that can be generalized in reactions (R1.1) through (R1.10) in Table 7.1.

Table 7.1 Summary of reaction rate constants used in this study

	Reactions	Reaction Type	Reaction heat, $\Delta H°_R$ (MJ/kmol)	$k = AT^n exp(-E/RT)$ (n=0)		Reference
				A	E(J/kmol)	
Heterogeneous Reactions						
R 1	$C(s) + ½ O_2 \rightarrow CO$	Partial combustion	-110.5	0.052	6.1×10^7	Chen et al.(2000)
R 2	$C(s) + CO_2 \rightarrow 2CO$	Gasification, Boudouard reaction	+172.0	0.0732	1.125×10^8	
R 3	$C(s) + H_2O \rightarrow CO + H_2$	Gasification	+131.4	0.0782	1.15×10^8	
Homogeneous Reactions						
R 4	$CO + ½ O_2 \rightarrow CO_2$	Combustion	-283.1	2.2×10^{12}	1.67×10^8	Westbrook and Dryer (1981)
R 5	$CO+H_2O(g)\leftrightarrow CO_2+H_2$	Water Gas shift	-41.0	2.75×10^{10}	8.38×10^7	Jones and Lindstedt(1998)
R 6	$CO + 3H_2 \leftrightarrow CH_4 + H_2O$	Methanation	-205.7	$k_f = 4.4\times10^{11}$	1.68×10^8	
				$k_{b,14} = 5.12\times10^{-}$	2.73×10^4	Benyon P.(2002)
R 7	$CH_{2.997}O_{0.3456} \rightarrow 0.3456CO + 0.1897H_2 + 0.6544CH_4$ (Two-step Volatiles Cracking)		+12.088	Eddy dissipation		N/A
R 8	$CH_4 + ½O_2 \rightarrow CO+2H_2$ Volatiles gasification via CH_4		-35.71			
R 9	$C_2H_2 + O_2 \rightarrow 2CO + H_2$ Volatiles gasification via C_2H_2		-447.83			
R10	$H_2 + ½ O_2 \rightarrow H_2O$	Oxidation	-242	$6.8\text{x}10^{15}$	$1.68\text{x}10^8$	Jones and Lindstedt (1998)
1) All $\Delta H°_R$ at 298K and 1 atm. 2) "+" Endothermic (absorbing heat), "-" Exothermic (releasing heat)						

In this study, the methanation reactions are not considered since the production of methane is negligible under the studied operating conditions. The volatiles are modeled to go

through a two-step thermal cracking process (R7) and gasification processes (R8, R9) with CH_4 or C_2H_2 as the intermediate products. The coal used in this study is Chinese Shanxi Pinghsuo coal, and its compositions are given in Table 7.2. The compositions of volatiles are derived from the coal's heating value, proximate analysis, and ultimate analysis.

For the reaction rate of water-gas shift (WGS) reaction (R5), Lu and Wang [4] tested Jones' rate by comparing the syngas composition results with the experimental data and decided to slow down the rate constant to A=2.75. Consequently, A=2.75, $E=8.38\times10^7$ is used for the WGS reaction rate in this study.

Table 7.2 The proximate and ultimate analyses of Chinese Shanxi Pingshuo coal

Coal	Pingshuo Coal
Proximate Analysis, wt %	
Moisture	4.31
VM	32.6
Ash	13.52
Fixed Carbon	49.57
Heating value (kcal/kg)	6612

Ultimate Analysis, wt %	
Moisture	2.04
Ash	12.69
C	70.94
H	4.78
N	0.78
S	0.58
O	8.19

7.1.3 Computational Model

The governing equations, turbulence models, radiation model, discrete phase model, devolatilization model, and reaction model have been stated in Chapter 1 explicitly, so they are not repeated here, but briefly summarized below. The time-averaged steady-state Navier-Stokes equations as well as the mass and energy conservation equations are solved. Species transport equations are solved for all gas species involved. The standard k-ε turbulence model is used to provide closure. The P1 model is used as the radiation model. CPD model is used as devolatilization model. The flow (continuous phase) is solved in Eulerian form as a continuum

while the particles (dispersed phase) are solved in Lagrangian form as a discrete phase. Stochastic tracking scheme is employed to model the effects of turbulence on the particles. The continuous phase and discrete phase are communicated through drag forces, lift forces, heat transfer, mass transfer, and species transfer.

7.1.3.1 Computational Domains

The computational domain and elements on the gasifier wall are shown in Figure 7.5. The computational domain contains roughly 1.1 million elements. A grid sensitivity study of 3-D geometries is conducted. Three different grids are used including a coarse grid (0.4 million cells), a medium grid (1.1 million cells), and a fine grid (1.6 million cells). The results of the temperature distribution along the gasifier shows a difference of 7% between the coarse and medium grids and 2% between the medium and the fine grids. In order to save computational time, the medium grid of 1.1 million cells is chosen. FLUENT 12.0.16 from ANSYS, Inc. is used as the CFD solver. The simulation is steady-state and uses the segregated solver, which employs an implicit pressure-correction scheme and decouples the momentum and energy equations. The SIMPLE algorithm is used to couple the pressure and velocity. Second order upwind scheme is selected for spatial discretization of the convective terms and species. For the finite rate model where the Eulerian-Lagrangian approach is used, the iterations are conducted alternatively between the continuous and the dispersed phases. Initially, two iterations in the continuous phase are conducted followed by one iteration in the discrete phase to avoid the flame from dying out. Once the flame is stably established, five iterations are performed in the continuous phase followed by one iteration in the dispersed phase. The drag, particle surface reaction, and mass transfer between the dispersed and the continuous phases are calculated. Based on the dispersed phase calculation results, the continuous phase is updated in the next iteration, and the process is repeated. Converged results are obtained when the residuals satisfy mass residual of 10^{-3}, energy residual of 10^{-5}, and momentum and turbulence kinetic energy residuals of 10^{-4}. These residuals are the summation of the imbalance in each cell, scaled by a representative for the flow rate.

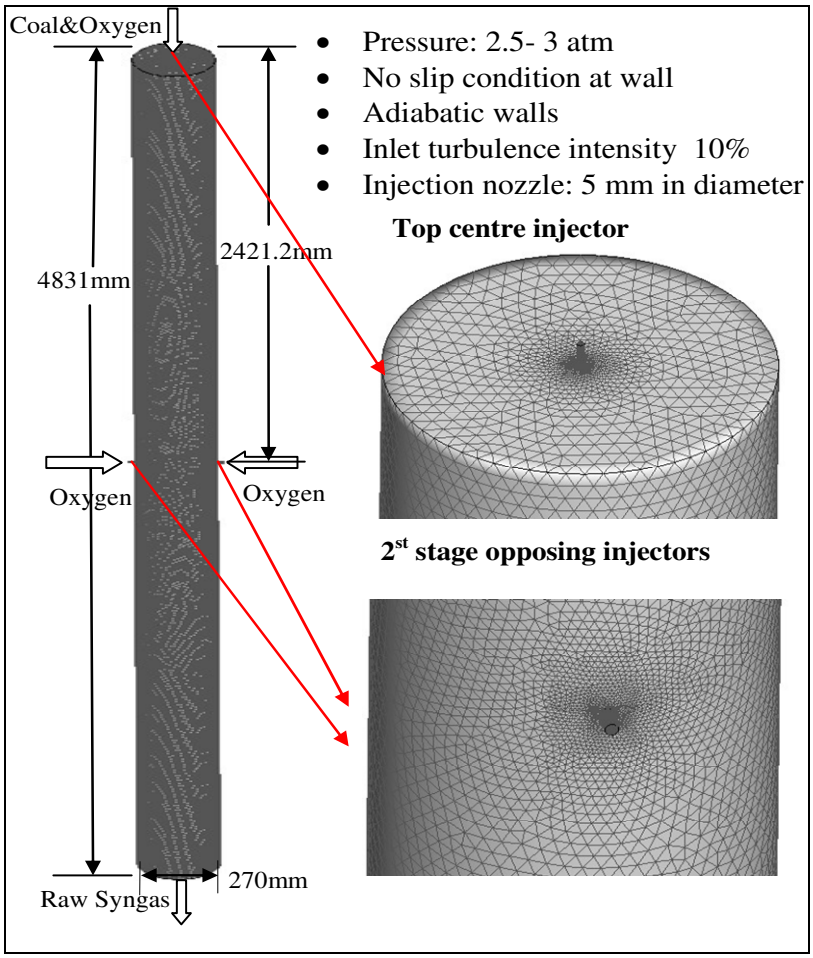

Figure 7.5 Meshed computational domain of the two-stage entrained-flow gasifier

7.1.3.2 Boundary and Inlet Conditions

The summary of the studied cases is listed in Table 7.3. In Case 1, a two-stage configuration is used with oxygen distribution of 100%-0% between the top and the second stages. The coal is fed as slurry. The total mass flow rate of the coal slurry is 92 kg/hr (0.026 kg/s), and the total volume flow rate of oxidant is 36.8 Nm^3/s (0.0146 kg/s). The top and the second injection nozzles are both 5 mm in diameter. To match the experimental conditions, the operating pressure is set as 3 bars for Case 1. From Case 2 to Case 8, the oxygen distribution is 100%-0%, 90%-10%, 80%-20%, 70%-30%, 60%-40%, 50%-50%, 40%-60% between the top and the second injection stages respectively. Total mass flow rate of the coal slurry is 85 kg/hr (0.024 kg/s), and the total volume flow rate of oxidant is 38.6 Nm^3/s (0.0153 kg/s). The operating pressure is 2.5 bars for Cases 2 to 8.

The above eight cases from 1-8 are set up with the same operating conditions as the experiments. The following five cases from Cases 9-12 increase the operating pressure to 25 bars at which no experiments have been conducted in the current facility. From Case 9 to Case 12, the oxygen distribution between the top and the second injection stages is 100%-0%, 80%-20%, 60%-40%, 40%-60% respectively. Total mass flow rate of the coal slurry is 85 kg/hr (0.024 kg/s), and the total volume flow rate of the oxidant is 17.4 Nm^3/s (0.006912 kg/s), which is 30% of the stoichiometric amount for complete combustion. The experimental Case 1 serves as the baseline case, which is used to calibrate the computational Case 1. The calibration is performed by tuning the stochastic time constant and the water-gas shift reaction rate.

Table 7.3 Parameters and operating conditions of the studied cases

	Case 1	Cases 2 - 8	Cases 9 - 12
O_2 distribution (top-second)	100%-0%	(100%-0%)-(40%-60%)	(100%-0%)-(40%-60%)
Coal slurry injection (kg/s)	0.026	0.024	0.024
O_2 injection (kg/s)	0.0146	0.0153	0.009216
Operating pressure (bars)	3.0	2.5	25

The oxidant is considered to be a continuous flow, and the coal particles are considered to be the discrete phase. The discrete phase includes the fixed carbon and liquid water droplets from both the inherent moisture content of coal (4.31% wt) and the injected water content form the coal slurry (57.1% wt). Other components of the coal, such as N, H, S, O, and ash, are injected as gas together with the oxidant in the continuous flow to keep the mass flow the same as in the experiments. N is treated as N_2, H as H_2, and O as O_2. S and ash are not modeled, and their masses are lumped into N_2. Since studying the effect of coal particle sizes on gasification performance is not in the objectives of this study, the coal slurry size is uniformly given as 50 μm for the purpose of conveniently tracking the change of particle sizes.

The walls are assigned as adiabatic with internal emissivity of 0.8. In case of dry wall, interactions between the droplets and wall usually manifest three major phenomena, including reflect, break-up and trap. The actual phenomenon depends on the incoming Weber number of

the droplet. Here, the Weber number is the ratio of kinetic energy of a droplet to the surface energy of a droplet ($We = \rho\, d_d\, v_d^2 / \sigma$). If the Weber number ($We_{in}$) is less than 10, the droplet will reflects elastically after it hits the wall. As the incoming We increases further to $We_{in} > 80$, the droplet falls into disintegration region which leads breaking-up the droplet to several small droplets. In the transition region of $30<We<80$, the droplet has the chance to either reflect or breakup. In the case of this study, since the Weber number is less than 10, the boundary condition of the discrete phase at walls is assigned as "reflect", which means the discrete phase elastically rebound off once reaching the wall. At the outlet, the discrete phase simply escapes/exits the computational domain. An area near the coal injection locations is initially patched with temperature of 1500K to simulate the ignition process of a real operation. The limit of the highest temperature is assigned as 5000K, and the limit of the lowest temperature is assigned as 400K. This will remove potential runaway conditions caused by erratic, unreasonably high, or low temperatures during the iteration process.

7.1.4 RESULTS AND DISCUSSIONS

The biggest challenge and uncertainty for comparison between the CFD simulation and experimental data are related to the measured water vapor amount, which will affect the evaluation of the water gas shift rate used in the CFD model. To obtain a quick overview of the possible equilibrium syngas output conditions, two different material balance methods are used to estimate the syngas species mole fractions at exit for Case 1.

7.1.4.1 Comparison between the calculated results of material balance method and experimental data

Case 1: Oxygen distribution between the top and the second stages: 100%-0%.

Total mass flow rate of the coal slurry: 92kg/hr (0.026kg/s).

Total volume flow rate of oxidant: 36.8Nm^3/s (0.0146kg/s).

Operating pressure: 3 bars.

Method 1:

Step 1. O_2 is consumed equally for $C+0.5O_2 \rightarrow CO$ and $CO+0.5O_2 \rightarrow CO_2$. After this step, O_2 has been consumed completely. The leftover char is 0.00054kg/s. CO_2 is produced with 0.020075kg/s.

Step 2. The leftover char is reacted for gasification: $C + CO_2 \rightarrow 2CO$ and $C + H_2O \rightarrow CO + H_2$. The calculation shows that char has been consumed completely by this step. CO is produced with 0.00189kg/s, and H_2 is produced with 4.5×10^{-5}kg/s. The leftover CO_2 is 0.019085kg/s.

Step 3. The volatiles are thermally cracked by the reaction: Volatiles $\rightarrow$0.3456CO + 0.1897 H_2 + 0.6544 CH_4. After this reaction, CO is 0.003604kg/s, H_2 is 1.122×10^{-4}kg/s, CH_4 is 0.00185kg/s.

Step 4. CO and H_2O are reacted by water-gas shift reaction: $H_2O+CO \leftrightarrow H_2+CO_2$. Since this reaction has both forward and backward directions, two conditions have been considered with a fast forward rate and a very slow rate. The fast forward rate approach assumes that all CO will be consumed by the steam or all steam will be consumed by CO depending on which has less amount than the other one. The very slow rate approach is treated as "no WGS reaction."

Table 7.4 shows the mole fractions of syngas composition for both experimental data and the material balance results. For an easy comparison, the data of syngas volume fractions at exit have been normalized by $CO+CO_2+H_2+CH_4=1$. Table 7.3 shows it is impossible that H_2O could reach 5% to 10% weight of total cleaned syngas at the exit, and mole fraction of CO at exit cannot be that high (41% vol.) as measured by the experiment. It is not clear how so much steam (H_2O) can be consumed. Typically, steam can be consumed either by C-steam gasification (R3) or WGS. The material balance shows that there is not sufficient C to react with all the amount of water existing in the gasifier to produce CO. On the other hand, if WGS is used to consume the steam, the material balance result shows that the steam composition can be reduced from 38% to 32%, but the CO is completely used up, which is contrary to the very high CO content from the experimental measurement. To keep CO high in the products, Method 2 is proposed.

Table 7.4 Normalized syngas composition at exit for hand calculation from 1st method and experimental data

Normailized	Exp. data	Materials balance without WGS	Material balance with complete WGS
CO (Vol)	41%	17.5%	0%
CO_2 (Vol)	25%	59%	65%
H_2 (Vol)	33%	7%	21%
CH_4 (Vol)	1%	15.7%	14%
H_2O (Weight)	5%-10%	38%	32%

Method 2:

Method 1 shows that the experimental data has more CO than the material balance's results. By examining all the global reactions, it can be found that CO can be produced by four reactions (R1, R2, R3 and R4). Therefore, to allow more CO to be produced and maintained, but not to be consumed so quickly by CO combustion (R4), Method 2 is proposed with the following steps.

Step 1. 1/3 of Char is equally consumed for three reactions: $C+0.5O_2 \rightarrow CO$, $C+H_2O \rightarrow CO + H_2$, and $C+CO_2 \rightarrow 2CO$. The calculation shows that the char is completely used for these three reactions, but there is still 0.00968kg/s O_2 leftover to be used for step 3.

Step 2. Volatiles are thermally cracked by the reaction: Volatiles $\rightarrow$0.3456CO + 0.1897 H_2 + 0.6544 CH_4.

Step 3. The leftover O_2 is reacted for $CH_4 + 0.5O_2 \rightarrow CO + 2H_2$, $H_2 + 0.5O_2 \rightarrow H_2O$ and $CO + 0.5O_2 \rightarrow CO_2$. O_2, H_2, and CH_4 are consumed completely after this step. This means there is sufficient O_2 to oxidize CH_4 and H_2 but not CO.

Step 4. CO and H_2O are reacted by water-gas shift reaction: $H_2O+CO \leftrightarrow H_2+CO_2$. Similar to Method 1, a fast forward rate and a very slow rate (equivalent to no WGS reaction) are considered, respectively.

Table 7.5 shows the mole fractions of syngas composition for both experimental data and material balance calculation results. To compare this easily, the data of syngas volume fractions at exit have been normalized by $CO+CO_2+H_2+CH_4=1$. The same conclusion can be drawn from Table 5: The experimental data result with very high CO content and low steam

content is difficult to achieve concurrently. Note that although the 53% (vol.) CO in Method 2 is much more than 17.5% (vol.) in Method 1, H_2 is completely consumed in Method 2 due to $H_2 + 0.5O_2 \rightarrow H_2O$.

Table 7.5 Comparison of the syngas composition with the experimental data using the 2nd material mass balance method. The volume fraction is normalized without water, which is separately listed as mass fraction in the last row.

Exit Syngas	Exp. data	Material balance without WGS	Material balance with complete WGS
CO (Vol)	41%	53%	14%
CO_2 (Vol)	25%	8%	46.5%
H_2 (Vol)	33%	0%	39.5%
CH_4 (Vol)	1%	0%	0%
H_2O (Weight)	5%-10%	28%	0%

7.1.4.2 Comparison between CFD results and experimental data

The computational cases 1-8 are conducted with the conditions matching those in the experiments. Among these eight cases, the detailed temperature and species distributions of Case 1 and Case 6 are exhibited to gain fundamental understanding of the thermal-flow behavior inside the gasifer. The conditions of these two cases are listed below:

Case 1: Oxygen distribution between the top and the second stages: 100%-0%.

Total mass flow rate of the coal slurry: 92kg/hr (0.026kg/s).

Total volume flow rate of oxidant: 36.8Nm^3/s (0.0146kg/s).

Operating pressure: 3 bars.

Case 6: Oxygen distribution between the top and the second stages: 60%-40%.

Total mass flow rate of the coal slurry: 85kg/hr (0.024kg/s).

Total volume flow rate of oxidant: 38.6Nm^3/s (0.0153kg/s).

Operating pressure: 2.5 bars

7.1.4.2.1 Case 1 (100%-0% for Oxygen distribution)

Case 1 is the two-stage oxygen-blown operation with the oxygen distribution being 100%-0% between the top and the second stages. Gas temperature and species mole fraction distribution on the horizontal and selected center vertical planes in the gasifier are shown in Figure 7.6. Since all the fuel is injected from the top, the gas temperature is higher in the top injection region than at the second stage location. Maximum gas temperature in the top injection stage reaches 2300K. The dominant reaction in the top injection stage is the intense char combustion ($C + ½ O_2 \rightarrow CO$ and $CO + ½ O_2 \rightarrow CO_2$) in the first stage and gasification reactions (mainly $C + ½ CO_2 \rightarrow CO$, $C + H_2O \rightarrow CO + H_2$) in the second stage. Due to the exothermic property of combustion process and endothermic property of gasification reactions, the temperature drops gradually from top injection to the exit of the gasifier. Oxygen is completely depleted through the char combustion in the top injection region.

Table 7.6 shows the temperature and syngas composition at exit for both CFD results and the experimental data of Case 1. Table 7.6a includes the steam, and Table 7.6b doesn't include the steam. When steam is included, Table 6a shows the CFD result deviates significantly from the experimental data. However, the CFD predicted steam's mass fraction (36%) is on par with the result obtained from the material balance Method 1 (Table 7.4). The steam composition is always presented as mass fraction in order to be directly compared with the experimental steam data, which is always given as the mass fraction.

To make the comparison easier by removing the uncertain measurement of steam, the data of syngas volume fractions at the exit in Table 7.6b have been normalized without including the steam as $CO+CO_2+H_2+CH_4=1$. From Table 7.6b, it can be clearly observed that the syngas composition predicated by the CFD results still deviates appreciably from the experimental data. The mass-weighted exit temperature is about 60K higher than the measured data. This higher CFD predicted exit temperature could be attributed to the assumption that the wall is adiabatic.

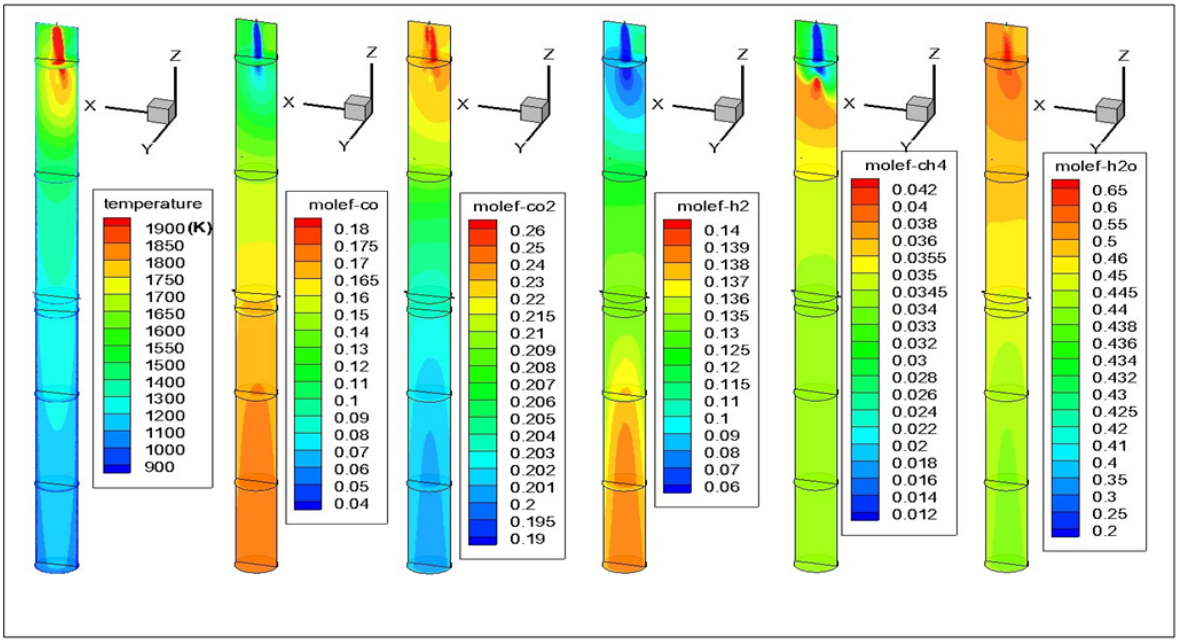

Figure 7.6 Gas temperature and species mole fraction distributions for Case 1 (100%-0% for oxygen distribution)

Table 7.6a Comparison of the CFD results with the experimental data at exit for Case1 (oxygen distribution: 100%-0%).

(Note: The syngas species in the experimental data is based on dry syngas. Some of the minor gases are not listed in the experimental data; hence the summation of the gas volume fractions is not 100%. The amount of experimental steam is separately listed as a mass fraction of the wet syngas. The CFD syngas composition is listed as volume fraction based on wet syngas except that the steam is listed as a mass fraction for an easy comparison with the experimental steam data.)

Case 1	Exp. data	CFD results
CO (Vol)	36.3%	17%
CO_2 (Vol)	22%	20%
H_2 (Vol)	28.7%	14%
CH_4 (Vol)	1.2%	3%
H_2O (Weight)	5%-10%	36%
Temperature (K)	954	1044

Table 7.6b Comparison of the CFD results with the experimental data at exit for Case 1. The syngas composition is normalized without water ($CO+CO_2+H_2+CH_4=1$)

Normalized composition	Exp. data	CFD results
CO (Vol)	41%	31%
CO_2 (Vol)	25%	37%
H_2 (Vol)	33%	26%
CH_4 (Vol)	1%	6%
Temperature (K)	954	1044

7.1.4.2.2 Case 6 (60%-40% for Oxygen distribution)

Case 6 is the two-stage oxygen-blown operation with oxygen distribution of 60%-40% between the first and the second stages. Gas temperature and species mole fraction distributions on the horizontal and center vertical planes in the gasifier are shown in Figure 7.7. The gas temperature is higher at the second stage injection region than at the top injection region. Maximum gas temperature reaches 2600K at the second stage injection location and 1900K at the top injection stage. The dominant reaction near the top injection location is the intense char combustion ($C + ½ O_2 \rightarrow CO$ and $CO + ½ O_2 \rightarrow CO_2$); then the endothermic gasification reactions occur in the region between the first and second stage injection locations as can be seen by increased CO and H_2 but reduced temperature. WGS also occurs, evident by reduced H_2O. At the second stage injection location, unburned char, CO and H_2 quickly react with injected Oxygen from two sides and release the second wave of combustion/oxidation heat ($C + ½ O_2 \rightarrow CO$, $CO + ½ O_2 \rightarrow CO_2$ and $H_2 + ½ O_2 \rightarrow H_2O$). The gasification reactions dominate the process after the oxygen is completely consumed in the region between the second stage injection location and the gasifier's exit.

Figures 7.8 and 7.9 show cross-sectional and mid-plane plots of the velocity vector, contours of temperature and mole fraction of CO_2 at the second injection stage for both case 6 (60%-40% for oxygen distribution) and case 3 (90%-10% for oxygen distribution) respectively. In case 6, 40% oxygen, which is injected from two opposing injectors at the second stage, squeezes the main flow laterally to both sides perpendicular to the injection direction (top and

bottom of Fig.7.8 (a) and (b)). The contours of temperature and mole fraction of CO_2 show that the chemical reactions are affected by the local flow behavior, which is demonstrated by the high temperature and CO2 concentration presented towards top and bottom in Fig. 7.8 (a) and (b). In case 3, only 10% oxygen is injected at the second stage. The opposing injecting effect is not strong enough to block the main flow, so the combustion reaction only takes place below the second stage, which is shown by the contours of temperature and mole fraction of CO_2 in Fig. 7.9.

Table 7.7 shows the temperature and syngas composition at exit for both CFD results, and the experimental data of Case 6. Table 7.7a includes the steam and Table 7b doesn't include the steam. When steam is included, Table 7a shows that the CFD results deviate significantly from the experiment data. However, the CFD predicted that the steam's mass fraction (36%) is on par with the result obtained from the material balance Method 1 (Table 7.4). To make comparison easier, the data of syngas volume fractions at exit have been normalized by $CO+CO_2+H_2+CH_4=1$, as shown in Table 7.7b. Similar to the conclusion of previous section, the syngas composition predicated by the CFD results still deviates appreciably from the experimental data, especially for the mass fraction of steam content and temperature at exit of the gasifier.

The calculated temperature is shown in Table 7.7 by two values. The first value (1550K) is the mass flow weighted average temperature over the cross-section on the exit plane, and the second value (1172K) is the mass flow weighted average temperature in the near-wall region (5mm to the wall). The near-wall temperature is more comparable to the experimental data (1150K) because the thermocouples were placed in cavities recessing in the wall, and the measured data reflects the hot gases temperature near the wall. Figure 7.10 shows the temperature contour on the cross-section of the exit plane. It clearly shows that the temperature changes significantly from the center at around 2000K to around 1150K in the near-wall region.

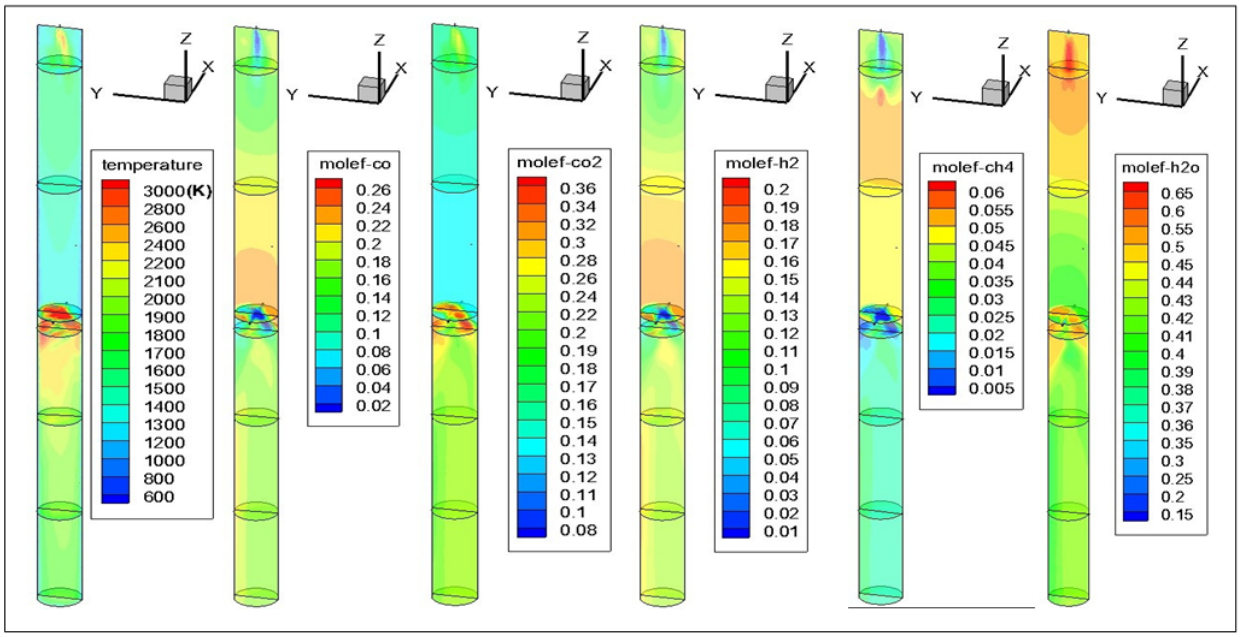

Figure 7.7 Gas temperature and species mole fraction distributions for Case 6 (60%-40% for oxygen distribution)

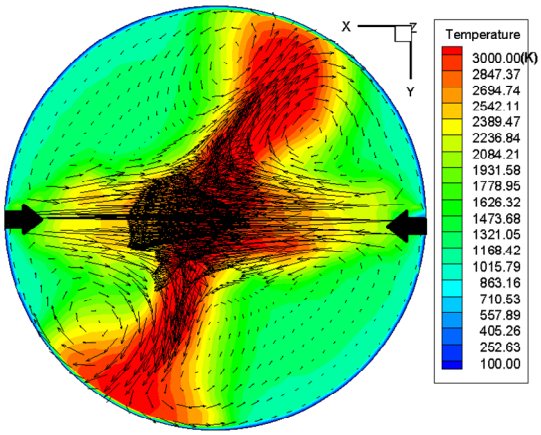

a) Cross-sectional temperature contour and velocity vector at the second injection

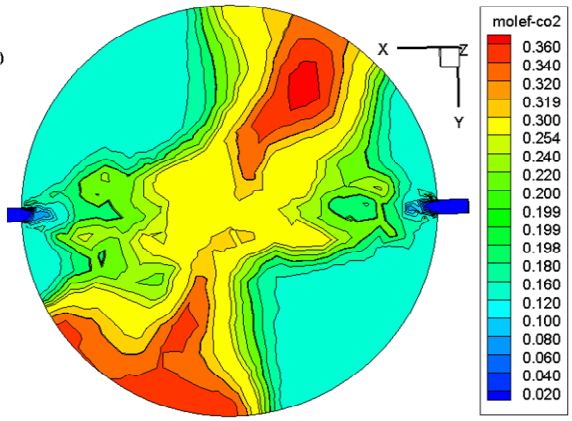

b) Cross-sectional mole fraction of CO_2 at the second injection

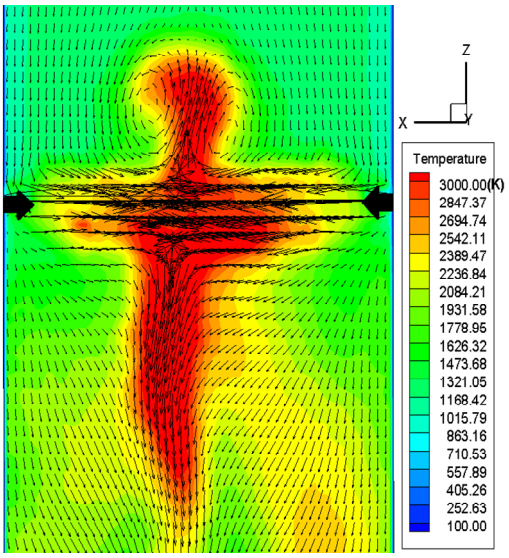

c) Mid-plane temperature contour and velocity vector near second injection

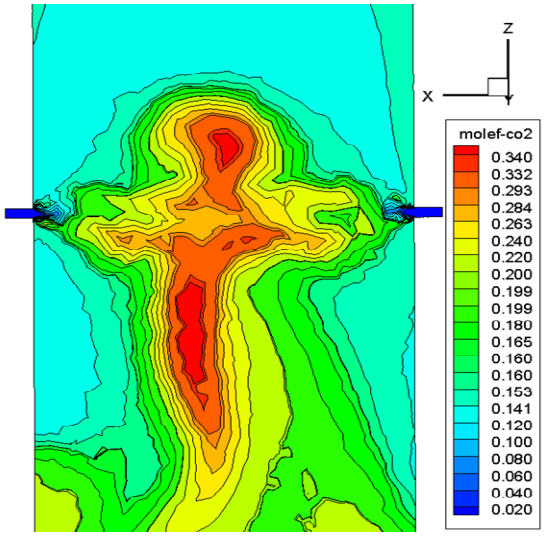

d) Mid-plane mole fraction of CO_2 near second injection

Figure 7.8 Cross-sectional and mid-plane plots of velocity vector, contours of temperature and mole fraction of CO_2 for Case 6 (60%-40% for oxygen distribution)

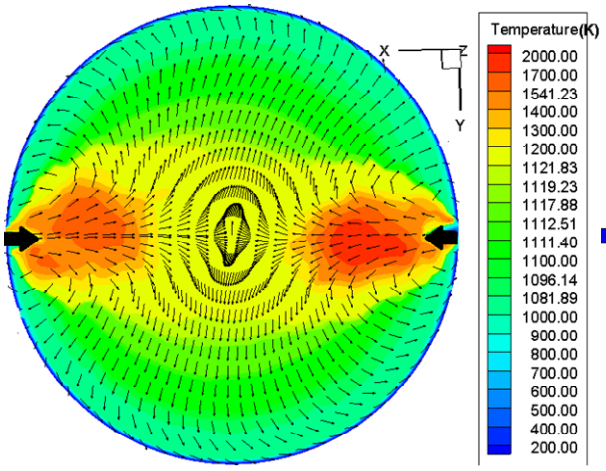

a) Cross-sectional temperature contour and velocity vector at second injection

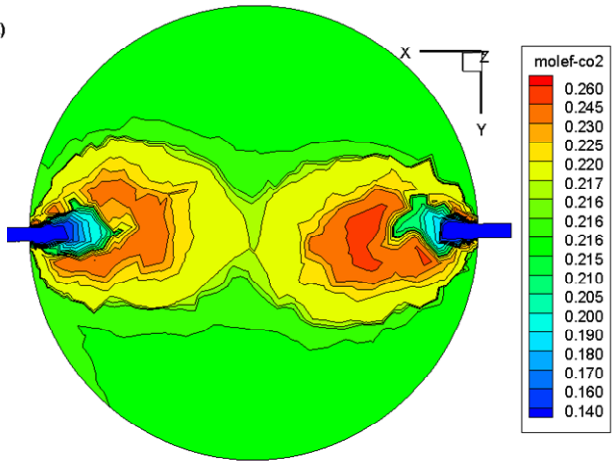

b) Cross-sectional mole fraction of CO_2 at the second injection

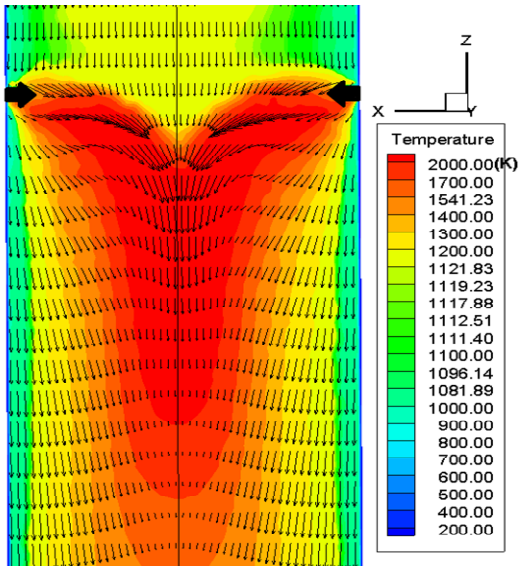

a) Mid-plane temperature contour and velocity vector at the second injection

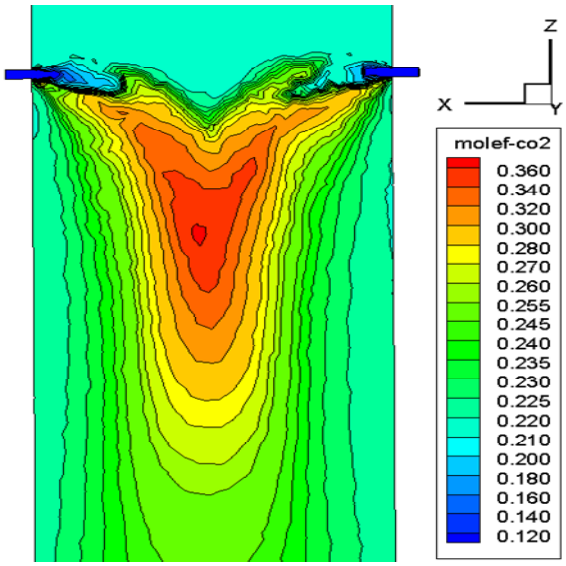

b) Mole fraction of CO_2 at the second injection

Figure 7.9 Cross-sectional and mid-plane plots of velocity vector, contours of temperature and mole fraction of CO_2 at second injection for Case 3 (90%-10% for oxygen distribution)

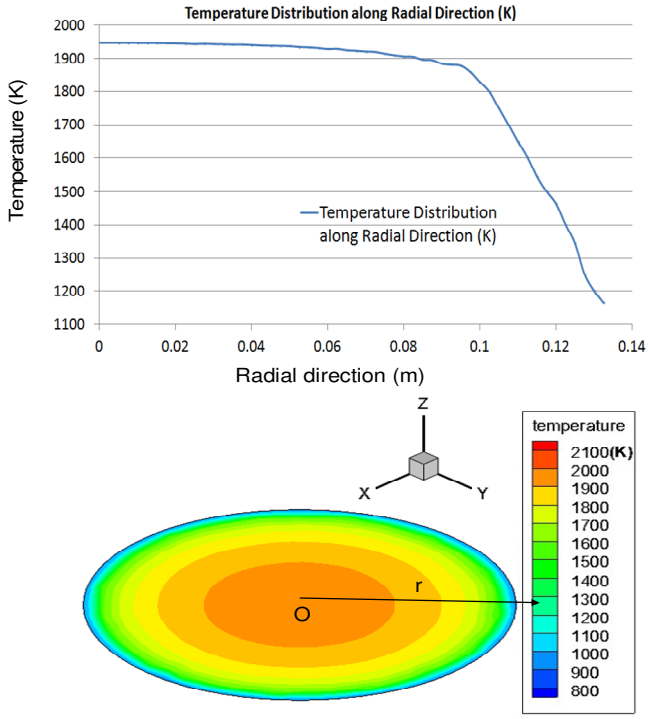

Figure 7.10 Gas temperature distribution at exit cross-sectional plane of the gasifier for Case 6 (60% - 40% for oxygen distribution)

Table 7.7 Comparison between the CFD result and the experimental data at exit for Case 6 (60%-40% for oxygen distribution). (a) All the syngas species are listed as the volume fraction except steam, which is separately listed as mass fractions. The experimental data has been normalized without steam, while the CFD volume compositions include the steam. (b) The syngas composition is normalized without water ($CO+CO_2+H_2+CH_4=1$).

Case 6	Exp. data	CFD results
CO (Vol)	41%	18%
CO_2 (Vol)	29%	22%
H_2 (Vol)	30%	14%
CH_4 (Vol)	0%	2%
H_2O (Weight)	5%-10%	36%
Temperature (K)	1150	1550 (cross-section average) 1172 (near-wall average)

(a)

Case 6	Exp. Data	CFD results
CO (Vol)	41%	31%
CO_2 (Vol)	29%	39%
H_2 (Vol)	30%	24%
CH_4 (Vol)	0%	6%
Temperature (K)	1150	1550 (cross-section average) 1172 (near-wall average)

(b)

7.1.4.2.3 Effect of Oxygen injection distribution under the experimental condition (Operating pressure: 2.5 bars, O_2: 0.6 of stoichiometric amount)

To investigate the effect of different oxygen-distribution feeding schemes on the gasification performance under the low operating pressure condition, seven computational simulations cases corresponding to the experimental conditions (operating pressure: 2.5 bars, O_2: 0.6 of stoichiometric amount for complete combustion) are conducted with the oxygen fed from top at 100%, 90%, 80%, 70%, 60%, 50%, and 40% respectively. These cases are numbered from Case 2 to Case 8 as shown in Table 7.3. The CFD results of these 7 cases are compared with the experimental data in Table 7.8, including the syngas composition at exit, the syngas temperature at four locations (T_{exit} = TE-300-4, T2 =TE-300-8, T3=TE-300-12, T4 = TE-300-13), carbon conversion rate (CCR), and the higher heating value (HHV). The comparisons are shown graphically in Figs. 7.11 and 7.12.

Table 7.8 CFD results of syngas compositions, syngas temperatures at different locations, carbon conversion rate, and HHV for Cases 2 to 8

O_2 distribution	Case 2 100%-0%	Case 3 90%-10%	Case 4 80%-20%	Case 5 70%-30%	Case 6 60%-40%	Case 7 50%-50%	Case 8 40%-60%
CO_2 (Vol)	0.256	0.252	0.245	0.233	0.222	0.238	0.240
CO (Vol)	0.113	0.117	0.140	0.160	0.170	0.154	0.125
H_2O (Vol)	0.520	0.516	0.475	0.455	0.430	0.460	0.515
H_2 (Vol)	0.082	0.090	0.115	0.130	0.158	0.130	0.107
CH_4 (Vol)	0.029	0.025	0.025	0.022	0.020	0.018	0.013
T4(K)	1892	1689	1627	1530	1450	1325	1174
T3(K)	1439	1301	1228	1186	1164	1154	1071
T2(K)	1237	1329	1590	1769	1934	2267	2484
T_{exit} (K)	1052	1101	1242	1314	1577	1647	1859
CCR	72.90%	74.62%	85.86%	93.02	98.88%	99.22%	99.94%
HHV(kJ/kmol)	76,551	79,810	91,795	100,929	**110,746**	99,434	86,890

Figures 7.11and 7.12 show that both the experimental data and the CFD results yield the same trend of change for temperature and syngas composition at the exit as the oxygen feeding distribution changes between two stages. When the percentage of oxygen injected from top reduces from 100% to 40%, the temperature decreases at the first stage (T4 and T3) and increases at the second stage (T2 and T_{exit}). This is because if less oxygen is injected from the top then less char will go through the exothermic combustion process and less combustion heat is released. At the first glance, the variation trends appear to reverse around 60%-50%. Therefore, the analysis and explanations are separated into two parts based on the oxygen distribution on the top: 100%-60% vs. 60%-40%.

100%-60% top O_2 injection – Mole fractions of CO and H_2 at the exit increase when the top injected oxygen reduces from 100% to 60% for CFD results (100% to 50% for experimental data), but they reduce when the top injected oxygen decreases from 60% to 40% for CFD results (50% to 40% for the experimental data). The mole fraction of CO_2 has the opposite changing trend.

60%-40% top O_2 injection – If the mass fraction of top injected oxygen continues to reduce below 60%, there is more unburned char going though the gasification process (mainly $C + ½ CO_2 \rightarrow CO$, $C + H_2O \rightarrow CO + H_2$), resulting in more production of CO and H_2 at the first stage. At the second injection stage, some of the injected oxygen reacts with CH_4 to produce CO and H_2. Therefore, the total amount of CO and H_2 increases, and CO_2 decreases at the exit of

gasifier. However, if more than 40%-50% of the total oxygen is injected from the second injection location, more CO and H_2, which were produced through the gasification process at the first stage, react with the oxygen through the combustion process at the second stage and result in more CO_2 and H_2O. Therefore, as indicated in Figs. 7.11 and 7.12, CO and H_2 decrease and CO_2 and H_2O increase at the exit of the gasifier when the portion of oxygen injected from the top is reduced from 60% to 40% based on the CFD results (or 50% to 40% based on experimental data).

Meanwhile, the carbon conversion rate increases, and the exit mole fraction of CH_4 reduces when the percentage of oxygen injected from the top reduces from 100% to 40%. The reason for this trend is that the unburned char and CH_4 react with oxygen through $C + ½\ O_2 \rightarrow CO$ and $CH_4 + ½\ O_2 \rightarrow CO + 2H_2$ at the second injection stage. When oxygen injected from the second stage increases beyond 40%, the carbon conversion rate reaches 99%.

One of the advantages of employing the two-stage oxygen control is to reduce the wall temperature gradient, and hence, reduction of thermal stress along the gasifier. The experimental results in Fig. 7.11a show that the overall near-wall temperature difference in the gasifier is reduced to a narrower range of 900 – 1200°C with a 60%-40% two-stage oxygen injection split from a wider range of 600-1500°C with 100% top injection. In contrast, the CFD result in Fig. 7.11b shows that the case of 80%-20% yields the most uniform syngas temperature ranging from 955°C to 1354°C, and the case of 60%-40% in Table 7.8 yields the highest syngas HHV (110,746 kJ/kmol). The near-wall temperature prediction in Fig. 7.11c shows lower values than those in Fig. 7.11b. The case of 80%-20% yields the lowest peak temperature and most uniform syngas temperature ranging from 850°C to 1100°C.

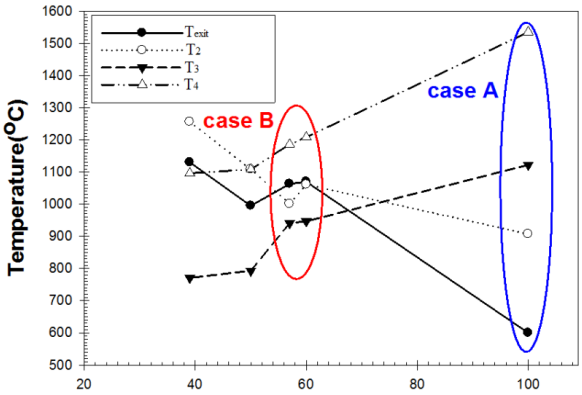

(a)

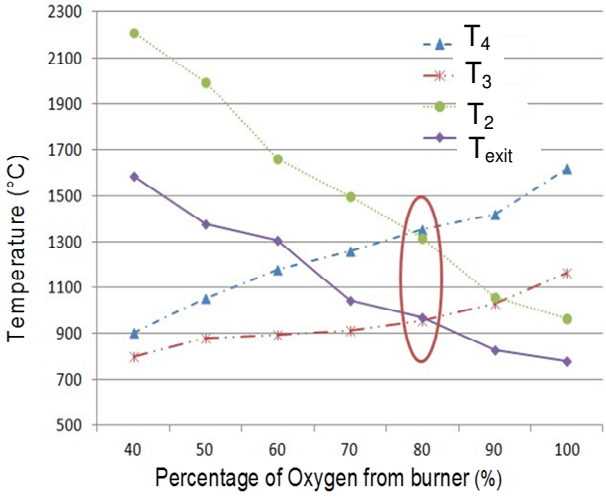

(b)

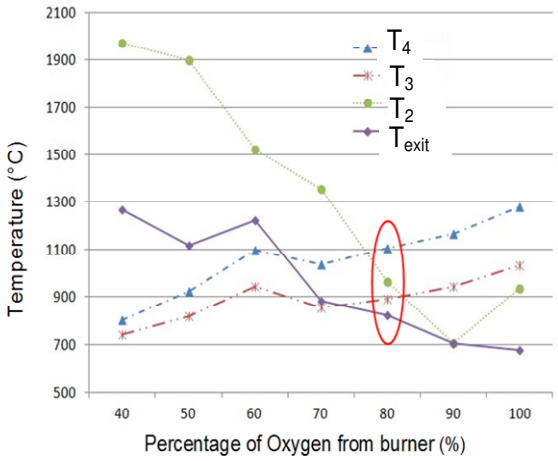

(c)

Figure 7.11 The effect of two-stage oxygen injection distribution on the gasifier wall temperature (a) experimental data (in wall cavities) (b) CFD results of mass-weighted syngas temperaturee for Cases 2 to 8 (c) CFD results for near-wall temperature (5mm to the wall) (Note: T_{exit} , T_2, T_3, and T_4 in this figure correspond to TE-300-4, 8, 12, and 13 in Fig. 7.2.)

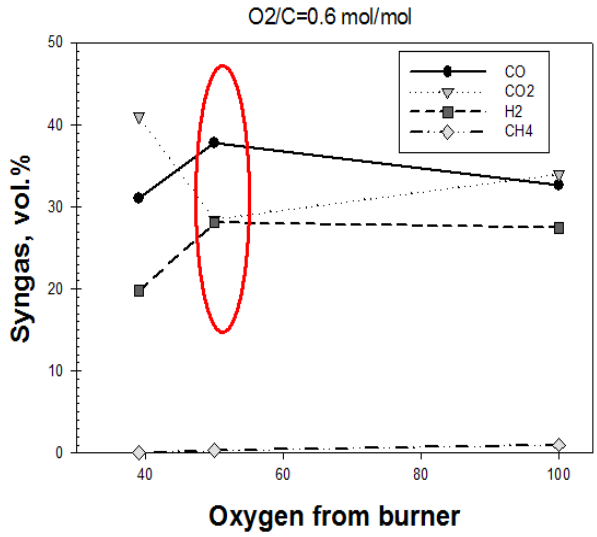

(a) Experimental data

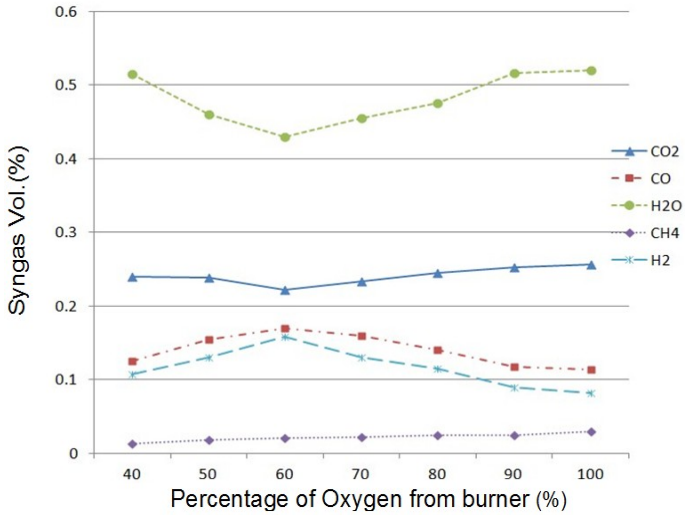

(b) CFD results

Figure 7.12 The effect of two-stage oxygen injection distribution on the syngas compostion for (a) experimental data and (b) CFD results (Cases 2 to 8)

7.1.4.2.4 Effect of Oxygen Injection Distribution under High Operating Pressure Condition (operating pressure: 25 bars, O_2: 0.4 of stoichiometric amount)

Since most of the gasifiers are operated under the condition with high pressures above 25 bars and low sub-stochiometric oxygen feeding below 40%, the rest of the analysis will be focused on presenting the CFD simulation at a high pressure (25 bars) and low oxygen ratio

(0.4 of the stoichiometric amount for complete combustion). In total, four cases (Cases 9 to 12 as listed in Table 7.3) have been conducted.

Similar to the discussion in previous section, the syngas composition and temperature at different locations, CCR and HHV for Cases 9- 12 are provided in Table 7.9 and Figs. 7.13. The results are summarized below.

1) Compared to the results of the low operating pressure cases, the carbon conversion rates for different oxygen injection distribution are all above 95% in high operating pressure cases. The longer particle residence time is the major reason for achieving a higher carbon conversion rate. The average residence time is about 6-7 seconds for the high pressure cases while it is 3-4 seconds for the low-pressure cases.

2) Both the high operating pressure and low pressure cases yield the same trend of change for exit average temperature as the oxygen feeding distribution changes between two stages.

3) Consistent with the low pressure cases, the changing trend of syngas composition reverses the direction at the 60%-40% case, and the 80%-20% case produces the lowest peak temperature and most uniform temperature in the gasifer.

4) As more oxygen is injected at the second stage, CO and CO_2 have the same trend of change as in the low pressure condition; however, H_2O and H_2 changes in the opposite direction.

5) The major differences between the high and the low pressure cases are: (a) the average temperature is much lower at each corresponding location in the 25 bars condition; (b) H_2 dominates the syngas composition (about 70% vol.) at 25 bars case. This phenomenon is caused by less oxygen injection and longer coal particle residence time. More coal particles have enough time to go through the gasification process, and the endothermic gasification reactions result in lower syngas temperature.

6) The 40%-60% case produces the syngas with the highest HHV in the 25 bar case vs. 60%-40% case in the 2.5 bars cases.

Table 7.9 CFD predicted syngas conditions at 25 bars for Cases 9 to 12

O_2 distribution	Case 9 100%-0%	Case 10 80%-20%	Case 11 60%-40%	Case 12 40%-60%
CO_2 Vol(Mass)	0.056(0.285)	0.057(0.275)	0.059(0.263)	0.053(0.268)
CO Vol(Mass)	0.103(0.328)	0.115(0.343)	0.131(0.359)	0.105(0.332)
H_2O Vol(Mass)	0.087(0.133)	0.078(0.126)	0.097(0.155)	0.078(0.140)
H_2 Vol(Mass)	0.714(0.176)	0.712(0.180)	0.674(0.153)	0.726(0.182)
CH_4 Vol(Mass)	0.037(0.072)	0.037(0.069)	0.036(0.063)	0.035(0.068)
T4(K)	1395	1162	1067	1014
T3(K)	1383	1247	1169	1116
T2(K)	1129	1220	1472	1506
T_{exit} (K)	838	915	986	1033
CCR	99.99%	95.34%	98.88%	99.97%
HHV(kJ/kmol)	236,767	239,225	233,663	240,397

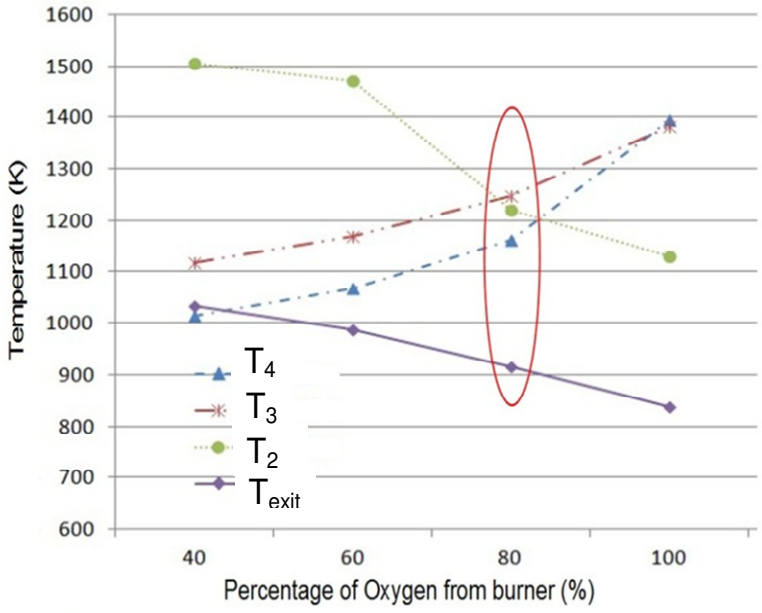

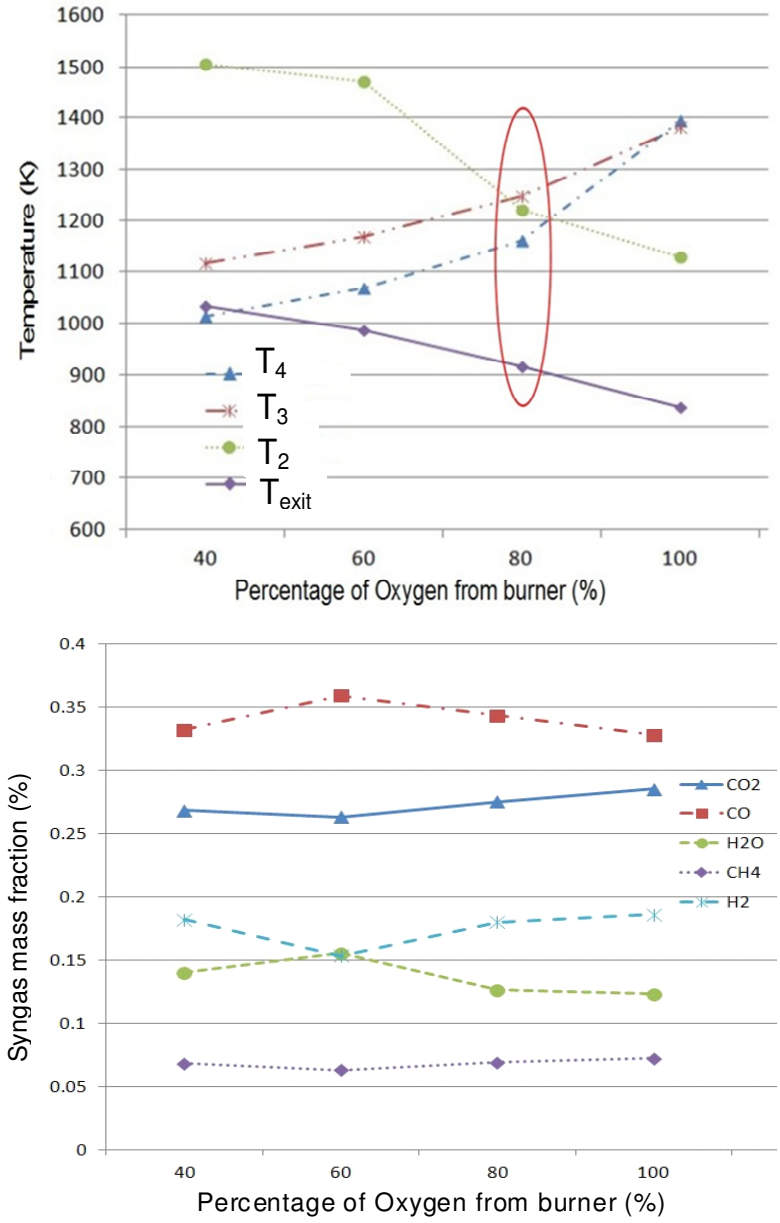

Figure 7.13 The effect of two-stage oxygen injection distribution on the syngas temperature and syngas composition (Mass fraction) for Cases 9 to 12 (Note: The temperature locations T1, 2,3,4 in this figure correspond to TE-300-4, 8, 12, and 13 in Fig. 7.2.)

7.1.5 Conclusion of Two-Stage Oxygen Injection

1. In the top-injection base case, the CFD predicts that the exit temperature is satisfactorily within 90°C (or 9%) from the experimental data. However, the CFD predicts relatively lower H_2 and CO composition but higher CO_2 at the exit.

2. The experiments at 2.5 bars show the 60%-40% oxygen distribution yields the most uniform wall temperature along the gaisifer.
3. In cases of split two-stage oxygen injections from 100% to 40% with 0.6 stoichiometric oxygen at 2.5 bars, the CFD predicts (a) the similar trend of changing temperature and syngas compositions in the experimental data, but lower H_2 and CO mole fractions than the experimental data, (b) the 80-20% case yields the lowest peak temperature and the most uniform gas temperature distribution along the gasifier, and (c) the 60%-40 case produces the syngas with the highest HHV.
4. The CFD's prediction of the effect of oxygen distribution under 25 bars operating pressure case shows that (a) the carbon conversion rates for different oxygen injection schemes are all above 95%, (b) H_2 (about 70% vol.) dominates the syngas composition at exit, (c) same as in the 2.5 bar cases, the 80-20% case yields the lowest peak temperature and most uniform gas temperature distribution along the gasifier, and (d) the 40-60% case produces the syngas with the highest HHV.
5. Chemical reactions are affected by the local flow behavior. Strong opposing injection of oxygen at second stage squeezes the main flow laterally to both sides perpendicular to the injection direction, making combustion spread towards both top and bottom of the second stage.
6. Two different material balance methods were conducted. The results show that the steam cannot be consumed down to only 5% - 10% (weight) of the syngas, and at the same time, also yields CO at a high level of 41% (vol) of the dry syngas under the experimental condition
7. Both experimental data and CFD predictions verify the hypothesis that it is feasible to reduce the peak temperature and achieve more uniform temperature in the gasifier by adequately controlling two-stage oxygen injection without changing the quality of the product syngas.

7.2 Investigation of a Syngas Quench Cooling Design

7.2.1 Introduction

The water quench section of the ITRI gasifier is shown in Figure 4.1 (b). The feedstock is mixed with water to form the coal slurry, and is injected with oxygen from top of the gasifier, while the syngas exits near bottom of the gasifier. The syngas is usually very hot (1400-1700K

or 2200-2600^{o}F for oxygen-blown gasification) and needs to be cooled for two purposes: (a) so that it may be transported without damaging downstream piping materials or other equipment and (b) to satisfy the lower-temperature requirement of the desulfurization and other cleaning processes.

The syngas cooling process would significantly reduce the thermal efficiency of the system if care is not taken to employ the energy cascading scheme to properly maintain the grade (or quality) of the energy during the heat transfer process by applying cooling at different temperature ranges with an optimum pinch point for each cooling stage in a sequentially descending order. Radiant syngas coolers have been usually employed to achieve the highest thermal efficiency. However, a radiant syngas cooler is large, bulky, and expensive, so the direct syngas quenching process has also been adopted for the benefits of reduced space, cost, and maintenance, although it is accompanied by reduced thermal efficiency. A rule of thumb is that a gasification system using a radiant syngas cooler will have approximately 2-3 percentage points higher thermal efficiency than a unit employing the quenching scheme. Recently, as carbon capture and sequestration (CCS) has become an important approach to curb global warming, the syngas quenching approach has become more popular in the gasification process because CCS typically employs the water-shift process (WGS) ($CO + H_2O \Leftrightarrow CO_2 + H_2$) to convert steam and CO to CO_2 and H_2, and, in this process, relatively low-temperature steam (below 600^{o}C, see Table 4.1) is required to allow the reaction to move in forward direction towards products. Since a large amount of relatively low-temperature steam is required, it might as well just directly employ quench cooling. This will allow preliminary water-shifting to occur and also utilize the quench chamber to serve as the first-stage shift reactor, thus removing the cost of installing an actual first-stage shift reactor. In addition to providing cooling and driving the WGS reaction, a water quench can also help clean out ash and other particulate matter. These additional benefits unfortunately are accompanied with another disadvantage: the unburned chars can also be washed away, causing a downgrade in the carbon conversion efficiency.

Since there are many different means to design a quench chamber, conducting experiments to investigate many different options are a time consuming and expensive process. To help narrow down the number of experimental variables and to guide design development, the objective of this project is to employ Computational Fluid Dynamics (CFD) to investigate

the syngas quench performance of a preliminary quench section design in a downdraft entrained-flow gasifier. The schematic of the preliminary design of the quench section is presented in Fig. 4.1 (b). The syngas flow enters the main chamber in the center of the quench section, impinges on the water bath surface, and deflects radially outward through eight openings to an annular outflow peripheral section that surrounds the main central chamber and is separated from the main chamber by a wall. The flow then moves upward and leaves the quench section through two outlets. The temperature and pressure of the incoming flow are 954 K and 3 atm, respectively. There are two injection locations: the primary one is located near the entrance of the quench section in the main flow chamber and another set of eight injectors serve as the secondary sprays. The primary injection provides the main water spray cooling with two pairs of opposing jets, separated 90o apart. The secondary sprays are located in the annular duct and spray water downward against the up-flowing gas. This set of secondary injectors is used to aid in fine-tuning the temperature and syngas composition.

The water bath level can be adjusted higher or lower to allow the raw syngas to penetrate into the water bath at different depths to further reduce the syngas temperature, augment the WGS reaction, and remove soot and dust.

The main goal of this study is to use the experimental results to calibrate the CFD model, especially the WGS reaction model. Then, use the calibrated model to help design different water spray strategies to achieve the targeted temperature and syngas composition.

7.2.2 Computational Model

The computational models, computational domain, as well as the boundary and inlet conditions of ITRI water quench simulation are clearly stated in Chapter 4, section 4.4 – 4.5, so they are not repeated here.

7.2.3 Results and Discussions

In this paper, investigation of syngas as the inlet flow is carried out with a syngas mass flow rate of 0.04 kg/s, a temperature of 954 K, and a pressure of 3 atm. The syngas compositions and inlet conditions are taken from the ITRI experimental data and shown in Table 4.8.

7.2.3.1 Calibration of WGS Rates

The calibration of WGS rates with experimental data of ITRI water quench experiment is detailed stated in Chapter 4, section 4.6, so it is not repeated here.

7.2.3.2 Effect of the Primary vs. the Secondary Injection

After calibration of the WGS rate is accomplished, the CFD model becomes a useful tool to help investigate parametric study interests. The first interest falls in examining the WGS performance of injecting water at the primary and secondary location, respectively. In these simulations, two cases are conducted: one with the total water injection of 0.0052 kg/s at the primary injection location alone and the second case with the same amount of water injection at the secondary injection alone. The simulation calculations are performed until the mass fractions of the various species are stabilized. The velocity contour and velocity vector plots of syngas at two different mid-planes placed perpendicular to each other are shown in Fig. 7.14.

It is clear seen from Fig. 7.14a that the syngas flow is been obstructed by the primary water injection in the main chamber when the primary injection is used. Figure 7.14b shows the change in flow field when the water spraying is switched from the primary to the secondary injection location. Selected syngas flow pathlines for the primary and secondary injection cases are shown in Fig. 7.15. From the flow pattern shown in both Figs. 7.14 and 7.15, the flow field is seen to be highly 3-D, consisting of complex vortices.

The CO_2, H_2, and temperature distributions for the primary water injection and secondary water injection cases are shown in Fig. 7.16. The syngas composition and temperature at outlet for both cases are listed in Table 7.10. The CO conversion (%) is approximately 16% in both cases. The primary injector seems slightly better in producing a higher H_2 concentration and HHV than the secondary injection. This slightly better WGS reaction is also reflected by the higher exit temperature for the primary injection case (875 K versus 844K) due to the exothermic behavior of the forward WGS reaction. Figure 7.16 shows the side-by-side comparison of temperature and multiple species distributions between these two cases.

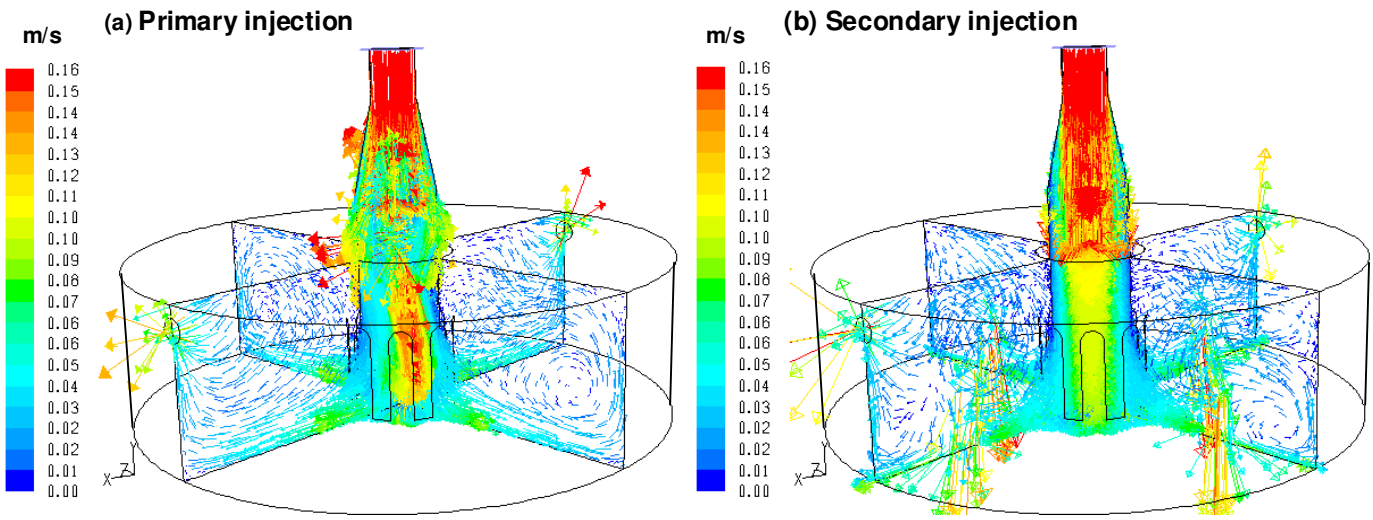

Fig. 7.14 Velocity vector fields on two selected planes for primary and secondary injection cases, respectively

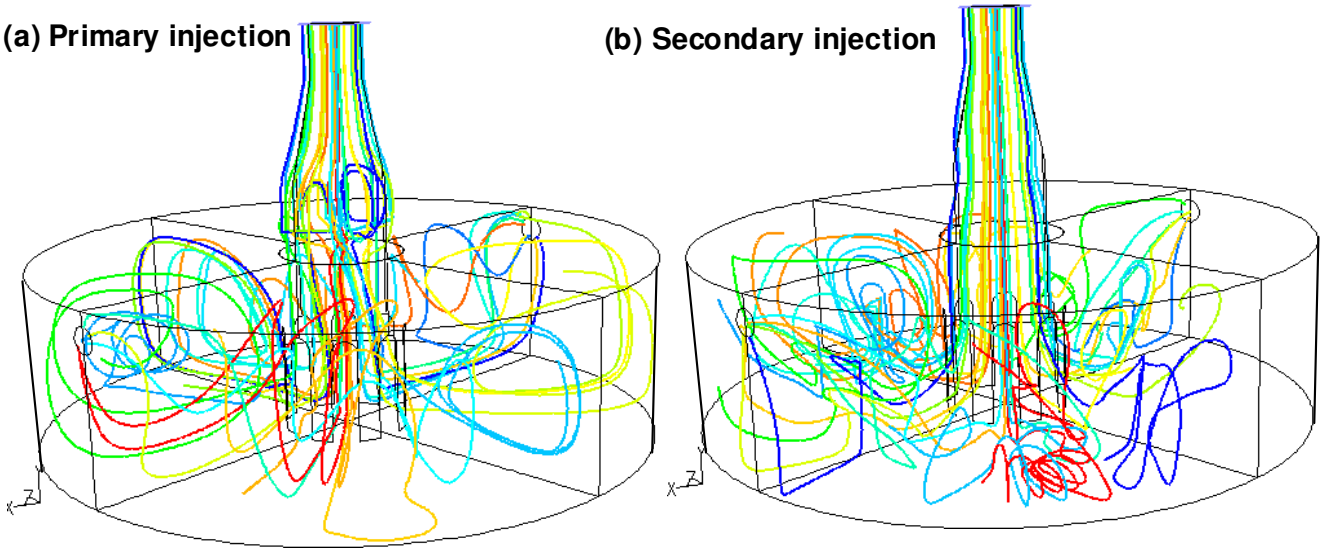

Fig. 7.15 Syngas pathline for primary and secondary injection cases

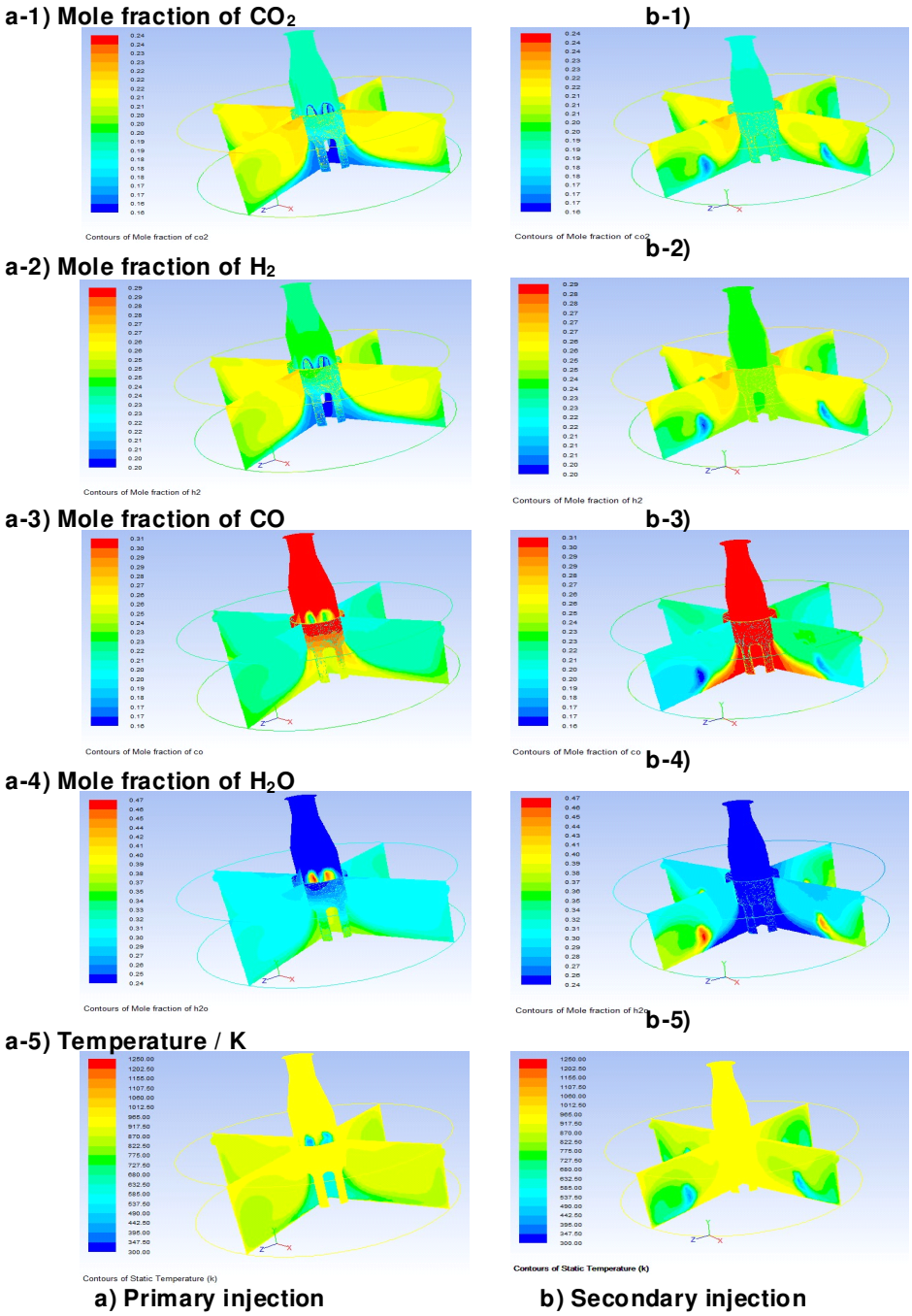

Fig. 7.16 Distributions of temperature and various species on two selected planes for primary and secondary injection cases using reaction rate A= 0.2512, E = 1.325 x 10^5 J/mol

Table 7.10 Effect of water injection location on syngas composition using reaction rate A= 0.2512 E = 1.325 x 10^5 J/mol

Mole fraction	Inlet	Primary injection outlet	Secondary injection outlet
H_2	0.24	0.26	0.25
CO_2	0.19	0.21	0.21
CO	0.31	0.22	0.22
CH_4	0.01	0.01	0.01
H_2O	0.25	0.30	0.31
Temp (K)	954	875	844
HHV(Base on 298K)		149 MJ/kmol (6.92MJ/kg)	146 MJ/kmol (6.59MJ/kg)

7.2.3.3 Effect of Water Level Gap in the Bottom Tank

As mentioned in the Introduction, the water bath level can be adjusted higher or lower to allow the raw syngas to penetrate into the water bath at different depths to further reduce snygas temperature, augment the WGS process, and remove soot or dust. Simulation of a gas stream penetrating into a liquid bath requires the employment of multiphase modeling using the Eulerian-Eulerian method. Coupling a Langrangian-Eulerian method, which tracks each individual liquid particle, with an Eulerian-Eulerian method which uses the void fraction to represent the gas and liquid composition, is a great challenge and beyond the scope of this paper. Therefore, the simulation is simplified by treating the gas-liquid interface as a wall which can't be penetrated. Although the phenomenon of gas penetrating into the liquid bath is not simulated, the simplified simulation can capture the effect of the water level height by calculating the changing flow velocity as the opening gaps are widened or narrowed due to changing water bath levels. As the gas flow accelerates through narrower openings, it is hypothesized that the WGS reaction could be increased and the heat transfer between the syngas and the water bath could increase, too. If this is true, controlling the water level would become an easy and low-cost method to fine-tune the exit syngas composition without using additional water. This is the motivation for studying the effect of the water level and for hoping to find an optimum level gap via CFD simulation.

The simulation results discussed in the previous sections consider the water level of 873mm from the primary injection location (water level gap). In addition to the baseline case of 873 mm, two additional cases with two different water level gaps including 700 mm and 1,050 mm are considered. The products and temperature distributions for these three cases are shown in Fig. 7.17 and Table 7.11. The result is listed in Table 7.11 and it shows that when the gap decreases from 1050 to 700 mm, the H_2 production decreases instead increases as previously hypothesized. The CO conversion rate decreases 7 percentage points (or 35%) from 20% to 13%, and the syngas outlet temperature decreases from 891 K to 871 K, correctly reflecting the decreased heat released during the WGS reaction. The trend of changing water level gaps on the WGS process is plotted in Fig. 7.18. The CO conversion rate varies almost linearly with the gap width. It then becomes interesting to find out why the previous hypothesis is not correct. After a few explorations, it is discovered that as the gases move faster through the narrower gaps, the average residence time decreases 11%: correspondingly from 0.396s to 0.355s, which results in less time for the WGS reaction to take place. Although the result is opposite to the previous hypothesis, it indicates that the water bath level could be used to control H_2 production within 1 percentage point (or 4%) without resorting to using a water spray. However, it needs to be emphasized that this result needs to be verified by experiments because the complex phenomenon of a gas stream penetrating into the water bath.

Table 7.11 Effect of water level gap on WGS using reaction rate A= 0.2512 E = 1.325 x 10^5 J/mol

Mole fraction	Inlet	Gap (700mm)	Gap (873mm)	Gap (1050mm)
H_2	0.24	0.25	0.26	0.26
CO_2	0.19	0.20	0.21	0.22
CO	0.31	0.23	0.22	0.21
CH_4	0.01	0.01	0.01	0.01
H_2O	0.25	0.31	0.30	0.30
CO conversion (%)		13	16	20
Temperature (K)	954	871	875	891
Average residence time (s)		0.355	0.373	0.396
HHV in kJ/kmol (Base on 298K)		149,145	148,767	145,937

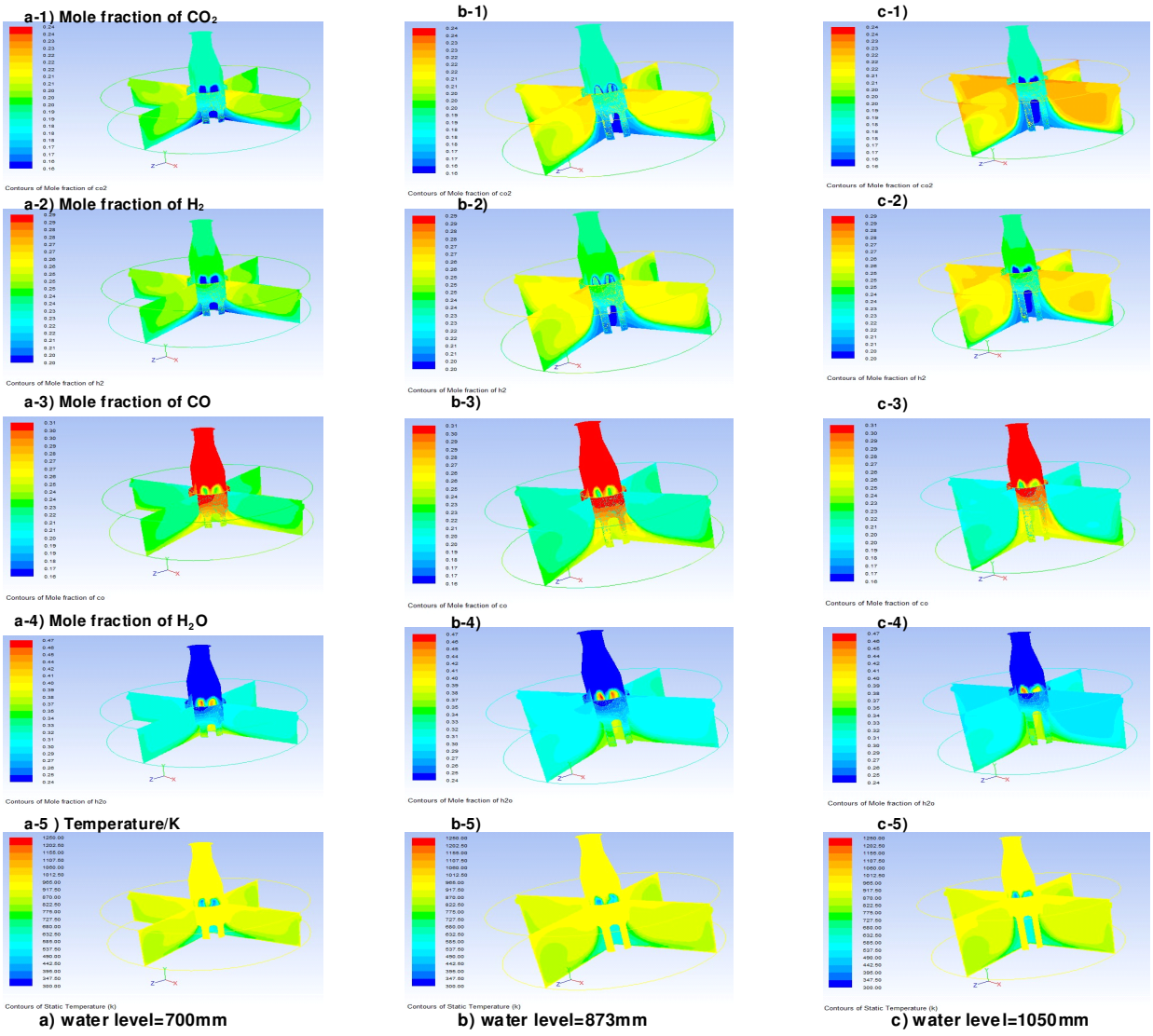

Fig. 7.17 Distribution of various species for three different water bath level gaps

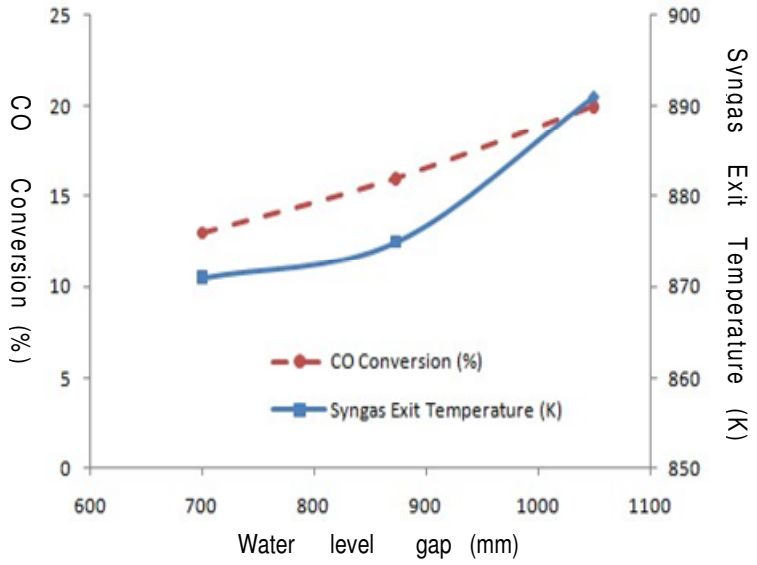

Fig. 7.18 Effect of water level gap on WGS and syngas temperature using reaction rate A= 0.2512 E = 1.325 x 10^5 J/mol

7.2.4. Conclusions of Water Quench Study

A CFD model has been developed to investigate the water quench section design of an oxygen-blown, slurry-fed, entrained flow coal gasifier. The calibrated Wade's WGS rate (A= 0.2512, E = 1.325 x 10^5 k/mol) is chosen for all of the parametric studies in this study. The conclusions of this study are stated as following:

1) The effect of injection locations (primary vs. secondary) on the WGS reaction is marginal. Both locations result in a 16% CO conversion rate. Spraying water in the primary location only provides a marginal advantage with an increase of 4% in H_2 production, 2% in HHV value, and 30K in temperature**.**

2) Using the water bath level to fine-tune the WGS is workable. When the water level gap decreases from 1050mm to 700 mm, the CO conversion rate decreases by 7 percentage points (or 35%) from 20% to 13%, and the syngas outlet temperature decreases by 20K (from 891 K to 871 K.) Beyond the gap of 1050mm, the effect of the water bath level is not noticeable.

CHAPTER EIGHT
TOPIC 5: STUDY OF COAL-TO-SYNTHETIC NATURAL GAS (SNG)

8.1 Introduction

Natural gas is one of the cleanest and most efficient to use of all energy sources, and it provides roughly 24% of the world's energy. The most recent Manufacturing Energy Consumption Survey (MECS) data published by the Energy Information Administration (EIA) of U. S. Department of Energy (DOE) indicates that the annual natural gas consumption by U. S. industries was about 6,468 trillion Btu for all purposes with about 90% of that (5,794 trillion Btu) consumed as fuel. The EIA 2013 report predicts that natural gas consumption would be about 70.0 billion cubic feet per day (Bcf/d) in 2013 and 69.6 Bcf/d by 2014. The projected year-to-year increases in natural gas prices will contribute to declines in natural gas used for electric power generation from 25.0 Bcf/d in 2012 to 22.5 Bcf/d in 2013 and 22.1 Bcf/d in 2014, although these forecast levels are still high by historical standards. The natural gas marketed production is projected to increase from 69.2 Bcf/d in 2012 to 70.0 Bcf/d in 2013 to 70.4 Bcf/d in 2014. Onshore production increases over the forecast period due to the increased production of shale gas, while federal Gulf of Mexico production declines. Natural gas pipeline gross imports, which have fallen over the past five years, are projected to remain near their 2012 level over the forecast. Liquified Natural Gas (LNG) imports are expected to remain at minimal levels of around 0.4 Bcf/d in both 2013 and 2014. Figure 8.1 shows the EIA's past and projected data of the U.S. natural gas consumption, production, and imports from 2011 to 2014.

Natural gas spot prices averaged $4.04 per MMBtu at the Henry Hub in May 2013, down 13 cents from the $4.17-per-MMBtu average seen in the previous month. The EIA expects the Henry Hub price will increase from an average of $2.75 per MMBtu in 2012 to $3.92 per MMBtu in 2013 and $4.10 per MMBtu in 2014. Current options and futures prices imply that market participants place the lower and upper bounds for the 95-percent confidence interval for September 2013 contracts at $3.03 per MMBtu and $5.21 per MMBtu, respectively. At this time a year ago, the natural gas futures contract for September 2012 averaged $2.48 per MMBtu and the corresponding lower and upper limits of the 95-percent confidence interval

were $1.51 per MMBtu and $4.07 per MMBtu. Figure 8.2 shows the EIA'a past and projected data of the U.S. natural gas price from 2009 to 2014.

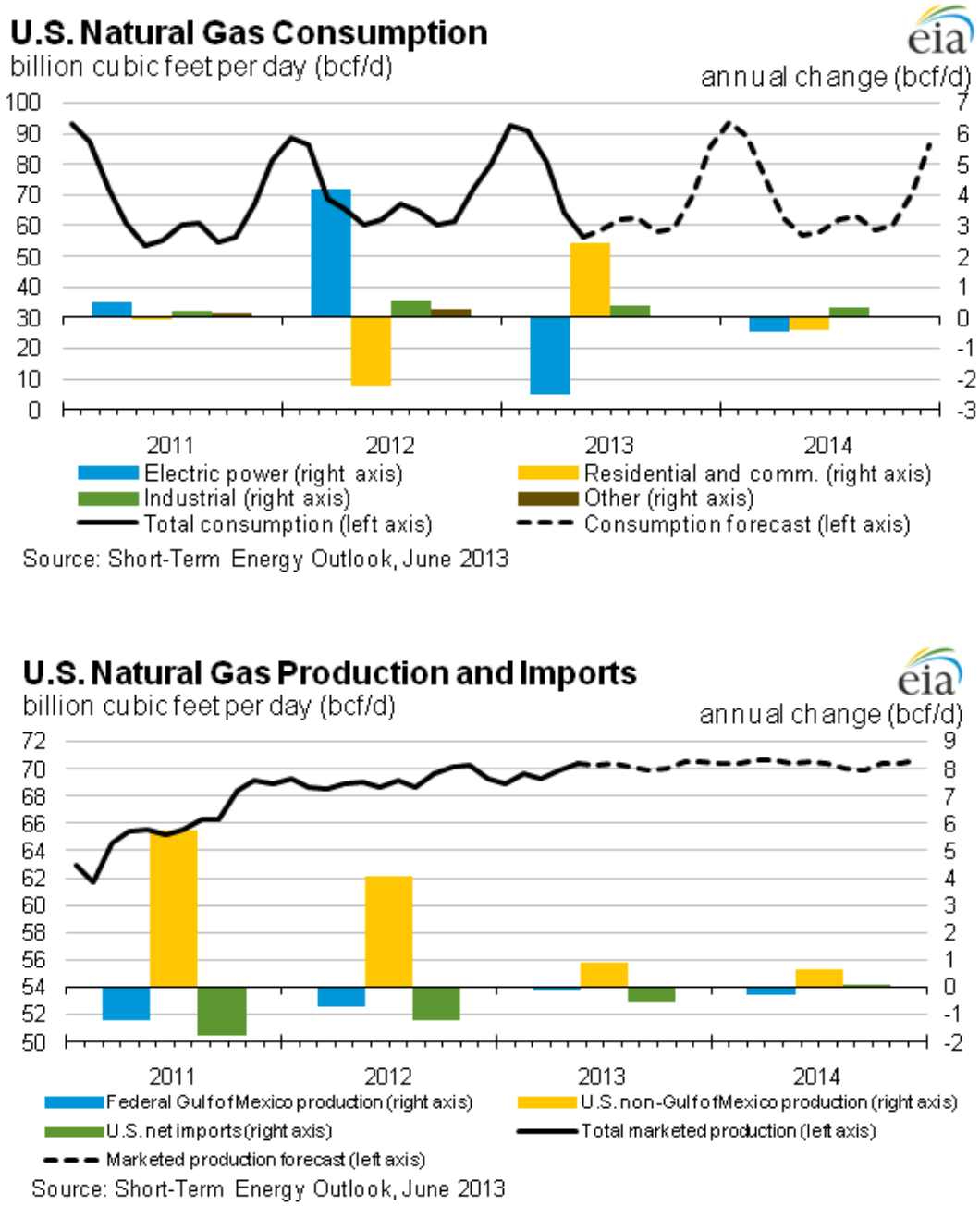

Figure 8.1 Past and projected U.S. natural gas consumption, production, and imports (Source: EIA short-term energy outlook, June 2013)

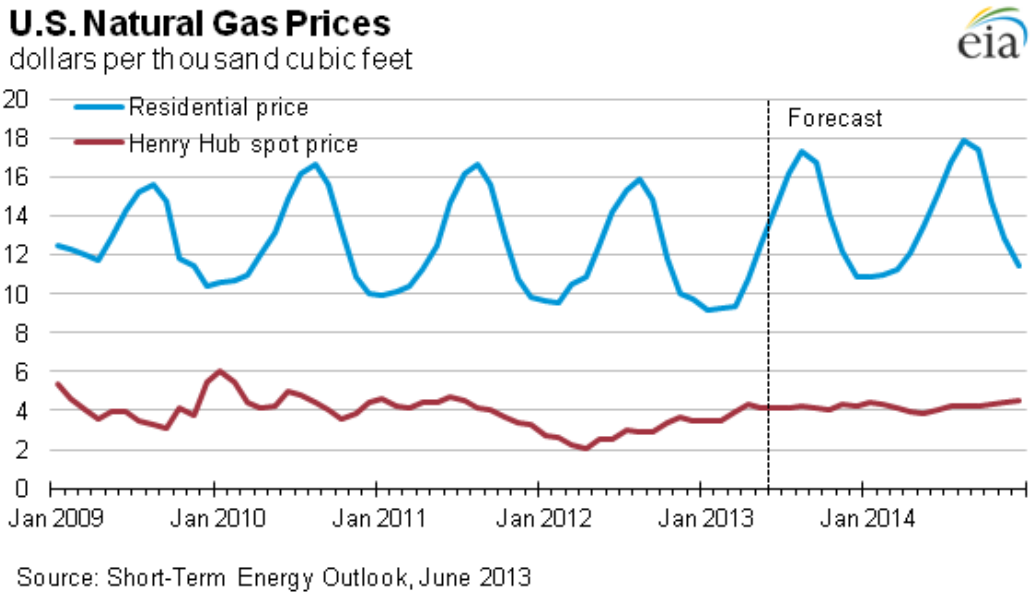

Figure 8.2 U.S. natural gas prices (Source: EIA short-term energy outlook, June 2013)

SNG can be produced from coal, petroleum coke, biomass, or solid waste. The carbon containing mass is gasified and then converted to methane, a large component of natural gas. From a national security standpoint, SNG techniques could reduce the reliance on imported energy resources by making the most out of an abundant American resource: coal. SNG could be liquefied and transported throughout the U.S. via existing pipeline infrastructure already in-place. Coal is much more evenly distributed throughout the world compared to oil and natural gas, and remains the world's most abundant fossil fuel, with an R/P ratio of more than 130 years, twice that of natural gas [BP report, 2008]. In countries with significant proven reserves of coal but a relative scarcity of natural gas, the Coal-to-SNG process is a promising technology that may provide clean synthetic natural gas for the growing demands of power generation and home utilization.

8.1.1 Market, Advantage and Challenge of SNG

SNG has a large potential market. Basically any application that currently uses natural gas could use SNG. In particular, gasification can be used on-site for industrial applications to produce SNG, allowing continued operation of natural gas equipment, but from a coal source. Other than producing electricity, industrial use of natural gas was about 28% of the total domestic consumption in United States [DOE/EIA, 2012]. A study from the National Energy

Technologies Laboratory (NETL) in 2007 researched on the feasibility of on-site gasifiers in industrial facilities for the production of SNG found that many industrial sites could benefit from the use of relatively small gasifier systems to either produce SNG or generate power, H_2, or syngas.

Several advantages are associated with producing SNG from coals. SNG can be produced through the gasification of coal or other carbonaceous fuel sources. Coal is abundant domestically, with current estimates predicting over two centuries worth of consumption at present rates. SNG is able to substitute for natural gas, a much scarcer and more volatile commodity than coal. In this way, gasification of coals to SNG helps increase fuel diversity, protecting against an over-reliance on a single energy source, and making utilization of coals much cleaner than the conventional coal burning scheme. Since SNG in use is identical to natural gas, SNG can be transported and distributed using existing natural gas infrastructure and utilized in existing natural gas–fired power plants or devices such as industrial burners, boilers, kilns, etc. Furthermore, natural gas is the fuel that powers most (but not quite all) U.S. chemical and refining processes, and natural gas methane is the feedstock for hydrogen production (for hydro-cracking, hydro-desulfurization, and ammonia) and syngas production (for methanol, and its derivatives e.g. MTBE, formaldehyde, and acetic acid). Natural gas condensate (ethane and propane) is an advantaged raw material via ethylene and propylene to much of the organic chemicals industry (compared to crude-oil-derived naphtha).

The biomass can also be used along with coal to produce SNG. The use of biomass would reduce the greenhouse gas emissions, as biomass is a carbon-neutral fuel. In addition, the development of SNG technology would also enhance other gasification-based technologies such as hydrogen generation, the Integrated Gasification Combined Cycle (IGCC), or coal-to-liquid technologies, as the production of SNG is at least similar to these other processes/technologies [Chandel and Williams, 2009]. The addition of a water-gas shift reaction system and methanation reactor to the base gasification and gas cleanup system, as illustrated in Figure 8.3, allows for the production of SNG that meets pipeline quality natural gas specifications. The Reference Plant uses a sour-shift reaction to increase the hydrogen concentration in a portion of the syngas from the gasifier, so that when this gas stream is mixed with the remainder of the syngas and is cleaned in the Rectisol® AGR system, the cleaned syngas has the proper hydrogen to carbon ratio (3:1) for methanation (DOE report, 2007).

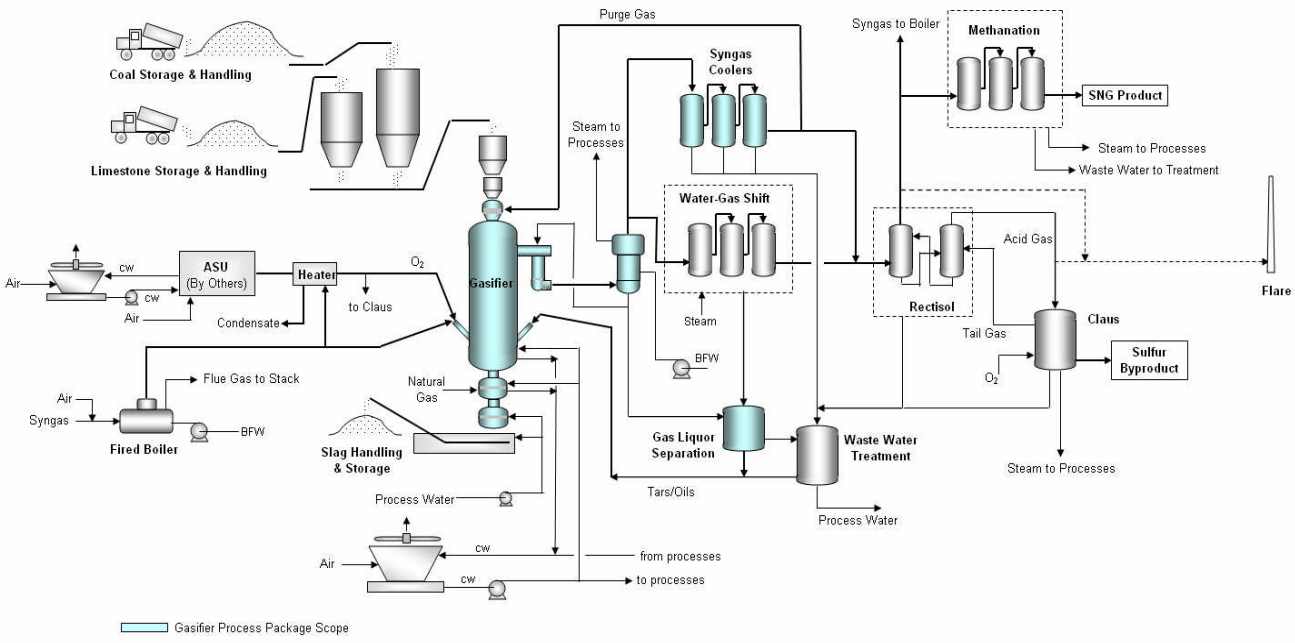

Figure 8.3 Sketch of Major Systems Comprising SNG Production Reference Plant (DOE report, 2007)

There are also many challenges associated with the deployment of SNG. In a 2007 NETL study, potential industrial customers of coal-to-SNG gasification for onsite use in natural gas applications indicated that reliability is important and needs to be near 100%, either through increased performance or redundancy. Some applications are able to also fire oil, allowing for onsite storage of the backup fuel. Availability is still a challenge for gasification, although some sites have achieved very high availability. The Great Plains Synfuels Plant in Beulah, North Dakota, for example, has consistently produced 90 to 92% of its rated output capacity [NTEL, 2007].

Producing SNG from coal is still more expensive than the natural gas it would replace. For this reason, NETL focuses on locations and applications where the gasifier could be integrated with an industrial process that uses natural gas. This would improve plant economics and would guard the facility against fluctuating natural gas prices, because existing coal transport infrastructure is well-developed, and coal is both abundant and relatively inexpensive. Another challenge to coal-to-SNG is in transporting a gaseous fuel, which can be difficult because of the gases' low densities. SNG must be cooled and then compressed for transport

through a close-to-capacity pipeline infrastructure. In addition, pipelines are restricted by geographical features like oceans, for example. It can be liquefied (called Liquefied Natural Gas or LNG) for transport by ships or trucks.

8.1.2. Commercial SNG plants planned in the U.S.

Table 8.1 shows that the 15 coal-to-SNG plants proposed in the U.S. are all in different stages of development. Some of these plants are also considering carbon capture and storage. For example, the joint ConocoPhillips/Peabody Energy project in the Midwest is considering CO_2 capture and storage for its mine-mouth facility (ConocoPhillips 2007), an Indiana Gasification LLC plant in southwest Indiana will demonstrate geologic CO_2 sequestration (Indiana Coal to SNG 2008), and Secure Energy Inc.'s plant in Illinois uses 10% biomass for SNG generation. [Chandel and Williams, 2009].

Table 8.1 Proposed commercial scale coal-to-SNG projects in the U.S. (Chandel and Williams, 2009) The current statuses of the cited plants are not updated in this table.

Project Name/Owner	**Location**	**Capacity (BCF/yr)**	**Capital Cost**	**Year of completion**	**Remarks**
Secure Energy Inc.	Illinois	20	$250 million	2009	The gasifier is 10% biomass-ready
Peabody Energy and Arclight Capital	Illinois	35			
Power Holdings of Illinois LLC	Illinois	50	$1 billion	2009	
Taylorville Energy Center (IGCC/SNG)	Illinois		$2 billion		50% of CO2 to be captured
Global Energy	Indiana				
GreatPoint Energy's Pilot Project	Massachusetts				
Oswego SNG Project – TransGas	New York		Planned	2010	

South Heart Coal Gasification Project (Great Northern Power Development, L.P. and Allied Syngas Corporation)	North Dakota	36.5	$1.4 billion	2012	CO_2 will be captured for Enhanced Oil Recovery (EOR) Applications in future
SES/Consol Coal-to-SNG Project	West Virginia				
Peabody/ GreatPoint SNG Project	Location undecided				
ConocoPhillips/ Peabody Energy	Midwest	50–70			
Lockwood Project	Texas	65.7		2011	CO_2 will be captured for EOR – fuel will be pet coke and biomass
Tondu's Nueces Syngas Plant	Texas				
Peabody Energy	Wyoming				

8.1.3. Coal-to-SNG Technology

Steam-oxygen gasification, hydrogasification, and catalytic steam gasification are the three gasification processes used in coal-to-SNG technology. So far, the proven and commercialized method of gasification for the coal-to-SNG process is the steam-oxygen gasification process.

8.1.3.1 Steam-oxygen gasification

In the steam-oxygen process of converting coal to SNG, coal is gasified with steam and oxygen. Oxygen is used for partial-combustion with char to provide enough energy used for gasification process. The gasification process produces carbon monoxide (CO), hydrogen (H_2),

carbon dioxide (CO_2), methane (CH_4), and higher hydrocarbons such as ethane (C_2H_6) and propane (C_3H_8). The gas composition depends upon the gasifier's operating conditions, i.e., temperature and pressure. At higher temperatures and pressures, the major products are CO and H_2. Three moles of H_2 are required to react with each mole of CO to produce one mole of CH_4. The concentration of H_2 in syngas is increased by a step called the water-gas shift reaction, which is followed by gas cleaning. The cleaned gas, consisting primarily of CO and H_2, reacts in the methanation reactor in the presence of a catalyst to produce CH_4 and H_2O. The resulting gas, after H_2O condensation and polishing, if required, is called synthetic natural gas (SNG). Figure 8.4 shows the flow diagram of the steam-oxygen gasification process. The essential components of the process are the air separation unit, the gasifier, the water-gas shift reactor, the syngas cleanup system, and the methanation reactor.

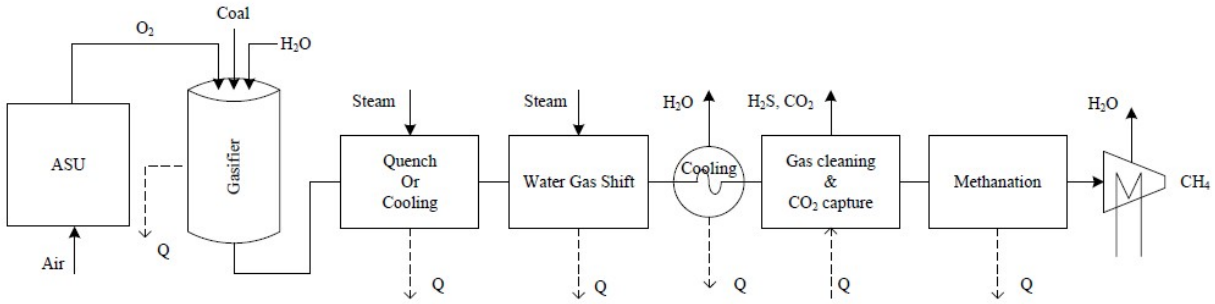

Figure 8.4 The steam-oxygen gasification process diagram (Chen, L., et al., 2009)

The methanation reaction with catalysts which are mainly ruthenium, cobalt, nickel and iron can be described by

$$CO + 3H_2 \Leftrightarrow CH_4 + H_2O \quad (8.1)$$

As the methanation reactions are highly exothermic and pressure-favorable, the methanation reactors are designed to run at low temperature and high pressure with catalysts. In the methanation reactor, CO and H_2 are converted to CH_4 and H_2O in a fixed-bed catalytic reactor. Since methanation is an exothermic reaction, the increase in temperature is controlled by recycling the product gas or by using a series of reactors. Steam is added to the reaction to avoid coke formation in the reactor. After the steam is removed from the product gases by condensation, SNG is ready for commercial applications. A conventional design for the methanation process uses three stages. Figure 8.5 shows the schematic diagram of the ADAM II

methanation process, illustrating the three-stage design (Hohlein et al., 1984). Three adiabatic methanation reactors, D 201, D 202 and D 203 are equipped with fixed catalytic beds. The syngas coming from the WGS unit is preheated to a temperature above the starting temperature of the catalyst. At each methanation reactor outlet, the gas compositions are approximately at chemical equilibrium. Heat is generated during the methanation reactions, so syngas cooling is needed between stages. The typical operating temperatures and compositions at the inlets and outlets of the three stages are shown in Table 8.2. (Chen, L., et al., 2009)

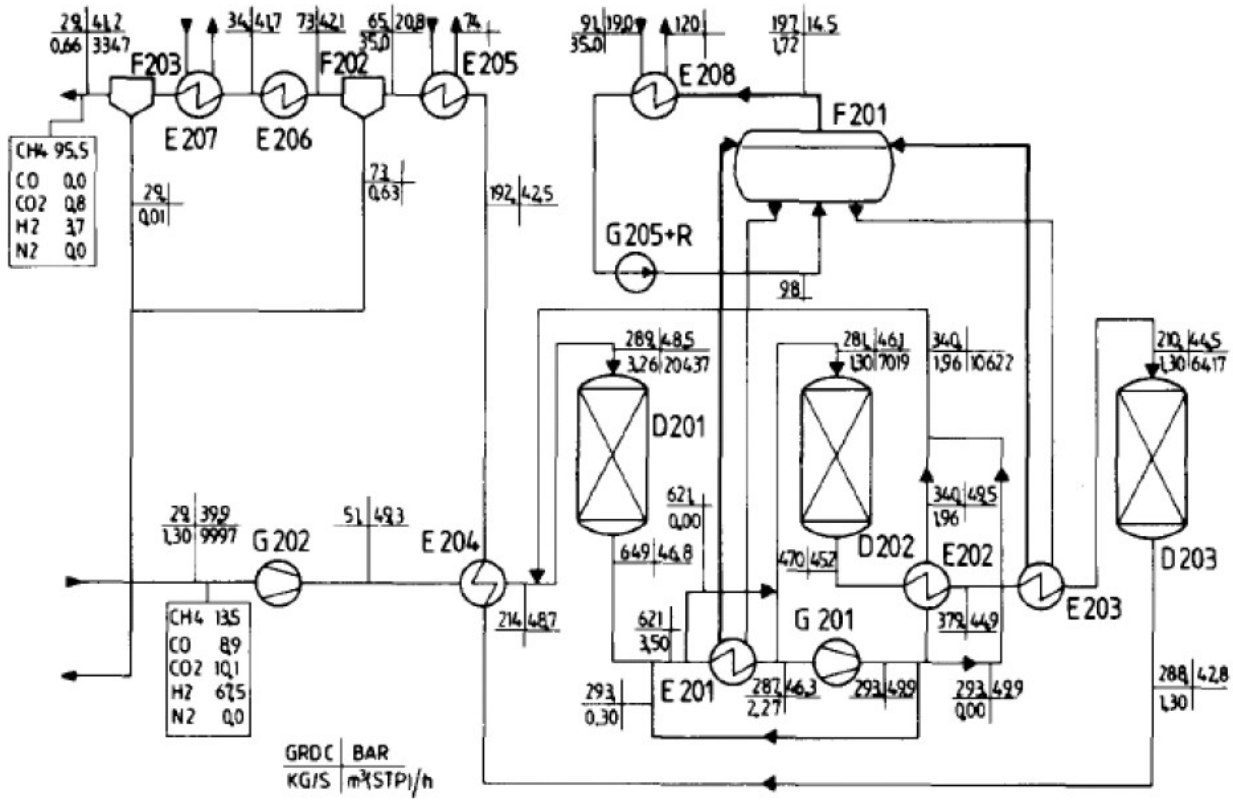

Figure 8.5 ADAM II 3-stage methanation process at 45 bar, 300-650 ºC (Hohlein et al., 1984)

Table 8.2 Typical operating conditions and gas compositions in the 3-stage methanation process. (Chen, L., et al., 2009)

		1st stage		2nd stage	3rd stage	Product
	Unit	Inlet	Outlet	Outlet	Outlet	(dry basis)
Gas flow rate	m3/h	962	832	282	271	149
P	bar	26.85	26.7	26.6	26.5	26.5
T	℃	306	651	485	343	16
H2O	mol%	15.58	28.7	39.57	44.96	0
CH4	mol%	23.29	34.68	43.15	46.79	85.01
CO	mol%	5.74	1.81	0.04	0	0
CO2	mol%	6.69	4.79	2.47	0.71	1.29
H2	mol%	44.90	25.70	9.97	2.63	4.78
N2	mol%	3.8	4.32	4.8	4.9	8.92

The steam-oxygen gasification process for SNG has been demonstrated in the Great Plains Synfuel Plant for 20 years and has proven to be successful in practice. The interest in the Coal to SNG concept has grown recently due to the process's capability for CO_2 capture and utilization in enhanced oil recovery. In the Great Plains Synfuel Plant (GPSP), more than 5 million tons of CO_2 have been sequestered up to 2006, which doubled the oil recovery rate of an oil field in Saskatchewan. A detailed process diagram of the GPSP is shown in Figure 8.6 (DOE, 2006). The plant consists of a coal and ash handling unit, an Air Separation Unit (ASU), a steam generator, a gasifier, a water gas shift reactor, and a methanation unit. Also included are the AGR plant (Rectisol) and Flue Gas Desulphurization (FGD) unit, which are used to remove the acid gas within the syngas and flue gas, respectively. Besides methane, the plant also produces ammonia, ammonium sulfate, naphtha, and phenol (carbolic acid) as by-products. Although demonstrating successful and economical clean synthetic fuels production, the GPSP can be further optimized in many aspects. For instance, the gasification technology, a Lurgi system, was adopted by the GPSP 20 years ago and may not be the most favorable option today because of its small coal processing throughput and large production of waste water. Choosing a technology that produces less waste could eliminate or diminish ancillary processes such as gas liquor separation, wastewater treatment, ash handling, and so on. However, replacing the gasification system would require the adjustment of other processes, principally the WGS and methanation systems.

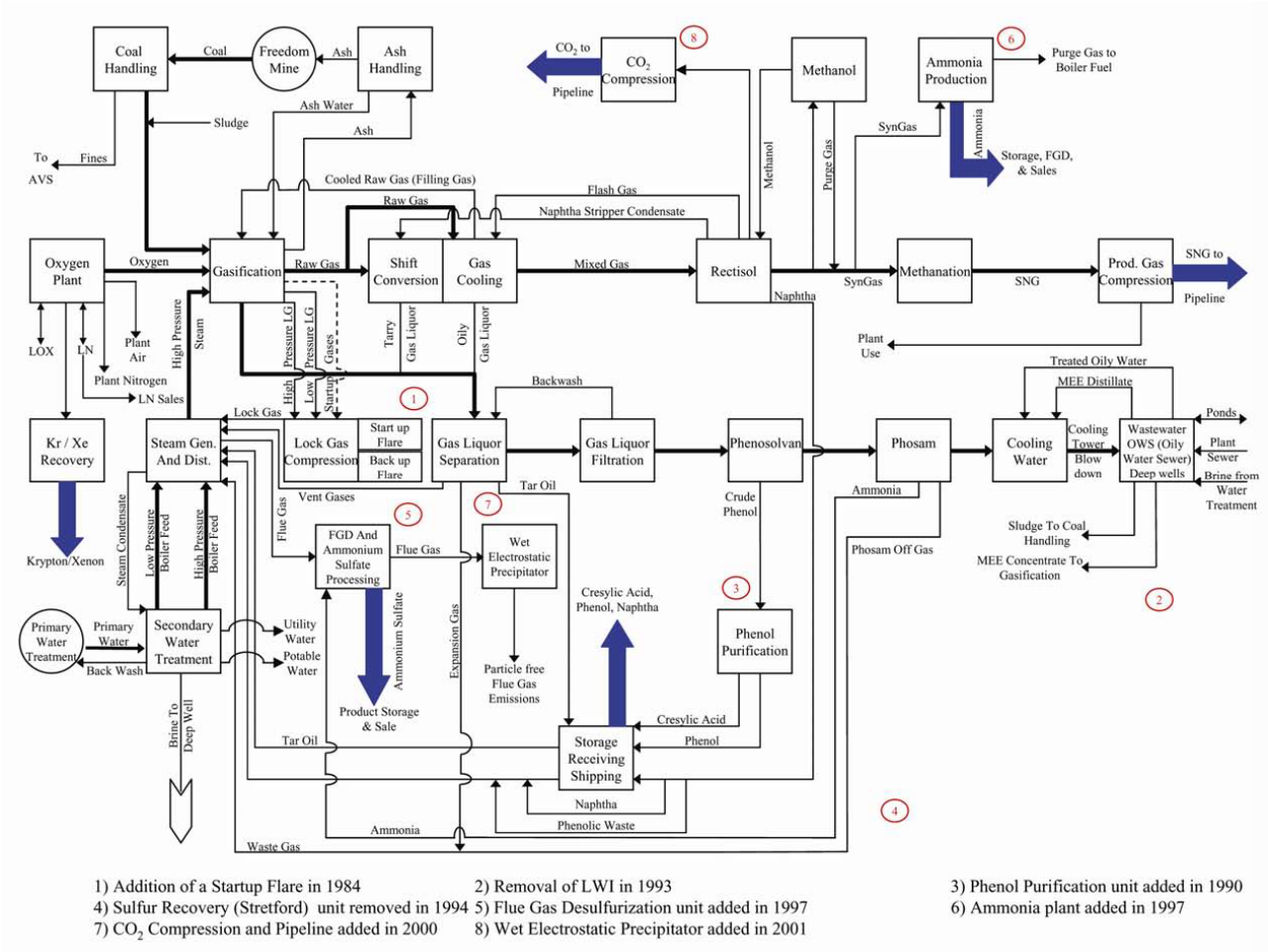

Figure 8.6 Detailed block flow diagram of the Great Plains Synfuel Plant. (Source: DOE report, April, 2006)

8.1.3.2 Hydrogasification

The hydrogasification process uses H_2 to gasify coal. H_2 reacts with coal to produce CH_4. The hydrogasification process is exothermic in nature. H_2 required for the gasification is either provided by an external source or by using a methane steam reformer. A portion of the CH_4 generated in the hydrogasification reactor is converted into CO and H_2 in the methane steam reformer. The methane steam reforming reaction is: $H_2O + CH_4 \rightarrow CO + 3H_2$. 1 mole of CH_4 produced from hydrogasification process could generate 3 moles of H_2 in the methane steam reformer. During the hydrogasification process, $C + 2H_2 \Leftrightarrow CH_4$, only 2 moles of H_2 are needed for producing one mole of CH_4. That is the reason why H_2 required for hydrogasification can be provided by using a methane steam reformer. If CO is shifted to CO and H_2, the above process

will lead to a net production of one mole of CH_4 and CO_2 from two moles of fixed carbon: $2C+2H_2O \rightarrow CH_4+CO_2$. A diagram of the hydrogasification process is shown in Figure 8.7. The hydrogasification process is still in the research stage and is not yet commercialized, although a few studies on the process were conducted as early as from the 1970s to the 1990s. Ruby et al. (2008) proposed a hydrogasification process which consists of a hydrogasification reactor, desulfurization and carbonizer reactors for CO_2 removal, and a methanation reactor.

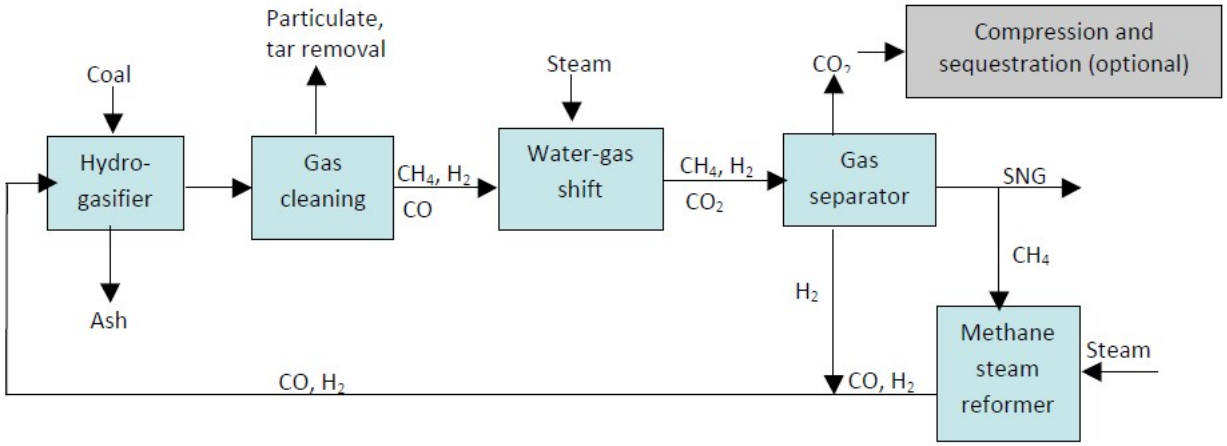

Figure 8.7 Hydrogasification process diagram (Chandel, M., and Williams, E., 2009)

Hydrogasification was originally developed in the early 1900s and there was a revived interest in the process during the 1970s and 80s as a result of increasing natural gas prices. The basic reaction is the direct methanation of carbon, as shown below.

$$C + 2H_2 \Leftrightarrow CH_4 \qquad \Delta H_{1000K} = -89.9 kJ/mol \tag{8.2}$$

Although this reaction is mildly exothermic, a significant amount of energy must be spent in bringing the reactants up to the operating temperature as well as to sustain the process. Methane production is favored at high pressures and the process is generally operated at temperatures ranging from 750 ºC to 1000 ºC (Higman and Burgt, 2003). A number of processes were developed and a few of these were operated satisfactorily in pilot plant scales. A major issue with hydrogasification process is the source of the hydrogen supply since hydrogen production can be expensive and hydrogen has a better market value. As natural gas prices have dropped

due to the recent development of hydraulic fracturing (or fracking), hydrogasification is not attractive, economically. In addition, the much slower reactivity of carbon with hydrogen compared to other gasifying agents further hinders the commercialization of hydrogasification. The reactivity of carbon with different species at 1073 K and 0.1 atmospheres are shown below (Walker et al., 1959).

$$r_{O_2} \gg r_{H_2O} > r_{CO_2} > r_{H_2}$$
$$10^5 \qquad 3 \qquad 1 \qquad 3.1^{-3}$$

Based on the above discussions, it is evident that, for SNG production to be commercially viable, the gasification process must solve the two major technical problems faced by conventional hydrogasification and methanation processes. These problems are the difficulties in supplying hydrogen in an inexpensive and simple manner, and also the low carbon conversion ratios observed during conventional hydrogasification based processes.

8.1.3.3 Hydromethanation (Catalytic steam gasification)

Catalysts can be used to enhance the reactions involved in gasification. Many gasifiers must operate at high temperatures so that the gasification reactions will proceed at reasonable rates. Catalysts can also be used to favor or suppress the formation of certain components in the syngas product. The primary constituents of syngas are hydrogen (H_2) and CO, but other products like methane are formed in small amounts. Catalytic gasification can be used to either promote methane formation, or suppress it. Disadvantages of catalytic gasification include increased materials costs for the catalyst itself, as well as diminishing catalyst performance over time. Catalysts can be recycled, but their performance tends to diminish with age. The relative difficulty in reclaiming and recycling the catalyst can also be a disadvantage. The detailed description of catalytic gasifier is stated in Chapter 1, section 1.2.4.3.

In the hydromethanation process, gasification and methanation occur in the same reactor in the presence of a catalyst. Steam is the only gasification agent used so that the water-gas shift and methanation steps are no longer necessary. The ideal reaction route is:

$$2C + 2H_2O \Leftrightarrow CH_4 + CO_2 \qquad (8.3)$$

However, with steam, low temperatures greatly limit the rate of reaction. At high temperatures, the thermodynamic environment is not favorable for methane production. Therefore,

introducing a catalyst at low temperature to facilitate the reaction is highly needed. Alkali metals catalyze carbon with steam to form CO and H_2 and, by doing so, increase the reaction rate several fold. Selection of the catalyst is based on its affinity to reacting with coal. KCl and K_2SO_4, for example, are ineffective despite their belonging to the alkali family (Probstein and Hicks, 1982). In the process of gasification, the actual catalyst is not retained in the gasifier, but is carried out with the ash. In order for a commercial plant to maximize profits, it is essential that a recycling loop be implemented to recover the catalyst for re-use in the coal gasification process. From end-to-end, in hydromethanation, coal is pulverized and mixed with the selected catalyst. Before feeding the impregnated catalyst-coal into the gasifier, it is dried to remove as much moisture from the fuel as possible. Gasifiers are then fed with the feedstock and begin introducing steam into the environment to perform the gasification. Beyond the hydromethanation process, carbon monoxide and hydrogen must be separated from the methane product. A cryogenic distillation process effectively separates methane from the synthesis gas (a process with an energy penalty lower than the oxygen separation from air in an ASU).

The advantages of hydrogasification and hydromethanation are that they do not use direct combustion to provide heat, so an air separation unit is not required to provide oxygen. Hence, there is less of an energy penalty for the process. Furthermore, the costs are lower, as the gasification and methanation occur at a lower temperature. The disadvantages of hydromethanation are the separation of the catalyst from the ash/slag and the loss of reactivity of the catalyst. A diagram of the hydromethanation process is shown in Figure 8.8.

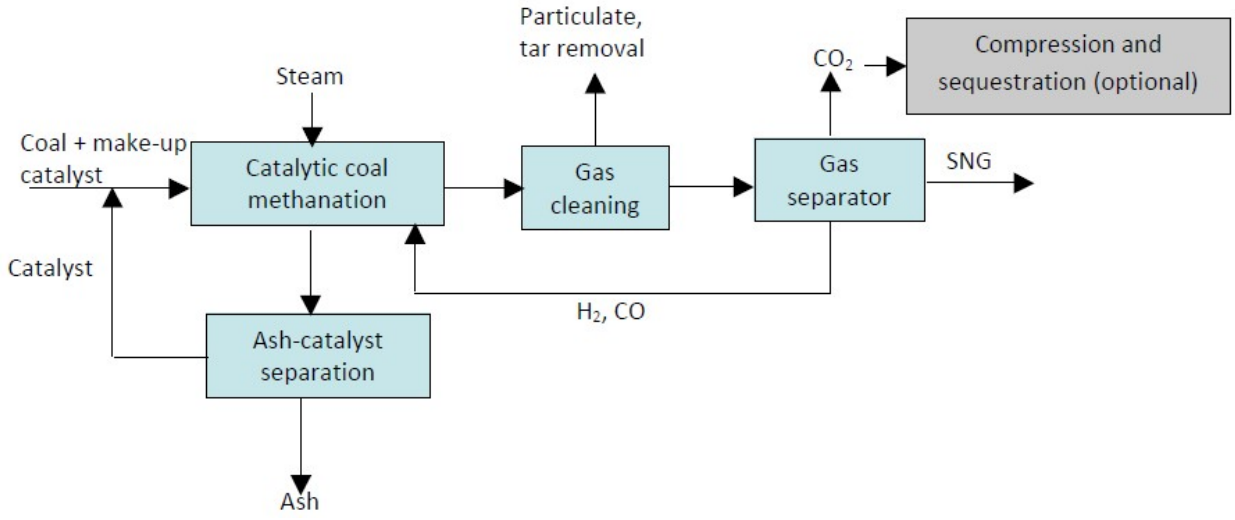

Figure 8.8 A diagram of hydromethanation process (Chandel, M., and Williams, E., 2009)

The hydromethanation process developed by Great Point Energy Inc. is considered to be a great advancement in SNG technology. The process involves a single reactor using a proprietary, recyclable catalyst developed in-house and made from abundant, low-cost metals. The catalyst was developed with the help of Southern Illinois University, the University of Toronto, and the University of Tennessee (Fairley 2007). The heat released in the SNG process is sufficient to sustain the gasification, eliminating the need to fire up the reactions with purified oxygen. The process was demonstrated with a weeklong pilot run in November 2007. The pilot plant for the process is a 60-foot-high gasifier with an internal diameter of 14 inches. The price of pipeline-quality natural gas by Great Point Energy's process could be less than $3 per MMBtu (Fairley 2007). Great Point Energy Inc. and Peabody were working together to commercialize the technology with the goal of developing a coal to SNG plant at or near Wyoming's Powder River Basin area (GreatPoint Energy 2008). The Company currently conducts tests at a pilot plant at the Energy and Environmental Research Center in Grand Forks, ND, which demonstrates the latest version of its technology and serves as a feedstock calibration facility for designing commercial plants (GreatPoint Energy (2013).

8.1.4 Use of biomass for SNG

SNG produced from biomass, also known as "bio-SNG," has the advantage of being carbon-neutral, and, in conjunction with CO_2 capture, the entire process could generate negative carbon emissions. The challenges of using biomass arise due to the chemical composition of biomass, lower calorific value, higher moisture content, and tar formation. The seasonal variation in the biomass supply and moisture content could require large amounts of storage space and large drying capacities for commercial-scale biomass gasification units. Another possible way of utilizing biomass would be in a coal-biomass co-gasification process. Co-gasification could make it possible to install large-scale gasification plants, which could be more commercially viable. Fluidized bed gasifiers may be better suited for biomass gasification than entrained-flow gasifiers as they can handle variations in size, density, moisture, and tar formation.

In Meijden's (2010) study, he categorized the gasification technologies associated with bio-SNG process in different ways. Based on the gasifier's type, they are: 1) entrained flow, 2) fluidized bed, and 3) fixed bed. Fluidized bed gasifiers can be divided into two main

categories: Bubbling Fluidized Bed (BFB) and Circulating Fluidized Bed (CFB). A bubbling bed is the classical approach where the gas at low velocities is used and fluidization of the solids is relatively stationary, with some finer particles being entrained. At higher gas velocities, a circulation of the bed material is required. This type of gasifier is called a Circulating Fluidized Bed (CFB) gasifier. The typical fluidization velocity in the circulating gasifier is normally between 3 and 10 m/s. The bed material and recycling char are removed from the product gases by a cyclone or another separation device. Those particles are recycled back to the gasifier via a non-mechanical valve. The gasification technologies can be implemented with a direct heating scheme or an indirect gasification/heating scheme. For indirect gasification/heating, the conversion of the fuel is being done in two separate reactors (indirect twin beds). The first reactor is for combustion to generate heat for the gasification process in the second reactor. The char and bed material (e.g. sand) are fed to the combustion reactor. The char is combusted to produce the required heat for the gasification reactor. The bed material (sand) carrying the required heat is then transported into the gasification reactor. The biomass in the gasification reactor is converted into producer (or product) gas and char (pyrolysis). Char and bed material are separated from the gas and returned into the combustion chamber by a solid gas separation device, such as a cyclone. The producer gas exits the gasifier and is sent to the gas cleanup system.

In Meijden's (2010) study, he used Aspen Plus to simulate a large scale SNG system with 1 GW (HHV) of input power. The net overall efficiency on the LHV basis, including electricity consumption and pretreatment, but excluding transport of biomass, is 54% for the BFB, 58% for the CFB with direct heating/gasification, and 67% for the CFB with the indirect heating/gasification technique.

In lieu of the high efficiency of indirect gasification, the Energy Research Centre of the Netherlands (ECN) has demonstrated SNG generation from biomass (Mozaffarian et al. 2003, 2004) using the indirect gasification technology at atmospheric pressure. The process is shown in Figure 8.9. The biomass is gasified in the riser of a gasification reactor and the remaining char is circulated to the combustor. In this process, the heat required for gasification is supplied by char combustion in the combustor. Steam is used for gasification and air is used for char combustion. The lab scale gasifier, developed in 2004, has a biomass capacity of 5 kg/h and operates at temperatures of 750ºC to 900ºC (Zwart et al. 2006). Direct heating/gasification was

also tested, which uses oxygen and steam for gasification via a bubbling fluidized bed and operates at 850ºC. The gas treatment in the integrated bio-SNG system consists of tar removal with organic scrubbing liquid technology, and sulfur and HCl removal with adsorbents.

Based on the experiments, the SNG system consists of an indirect gasifier, the so-called MILENA gasifier, a tar removal system which recycles tar to the gasifier, a gas cleaning and WGS reactor, and a methanation combined reactor. The gasifier contains separate sections for gasification and combustion. The gasification section consists of three parts: the gasifier riser, settling chamber, and downcomer. The red arrows in Figure 8.9 represent the circulating bed material. The gasifier working at 850ºC produces nearly nitrogen-free syngas and a high amount of methane. Tar is recycled to the gasifier in order to increase efficiency, whereas the tar-free syngas is cleaned from other contaminants (e.g., sulfur and chlorine). The clean syngas is fed to a combined shift and methanation process, converting the syngas into SNG. After methanation, further upgrading (e.g., CO_2 and H_2O removal) is required in order to comply with the desired SNG specifications. The overall net thermal efficiency is reported as 70% by Low Heating Value (LHV) basis (approximately 64% HHV basis). Forty percent of the carbon of the biomass becomes part of the SNG and an equal amount of carbon is captured as CO_2. The remaining 20% of the carbon in biomass becomes flue gas from the process.

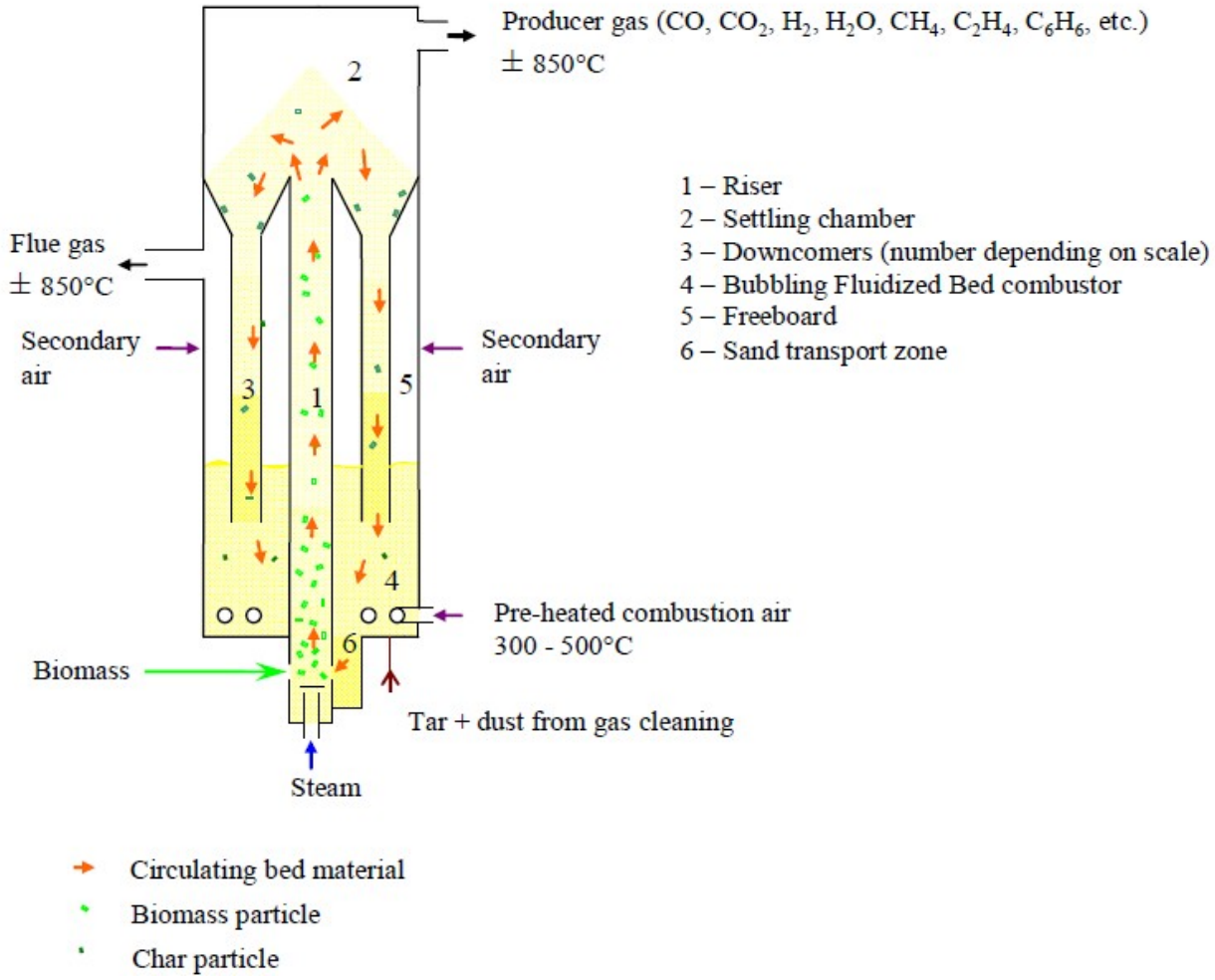

Figure 8.9 Simplified scheme of MILENA biomass gasification process (C.M. van der Meijden, 2010)

8.1.5 Recent research on SNG

Recently, The Arizona Public Service Company (APS) along with the Department of Energy and other partners are developing a hydrogasification process to co-produce SNG and electricity from western coals. The objective of the $12.9 million project is to develop and demonstrate an engineering scale hydrogasification process which can produce SNG at a cost of less than $5/MMBtu and can utilize low rank western coal (NETL, 2008). The Western Research Institute (WRI) is working on the development of a gasification process which uses counter-current cyclonic methods in a unique sequence that causes activated carbon char to

react with synthesis gas, both derived from coal. The method does not require pure oxygen to produce the synthesis gas (WRI, 2008).

KBR developed a new KBR TRIG gasification-based coal-to-SNG. The process shown in Figure 8.10 is well suited for a wide range of feedstocks, particularly low-rank coals that are low-cost and abundant. The process scheme offers a technically robust and energy efficient design, with several advantages over comparable gasification processes. The economics of building mine-mouth 150,000 standard cubic feet per day coal-to-SNG facilities using KBR's TRIG gasification technology is currently being investigated for various western U.S. locations (Ariyapadi et al., 2008). Figure 8.10 depicts a simplified block flow diagram illustrating the connectivity between major process units of the KBR system. A cluster of three TRIG gasifiers supply the necessary syngas feed with the appropriate H_2: CO ratio to the methanation unit. The main process units include gasification, shift, COS hydrolysis, ammonia scrubbing, mercury removal, acid gas removal, sulfur removal, CO_2 compression, methanation, and SNG drying and compression. The detail of each section is described by Ariyapadi et al. (2008).

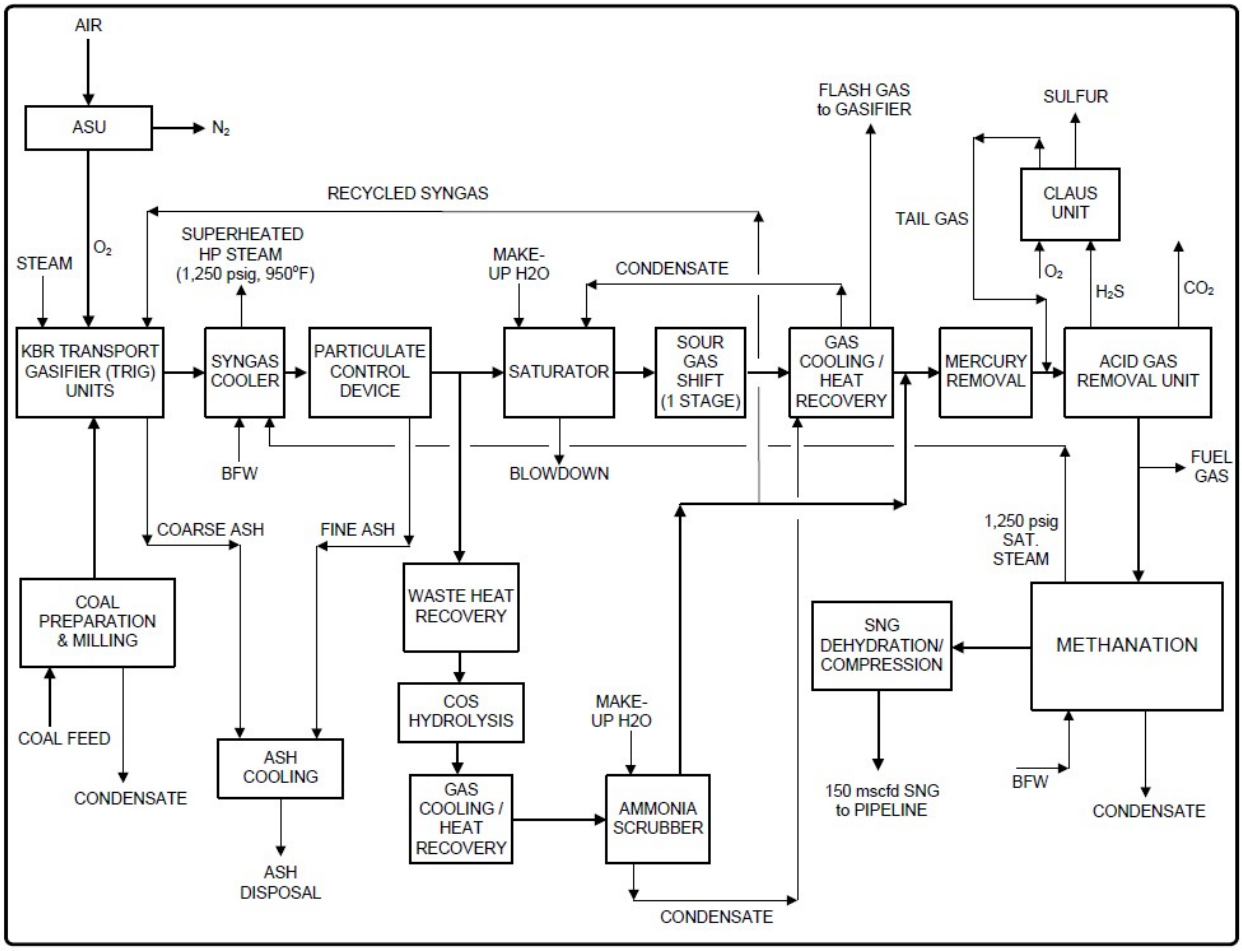

Figure 8.10 Block Flow Diagram of KBR TRIG Coal-to-SNG Process (Ariyapadi et al. 2008)

A new SNG production technology, called the steam hydrogasification reactor (SHR), which is based on a combination of the hydrogasification and steam pyrolysis reactions, is newly developed by the University of California, Riverside. The configuration of this process allows the use of recycled hydrogen as feed, thus eliminating the hydrogen supply problem. This steam hydrogasification process generates a product gas stream with high methane content. The composition of the product gas from steam hydrogasification can be controlled by varying the steam to carbon and H_2 to carbon ratios of the feed. Methane concentration of the SHR product gas can be varied from 10 to 30 % on a molar basis. The product gas also contains CO, CO_2, H_2, and a considerable amount of unreacted steam. In the SHR gasifier, the feed is transported into the reactor via a slurry. The slurry feed eliminates the need for cumbersome

reactor feed systems such as a lock hopper. This also simplifies feedstock processing since drying the feed is not necessary. A portion of the necessary steam enters the reactor as liquid water that is part of the slurry and the rest of the steam is superheated and fed along with the hydrogen. Steam hydrogasification of carbonaceous feedstocks results in improved carbon conversion compared to hydrogasification. An SHR also generates a product gas with a considerable amount of methane compared to conventional partial oxidation gasifiers. The steam hydrogasification reactor can be coupled with a shift reactor, resulting in a gasifier configuration that generates a syngas with high methane concentrations. This configuration also allows considerable control over the final product gas composition. Figure 8.11 shows the process configuration involving SHR gasification to produce syngas with a high methane content. The slurry made of the carbonaceous feed (coal) and water, along with the recycled hydrogen are fed to the SHR, operating at approximately 850 ºC and 400 psi.

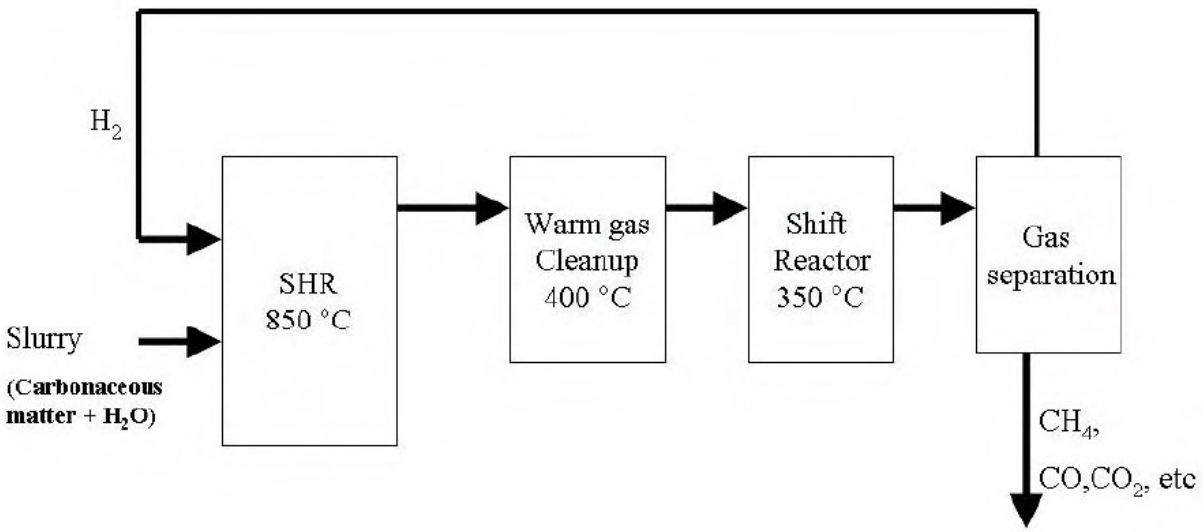

Figure 8.11. Schematic diagram of a steam hydrogasification reactor (SHR) method to produce high CH_4 production (Chan and Norbeck, 2009)

The SHR generates a high methane content product gas that is subjected to warm gas cleanup in order to remove contaminants such as sulfur. The gas cleanup must be performed at a temperature above the dew point of water. This will allow the unreacted steam from the SHR to be directly fed into the shift reactor along with the product gas. In this case, the shift reactor will be operated as a 'sour-shift' reactor with a sulfur tolerant catalyst. In the shift reactor, the CO

present in the clean product gas reacts with the steam to produce H_2. Methane is inert in the shift reactor. Alternatively, the product gas will be cooled down and H_2 can be recycled to the SHR as feed. The recycled hydrogen stream eliminates the hydrogen supply problem. The final product gas in either case contains a high quantity of methane. The experimental results of the steam hydrogasification of coal and wood mixtures in a batch reactor are presented by Chan and Norbeck (2009). Their results show that the carbon conversion values at 700 ºC were approximately 60%, whereas, at 800 ºC, the values were closer to 80%. Their simulation results show that the product gas from an SHR gasifier contains considerable amounts of methane. The concentration of methane increases with decreasing H_2O/Feed mass ratio and increasing H_2/C feed mole ratio. Operating at higher pressures also favors an increase in methane production.

Tunå (2008) evaluated twelve different systems for production of SNG by using Aspen Plus. The system consists of three gasifiers: an entrained-flow, fluidiszd-bed, and indirect gasifier. Both an isothermal methanation process and an adiabatic methanation process have been modeled. Gas cleanup was performed using both conventional zinc oxide desulfurization with PSA upgrade and a Rectisol® wash. The simulation results show that SNG efficiencies from biomass to methane of 50% are possible with either gasifier. The fluidized-bed and indirect gasifiers were able to produce SNG with an efficiency around 67%. Furthermore, utilizing a Rectisol gas cleanup system does not have a significant negative impact on SNG efficiency, but it affects overall efficiency. The simplest system—zinc oxide desulphurization with PSA gas cleanup—coupled with either methanation system is considered by Tuna as the most promising choice. It is based on well-established, widely-used equipment and it offers better efficiency than a wet-gas cleanup process such as Rectisol. If there is a significant amount of sulfur in the gas stream that needs to be removed, or if the carbon dioxide needs to be captured and removed, the Rectisol method will become a competitive option. Typically, carbon dioxide capture is not necessary for biomass-based plants as the carbon emissions are considered neutral.

Chen et al. (2009) reviewed the state-of-the-art technologies for Coal-to-SNG, conducted a thermodynamic parametric study of the main components in this process, and and also made an efficiency assessment of the overall energy system, implementing different gasification technologies, including the hydromethanation process. Their results show the O_2/Carbon ratio to be about 0.25 - 0.3 and the H_2O/Carbon ratio to be about 1.5 – 2, which are

favorable ranges to produce a CH_4-rich syngas with a high H_2/CO ratio. Higher pressure is favorable to the hydromethanation reaction and increases methane yield. The analysis shows that moving-bed, dry ash gasification achieves a higher energy conversion efficiency (67%) than entrained flow gasification (57%) for the overall Coal-to-SNG process. Hydromethanation is a promising route with about 70% energy efficiency. However, it is still under development because of the challenges for separating the catalyst from the ash/slag and recovering the loss of reactivity of the catalyst.

Chandel and Williams (2009) examined the different technologies for producing SNG, as well as the production costs and the environmental impacts of SNG. Their paper identified the conditions under which SNG production could be economically viable. In a low-carbon economy, the development of the carbon capture and storage would be one of the critical factors in the future development of SNG. In the absence of carbon capture and storage and carbon allowance price in the future, the SNG could be expensive and may not be economically viable. Higher natural gas prices and the selling of CO_2 to enhance oil recovery could make SNGs economically viable. The levelized cost of producing SNG is $8.42/MMBtu for plants using bituminous coal and $9.53/MMBtu for those using sub-bituminous coal. With CO_2 sequestration, SNG costs would increase to $9.15/MMBtu for bituminous coals and $10.55/MMBtu for sub-bituminous coals. They also examined the cost of producing Bio-SNG and they reported that, for keeping the bio-SNG price lower than $12/MMBtu, the biomass price should not exceed $2.2/MMBtu. The cost of producing SNG ($8.42-9.53/MMBtu) provided by the analysis of Chandel and Williams (2009) is much more expensive than that ($5/MMBtu) taken from the NETL's report (2008) mentioned earlier. This further exemplifies the uncertainty in evaluating the true production cost of SNG.

8.1.6 Methanation reaction rates

The tail end of an SNG plant must necessarily employ a catalytic methanation step in order to upgrade the heating value to approximately 950 Btu/SCF. This step typically involves the methanation reaction shown in Equation 8.1, which is accompanied by a relatively high heat of reaction (ΔH_R = 49.3 kcal/mol). Although the methanation of trace quantities of CO has been practiced commercially for many years in ammonia plants, SNG methanation from coal poses a more severe problem due to the high concentrations of CO in the synthesis gas. With nickel

methanation catalysts, the reaction rates are relatively high, and, consequently, heat is also liberated at very high rates. Problems connected with localized coking and catalyst sintering generally lead to reactor design concepts which employ high recycle ratios as first suggested by Dent et al. (1948). Since the catalyst is always in contact with a reacting gas mixture, which contains all or most of the five components involved in methanation synthesis: H_2, CO, CO_2, H_2O, and CH_4, Saletore and Thomson (1977) decided to conduct an experimental study to determine the methanation reaction rates for synthesis feeds containing all five components. They also investigated the effect of steam's high partial pressures on the methanation reaction rate. This was motivated by the fact that steam may be added to the synthesis gas in order to inhibit carbon deposition (Dent et al., 1948) and at least one methanation reactor's design concept utilizes a large excess of steam (White, 1975).

Early work on methanation kinetics was accomplished at the University of Michigan (Akers and White, 1948) utilizing a 3.2 mm commercial nickel catalyst. They correlated their results by assuming that the rate-determining steps were surface reactions, although there was some evidence of strong pore diffusion effects. Binder and White (1950) utilized CO_2 in place of CO and found that the rate of CO_2 methanation, $CO_2 + 4H_2 \rightarrow CH_4 + 2H_2O$ (ΔH_R = 165 MJ/kmol), was two orders of magnitude less than the CO methanation rate. Schoubye (1969, 1970) employed small-sized nickel catalysts at high pressures and concluded that the reaction order with respect to CO was -0.5 at high CO concentration (over 20%) and that the data was best correlated by assuming that H_2 adsorption determined the reaction rate. Negative reaction orders with respect to CO were also found by Betta et al. (1974) and Vannice (1975), although they all worked at pressures of 1 atm or less. Saletore and Thomson (1977) conducted the measurements of the methanation reaction rate with a 1.6-mm nickel catalyst utilizing feed compositions typical of recycle reaction configurations and product streams with a high CO_2 content. The apparent reaction orders for hydrogen and steam were found to be 0.85 and -0.9 respectively, but there was no significant dependency of the methanation rate on the carbon oxides. JRostrup-Nielsen, et al. (2007) investigated the high temperature methanation sintering and structure sensitivity by doing experiments and found that high temperature methanation plays a role in the manufacture of SNGs. The key problem is resistance to sintering, which results in a decrease of both the metal surface area and the specific activity. Paraskevi, et al. (2008) investigated the catalytic performance of Al_2O_3-supported noble metal catalysts for the

methanation of CO, CO_2, and their mixture with respect to the nature of the dispersed metallic phase (Ru, Rh, Pt, Pd). Results show that the catalytic performance, apparent activation energy, and selectivity of reaction products for the solo- or co-methanation of CO/CO_2 depend strongly on the nature of the metallic phase. Generally, methanation activity is much higher for Ruthenium and Rhodium catalysts, compared to Palladium or Platinum, which tend to enhance the WGS reaction.

For the simulations in the other chapters of this dissertation, the methanation reactions have been excluded due to low methane production in the previously studied gasification process. However, for this chapter, since it has improved, the simulation will focus on modeling the methanation reactions in the coal gasification process.

For simulating methanation, Watanabe and Otaka (2006) performed a numerical simulation with the coal gasification model on the Japanese 2 tons/day, research-scale coal gasifier supported by the Central Research Institute of Electric Power Industry (CRIEPI). The rate constants of the methanation reaction that they used were A = 5.12 x 10^{-14} and E = 2.73x 10^4 J/kmol for the forward reaction rate and A = 4.4 x 10^{11} and E = 1.68 x 10^8 J/kmol for the backward reaction rate. The influence of the air ratio on gasification performance, gas temperature distribution, and product gas composition were presented and discussed in their paper. NETL (2012) only included the forward methanation reaction in the coal gasification model. The constants they used were A = 5.12 x 10^{-14} and E = 2.73x 10^4 J/kmol.

Since methanation is a reversible catalytic reaction, most of the reaction rates for the methanation reaction were obtained from experiments with specific catalysts under laboratory conditions of relatively narrow ranges of pressure and temperature. However, the pressure and temperature conditions are very different than the operating conditions in an entrained-flow coal gasifier. Therefore, it is not clear how the published reaction rates can be trustfully used to predict the actual methanation reaction rate in a gasifier without the presence of catalysts and under different temperature and pressure conditions than those used in the laboratory. Due to the unavailability of appropriate methanation reaction rates for broad operating conditions in actual gasifiers without using catalysts, the objective of this study is to obtain an appropriate representative methanation global reaction rate under non-catalytic gasification conditions. Considering that almost all the available syngas data including CH_4 is obtained after the quench and desulfurization processes, rather than immediately at the exit of gasifier, and that the syngas

composition changes after these processes, the simulation result can't be adequately compared with these available commercial or experimental data. Therefore, this study focuses on investigating the effect of the methanation reaction rates on the gasification process by studying the sensitivity of the exit syngas temperature and composition on a wide range of methanation reaction rates. Since the reactivity of carbon with hydrogen, $C + 2H_2 \rightarrow CH_4$, is several orders of magnitude lower compared to other gasifying agents, the heterogeneous reaction is not considered in this study, and will be included in the future study.

In this study, the forward and backward rates provided by Jones and Lindstedt (1998) are used as the reference methanation reaction rate constants with catalyst. The rate constants of the methanation reaction is $A = 5.12 \times 10^{-14}$ and $E = 2.73 \times 10^{4}$ J/kmol for the forward reaction rate and $A = 4.4 \times 10^{11}$ and $E = 1.68 \times 10^{8}$ J/kmol for the backward reaction rate.

8.2 Global Gasification Chemical Reactions

This study deals with the global chemical reactions of coal gasification that can be generalized in reactions (R1.1) through (R1.11) in Table 8.2.

Table 8.3 Summary of reaction rate constants used in this study

Reactions		Reaction Type	Reaction heat, ΔH°_R (MJ/kmol)	$k = AT^n\exp(-E/RT)$ (n=0)		Reference
				A	E(J/kmol)	
Heterogeneous Reactions						
R 1.1	$C(s) + ½\ O_2 \rightarrow CO$	Partial combustion	-110.5	0.052	6.1×10^7	Chen et al.(2000)
R 1.2	$C(s) + CO_2 \rightarrow 2CO$	Gasification, Boudouard reaction	+172.0	0.0732	1.125×10^8	
R 1.3	$C(s) + H_2O \rightarrow CO + H_2$	Gasification	+131.4	0.0782	1.15×10^8	
R 1.4	$C + 2H_2 \Leftrightarrow CH_4$	Hydrogasification	+89.9	N/A		
Homogeneous Reactions						
R 1.5	$CO + ½\ O_2 \rightarrow CO_2$	Combustion	-283.1	2.2×10^{12}	1.67×10^8	Westbrook and Dryer (1981)
R 1.6	$CO+H_2O(g)\leftrightarrow CO_2+H_2$	Water Gas shift	-41.0	2.75×10^{10}	8.38×10^7	**Jones and Lindstedt (1998)**
R 1.7	**$CO + 3H_2 \leftrightarrow CH_4 + H_2O$**	**Methanation**	**-205.7**	**$k_f = 5.12\times10^{-14}$** **$k_b = 4.4\times10^{11}$**	**2.73×10^4** **1.68×10^8**	
R 1.8	$CH_{2.761}O_{0.264}N_{0.055}S_{0.048}Cl_{0.005} \rightarrow 0.256CO+0.466H_2+0.33CH_4+0.2C_2H_2+0.0275N_2+0.005HCl+0.04H_2S+0.008COS$	Two-step Volatiles Cracking	+4.75	Eddy dissipation		N/A
R 1.9	$CH_4 + ½O_2 \rightarrow CO+2H_2$	Volatiles gasification via CH_4	-35.71			
R 1.10	$C_2H_2 + O_2 \rightarrow 2CO + H_2$	Volatiles gasification via C_2H_2	-447.83			
R1.11	$H_2 + ½\ O_2 \rightarrow H_2O$	Oxidation	-242	$6.8\text{x}10^{15}$	$1.68\text{x}10^8$	Jones and Lindstedt (1998)
1) All ΔH°_R at 298K and 1 atm. 2) "+" Endothermic (absorbing heat), "-" Exothermic (releasing heat)						

Reaction R 1.4 is not considered in this study since the reactivity of carbon with hydrogen is several orders of magnitude lower compared to other gasifying agents. The volatiles are modeled with a two-step thermal cracking process (R 1.8) and gasification processes (R 1.9 and 1.10) with CH_4 and C_2H_2 as intermediate by-products. The coal used in this study is Illinois No.6 coal, whose composition is given in Table 8.3. The compositions of the volatiles are derived from the coal's heating value, proximal analysis, and ultimate analysis. The oxidant is considered to be a continuous flow and the coal particles are considered to be a discrete phase. The volatiles are modeled to be thermally cracked to CO, H_2, CH_4, and C_2H_2. The N, Cl, and S components are assumed to be converted to N_2, HCl, and H_2S and COS, respectively. Based on the DOE/NETL report (2011), the mole ratio of H_2S/COS is modeled as 5:1. All of the products from cracking the volatiles are considered to be a continuous gas phase.

Table 8.4 The proximal and ultimate analyses of Illinois No.6 bituminous coal

Coal	Illinois No.6
Proximal Analysis (wt%)	
Moisture	11.12
VM	34.99
Ash	9.7
Fixed Carbon	44.19
Heating value (MJ/kg)	27.1

Ultimate Analysis (wt%)	
Moisture	11.12
Ash	9.7
C	63.75
H	4.5
N	1.25
S	2.51
O	6.88
Cl	0.29

8.3 Computational Model

The governing equations, turbulence models, radiation model, discrete phase model, devolatilization model, and reaction model have been stated in Chapter 2 explicitly, so they are not repeated here. Only a brief summary is given, below. The time-averaged, steady-state Navier-Stokes equations as well as the mass and energy conservation equations are solved. The

species transport equations are solved for all gas species involved. The standard k-ε turbulence model is used to provide closure through the Reynolds shear stresses. The P1 model is used as the radiation model. The CPD model is used as the devolatilization model. The flow (continuous phase) is solved using the Eulerian method as a continuum while the particles (dispersed phase) are solved using the Lagrangian method as a discrete phase. A stochastic tracking scheme is employed to model the effects of turbulence on the particles. The continuous phase and discrete phase are communicated through drag forces, lift forces, heat transfer, mass transfer, and species transfer.

8.3.1 Computational Models and Assumptions

The computational domain and elements on the gasifier wall are shown in Figure 8.12. The grid consists of 1,106,588 unstructured tetrahedral cells. The buoyancy force is considered. The varying fluid properties, such as density, specific heat value, thermal conductivity, absorption coefficient, etc. are calculated for each species as a function of temperature and pressure by using a *piecewise polynomial approximation* method. The properties of the gas mixture are calculated using a mass weighted average method.

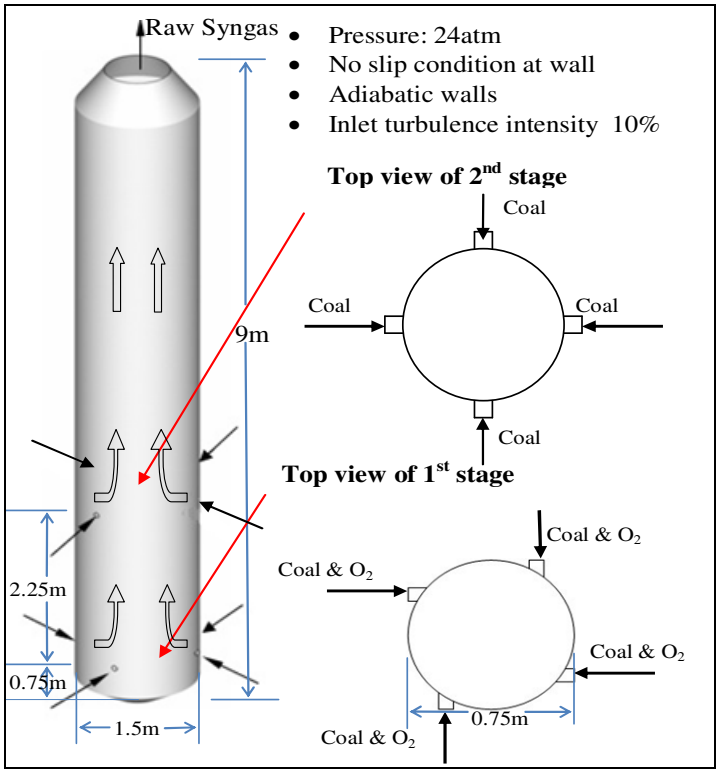

Figure 8.12 Schematic of the two-stage entrained-flow gasifier

8.3.2 Boundary and Inlet Conditions

The total mass flow rates of the dry coal and the oxidant are 10.5 kg/s and 7.64 kg/s, respectively. The total mass flow rate of the coal slurry case is 17.5 kg/s. The difference in fuel mass flow rates is caused by water added for making the coal slurry. The coal/water weight ratio of the coal slurry varies from 60%-40%. Oxidant/coal slurry feed ratio is such that the stoichiometric ratio remains at 0.3. The stoichiometric ratio is defined as the percentage of oxidant provided over the theoretical stoichiometric amount needed for complete combustion of carbon. For the dry coal case, N_2 (5% of the total weight of the oxidant) has been injected with O_2 to transport the coal power into the gasifier.

The oxidant is considered to be a continuous flow, while the coal slurry is considered to be a discrete flow. The discrete phase only includes the fixed carbon and water from the inherent moisture content of the coal (8.25% wt.) and the water added to make the slurry. The slurry coal is treated as particles containing both coal and liquid water. The walls are all set to be adiabatic and are imposed with the no-slip condition (i.e., zero velocity). The boundary condition of the discrete phase at the walls is considered to be "reflect," which means that the discrete phase elastically rebounds off once reaching the wall. The operating pressure inside the gasifier is set at 24 atm. The outlet is set at a constant pressure of 24 bars. From here, the syngas is considered to be a continuous flow, and the coal and char from the injection locations are considered to be discrete particles. The particle size is uniformly given as spherical droplets with a uniform arithmetic diameter of 50 μm. Although the actual size distribution of the coal particles is non-uniform, a simulation using uniform particle size provides a more convenient way to track the devolatilization process of coal particles than a non-uniform size distribution.

8.4 Results and Discussions

8.4.1 Jones and Lindstedt's forward and backward methanation reaction rates (dry coal case)

The first step in the simulation is to use Jones's and Lindstedt's forward and backward methanation reaction rates for the dry coal case. The result of the syngas composition and temperature at the exit of the gasifier is shown in Table 8.4. Due to the high backward rate, reactants cannot be totally consumed and no CH_4 is produced at the exit of the gasifier. The result is the same when only the backward rate is considered in the simulation.

Table 8.5 exit syngas composition and temperature by using the Jones and Lindstedt's forward and backward rates (dry coal case)

Dry coal case	Forward rate: A=5.12×10^{-14}, E= 2.73×10^{4} J/kmol Backward rate: A=4.4×10^{11}, E= 1.68×10^{8} J/kmol
CO	0.38
CO_2	0.12
H_2	0.32
H_2O	0.11
CH_4	<0.01
C_2H_2	0.04
Other species	0.03
Temperature (K)	2142

8.4.2 Investigation of the sensitivity of methane production by varying methanation reaction rates of the dry coal cases

Since the non-catalytic reaction rates for methanation are not known, the CFD scheme can be used as a convenient tool to investigate the sensitivity of methane production on the variation of the methanation reaction rates. The first approach is to only consider the forward rate as the representative of the net global rate of the methanation reaction. The sensitivity study is performed by consecutively changing the pre-exponential rate constant, A, from 5.12×10^{-14} to 5.12×10^{11}, while the activation energy is kept the same as the original value (E = 2.73×10^{4} J/kmol). Table 8.5 shows the result of this sensitivity study in terms of syngas temperature and composition at the gasifier exit. It can be seen that the increased volume fractions of CH_4 (from 0.04 to 0.18) and H_2O (from 0.13 to 0.22) at the exit, and the decreased volume fractions of H_2 (from 0.26 to 0) and CO (from 0.35 to 0.26) adequately indicate the faster rate of the reaction: $CO + 3\ H_2 \rightarrow CH_4 + H_2O$ as the pre-exponential constant value (A) increases from 5.12×10^{-14} to 5.12×10^{11}. The increased exit temperature from 2237 to 2256 K also adequately reflects the exothermic nature of the methanation process. The syngas composition remains the same when

the A value decreases below 5.12×10^{-7} or increases above 5.12×10^{7}. From this sensitivity study, it can be concluded that the approach of using one net global reaction forward rate can be used to match the experimental data once it is available in the future.

Table 8.6 Sensitivity study of methane production and syngas composition on varying the pre-exponential value, A of the Jones and Lindstedt's reaction rate for dry coal cases

A	5.12×10^{-14}	5.12×10^{-7}	5.12	5.12×10^{7}	5.12×10^{11}
CO	0.35	0.35	0.31	0.27	0.26
CO_2	0.14	0.14	0.19	0.23	0.24
H_2	0.26	0.26	0.10	< 0.01	< 0.01
H_2O	0.13	0.13	0.20	0.22	0.22
CH_4	0.04	0.04	0.11	0.18	0.18
C_2H_2	0.04	0.04	0.05	0.06	0.06
Other species	0.03	0.03	0.04	0.03	0.03
T (K)	2237	2238	2487	2520	2556

8.4.3 Investigation of the sensitivity of methane production by varying methanation reaction rates of coal slurry cases

Coal slurry cases have also been studied. Table 8.6 shows that the results of the slurry coal cases are similar to the dry coal cases with increased volume fractions of CH_4 and H_2O, but decreased volume fractions of CO and H_2. The syngas composition remains the same when the A value decreases below 5.12×10^{-7} or increases above 5.12×10^{7}. The only difference between the dry and slurry cases is that the concentration of CH_4 is higher in the dry case (0.18) than in the slurry case (0.11).

Table 8.7 Sensitivity study of methane production and syngas composition on varying the pre-exponential value A of Jones and Lindstedt's reaction rate for coal slurry cases

A	5.12×10^{-14}	5.12×10^{-7}	5.12	5.12×10^{7}	5.12×10^{11}
CO	0.26	0.26	0.23	0.20	0.20
CO_2	0.09	0.09	0.11	0.13	0.13
H_2	0.17	0.17	0.07	< 0.01	< 0.01
H_2O	0.39	0.39	0.45	0.49	0.49
CH_4	0.03	0.03	0.07	0.11	0.11
C_2H_2	0.03	0.03	0.03	0.04	0.04
Other species	0.03	0.03	0.04	0.03	0.03
T (K)	1672	1671	1837	1878	1879

8.5 Conclusion of Chapter Eight

In this chapter, the state-of-the-art, coal-to-synthetic natural gas (SNG) techniques have been reviewed. Steam-oxygen gasification, hydrogasification, and catalytic steam gasification are the three major gasification processes used in coal-to-SNG production. So far, only the steam-oxygen gasification process is commercially proven, by installing a methanation reactor downstream of the gasification process after syngas is produced and cleaned. The methanation process is not considered to be an effective means of synthetic natural gas production due to different reasons including relatively poor efficiency. Therefore, a methanation reactor with catalysts downstream of the gasifier is needed for an SNG process. The methanation reaction rates have also been studied in this chapter. Since the non-catalytic reaction rates for methanation are not known, a CFD scheme can be used as a convenient tool to investigate the sensitivity of methane production on the variation of the methanation reaction rates. The sensitivity study is performed by keeping the activation energy of Jones and Lindstedt's rates intact but changing the pre-exponential constant value, A. Only the forward rate is used to represent the net global rate of the methanation reaction. The result shows that the production of CH_4 can be adequately achieved by varying the pre-exponential constant value (A) of the methanation reaction rates between 5.12×10^{-7} and 5.12×10^{7}. From this sensitivity study, it can

be concluded that the approach of using one net global reaction forward rate can be used to match the experimental data once it is available in the future.

CHAPTER NINE
TOPIC 6: INVESTIGATION OF ASH DEPOSITION BEHAVIOR IN AN ENTRAINED FLOW COAL GASIFICATION PROCESS

9.1 Abstract of Chapter Nine

Fly ash deposition is an important phenomenon associated with ash/slag handling and discharge in the entrained-flow coal gasification process. Fouling and slagging inside the gasifier may cause reliability and safety problems because they can impose strong negative effects on the gasifier wall in the way of heat transfer and chemical corrosion. For these reasons, this chapter focuses on investigating the ash deposition mechanism inside of a two-stage entrained-flow gasifier. The computational model is developed in order to simulate the gasification process with a special effort spent on modeling ash formation, fly ash, and ash deposition. The Eulerian-Lagrangian approach is applied to solve the reactive thermal-flow field and particle trajectories with heterogeneous reactions. The governing equations include the Navier-Stokes equations, twelve species transport equations, and ten global chemical reactions consisting of three heterogeneous reactions and seven homogeneous reactions. The coal/ash particles are tracked with the Lagrangian method. The effects of different coal/ash injection schemes and different coal types on ash deposition have been investigated. The results show that the two-stage fuel feeding scheme could distribute the ash throughout a larger gasifier's volume and, hence, could reduce the peak ash deposition rate and make the ash distribution more uniform inside the gasifier. Gasification of a coal with high ash content results in a high ash deposition rate, low syngas higher heating value (HHV), and low carbon conversion rate. Almost 48% of the un-reacted char will deposit on the wall before it completely gasifies. A char recycling scheme is needed to increase the carbon conversion rate if a high-ash coal is used for gasification.

9.2 Introduction

Gasification is an incomplete combustion process, converting a variety of carbon-based feedstock into clean synthetic gas (syngas), which is primarily a mixture of hydrogen (H_2) and carbon-monoxide (CO) as fuels. Feedstock is partially combusted with oxygen at high

temperature and pressure, using less than 30% of the oxygen required for complete combustion (i.e., 30% of the stoichiometric amount). The syngas produced can be used as a fuel, usually for boilers or gas turbines to generate electricity. It can also be made into a substitute natural gas (SNG), hydrogen gas, and/or other chemical products. Gasification technology is applicable to any type of carbon-based feedstock, such as coal, heavy refinery residues, petroleum coke, biomass, and municipal wastes. To help understand the gasification process in gasifiers and subsequently use the learned knowledge to guide the design of more compact, more cost-effective, and higher performance gasifiers, computational fluid dynamics (CFD) has been widely employed as a useful tool to achieve these goals.

Coal ash is the mineral residue that is obtained as a byproduct of the combustion and gasification of coal. When burned or gasified in industrial reactors, these mineral residuals are discharged from the flue gas or synthetic gas in the forms of fly ash, bottom ash, and slag. Fly ash, which constitutes 85% - 90% of the overall ash, is a fine, light gray powder made up of glassy spheres from less than 1 to more than 100 microns in size, (98% smaller than 75 microns; 70% - 80% smaller than 45 microns). The material has a bulk density of about 0.8 - 1 ton per cubic meter and a maximal density of 1,000 - 1,400 kg/m^3. Fly ash contains cenospheres - hollow spherical particles that have an especially low bulk density of 0.4 - 0.6 tons per cubic meter and constitute up to 5% of the ash weight. Cenospheres are suitable for certain special industrial applications. Bottom Ash, which constitutes about 10% - 15% of the overall ash, has an appearance similar to dark-gray, coarse sand, and its particles are clusters of small granules, up to 10 mm in diameter (60% - 70% smaller than 2 mm. 10% - 20% smaller than 75 microns). It has a bulk density of about 1 ton per cubic meter and a maximal density (modified) of 1,200 - 1,500 kg/m^3 (Israeli National Coal Board, 2013). Most entrained-flow coal gasifiers are designed to operate at temperatures above the ash fusion temperature, in which the ash melts and deposits along the wall, forming a slag layer. Up to 90% of the ash can be discharged as molten slag from the bottom of the furnace or gasifier to a water-quenched slag hopper, where it forms crystal pellets (Chen, et al., 2012). Slagging gasification has the advantages of higher energy efficiency, broader feedstock selection, as well as a higher utilization value of the low-carbon content slag residuals (Beér 2000, Feng, et al., 2003). However, the challenges of ash deposition and slag formation also need to be addressed carefully in the coal gasification process. The fouling and slagging may damage the gasifier equipment and cause maintenance

problems if the optimum operating condition is not reached. For instance, the accumulation and subsequent shedding of large ash deposits could restrict syngas flow, and the molten slag may cause excessive corrosion on the gasifier's refractory wall. Moreover, the slag may encounter a discharging problem when its viscosity becomes high due to gradual solidification (Shao, 2011). Therefore, a good understanding of the ash deposition and slag formation behaviors is imperative to the gasifier's design and optimization as well as operation and maintenance.

Commonly, fouling is initiated by the deposition of ash within a thin layer of condensed vapor. The composition is mainly high in alkali metals (Couch, 1994). The deposition behavior of particles can be explained by the surface deposition of sticky minerals and surface tension of the molten slag. For most cases, the innermost layers consist primarily of small particles, largely formed from sodium (Na), calcium (Ca), and magnesium (Mg) being transported to the surface by vapor phase diffusion and thermophoresis. The initial deposit layers can provide a sticky surface that traps incoming particles. Moreover, the initial layers could provide fluxing materials that will cause larger particles to melt. As a result of the insulating effect of the deposit layer on the surface, the outer layers are formed at higher temperature, which causes the ashes to melt, the molten slag to slide down the surface, and to cause the particles (ash) to interact with the liquid phase (slag). Once the liquid phase has formed at the outer layers, it becomes an efficient collector of ash particles, regardless of the individual melting characteristics of the particles (Xu, et al., 2007).

Ash deposition mechanisms have been widely investigated in coal/biomass combustion reactors. Shao [2011] investigated the ash deposition that occurs during the co-firing of biomass/peat with coal in a pilot-scale fluidized-bed reactor. His study discovered that the fluidized-bed combustion of an individual fuel or a fuel blended with another fuel of higher moisture content produced not only a more uniform temperature profile along the fluidized-bed column but also reduced the ash deposition rate. A higher chlorine concentration in the feed would generally result in a higher tendency of ash deposition. Adding sulfur into the fuel could effectively decrease the chloride deposition in the ash deposits via sulfation. The sulfur addition could also reduce the ash deposition rate for the combustion of lignite, while it slightly increased the ash deposition rate for the peat fuel. Barroso et al. [2006] studied coal ash deposition in an entrained-flow reactor by using ASTM procedures and Computer-Controlled Scanning Electron Microscopy (SEM) The influence of coal type, blend composition, and

operating conditions were investigated separately. A consistent relationship was found between the deposit growth rates and the aerodynamic diameter of the fly ash particles. Fernandez-Turiel, et al. [2004] experimentally studied the ash deposition in a pulverized coal-fired power plant after high-calcium lignite combustion. They discovered that the formation of ash deposits was closely associated with gas-solid reactions. No liquid phases seemed to contribute to either the adhesion to walls or the joining of particles together. On the other hand, alkaline element compounds had no role in the buildup of deposits. Regarding ash deposition in the coal gasification process, Xu et al. [2007] investigated the low temperature ash deposition behavior in a coal gasifier by using an experimental method. A laminar drop tube furnace was utilized in the experiment to simulate ash deposition behavior. They found that the variations of flue gas temperature play an important role in the deposition of ash. Also, the ash deposition rate increases with bigger coal particle size or higher deposit surface temperature and flue gas temperature. Cao, et al. [2011] investigated the characteristics and mechanism of fly ash deposited in the Shell coal gasification process. The chemical composition, particle size distribution, surface topography, and elemental composition of fly ash samples derived from coal A and coal B were studied by an X-ray fluorescence spectrometer, a JX-2000 microscopic image analyzer, and a computer-controlled scanning electron microscope, respectively. The results showed that the ash deposition characteristics are determined by the surface properties and elemental composition of the fly ash particles in different coal types.

The CFD modeling of the ash deposition and slag formation mechanisms has been further developed in the recently years. Ahmadi, et al. [2011] developed a computational model for simulating the gas flow, thermal conditions, and ash transport and deposition patterns in the hot gas filtration systems. The ash particle transport and deposition pattern was analyzed with the Largrangian particle tracking approach. Schulze [2011] developed a CFD based deposit formation model for biomass-fired boilers. The model considered the condensation of ash vapors; deposition of coarse, salt-rich and silica-rich fly ash particles; brittle and ductile erosion of the deposit layer by non-sticky particles; aerosol formation; and ash deposition under the consideration of a single particle size class. Yong et al. [2012] proposed a set of particle trap criteria for the slag-particle interaction and applied it in a 1-D slag flow model. Chen, et al. [2012] expanded Yong's slag model, along with sub-models designed to assess char-slag interaction and wall burning, and implemented it in 3-D CFD simulations of oxy-coal

combustion. The slag deposition and thickness distribution along the circumference of the furnace wall due to a non-uniform flow field was presented. However, the CFD modeling of the ash deposition mechanism in an entrained flow coal gasification process has not been well developed. The purpose of this study is to incorporate the ash deposition mechanism into the complete coal gasification model. Each coal particle has been tracked by the Lagrangian method to go through the processes of: coal surface moisture evaporation, devolatilization, coal combustion, coal gasification, and ash deposition. The ash deposition rates along the gasifier wall are investigated and compared among different cases by employing different coal feeding schemes and using different coal types. Moreover, the effect of the ash deposition rates on the gasification performance, including syngas temperature, composition higher heating value (HHV), and carbon conversion rate are also investigated in this study.

9.3 Global Gasification Chemical Reactions

This study deals with the global chemical reactions of coal gasification that can be generalized in reactions (R1) through (R11) in Table 9.1.

In this study, the volatiles are modeled to go through a two-step thermal cracking process (R7-8) and the gasification processes (R9-10) with CH_4 and C_2H_2 as the intermediate products. The empirical finite rate of the water gas shift reaction, A = 2.75, E = 8.38×10^7 kJ/kmol, is adopted based on the investigation carried out by Lu and Wang [2013].

In order to investigate the effect of the ash content in the coal on the gasification performance, two types of coal with different ash contents are selected in this study. One is Illinois No. 6 coal (Il-6) with an ash content of 9.7% by weight, whose composition is given in Table 9.2. The other coal is West Kentucky No. 11 (WK-11) with an ash content of 31.83% by weight, whose composition is given in Table 9.3. The compositions of the volatiles are derived from each coal's heating value, proximate analysis, and ultimate analysis: $CH_{2.761}O_{0.264}N_{0.055}S_{0.048}Cl_{0.005}$ for Il-6 and $CH_{3.187}O_{0.336}N_{0.06}S_{0.01}$ for WK-11. The oxidant is considered to be a continuous flow, and the coal particles are considered to be the discrete phase. The coal particles include the fixed carbon, volatiles, inherent moisture, and ash. In order to include the resistance of driving the inherent moisture out of the pores of the coals, a simple model is applied by increasing the standard latent heat of H_2O by 20%. For surface water, the standard latent heat is used. The volatiles are modeled such that they are thermally cracked to CO, H_2,

CH_4, C_2H_2, N_2, HCl, H_2S, and COS. Based on DOE/NETL's report (2011), the ratio of H_2S/COS is given to be 5:1. All these cracked volatile products are considered to be part of the continuous gas phase.

Table 9.1 Summary of reaction rate constants used in this study

Reactions		Reaction Type	Reaction heat, ΔH°_R (MJ/kmol)	$k = AT^n\exp(-E/RT)$ (n=0)		Reference
				A	E(J/kmol)	
Heterogeneous Reactions						
R 1	$C(s) + ½\ O_2 \rightarrow CO$	Partial combustion	-110.5	0.052	6.1×10^7	Chen et al.(2000)
R 2	$C(s) + CO_2 \rightarrow 2CO$	Gasification, Boudouard reaction	+172.0	0.0732	1.125×10^8	
R 3	$C(s) + H_2O \rightarrow CO + H_2$	Gasification	+131.4	0.0782	1.15×10^8	
Homogeneous Reactions						
R 4	$CO + ½\ O_2 \rightarrow CO_2$	Combustion	-283.1	2.2×10^{12}	1.67×10^8	Westbrook and Dryer (1981)
R 5	$CO+H_2O(g)\leftrightarrow CO_2+H_2$	Water Gas shift	-41.0	2.75×10^{10}	8.38×10^7	**Jones and Lindstedt (1998)**
R 6	**$CO + 3H_2 \leftrightarrow CH_4 + H_2O$**	**Methanation**	**-205.7**	**$k_f = 5.12\times10^{-14}$**	**2.73×10^4**	
				$k_b = 4.4\times10^{11}$	**1.68×10^8**	**Benyon P.(2002)**
R 7	$CH_{2.761}O_{0.264}N_{0.055}S_{0.048}Cl_{0.005} \rightarrow 0.256CO+0.466H_2+0.33CH_4+0.2C_2H_2+0.0275N_2+0.005HCl+0.04H_2S+0.008COS$	Two-step Volatiles Cracking for Il-6 coal	+4.75	Eddy dissipation		N/A
R 8	$CH_{3.187}O_{0.336}N_{0.06}S_{0.01} \rightarrow 0.8575H_2+0.334CO+0.264CH_4+0.2C_2H_2+0.03N_2+0.008H_2S+0.002COS$	Two-step Volatiles Cracking for WK-11 coal	+140			
R 9	$CH_4 + ½O_2 \rightarrow CO+2H_2$	Volatiles gasification via CH_4	-35.71			
R10	$C_2H_2 + O_2 \rightarrow 2CO + H_2$	Volatiles gasification via C_2H_2	-447.83			
R11	$H_2 + ½\ O_2 \rightarrow H_2O$	Oxidation	-242	$6.8\text{x}10^{15}$	$1.68\text{x}10^8$	Jones and Lindstedt (1998)

1) All ΔH°_R at 298K and 1 atm. 2) "+" Endothermic (absorbing heat), "-" Exothermic (releasing heat)

Table 9.2 The proximate and ultimate analyses of Il-6 coal

Coal	Il-6
Proximate Analysis (wt %)	
Moisture	11.12
VM	34.99
Ash	9.7
Fixed Carbon	44.19
Heating value (MJ/kg)	27.1

Ultimate Analysis (wt %)	
Moisture	11.12
Ash	9.7
C	63.75
H	4.5
N	1.25
S	2.51
O	6.88
Cl	0.29

Table 9.3 The proximate and ultimate analyses of WK-11 coal

Coal	WK-11
Proximate Analysis (wt %)	
Moisture	10.28
VM	26.11
Ash	31.78
Fixed Carbon	31.83
Heating value (MJ/kg)	18.829

Ultimate Analysis (wt %)	
Moisture	10.28
Ash	31.78
C	44.56
H	3.382
N	0.8972
S	3.391
O	5.706

9.4 Computational Model

The governing equations, turbulence models, radiation model, discrete phase model, devolatilization model, and reaction model have been stated in Chapter 1 explicitly, so they are not repeated here, but briefly summarized below. The time-averaged, steady-state Navier-Stokes equations as well as the mass and energy conservation equations are solved. Species transport equations are solved for all gas species involved. The standard k-ε turbulence model with standard wall function is used to provide closure. The P1 model is used as the radiation model. The Chemical Percolation Devolatilization (CPD) model is used as the devolatilization model.

The flow (continuous phase) is solved in Eulerian form as a continuum while the particles (dispersed phase) are solved in Lagrangian form as a discrete phase. A stochastic tracking scheme is employed to model the effects of turbulence on the particles. The continuous phase and discrete phase are communicated through drag forces, lift forces, heat transfer, mass transfer, and species transfer.

9.4.1 Discrete Phase Modeling

Gasification or combustion of coal particles undergoes the following global processes: (1) inert heating, (2) evaporation of surface moisture, (3) devolatilization and demoisturization, (4) coal combustion and gasification, and (5) ash deposition. The initially inert coal particles will go through a heating process to increase the particle temperature. When the surface temperature of a coal particle reaches the vaporization temperature, T_{vap}, the surface moisture starts to evaporate. Water evaporation continues until the droplet reaches the boiling point, T_{bp}, when the inherent moisture starts to evaporate and gets driven out. In the meantime, devolatilization takes place when the temperature of the coal particle reaches the vaporization temperature of the volatiles, and remains in effect until the volatiles are completely vaporized out of the coal particles. Here, the vaporization temperature refers to combusting materials (volatiles), and is different from the vaporization temperature of surface moisture. Silaen and Wang [2008] compared the effect of four different devolatilization models on the gasification process. They concluded that the rate calculated by the Kobayashi two-competing rates devolatilization model is very slow, while that of the Chemical Percolation Devolatilization (CPD) model gives a more reasonable result. Therefore, the CPD model was chosen for this study. The CPD model considers the chemical transformation of the coal structure during devolatilization. It models the coal structure transformation as a transformation of a chemical bridge network, which results in the release of light gases, char, and tar. The initial fraction of the bridges in the coal lattice is 1, and the initial fraction of char is 0. The lattice coordination number is 5. The cluster molecular weight is 400, and the side chain molecular weight is 50.

9.4.2 Particle reactions

The reactions of the particles occur after the devolatilization process has finished. The rate of depletion of solid due to a surface reaction is expressed as:

$$\overline{R} = A\eta YR \tag{9.1}$$

$$R = k\left(p_n - \frac{R}{D} \right)^N \tag{9.2}$$

where

$\overline{R}$ = rate of particle surface species depletion (kg/s)

A = particle surface area (m^2)

Y = mass fraction of the solid species on the surface of the particle

η = effectiveness factor (dimensionless)

R = rate of particle surface species reaction per unit area (kg/m^2-s)

p_n = bulk concentration of the gas phase species (kg/m^3)

D = diffusion rate coefficient for reaction

k = kinetic reaction rate constant (units vary)

N = apparent order of reaction.

The kinetic reaction rate constant is usually defined in an Arrhenius form as

$$k = AT^n e^{-(E/RT)} \ . \tag{9.3}$$

For reaction order N = 1, the rate of particle surface species depletion is given by

$$\overline{R} = A\eta Y p_n \frac{kD}{D+k} \ . \tag{9.4}$$

For reaction order N = 0,

$$\overline{R} = A\eta Y k \ . \tag{9.5}$$

For reaction order N = 0, the unit for the kinetic reaction rate constant, k, is kg/m^2-s.

In the CFD software used, ANSYS/FLUENT, the reaction order of the particle reactions are all equal to 0. Thus, Eq. 9.1 is used to calculate the rate of depletion of the solid, $\overline{R}$ (kg/s). The kinetic reaction rate constant, k (kg/m^2-s), is to be supplied by the user.

The kinetic reaction rate constants, k, for the solid-gas char reactions are determined by the kinetic reaction rate constants adopted from published literatures as presented in Table 9.1.

9.4.3 Ash deposition model

The discrete phase motion is represented by a sufficient number of representative coal particles. The trajectory of each coal particle is calculated by a stochastic tracking method. Each coal particle will go through all the processes stated above: surface moisture evaporation,

devolatilization, coal oxidation, and gasification. The unburned char and ash will either be entrained to the exit of the gasifier by the syngas, or get stuck on the wall and form slag. Slag will be formed when the operating temperature of the gasifier is above the ash fusion temperature. The ash deposition rate in this study is defined as:

$$R_{deposition} = \sum_{P=1}^{N_{particles}} \frac{\dot{m}_p}{A_{face}} \tag{9.6}$$

$N_{particle}$ is the total number of particles stick on the wall cells, which is tracked by Lagrangian method, m_p is the mass of each particle, A_{face} is the area of the cell face at the wall. In this preliminary study, only the ash deposition rate is considered for the ash deposition mechanism. The particle-wall interaction and slag forming mechanism will be in a future study.

9.4.4 Coal particle motion theory

In this study, coal particles are treated as a discrete phase, so the Lagrangian method is adopted to track each particle. The discrete phase is justified in entrained-flow gasification process because the average particle concentration is lower than 10%. Particles in the airflow can encounter inertia and hydrodynamic drag. Because of the forces experienced by the particles in a flow field, the particles can be either accelerated or decelerated. The velocity change is determined by the force balance on the particle, which can be formulated by:

$$\frac{du_p}{dt} = F_D + F_g + F_x \tag{9.7}$$

where F_D is the drag force per unit particle mass and:

$$F_D = \frac{18\mu}{\rho_p d_p^2} \frac{C_D Re}{24} (v - v_p) m_p \tag{9.8}$$

where m_p is the particle mass, d_p is the particle diameter, v is the fluid phase velocity, v_p is the particle velocity, ρ is the fluid phase density, ρ_p is the particle density, g is gravity, μ is the fluid phase molecular viscosity, and C_D is the drag coefficient. The gravitational force, F_g, is calculated as the second term in equation 9.7 as:

$$F_g = \frac{g(\rho_p - \rho)}{\rho_p} m_p \tag{9.9}$$

The relative Reynolds number, Re, is defined as:

$$\mathrm{Re} = \frac{\rho d_p \left| v_p - v \right|}{\mu} \tag{9.10}$$

F_x in equation 9.1 is an additional acceleration (force/unit particle mass) term, and typically includes the "virtual mass" force, thermophoretic force, Brownian force, Saffman's lift force, etc.

9.4.4.1 Virtual mass force

The "virtual mass" force is the force required to accelerate the fluid surrounding the particle. This force can be written as:

$$F_x = \frac{1}{2}\frac{\rho}{\rho_p}\frac{d}{dt}(u - u_p) \tag{9.11}$$

This force is important only when $\rho > \rho_p$. It is not included in this study since the density of each coal particle is much larger than the density of the surrounding gas mixture.

9.4.4.2 Brownian force

The Brownian force is caused by the random impacts of the particles with agitated gas molecules. For submicron-sized particles, the Brownian force could be quite important. In particular, near solid surfaces where the intensity of turbulence becomes negligibly small, the Brownian force could be an important transport mechanism. In this study, the size of each coal particle is 50μm, so the Brownian force is not included.

9.4.4.3 Saffman's lift force

The Saffman's lift force, or lift due to shear, is based on the derivation from Li and Ahmadi [17], which is expressed in a generalized form originating from Saffman [18]:

$$\vec{F} = \frac{2Kv^{1/2}\rho d_{ij}}{\rho_p d_p (d_{lk} d_{kl})^{1/4}} (\vec{v} - \vec{v_p}) \tag{9.12}$$

where K = 2.594 and d_{ij} is the deformation tensor. This form of the lift force is intended for small particle Reynolds numbers. Also, the particle Reynolds number based on the particle-fluid velocity difference (slip velocity) must be smaller than the square root of the particle. The

Reynolds number is based on the shear field. In this study, Saffman's lift force reaches about 30% of F_g, so it is included in the particle motion model.

9.4.4.4 Magnus Force

The Magnus force is the lift force acting on a particle that develops due to its rotation. The lift is caused by the pressure difference between both sides of the particle, resulting from the velocity difference between the same due to rotation. Kallio and Reeks [1989] noted that, in most regions of the flow field, the Magnus force is not important and at least an order of magnitude smaller than the Saffman force. As a consequence, it is ignored in this study.

9.4.4.5 Thermophoretic Force

When a particle exists in a flow field with temperature gradients, the force that arises on the particle due to this temperature gradient is called the thermophoretic force. This force is caused by the unequal momentum between the particle and the fluid. The higher molecular velocities on one side of the particle due to the higher temperature give rise to more momentum exchange and a resulting force in the direction of decreasing temperature. An extensive review of thermophoresis by Talbot et al. [1980] indicated that the following equation for the thermophoretic force, F_x, provides the best fit with experimental data over a wide range of Knudsen numbers:

$$F_x = -\frac{6\pi d_p \mu^2 C_s (K + C_t Kn)}{\rho(1+3C_m Kn)(1+2K+2C_t Kn)} \frac{1}{m_p T} \frac{\partial T}{\partial x} \tag{9.13}$$

where

Kn = Knudsen number = $2\lambda/dp$

λ = mean free path of the fluid

$K = k/k_p$

k = fluid thermal conductivity based on translational energy only = $(15/4)\,\mu R$

k_p = particle thermal conductivity

$C_S = 1.17$

$C_t = 2.18$

C_m = 1.14

m_p = particle mass

T = local fluid temperature

μ= fluid viscosity

This expression assumes that the particle is a sphere and that the fluid is an ideal gas. In this study, the local temperature gradient in the flow field is important because of local combustion and gasification reactions between the coal particles and gas mixture. Therefore, the thermophoretic force is considered in this study.

9.4.5 Turbulent Dispersion of Particles

The dispersion of particles due to turbulence in the fluid phase is predicted by using a stochastic tracking scheme, which is modeled with the eddy lifetime. In this model, each eddy is characterized by the Gaussian-distributed, random velocity fluctuations u', v', w', and a time scale τ_e. Therefore, the particle trajectories are calculated by using the instantaneous flow velocity (u) rather than the average velocity ($\bar{u}$). The velocity fluctuation is then given as:

$$u = \bar{u} + u', \qquad u' = \zeta\left(\overline{u'^2}\right)^{0.5} = \zeta(2k/3)^{0.5} \qquad (9.13)$$

where ζ is a normally distributed random number. This velocity will apply during a characteristic lifetime of the eddy (t_e), calculated from the turbulence kinetic energy and dissipation rate. After this time period, the instantaneous velocity will be updated with a new ζ value until a full trajectory is obtained.

9.4.6 Computational Models and Assumptions

The computational domain and elements on the gasifier wall are shown in Figure 9.1. The grid consists of 1,106,588 unstructured tetrahedral cells. In the simulation, the buoyancy force is considered, varying fluid properties are calculated for each species and the gas mixture, and the walls are assumed impermeable and adiabatic. Since each species' properties, such as density, C_p-value, thermal conductivity, absorption coefficient, etc. are all functions of temperature and pressure, their local values are calculated by using a *piecewise polynomial approximation* method. The mixture properties are calculated by taking the mass-weighted

average. The flow is steady and the no-slip condition (zero velocity) is imposed on the wall surfaces.

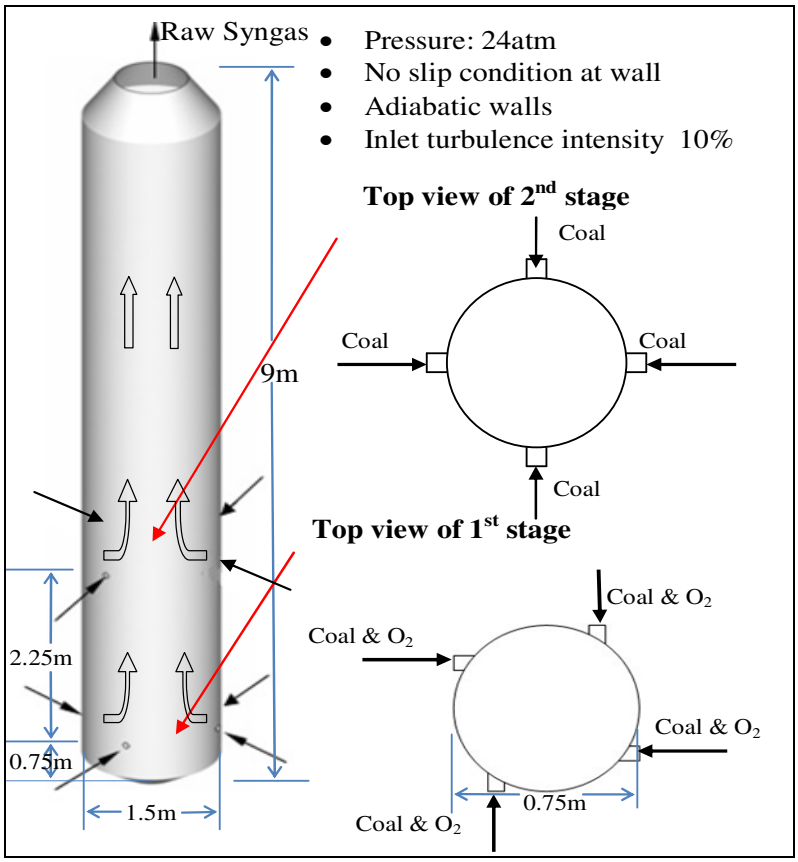

Figure 9.1: Schematic of the two-stage entrained-flow gasifier

9.4.7 Boundary and Inlet Conditions

The total mass flow rates of the Il-6 bituminous coal and the oxidant are 11.4 kg/s and 7.64 kg/s, respectively. The total mass flow rate of WK-11 coal and the oxidant are 11.4 kg/s and 5.36 kg/s, respectively. The gasifier's capacity is around 1000 tons of coal perday, and the energy output rate is around 110 MW. These oxidant/coal slurry feed rates both give the same O_2/C stoichiometric equivalence ratio of 0.3. The equivalence ratio is defined as the percentage of oxidant provided over the stoichiometric amount for complete combustion of carbon. For the dry coal case, N_2 (5% of the total weight of the oxidant) has been injected with O_2 to transport the coal powder into the gasifier. Both moisture and ash are treated as part of the coal particles

in the discrete phase model, while N is treated as N_2, Cl as HCl, and S as H_2S/COS through the volatile cracking model. All of these cracked volatile products are considered to be a continuous gas phase.

The oxidant is considered to be a continuous flow, and the dry coal is considered to be a discrete flow. The discrete phase includes surface moisture, volatile matters, fixed carbon, and ash. The walls are all set to be adiabatic and are imposed with the no-slip condition (i.e., zero velocity). The boundary condition of the discrete phase at the walls is assigned as "trap," which means that the unburned char and ash particles will stick on the wall when they reach the wall boundary. This is the simplest model for ash deposition based on the assumption that the slagging wall is extreme sticky, so it traps all of the incoming particles once they touch the wall. More complex models will be established to investigate the criteria of the ash "trap" and "rebound" conditions, which are related to the characteristics of the particles' incoming velocities, diameters, and approaching angles; the slag surface tension; and the local wall temperature. The operating pressure inside the gasifier is set at 24 atm. The outlet is set at a constant pressure of 24 atm. The syngas is considered to be a continuous flow, and the coal particles from the injection locations are considered to be discrete particles. The particles are considered to be perfectly spherical droplets of uniform size with a diameter of 50 μm each. Although the actual size distribution of the coal particles is non-uniform, a simulation using a uniform particle size distribution provides a more convenient way to track the devolatilization process of coal particles than a non-uniform size distribution.

The computation is performed using the finite-volume-based commercial CFD software, FLUENT 14.0, from ANSYS, Inc. The simulation is steady-state and uses the pressure-based solver, which employs an implicit pressure-correction scheme and decouples the momentum and energy equations. The SIMPLE algorithm is used to couple the pressure and velocity. The second-order upwind scheme is selected for spatial discretization of the convective terms. For the gas/particle phase coupling, where the Eulerian-Lagrangian approach is used, the iterations are conducted by alternating between the continuous and the discrete phases. Initially, one iteration in the continuous phase is conducted followed by one iteration in the discrete phase to avoid having the flame die out. The iteration number in the continuous phase gradually increases as the flame becomes more stable. Once the flame is stably established, fifteen iterations are performed in the continuous phase followed by one iteration in the discrete phase.

The drag, particle surface reactions, and mass transfer between the discrete and the continuous phases are calculated. Based on the discrete phase calculation results, the continuous phase is updated in the next iteration, and the process is repeated.

Converged results are obtained when the residuals satisfy a mass residual of 10^{-3}, an energy residual of 10^{-5}, and momentum and turbulence kinetic energy residuals of 10^{-4}. These residuals are the summation of the imbalance in each cell.

The following four cases are studied.

Case 1:Il-6 coal, 100% - 0% distribution only in the first stage

Case 2:Il-6 coal, 50%-50% equal distribution in 2 stages

Case 3: Il-6 coal, 25%-75% distribution in 2 stages

Case 4: WK-11 coal, 50%-50% equal distribution in 2 stages

The summary of the studied cases are listed in Table 9.4. In the baseline (Case 1) of this study, a dry-fed, two-stage configuration is used with a fuel distribution of 100%-0% between the first and the second stages.

9.5 Results and discussions

9.5.1 Effect of different coal injection schemes on ash deposition rate

One of the purposes of employing a two-stage coal injection scheme is to keep the gasifier temperature low downstream from the 2nd stage, and, thus, extend the life of the refractory bricks, decrease the gasifier shut-down frequency for maintenance, and reduce maintenance costs. By only injecting a certain amount of dry coal without oxygen in the second gasifier stage, only endothermic gasification reactions will occur, thus lowering the exit temperature of the syngas compared to a one-stage injection scheme. Table 9.4 shows the results of syngas composition, temperature, and higher heating value (HHV) at the exit of the gasifier for Cases 1, 2, and 3. The more coal is injected into the second stage of the gasifier, the lower the syngas temperature is at the exit of the gasifier. The exit syngas temperature decreases from 2,079 K (Case 1) to 1,902 K (Case 2), and further to 1,819 K (Case 3). The results show that the carbon conversion rates are the same for each coal feeding scheme: all three cases reach 98% carbon conversion, but the syngas higher heating value (HHV) increases from 205,896

kJ/kmol to 208,726 kJ/kmol when the coal (no oxygen) feeding at the second stage increases from 0% to 75%.

Figure 9.2 shows the selected coal particle traces inside of the gasifier. The tangential fuel injectors at the first stage make the coal particles spiral upward, providing more surface interaction between the solid particles and the continuous flow. Most of the coal particles move closer to the wall rather than occupy the central part of the gasifier due to the centrifugal force generated by the spiraling motion. In addition to the pathlines plots shown in Figure 9.2, this phenomenon can be also evidenced in the coal particle concentration plots shown in Figure 9.3 for all three cases with or without second-stage injections. In Case 1, 100% of the coal particles are injected at the first stage, so the highest particle concentration appears in the lower part of the gasifier, close to the second fuel injection area. In Case 2, 50% of the coal particles are injected at the second stage, so the particle concentration is distributed more uniformly along the gasifier compared to Case 1, although the highest particle concentration still appears in the lower part of gasifier. In Case 3, heavy loads of particle concentration start to show up in the upper part of gasifier, since 75% of the coal particles are injected at the second stage. All of the characteristics of coal particle movement are shown as pathlines in Figure 9.2, and the distribution of particle concentration inside the gasifier is shown in Figure 9.3. Both of these factors directly affect the ash deposition phenomenon. Figure 9.4 shows the contour and area-averaged ash deposition rates along the gasifier height for the first three cases. In Case 1, the ash deposition rate in the upper part of the gasifier is much higher than it is in the bottom of gasifier. The highest ash deposition rate is around 0.051 kg/m^2-s, appearing at the height of 4 m, which is roughly 1 m higher than the second fuel injection stage. In Case 2, as 50% of the coal is injected at the second stage, the peak ash deposition rate appears at the same location as Case 1, but the value is reduced to 0.032 kg/m^2-s, which is 63% of the value seen in Case 1. The ash deposition rate in the upper part of the gasifier decreases from Case 1 because 50% of the coal particles are injected at the second stage. In Case 3, since 75% of the coal is injected at the second stage, the peak ash deposition rate shifts to the upper part of gasifier, at the height of 7.5 m. The peak value is about 0.027 kg/m^2-s, which is about 53% of the peak deposition rate in Case 1. Compared to the one-stage fuel injection scheme, the two-stage fuel injection scheme could distribute ash deposition into a larger gasifier's area and, hence, reduce peak ash deposition, locally. A more uniform ash distribution can hypothetically form a more uniformly-

distributed, solidified slag layer to protect the wall refractory. However, when the slag layer grows thicker, the outer layer will start to flow down as molten slag. Another slagging model will be needed to simulate the ash melting and molten ash solidification and flowing phenomena. The ash deposition rate predicted by this study can serve as a useful boundary condition for slagging models.

Table 9.4 The syngas composition, temperature and higher heating value (HHV) at the exit of gasifier for Cases 1, 2, and 3

Syngas (vol%)	Case 1 100%-0%	Case 2 50%-50%	Case 3 25%-75%
CO	0.39	0.39	0.40
CO_2	0.11	0.11	0.10
H_2	0.32	0.32	0.32
H_2O	0.10	0.11	0.10
Other species	0.08	0.07	0.08
T (K)	2079	1902	1819
HHV (kJ/kmol)	205,896	206,303	208,726
Carbon Conversion Rate	98%	98%	98%

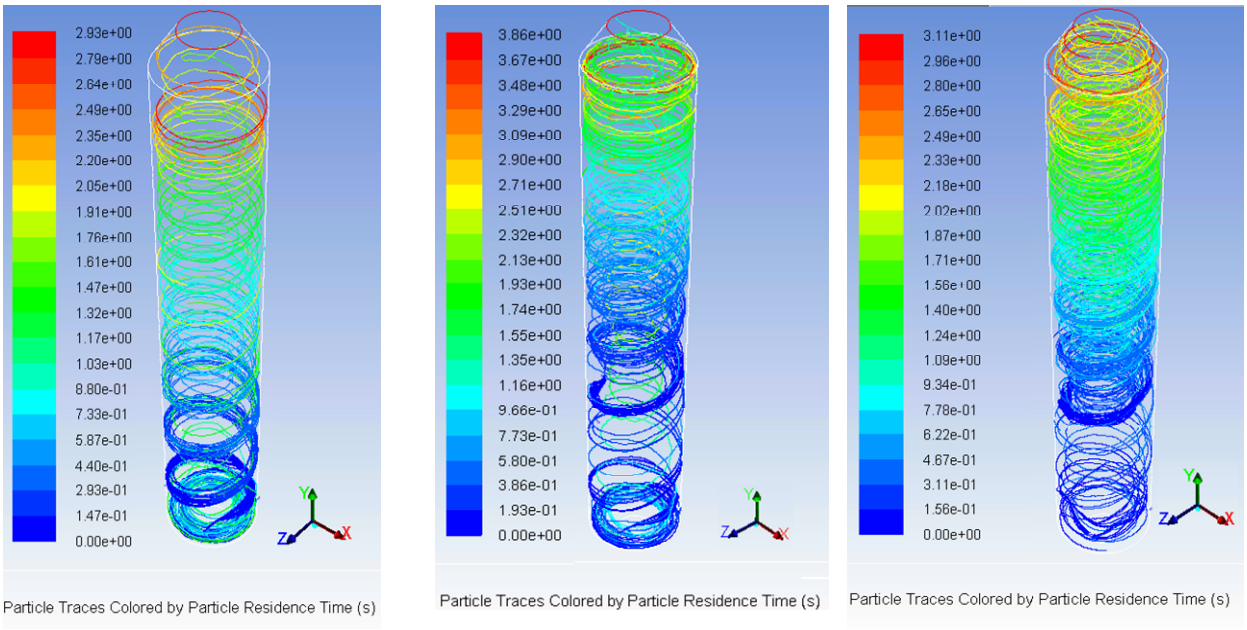

100%-0%
Case 1

50%-50%
Case 2

25%-75%
Case 3

Figure 9.2. Coal particle traces for Cases 1, 2, and 3

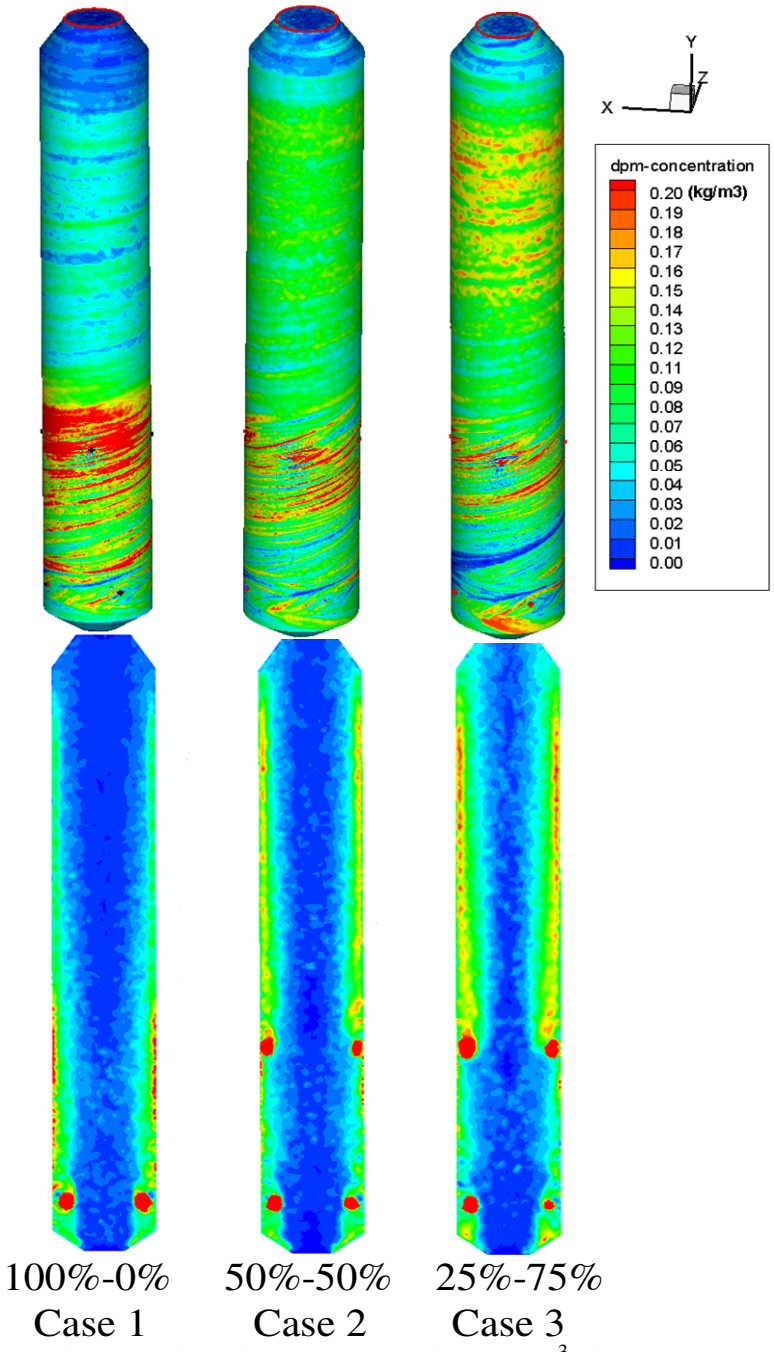

Figure 9.3. Contour of the coal particle concentration (kg/m^3) for Cases 1, 2, and 3. The upper figures show the coal particle concentration on the wall while the lower figures show the coal particle concentration on the central plane.

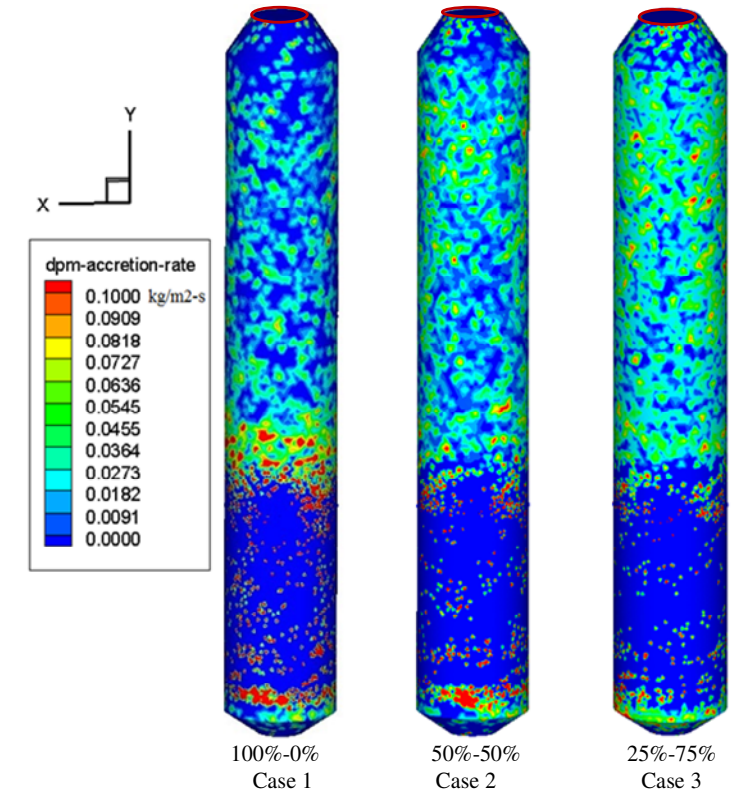

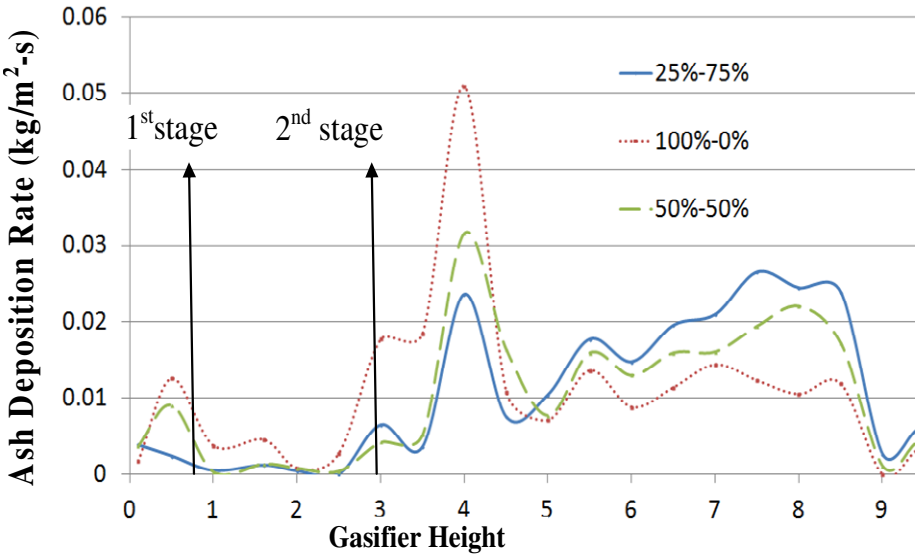

Figure 9.4. Area-weighted average ash deposition rates along the gasifier for Cases 1- 3

9.5.2 Effect of different types of coal on ash deposition rate

In order to investigate the effects of using coals with different ash contents on the ash deposition rate in the gasifier, West Kentucky (WK) No. 11 coal has been used as a

representative of coals with high ash content. In this case, the ash content is 31.78% by weight. The detailed WK-11 coal information is shown in Table 9.3. The 50%-50%, two-stage coal feeding scheme is employed, and the result is compared with the previously described Case 2. Table 9.5 shows the comparison of syngas composition, temperature, and HHV at the exit between Cases 2 and4. It can be seen that WK-11 coal has a poor gasification performance because of the low carbon conversion rate, 52%. WK-11 coal has 31.78% ash content, which is about two times more than the ash content in Il-6 coal. This non-reactive, high ash content seems to inhibit the effective reaction of carbon in the coal particles. Thus, most of the particles that hit the wall, and are subsequently trapped by it, contain unburned char. The low carbon conversion rate leads to a lower syngas HHV. Based on the total syngas HHV rate at the exit of the gasifier, the value in Case 4 (WK- 11 coal) is 114,432 kW, only 61% of the value 188,706 kW in Case 2 (Il-6 coal). Figure 9.6 shows the area-weighted average of the ash deposition rates along the gasifier walls for Cases 2 and 4. The peak ash deposition rates of both cases appear at the same location: at the height of 4 m. However, the peak ash deposition rate for Case 4 is around 0.35 kg/m^2-s, which is about 11 times the value found in Case 2. Table 9.5 shows both the char and ash deposition rates for Cases 2 and 4. The large difference of the ash deposition rates between Case 4 and Case 2 is caused by two reasons. First, the ash content of WK-11 coal is 3.3 times that of Il-6. The total ash deposition rate at the wall in Case 4 is 3.619 kg/s, which is 3.9 times that of Case 2 (0.922 kg/s). Second, most of the coal particles are trapped by the wall before they can completely react with the oxygen and syngas. The total un-reacted char deposition on the wall in Case 4 is 1.752 kg/s, which is 19 times that of Case 2. If using WK-11 coal for gasification, the large amount of un-reacted char is deposited on the wall together with the ash, and the carbon conversion rate is very low, only 52%. Since almost no char can escape to the exit of the gasifier (0.007 kg/s in Case 4), the char recycling scheme cannot help to increase the carbon conversion rate or improve the gasification performance if a high ash content coal is used.

Table 9.5 The syngas composition, temperature and HHV at exit of gasifier for Case 2, 4

Syngas (vol%)	Case 2 Il-6	Case 4 WK-11
CO	0.39	0.28
CO_2	0.11	0.10
H_2	0.32	0.34
H_2O	0.10	0.19
Other species	0.08	0.09
Exit T (K)	1902	1015
HHV (kJ/kmol)	206,303	184,142
Total HHV rate (kJ/s)	188,706	114,432
Carbon Conversion Rate	98%	52%
Char at exit (kg/s)	0.010	0.007
Total char deposition on thewall (kg/s)	0.092	1.752
Ash at the exit (kg/s)	0.097	0.016
Total ash deposition on the wall (kg/s)	0.922	3.619

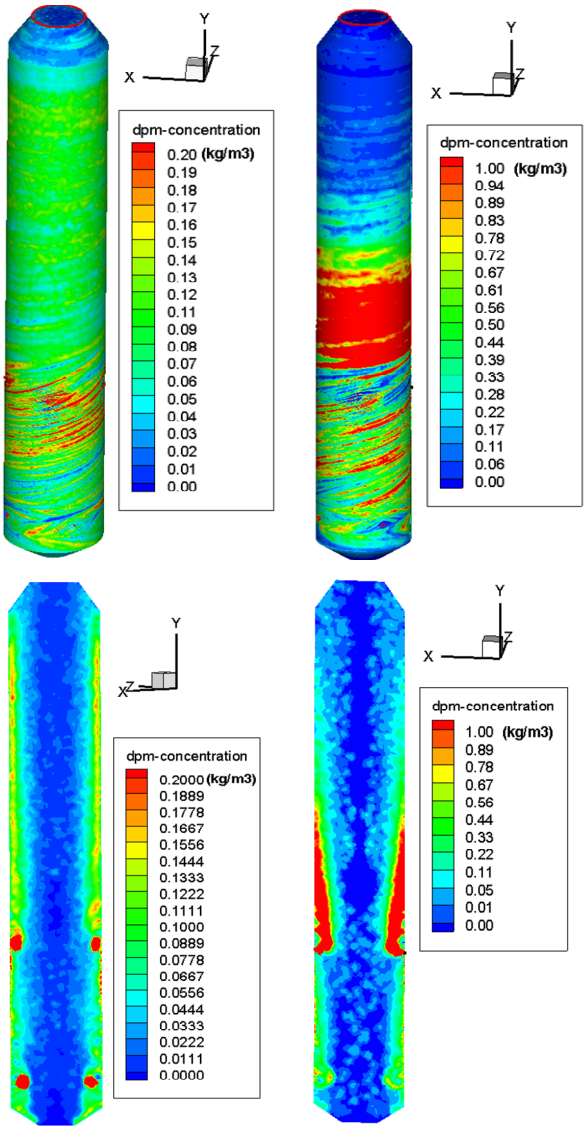

Il-6 coal Case 2

WK-11 coal Case 4

Figure 9.5 Coal particle concentrations for Cases 2 and 4. (The upper figures show the coal particle concentration on the wall while the lower figures show the coal particle concentration on the central plane)

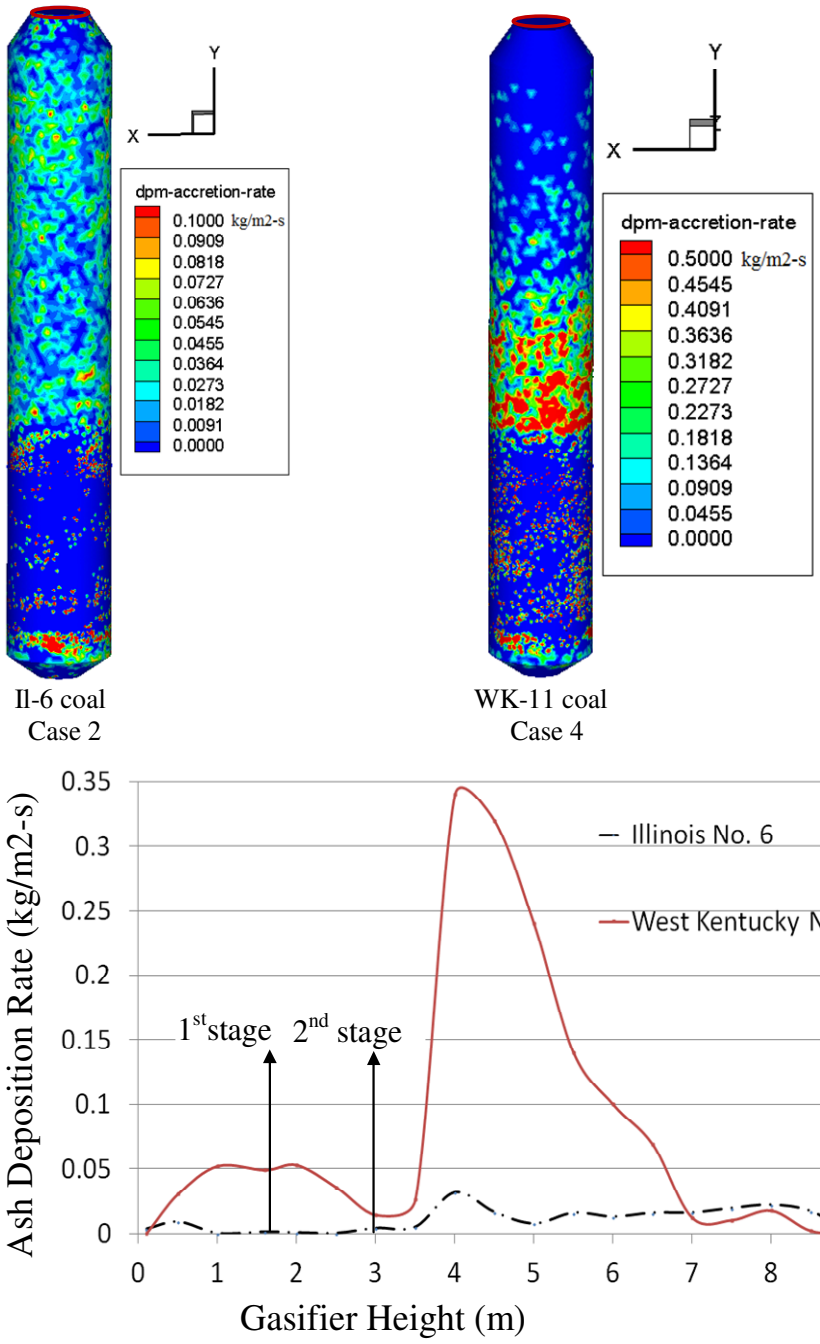

Figure 9.6 Area-weighted average ash deposition rates along the gasifier wall for Cases 2 and 4

9.6 Conclusions of Chapter Nine

In this study, the ash deposition has been modeled by assuming that all of the particles will be trapped on the wall once they touch the wall. The ash deposition rate and deposition

distribution are investigated by modeling the complete coal gasification process. Each coal particle has been tracked by the Lagrangian method as it goes through the process of coal surface moisture evaporation, devolatilization, coal combustion, coal gasification, and ash deposition. Both moisture and ash are treated as part of the coal particles in the discrete phase model. The ash deposition rates along the gasifier wall are investigated and compared between different cases by employing different coal feeding schemes and using different coal types. Moreover, the effect of the ash deposition rate on gasification performance, including syngas temperature, composition, and higher heating value (HHV), in addition to the carbon conversion rate are also investigated in this study. This study considers both a low-ash coal (Il-6) and a high-ash coal (WK-11). The conclusions are summarized below:

- Compared to the case using one-stage fuel feeding, the peak ash deposition rate for the case using a 50%-50% fuel feeding scheme appears in the same location of the gasifier, at the height of 4m, but the value decreases to 63% of that from the one-stage feeding case. In the case using a 25%-75% fuel feeding scheme, the peak ash deposition rate appears at the height of 7.5m, and the value decreases to 53% of that from the one-stage fuel feeding case.
- A two-stage fuel feeding scheme could distribute the ash into a larger gasifier's wall surface area and, hence, reduce the peak ash deposition rate and make the ash distribution more uniform within the gasifier.
- Compared to the low-ash-content coal (Ill-6) gasification, the high-ash-content coal (WK-11) gasification has both a high peak ash deposition rate and a high overall ash deposition rate. The peak ash deposition rate of WK-11 is around 0.35 kg/m^2-s, which is about 11 times that of Il-6. The overall area-weighted average ash deposition rate on the gasifier wall of WK-11 coal is 0.12 kg/m^2-s, which is 6.7 times that of Il-6 (0.018 kg/m^2-s).
- The high-ash-content coal gasification has a low syngas HHV and carbon conversion rate. The total syngas HHV of WK-11 is 114,432 kJ/s, only 61% of the value (188,706 kJ/s) of Il-6. The carbon conversion rate in WK-11 coal is 52%: that means that 48% un-reacted chars have deposited on the wall before they complete the coal gasification reactions. Since almost no char escapes to the exit of the gasifier (0.007 kg/s in Case 4), a

char recycling scheme cannot help to increase the carbon conversion rate or improve the gasification performance if a high ash content coal like WK-11 is used.

CHAPTER TEN
CONCLUSIONS

10.1 Summary

A comprehensive modeling and numerical investigation of entrained-flow coal gasifier have been conducted. A fundamental study is carried out to calibrate Water-Gas-Shift (WGS) reaction rates under non-catalytic condition with experimental data of both water quench process and gasification process. Another study focuses on investigating applications of five different radiation models to coal gasification process. A study of low rank coal gasification is also conducted, the gasification performance has been compared with high rank coal gasification. In the study of coal to synthetic natural gas (SNG) process, the state-of-art SNG techniques, as well as the mathanation reaction rates have been reviewed and investigated. In the study of ash deposition mechanism in coal gasification process, the ash deposition rates along the gasifier wall are investigated in different cases by employing different coal feeding schemes and using different coal types. A collaborative study has been conducted with the Industrial Technology Research Institute (ITRI) of Taiwan to help with its design and modifications of a demonstration coal gasifier (two-stage oxygen feeding configuration design and water quench design). In return, ITRI's experimental data and operating experience are shared with the University of New Orleans.

10.2 Conlustions

10.2.1 Calibration of WGS reaction rates

The WGS reaction rate has been discovered to affect notably the result of CFD modeling of coal gasification processes in a gasifier. Almost all of the published WGS rates were conducted with catalysts under limited temperature ranges and at a certain fixed pressure condition. Only a few WGS rates were obtained without involving catalysts, but they were performed under supercritical (water) conditions. Therefore, employing any of the published WGS reaction rates to simulate the coal gasification process in a gasifier, which usually doesn't use catalysts and doesn't operate at the same temperature or pressure conditions as in the laboratory conditions, is likely to result in misleading or uncertain results. To help calibrate the

global WGS reaction rates, three published WGS reaction rates are used in this study. They are Jones's rate (A = 2.75×10^{10}, E = 8.38×10^{7} J/kmol,) Wade's rate (A = 2.512×10^{5}, E = 1.325×10^{5}J/mol,) and Sato's rate (A = 105.58 ±1.38, E = 1.16x 105 J/mol.) The study is focused on both water quench section of ITRI gasifier, which only involves WGS reaction, and fully gasification process in the Japanese CRIEPI gasifier. Calibrated WGS rates are derived from comparing CFD results the experimental data, as well as with thermodynamic equilibrium results. The conclusions are:

1) All of the originally published rates cannot work well in the simulation of both water quench process and coal gasification process due to different temperature and pressure range. Adding the backward WGS reaction rate (Jones' rate) as a separate reaction equation results in the same gas composition and temperature at the gasifier exit as the case without adding the backward WGS reaction rate.
2) For water quench part, the result of employing the forward and backward rates from NETL is very similar to that of Jones' rate—the forward rate dominates the process (too fast) and the computed mole fractions of H_2 and CO_2 are higher than the experimental data while that of CO is lower.
3) Applying the chemical equilibrium approach further verifies that original WGS rates are too fast in applying in the range of water quench operation parameters.
4) Each of the three rates are slowed down by consecutively reducing the pre-exponential rate constant, A, while the activation energy is kept the same as the original value. The results show that all three WGS reaction rates can match the experimental data well by reducing the value of the pre-exponential rate constant, A. For the results of gasification process, the exit temperature can be matched within 2% (20K). The mole fractions of CO and H_2O can be matched fairly well within 4 percentage points (or 10%); however, the simulated H_2 mole fractions are always 7-9 percentage points (or about 40%) higher than the experimental data.
5) The calibrated global WGS reaction rates that best match the experimental data of ITRI water quench process are:

- Modified Jones's rate: A = 2.75, E = 8.38×10^{7} J/kmol
- Modified Wade's rate: A = 2.512×10^{-3}, E = 1.325×10^{5}J/mol and
- Modified Sato's rate: A = 1×10^{-3}, E = 1.16×10^{5} J/mol

6) The calibrated global WGS reaction rates that best match the experimental data of Japanese CRIEPI coal gasification process are:

- Modified Jones's rate: A = 2.75, E = 8.38×10^7 J/kmol
- Modified Wade's rate: A = 2.512×10^{-3}, E = 1.325×10^5J/mol and
- Modified Sato's rate: A = 1×10^{-3}, E = 1.16×10^5 J/mol

7) There is a two orders of magnitude difference of the pre-exponential rate constant, A, between the calibrated WGS reaction rates derived from these two different simulations. This deviation is mainly caused by two different types of experiments. For the WGS rate which calibrated by the water quench experimental data, is only involved WGS reaction, the operating pressure is 3atm, the temperature range inside of domain is around 700K-1000K. For the real entrained flow gasification process, it is involved nine reactions, include devolatilization, combustion and gasification process. More species and reactions make the case become much more complicated than water quench process. Furthermore, the operating pressure of the gasification process is 20 atm, the temperature range is approximate 1000K-1700K. All these factors could affect the WGS reaction rate in different reaction processes.

It needs to be emphasized that the modified reaction rates are obtained under air-blown and dry-fed operating conditions. These modified rates may not be applicable to slurry-fed or oxygen-blown gasifiers because the higher water vapor concentration in slurry-fed gasifiers and higher operating temperatures in oxygen-blown gasifiers may affect the global WGS rate. More studies, as well as more adequate experimental data, are needed in the future. The adequate data are those data taken immediately at the end of gasification section but right before the syngas cooling section in the gasifier, and it is important that the water vapor concentration must be included. An alternative approach is to include the kinetics of elementary reactions instead of taking a global data match on the condition that the adequate elementary reactions are known.

10.2.2 Effect of radiation models

Five different radiation models have been tested through three different operating conditions of gasification process. The results of syngas composition, syngas temperature, as well as the inner wall temperature in each case have been compared. The conclusions are the following:

a. Rosseland model does not yield reasonable and realistic results for gasification process. It either predicts an uncharacteristic nearly-constant syngas and wall temperature distributions along the gasifer for the slurry coal cases or a unreasonably large swing of temperature from very high to very low and back to very high value along the gasifier for the dry-coal feed case.
b. Inner wall temperature is more uniform in the case of S2S model than any other radiation models, since S2S model only considers the enclosure radiation transfer without including participating media.
c. The effect of radiation is much more significant in predicting the inner wall temperature than syngas temperature distribution.
d. The P1 model always predicts the lowest inner wall temperature in all the cases.
e. The DTRM model predicts very high syngas and wall temperatures in the dry coal feed case. In the one-stage coal slurry case, DTRM result is close to the S2S result.
f. DO and DTRM model take about twice more CPU time than the other models.

In this study, the various radiation models yield uncomfortably large uncertainties in predicting syngas composition (18%), syngas temperatrure (21%), and wall temperature (28%). No solid conclusion can be derived from this study without a comparison with detailed experimental data consisting of local syngas composition and temperature information, as well as of the inner wall temperature distribution of the gasifier. However, it is fair to note that the Rosseland model does not seem to work reasonably well for simulating the gasification process. The P1 method seems to behave stably and is robust in predicting the syngas temperature and composition, but it seems to underpredict the gasifier's inner wall temperature.

10.2.3 Study of low-rank coal gasification

This study focuses on low-rank coal gasification study. South Hallsville lignite as low-rank coal and Illinois No.6 bituminous coal as high-rank coal are used in this study. Several comparisons have been conducted on the same operation conditions: 1) low-rank coal vs. high-rank coal; 2) one-stage injection vs. two-stage injection; 3) low-rank coal with pre-drying process vs. no pre-drying process; 4) dry coal feeding without steam injection vs. with the steam injection at the second stage. Several conclusions are drawn as follows:

1) Syngas produced from lignite has 21% (538 K) lower exit temperature and 18% (30222 kJ/kmol) greater HHV than syngas produced from Illinois #6 (high-rank coal). Based only on this result of HHV value, low-rank coal could be a better alternative fuel for coal gasification process.

2) One-stage fuel feeding scheme and two-stage fuel injection scheme have similar syngas composition and HHV at the exit. However, the two-stage fuel feeding scheme could provide lower wall temperature (around 100 K) in the lower half of the gasifier than the single-stage injection scheme. Introduction of the second injection with a pair of opposing jets produces a flattened plane stretching the hot reaction zone laterally toward wall, resulting to the peak wall temperature about 0.3 meter downstream of the second injection location.

3) Without pre-drying, the high inherent moisture content in the lignite the produced syngas HHV reduces 27% and mole fraction of both H_2 and CO reduce 33%, while the water vapor content increases 121% (Vol). The low-rank coal without pre-drying process will take longer time to finish demoisturization and devolatilization process, resulting in delayed combustion and gasification process.

4) When coal slurry with the mass ratio of total water (inherent moisture + surface moisture) 40% - 60%, is injected into the gasifier at second stage for the pre-dried lignite, the exit syngas temperature reduces 15% (323 K) from Case 1. The syngas HHV in Case 5 decreases 39% (77,951kJ/kmol).

10.2.4 Study of Coal-to-Synthetic Natural Gas process (SNG)

In this chapter, the state-of-art coal-to-synthetic natural gas (SNG) techniques have been reviewed. Steam-oxygen gasification, hydrogasification, and catalytic steam gasification are the three major gasification processes used in coal-to-SNG production. So far, only the steam-oxygen gasification process, is commercially proven, by installing a methanation reactor downstream of the gasification process after syngas is produced and cleaned. Methanation process is not considered to be an effective means of synthetic natural gas production due to different reasons including relatively poor efficiency under desired process conditions. Therefore, the methanation reactor with catalysts downstream of the gasification is needed for SNG process. The mathanation reaction rates have also been studied in this chapter. Since the non-catalytic reaction rates for methanation are not known, the CFD scheme can be used as a

convenient tool to investigate the sensitivity of methane production on the variation of methanation reaction rates. The sensitivity study is performed by keeping the activation energy intact but changing the pre-exponential constant value (A) of the mathanation reaction rates. Only the forward rate is used to represent the net global rate of mathanation reaction. The result shows that production of CH_4 can be adequately achieved by varying the pre-exponential constant value (A) of the mathanation reaction rates between 5.12×10^{-7} and 5.12×10^{7}. From this sensitivity study, it can be concluded that the approach of using one net global reaction forward rate can be used to match the experimental data once they are available in the future.

10.2.5 Study of ash deposition model

In this study, the ash deposition has been investigated by modeling the complete coal gasification process. Each coal particle has been tracked by Lagrangian method to go through the process of coal surface moisture evaporation, devolatilization, coal combustion, coal gasification and ash deposition. The ash deposition rates along the gasifier wall are investigated and compared between different cases by employing different coal feeding schemes and using different coal types. Moreover, the effect of ash deposition rates on the gasification performance, including syngas temperature, composition higher heating value (HHV) and carbon conversion rate are also investigated in this study. The conclusions are summarized as following:

- Compared to the case of one-stage fuel feeding, the peak ash deposition rate for the case of 50%-50% fuel feeding appears in the same location of gasifier, at the height of 4m, but the value decreases to 63%. In the case of 25%-75% fuel feeding, the peak ash deposition rate appears at the height of 7.5m, and the value reduces to 53% of it in the one-stage fuel feeding case.
- Two-stage fuel feeding scheme could distribute deposited ash into a larger gasifier's volume and hence reduces the peak ash deposition rate and make ash distribution more uniform in the gasifier.
- Compared to the low-ash-content coal gasification, the high-ash-content coal gasification has both high peak ash deposition rate and high overall ash deposition rate. The peak ash deposition rate of Case 4 (West Kentucky No. 11 coal) is around $0.35 kg/m^2$-s, which is about 11 times of the value in Case 2 (Illinois No.6 coal). The

overall area-weighted average ash deposition rate on the gasifier wall in Case 4 is 0.12kg/m^2-s, which is 6.7 times of the value in Case 2, 0.018kg/m^2-s.

- The high-ash-content coal gasification has very low syngas HHV and carbon conversion rate. The total syngas HHV in Case 4 (West Kentucky No. 11 coal) is 109639kJ/s, only 59% of the value in Case 2 (Illinois No.6 coal), which is 184616kJ/s. The carbon conversion rate in Case 4 is 52%, that means 48% un-reacted char will deposit on the wall before they complete the coal gasification reactions. The char recycling scheme is needed to increase the carbon conversion rate if the coal with high ash content is used for gasification, such as West Kentucky No. 11 coal.

10.2.6 Study of two-Stage oxygen feeding scheme

1. In the top-injection base case, the CFD predicts that the exit temperature is satisfactorily within 90^{o}C (or 9%) from the experimental data. However, the CFD predicts relatively lower H_2 and CO composition but higher CO_2 at the exit.
2. The experiments at 2.5 bars show the 60%-40% oxygen distribution yields the most uniform wall temperature along the gaisifer.
3. In cases of split two-stage oxygen injections from 100% to 40% with 0.6 stoichiometric oxygen at 2.5 bars, the CFD predicts (a) the similar trend of changing temperature and syngas compositions in the experimental data, but lower H_2 and CO mole fractions than the experimental data, (b) the 80-20% case yields the lowest peak temperature and the most uniform gas temperature distribution along the gasifier, and (c) the 60%-40 case produces the syngas with the highest HHV.
4. The CFD's prediction of the effect of oxygen distribution under 25 bars operating pressure case shows that (a) the carbon conversion rates for different oxygen injection schemes are all above 95%, (b) H_2 (about 70% vol.) dominates the syngas composition at exit, (c) same as in the 2.5 bar cases, the 80-20% case yields the lowest peak temperature and most uniform gas temperature distribution along the gasifier, and (d) the 40-60% case produces the syngas with the highest HHV.
5. Chemical reactions are affected by the local flow behavior. Strong opposing injection of oxygen at second stage squeezes the main flow laterally to both sides perpendicular to the

injection direction, making combustion spread towards both top and bottom of the second stage.

6. Two different material balance methods were conducted. The results show that the steam cannot be consumed down to only 5% - 10% (weight) of the syngas, and at the same time, also yields CO at a high level of 41% (vol) of the dry syngas under the experimental condition

7. Both experimental data and CFD predictions verify the hypothesis that it is feasible to reduce the peak temperature and achieve more uniform temperature in the gasifier by adequately controlling two-stage oxygen injection without changing the quality of the product syngas.

10.2.7 Study of a syngas quench cooling design

A CFD model has been developed to investigate the water quench section design of an oxygen-blown, slurry-fed, entrained flow coal gasifier. The calibrated Wade's WGS rate (A= 0.2512, E = 1.325 x 105 k/mol) is chosen for all of the parametric studies in this study. The conclusions of this study are stated as following:

1) The effect of injection locations (primary vs. secondary) on the WGS reaction is marginal. Both locations result in a 16% CO conversion rate. Spraying water in the primary location only provides a marginal advantage with an increase of 4% in H2 production, 2% in HHV value, and 30K in temperature.

2) Using the water bath level to fine-tune the WGS is workable. When the water level gap decreases from 1050mm to 700 mm, the CO conversion rate decreases by 7 percentage points (or 35%) from 20% to 13%, and the syngas outlet temperature decreases by 20K (from 891 K to 871 K.) Beyond the gap of 1050mm, the effect of the water bath level is not noticeable.

REFERENCES

Adanez, J., and Labiano, F., 1990, "Modeling of Moving-Bed Coal Gasifiers," *Industrial & Engineering Chemistry Results*, Vol. 29, pp. 2079-2088.

Ajilkumar, A., Sundararajan, T., and Shet, U., 2009, "Numerical Modeling of a Steam Assisted Tubular Coal Gasifier," *International Journal of Thermal Sciences*, Vol. 48, pp. 308-321.

Ariyapadi, S., Shires, P., Bhargava, M., and Ebbern, D., 2008, "KBR's Transport Gasifier (TRIG™) – an Advanced Gasification Technology for SNG Production from Low-Rank Coals," Presented at the Twenty-fifth Annual International Pittsburgh Coal Conference September 29 – October 02, 2008, Pittsburgh, PA.

Ahmadi, G., Mazaheri, A., Liu, C., and Gamwo, I., 2002, "Computer Modeling of Flow, Thermal Condition and Ash Deposition in a Hot-Gas Filtration Device," 5th International Symposium on Gas Cleaning at High Temperatures, Morgantown, WV (US), 09/17/2002--09/20/2002.

Anthony, D., Howard, J., Hottel, H., and Meissner, H., 1975, "Rapid Devolatilization of Pulverized Coal," *Symposium (International) on Combustion,* Vol.15, pp.1303-1317.

Beeley, T., Crelling, J., Gibbins, J., Hurt, R., Lunden, M., Man, C., Williamson, J., and Yang, N., 1996, "Transient High-Temperature Thermal Deactivation of Monomaceral-rich Coal Chars," Twenty-Sixty Symposium (International) on Combustion. The Combustion Institute, Pittsburgh, in press.

Biba, V., Macak, E., Klose, E., and Malenha, I., 1978, "Mathematical Model for the Gasification of Coal under Pressure," *Industrial & Engineering Chemistry Process Design and Development*, Vol. 17, pp, 92-98.

Blander, M., Sinha, S., Pelton, A., and Eriksson,G., 1989, "Calculations of the Influence of Additives on Coal Combustion Deposits,"
https://web.anl.gov/PCS/acsfuel/preprint%20archive/Files/34_2_DALLAS_04-89_0340.pdf

Barroso, J., Ballester, J., Ferrer, L., and Jiménez, S., 2006, "Study of Coal Ash Deposition in an Entrained Flow Reactor: Influence of Coal Type, Blend Composition and Operating Conditions," *Fuel Processing Technology*, Vol.87, pp.737–752.

Bartle, K., Perry, D., and Wallace, S., 1987, "The Functionality of Nitrogen in Coal and Derived Liquids: an XPS Study," *Fuel Processing Technology*, Vol. 15, pp. 351-361.

Benyon P., 2002, "Computational Modelling of Entrained Flow Slagging Gasifiers," PhD thesis, School of Aerospace, Mechanical & Mechatronic Engineering, University of Sydney, Australia.

British Petroleum, 2005, *BP Statistical Review of World Energy*.

Betta. R. A., Piken, A. G., and Shelef, M., 1974, "Heterogeneous Methanation: Initial Rate of CO Hydrogenation on Supported Ruthenium and Nickel," *Journal of Catalysis*, Vol. 35, pp. 54-64.

Brewster, M., and Kunitomo, T., 1984, "The Optical Constants of Coal, Char, and Limestone," *Journal of Heat Transfer*, Vol. 106, pp. 678-683.

Bilger, R., 1993, "Conditional Moment Closure for Turbulent Reacting Flow," *Physics of Fluids*, Vol. 5, pp. 436–444.

Beér, J., 2000, "Combustion Technology Developments in Power Generation in Response to Environmental Challenges." *Progress in Energy and Combustion Science*. Vol. 26, pp. 301-27.

Bockelie, M., Denison ,M., Chen, Z., Linjewile, T., Senior, C., and Sarofim, A., 2002, "CFD Modeling For Entrained Flow Gasifiers," Proceedings of the Gasification Technologies Conference 2002, San Francisco, CA.

Bockelie, M., Denison, M., Chen, Z., Linjewile, T., Senior, C., and Sarofim, A., 2002,"CFD Modeling For Entrained Flow Gasifiers in Vision 21 Systems," Proceedings of the Pittsburgh Coal Conference 2002, Pittsburgh, PA.

Bockelie, M.J., Denison, M., Chen, Z., Linjewile, T., Senior, C., and Sarofim, A., "Using Models to Select Operating Conditions for Gasifiers," Proceedings of the Pittsburgh Coal Conference 2003, Pittsburgh, PA.

Boysan, F., Weber, R., and Swithenbank, J., 1983, "Mathematical Modelling of an Entrained Coal Gasifier", 1983 International Gas Research Conference.

Buckius, R., and Hwang, D., 1980, "Radiation Properties for Polydispersions: Application to Coal," *ASME Journal of Heat Transfer*, Vol. 102, pp. 99-103.

Burchill, P., and Welch, L., 1989, "Variation of nitrogen content and functionality with rank for some UK bituminous coals," *Fuel*, Vol. 68, pp. 100.

Cao, Z., Sun, L., Cao, X., and He, Y., 2011, "Study on Fly Ash Adhesion Characteristics and Deposition Mechanism in Shell Coal Gasification Process," *Advanced Materials Research*, Vol. 233 – 235, pp. 789-793.

C.M. van der Meijden, 2010, "Development of the MILENA Gasification Technology for the Production of Bio-SNG," Eindhoven University of Technology Library, ISBN: 978-90-386-2363-4.

Chapyak, E., Blewett, P., and Cagliostro, D., 1983, "Verification Studies of Entrained-Flow Gasification and Combustion Systems with the Simmer-II Code," 10th IMACS World Congress on System Simulation and Scientific Computation.

Chan,P., and Norbeck, J., 2009, "Production of Methane Rich Fuel Gas from Coal using Steam Hydrogasification," Presented at the Twenty-sixth Annual International Pittsburgh Coal Conference September 21 – 24, 2009, Pittsburgh, PA.

Chandrasekhar, S., 1950, *Radiative Transfer*, Oxford University Press, London

Chandel, M., and Williams, E., 2009, "Synthetic Natural Gas (SNG): Technology, Environmental Implications, and Economics," Climate Change Policy Partnership. http://www. netldev netl.doe.gov.

Chodankar, C., Feng, B., and Klimenko, A., 2009, "Numerical Modeling of Underground Coal Gasification Process for Estimation of Product Gas Composition," Paper 25-3, presented at the 26rd International Pittsburgh Coal-Gen Conference, Pittsburgh, Pennsylvania, Sept. 20-23, 2009.

Chen, L., Nolan, R., and Avadhany, S., 2009, "Thermodynamic Analysis of Coal to Synthetic Natural Gas Process," http://www.mit.edu/people/leichen/Thermodynamic_Analysis_of_the_coal_to_SNG_process.pdf

Chen, C., Horio, M., and Kojima, T., 2010, "Numerical Simulation of Entrained Flow Coal Gasifiers," *Chemical Engineering Science*, Vol. 55, pp. 3861-3883.

Chen, M., 2010, "Numerical Simulation Analyses of an Entrained-bed Gasification Reactor," Paper 45-4, presented at the 27th International Pittsburgh Coal Conference, Istanbul, Turkey, October 11 – 14, 2010.

Chen, C., Miyoshi, T., Kamiya, H., Horio, M., and Kojima, T., 1999, "On the Scaling-up of a Two-Stage Air Blown Entrained Flow Coal Gasifier," *The Canadian Journal of Chemical Engineering*, Vol. 77, pp. 745-750.

Chen, C., Horio, M., and Kojima, T., 2000(a), "Numerical Simulation of Entrained Flow Coal Gasifiers. Part I: Modeling of Coal Gasification in an Entrained Flow Gasifier," *Chemical Engineering Science,* Vol. 55, pp. 3861-3874.

Chen C., Horio M., and Kojima T., 2000(b), "Numerical Simulation of Entrained Flow Coal Gasifiers. Part II: Effects of Operating Conditions on Gasifier Performance," *Chemical Engineering Science*, Vol. 55, pp. 3875-3883.

Choi, Y., Li, X., Park, T., Kim, J., and Lee, J., 2001, "Numerical Study on the Coal Gasification Characteristics in an Entrained Flow Coal Gasifier," *Fuel*, Vol. 80, pp. 2193-2201.

Choi, Y., Li, X., Park, T., Kim, J., and Lee, J., 2001, "Numerical Analysis of the Flow Field inside an Entrained-Flow Gasifier," *Korean Journal of Chemical Engineering,* Vol. 18, pp. 376-381.

Chen, W., Hsieh, T., and Jiang, T., 2008, "An Experimental Study on Carbon Monoxide Conversion and Hydrogen Generation from Water Gas Shift Reaction," *Energy Conversion and Management*, Vol. 49, pp. 2801-2808.

Chen, L., Yong, S., and Ghoniem, A., 2012, "Modeling the Slag Behavior in Three Dimensional CFD Simulation of a Vertically-oriented Oxy-coal Combustor," The 37th International Technical Conference on Clean Coal & Fuel Systems, Clearwater FL, June 3-7, 2012.

Choi, Y., and Stenger, H.G., 2003, "Water Gas Shift Reaction Kinetics and Reactor Modeling for Fuel Cell Grade Hydrogen," *Journal of Power Sources*, Vol. 124, pp. 432–439.

Cumber, P., Fairweather, M., and Ledin, H., 1998, "Application of Wide Band Radiation Models to Non-homogeneous Combustion Systems," *International Journal of Heat and Mass Transfer*, Vol. 11, pp. 1573-1584.

Coimbra, C., Azevedo, J., and Carvalho, M., 1994, "3-D Numerical Model for Predicting NOx Emissions from an Industrial Pulverized Coal Combustor," *Fuel*, Vol. 73, pp. 1128–1134.

Costen, P., Lockwood, F., and Siddique, M., 2000, "Mathematical Modeling of Ash deposition in Pulverized Fuel-fired Combustors," *Proceedings of the Combustion Institute*, Vol. 28, pp. 2243–2250.

Couch, G., 1994, "Understanding Slagging and Fouling in pf Combustion." London, IEA Coal Research.

Denn, M., Wei, J., Yu, W., and Cwiklinski, R., 1982, "Detail Simulation of a Moving-Bed Gasifier," Research Project 1268-1, M.I.T., USA

Dent, F., Moignard, L., Eastwood. A., Blackturn, W., and Hebden, D., 1948, "An investigation into the Catalytic Synthesis of Methane for Town Gas Manufacture," *Gas Res. Board Comm.,* Vol. 20, pp. 106-121.

DeSai, P., Wen, C., Bissett, L., 1978, "Computer Modeling of the Morgantown Energy Research Center's Fixed Bed Gasifier," MERC/CR-78/3, U.S. Department of Energy, Morgantown, WV.

DalSecco, S., Mechitoua, N., and Simonin, O., 1995, "Three-dimensional Modeling of Coal Combustion and NO Formation in a 250MW Coal-fired Furnace," Proceedings of the Third International Conference on Combustion Technology for a Clean Environment Paper 31-2.

DOE/NETL Report, 2007, "Industrial Size Gasification for Syngas, Substitute Natural Gas and Power Production," National Energy Technology Laboratory.

DOE/NETL Report, 2011, "Cost and Performance Baseline for Fossil Energy Plants Volume 3a: Low Rank Coal to Electricity: IGCC Cases," National Energy Technology Laboratory.

DOE Report, 2006, "Practical Experience Gained during the First Twenty Years of Operation of the Great Plains Gasification Plant and Implications for Future Projects," Department of Energy.

Dilip A. Saletore and Wllllam J. Thomson, 1977, "Methanation Reaction Rates for Recycle Reactor Compositions," *Ind. Eng. Chern., Process Des. Dev.,* Vol. 16, pp. 70-75.

Duan, R., Koshizuka, S. and Oka, Y., 2003 "Droplet Breakup Under Impulsive Acceleration Using Moving Particle semi-Implicit Method," 11th International Conference on Nuclear Engineering, Tokyo, Japan, April 20-23, 2003, Paper No: ICONE11-36029.

Edwards, D.K., and Balakrishnan, A., 1973, "Thermal Radiation by Combustion Gases," *International Journal of Heat and Mass Transfer,* Vol. 16, pp. 25-40.

Essenhigh, R., 1981, *Chemistry of Coal Utilization, Second Supplementary Volume*, John Wiley and Sons*,* New York.

Faltsi-Saravelon, O., and Wild, P.N., 1995, "Prediction of NO Emissions from a Swirling Coal Flame," Proceedings of the Third International Conference on Combustion Technology for a Clean Environment Paper 20-2.

Fernandez-Turiel, J., Georgakopoulos, A., Gimeno, D., Papastergios, G., and Kolovos, N., 2004, "Ash Deposition in a Pulverized Coal-fired Power Plant after High-calcium Lignite Combustion," *Energy & Fuels*, Vol.18, pp.1512-1518.

Feng, J., Shen, Y., and Yang, R., 2003, "Principles and calculations of boilers," *3rd edition ed.* Beijing: Science press; 2003.

Field, M., 1970, "Measurements of the Effect of Rank on Combustion Rates of Pulverized Coal," *Combust Flame*, Vol. 14, pp. 237-248.

Fiveland, W., 1988, "Three-dimensional Radiative Heat-transfer Solutions by the Discrete-ordinates Method," *Journal of Thermophysics*, Vol. 2, pp. 309–316.

Fiveland, W., and Wessel, R., 1988, "Numerical Model for Predicting Performance of Three-dimensional Pulverized-fuel Fired Furnaces," *Journal of Engineering for Gas Turbines and Power,* Vol. 110, pp. 117–126.

FLUENT 6.3 User's Guide, September 2006.

Fletcher, T., 1983, "Two-dimensional Model for Coal Gasification and Combustion," PHD Dissertation, Brigham Young University.

Fletcher, T., Kerstein, A., Pugmire, R., and Grant, D., 1990, "Chemical Percolation Model for Devolatilization. 2. Temperature and Heating Rate Effects on Product Yields," *Energy and Fuels*, Vol. 4, pp. 54-60.

Fletcher, T., Smith, P., and Smoot, L., 1984, "Evaluation of a 2-D Coal Combustion Model," Proceedings of 1984 Spring Meeting of the Western States Section of the Combustion Institute, Boulder, CO.

Fletcher, T., and Kerstein, A., 1992, "Chemical Percolation Model for Devolatilization: 3 Direct Use of ^{13}C NMR Date to Predict Effects of Coal Type," *Energy and Fuels*, Vol. 6, pp. 414-431.

Foster, P., and Howarth, C., 1968, "Optical Constants of Carbon and Coals in the Infrared," *Carbon*, Vol. 6, pp. 719-729.

Fairley, P., 2007, "Cheaper Natural Gas from Coal," http://www.technologyreview.com/Biztech18119.

GreatPoint energy, 2008a. http://www.greatpointenergy.com.

Given, P., Marzec, A., Barton, W., Lynch, L., and Gerstein, B., 1986, "The Concept of a Mobile or Molecular Phase within the Macromolecular Network of Coals: a Debate," *Fuel,* Vol. 65, pp. 155-163.

Gibson, M., and Euker, C., 1975, "Mathematical Modeling of Fluidized Bed Coal Gasification," Preprint in AlChE Symposium, Los Angeles.

Gupta, A., and Thodos, G., 1963, "Direct Analogy between Mass and Heat Transfer to Beds of Spheres," *AlChE Journal*, Vol. 9, pp. 751-754.

GreatPoint Energy, 2008b. "GreatPoint Energy announces coal supply partnership with Peabody Energy and enters into agreement to build natural gas manufacturing facilities in Powder River," Basin. http://www.greatpointenergy.com/GPE - Peabody1 - 25 - 08.pdf.

Grant, D., Pugmire, R., Fletcher, T., and Kerstein, A., 1989, "Chemical Percolation of Coal Devolatilization Using Percolation Lattice Statistics," *Energy and Fuels*, Vol. 3 pp. 175-186.

Grenoble, D., and Estadt, M., 1981, "The Chemistry and Catalysis of the Water Gas Shift Reaction 1, the Kinetics over Supported Metal Catalysts," *Journal of Catalysis,* Vol. 67, pp. 90-102.

Grosshandler, W., 1980, "Radiative Heat Transfer in Non-homogeneous Gases: a Simplified Approach," *International Journal of Heat and Mass Transfer*, Vol.23, pp. 1447-1459.

Grosshandler W., and Monteiro S., 1982, "Attenuation of Thermal Radiation by Pulverized Coal and Char," *International Journal of Heat Transfer*, Vol. 104, pp. 587-593.

Genetti, B., 1999, "An Advanced Model of Coal Devolatilization Based on Chemical Structure," Master Thesis, Brigham Young University Saxena, S., *Progress in Energy and Combustion Sciences*, Vol. 16, pp. 55-94.

Guenther, C., and Zitney, S., 2005, "Gasification CFD Modeling for Advanced Power Plant Simulation," Proceedings of the 22th International Pittsburgh Coal Conference, Pittsburgh, Pennsylvania, September 12-15, 2005.

Gururajan, V. S., Agarwal, P. K., and Agnew, J. B., 1992, " Mathematical Modeling of Fluidized Bed Coal Gasifiers," *Chemical engineering research & design*, Vol. 70, No. A3, pp. 211-238, ISSN : 0263-8762.

Hirth, T., and Franck, E., 1991, "Oxidation and Hydrothermolysis of Hydrocarbons in Supercritical Water at High Pressures," *Ber. Bunsenges. Phys. Chem*., Vol. 97, pp. 1091-1097.

Higman, C., and M. van der Burgt, *Gasification*, Elsevier, 2003.

Hla, S., Park, D., Duffy, G., Edwards, J., Roberts, D., Ilyushechkin, A., Morpeth, L., and Nguyen, T., 2009, "Kinetics of High-temperature Water-Gas Shift Reaction over Two Iron-based Commercial Catalysts Using Simulated Coal derived Syngases," *Chemical Engineering Journal*, Vol. 146, pp. 148–154

Hobbs, L., Radulovict, P., and Smoot, D., 1992, "Modeling Fixed - bed Coal Gasifiers," *AlChE Journal*, Vol. 38, pp. 681-702.

Hobbs, M., 1990, "Modeling Counter Current Fixed Bed Coal Gasification," PhD Dissertation, Provo. UT., Brigham Young University.

Holgate, H., Webley, P., and Tester, J., 1992, "Carbon Monoxide Oxidation in Supercritical Water: the Effects of Heat Transfer and the Water-Gas-Shift Reaction on Observed Kinetics," *Energy & Fuels,* Vol.6, pp. 586-597

Hohlein, B.; Niessen, H.; Range, J.; Schiebahn, H. J. R.; Vorwerk, M., "Methane from synthesi s gas and operation of high-temperature methanation". *Nuclear Engineering and Design* 1984, 78, (2), 241-250.

Hottel, H., and Howard, J., 1971, "New Energy Technology: Some Facts and Assessments," *New Energy Technology*, Cambridge, MA MIT Press.

Hughes, R., Lu, D., Majeski, A., Corber, A., and Anthony, B., 2010, "Entrained Flow Slagging Slurry Gasification and the Development of Computational Fluid Dynamics Models at CanmetENERGY," 2010 International Pittsburgh Coal Conference, Istanbul, Turkey October 11 – 14, 2010.

Hurt, R., and Gibbins, J., 1995, “Residual Carbon from Pulverized Coal Fired Boilers: 1. Size Distribution and Combustion Reactivity,” *Fuel*, Vol. 74, pp. 471-482.

Hurt, R., Davis, K., Yang, N., Headley, T., and Mitchell, G., 1995, “Evolution of Char Chemistry, Crystallinity, and Ultrafine Structure during Pulverized-coal Combustion,” *Combustion and Flame*, Vol. 100, pp. 31-40.

Hurt, R., and Davis, K., 1994, “Near-extinction and final burnout in coal combustion,” Twenty-Fifth (International) Symposium on Combustion, The Combustion Institue, Pittsburgh, Vol. 25, pp. 561-568.

Hottel, H., and Sarofim, A., 1967, *Radiative Transfer*, McGraw-Hill.

Holt, N., 2004, "Gasification Process Selection – Trade-offs and Ironies," Proceedings of the Gasification Technology Conference 2004, Washington, DC.

IM, K., and Ahluwalia, R., 1992, “Radiation Properties of Coal Combustion Products,” *International Journal of Heat and Mass Transfer*, Vol. 36, pp. 293-302.

Jones, W.P., and Lindstedt, R.P., 1998, “Global Reaction Schemes for Hydrocarbon Combustion,” *Combustion and Flame*, Vol. 73, pp. 233-240.

Johnson, J.L., 1979, *Kinetics of Coal Gasification: a Compilation of Research*, John Wiley and Sons, New York, NY.

Kallio, G., and Reeks, M., 1989, “A Numerical Simulation of Particle Deposition in Turbulent Boundary Layers, International Journal of Multiphase Flow,” Vol. 15, No. 3, pp. 433-446.

Karthikeyan, M., Wu, Z., and Mujumdar, A., “Low-Rank Coal Dry Technologies-Current Status and New Developments,” *Dry Technology*, Vol. 27, pp. 403-415.

Keiski, R., Salmi, T., Niemisto, P., Ainassaari, J., and Pohjola, V., 1996, “Stationary and Transient Kinetics of the High Temperature Water Gas Shift Reaction,” *Applied Catalysis A: General,* Vol. 137, pp. 349-370.

Kelemen, S., Gorbaty, M., and Kwiatek, P., 1994, “Quantification of Nitrogen Forms in Argonne Premium Coals,” *Energy & Fuels,* Vol. 8, pp. 896.

Kelemen, S., Gorbaty, M., Vaughn, S., and Kwiatek, P., 1993, “Transformation Kinetics of Organic Sulphur Forms in Argonne Premium Coals During Pyrolysis,”*ACS Division of Fuel Chemistry Preprints*, Vol. 38, pp. 384-392.

Kobayashi, H., Howard, J., and Sarofim, A., 1976, “Coal Devolatilization at High Temperatures,” 16th Symp. (Int'l.) on Combustion, The Combustion Institute.

Koryabkina, N., Phatak, A., Ruettinger, W., Farrauto, R., and Ribeiro, F., 2003, "Determination of Kinetic Parameters for the Water–Gas Shift Reaction on Copper Catalysts under Realistic Conditions for Fuel Cell Applications," *Journal of Catalysis*, Vol. 217, pp. 233-239.

Krevelen, D., 1981, *Coal: Typology, Chemistry, Physics, and Constitution*, Elsevier, New York.

Kusar, H., Hocevar, S., and Levec, J., 2006, "Kinetics of the Water-Gas-Shift Reaction over Nanostructured Copper–Ceria Catalysts," *Applied Catalysis B: Environmental*, Vol. 63, pp. 194–200.

Kuo, K. Y., 1986, *Principles of combustion*, John Wiley and Sons, New York.

Kumar, M., Zhang, C., Monaghan, R., Singer, S., and Ghoniem, A., 2009. "CFD simulation of Entrained Flow Gasification with Improved Devolatilization and Char Consumption Submodels," Proceedings of the ASME International Mechanical Engineering Congress and Exposition, Lake Buena Vista, FL, USA. Nov. 13-19, 2009.

Kumar, M., and Ghoniem, A., 2012, "Multiphysics Simulations of Entrained Flow Gasification. Part II: Constructing and Validating the Overall Model," *Energy Fuels,* Vol. 26, pp. 464-479.

Lang, Y., Zitney, S., and Biegler, L., 2011, "Optimization of IGCC Processes with Reduced Order CFD Models," *Computers & Chemical Engineering,* Vol. 35, pp. 1705-1717.

Lasa, H., and Mok, L.K., 1981, "Entrained Coal Gasifiers: Modeling the Particle Acceleration," *The Canadian Journal of Chemical Engineering*, Vol. 59, pp. 658-661.

Lockwood, F., Papadopoulos, C., and Abbas, A., 1988, "Prediction of a Corner-fired Power Station Combustor," *Combustion Science and Technology*, Vol.158, pp. 5–23.

Li, Z., Wei, F., and Jin. Y., 2003, "Numerical Simulation of Pulverized Coal Combustion and NO Formation*," Journal of Chemical Engineering Scie*nce, Vol. 58, pp. 5161-5171.

Luan Y., Chyou, Y., Wang, T., 2011, "Numerical Analysis of Gasification Performance via Finite-rate Model in a Cross-type Two-stage Gasifier," The 28th International Pittsburgh Coal Conference, Pittsburgh, PA, USA, Sept. 12-15, 2011.

Lu, X., and Wang, T., 2013, "Water-Gas Shift Modeling in Coal Gasification in an Entrained-flow Gasifier Part 1: Development of Methodology and Model Calibration," DOI information: 10.1016/j.fuel.2013.02.023, *Fuel*, Vol. 108, pp. 629-638.

Lu, X., and Wang, T., 2013, "Water-Gas Shift Modeling in Coal Gasification in an Entrained-flow Gasifier Part 2: Gasification Application," DOI information: 10.1016/j.fuel.2013.02.024, *Fuel*, Vol. 108, pp. 620-628.

Li, A., and Ahmadi, G., 1992, "Dispersion and Deposition of Spherical Particles from Point Sources in a Turbulent Channel Flow," *Aerosol Science and Technology*, Vol. 16, pp. 209-226.

Linares-Solano, A., Mahajan, O.P., Philip, L., and Walker, P.L., 1979, "Reactivity of Heat-treated Coals in Steam", *Fuel*, Vol. 58, pp. 327-332.

Li, Z., Li, R., and Zhou, L., 2000, "Experimental Study of a High-efficiency and Low Pollution Pulverized-coal Swirl Burner under Cold-state Test Condition," *Journal of Engineering for Thermal Energy & Power* ,Vol. 6, pp. 640–643.

Lee, S., and Tien, C., 1981, "Optical Constants of Soot in Hydrocarbon Flames," *Eighteenth Symp. (Int.) on Combustion*, Combustion Institute, Pittsburgh, pp. 1159-1166.

Lauder, B.E., and Spalding, D.B., *Lectures in Mathematical Modeling of Turbulence*, Academic Press, London, England, 1972.

Lockwood, F., and Shah, N., 1981, "A New Radiation Solution Method for Incorporation in General Combustion Prediction Procedures," *Eighteenth Symposium (International) on Combustion*, Combustion Institute, Pittsburgh, 1981, pp. 1405-1414.

Martula, D., Hasegawa, T., Lloyd, D., and Bionnecaze, R., 2000, "Coalescence-Induced Coalescence of Inviscid Droplets in a Viscous Fluid," *Journal of Colloid and Interface Science,* Vol. 232, pp. 241–253.

Modest, M.F., 2003, *Radiative Heat Transfer*, Academic Press.

Mozaffarian, M., and Zwart, R., 2003, "Feasibility of Biomass/waste Related SNG Production Technologies," http://www.ecn.nl/publications.

Mozaffarian, M., Zwart, R., Boerrigter, H., Deurwaarder, E., Kersten, S., 2004, "Green Gas as SNG (synthetic natural gas) - A Renewable Fuel with Conventional Quality," http://www.ecn.nl/ publications.

Mueller, C., and Kremer, H., 1995, "Modeling of an Industrial Scale Gas-burner using 9nite-rate Chemistry-options and Restrictions Resulting from Eddy-Break up Based Models," Proceedings of the third International Conference on Combustion Technology for a Clean Environment Paper 7.1, Lisbon.

Niksa, S., 1995, "Flash chain Theory for Rapid Coal Devolatilization Kinetics. 6. Predicting the Evolution of Fuel Nitrogen from Various Coals ," *Energy and Fuels*, Vol. 9, pp. 467-478.

O'Rourke, P., and Amsden, A., 1987, "The Tab Method for Numerical Calculation of Spray Droplet Breakup," SAE Technical Paper 872089.

O'Rourke, P. J., 1981, "Collective Drop Effects on Vaporizing Liquid Sprays" PhD dissertation, Princeton University, New Jersey.

Qiang, L., Ti-min C., Guo, E., and Chunbo, H., 2006, "Droplet Collision and Coalescence Model," *Applied Math and Mechanics*, Vol. 27(1), pp. 67–73.

Pan, Y. and Suga, K., 2005, "Numerical Simulation of Binary Liquid Droplet Collision," *Physics of Fluids,* Vol. 17, pp. 82-105.

Papadakis, G., and Bergeles, G., 1994, "Prediction of Staged Coal Combustion in Three-Dimensional Furnaces" *Journal of the Institute of Energy*, Vol. 67, pp. 156–167.

Park, N., Kobayashi, T., and Taniguchi, N., 2000, "Application of Flame-wrinkling LES Combustion Models to a Turbulent Premixed Combustion Around Bluff Body," Proceedings of the Third International Symposium on Turbulence, *Heat and Mass Transfer*, Nagoya, Aichi Shuppan, pp. 847–854.

Pope, S., 1985, "PDF Methods for Turbulent Reactive Flows," *Progress in Energy and Combustion Science*, Vol. 11, pp. 119–192.

Philip, L., Walker, P.L., Matsumoto, S., Hanzawa, T., Muira, T., and Ismail, I., "Catalysis of Gasification of Coal-derived Cokes and Chars," *Fuel,* Vol. 62, pp. 140-149.

Probstein, R., Hicks, R., 1982, *Synthetic fuels*. McGraw-Hill, New York.

NETL, 2008, "Gasification Technologies, Development of a Hydrogasification Process for CO ‐ production of Substitute Natural Gas (SNG) and Electric Power from Western Coals Description," http://www.netl.doe.gov/publications/factsheets/project/Proj410.pdf.

Paraskevi P., Dimitris K., and Xenophon V., 2008, "Selective Methanation of CO over Supported Noble Metal Catalysts: Effects of the Nature of the Metallic Phase on Catalytic Performance," *Applied Catalysis A: General*, Vol. 344, pp. 45–54.

Ranz, W. E. and Marshall Jr. W. R., 1952, "Evaporation From Drops Part I," *Chem. Eng. Prog*, Vol. 48, pp. 141-146.

Ranz, W.E., and Marshall, W.R., 1952, "Evaporation from Drops Part 2," *Chem. Eng. Prog*, Vol. 48, pp. 173-180.

Rase, H.F., *Chemical Reactor Design for Process Plants: Volume two – Case Studies and Design Data*, John Wiley and Sons, 1977.

Rabbitts, M., Van Den Houten, G., Glasser, D., and Bryson, A., 1983, "Modelling of Residence Time Distribution in an Entrained Flow Coal Gasifier Reactor," *ChemSA*, Vol. 9, pp. 220-223.

Rehm, M., Seifert, P., Meyer, B., 2009, "Theoretical and Numerical Investigation on the EDC-Model for Turbulence–chemistry Interaction at Gasification Conditions," *Computers & Chemical Engineering*, Vol. 33, pp. 402-407.

Rhodes, C., Hutchings, G., and Ward, A., 1995, "WGSR: Finding the Mechanistic Boundary," *Catalysis Today*, Vol. 23, pp. 43-48.

Rhodes, C., and Hutchings, G., 2003, "Studies of the Role of the Copper Promoter in the Iron Oxide/ Chromia High Temperature Water Gas Shift Catalyst," *Physical Chemistry Chemical Physics*, Vol. 5, pp. 2719–2723.

Rinard, I., and Benjamen, B., 1985, "Great Plains ASPEN Model Development: Gasifier Model, Literature Review and Model Specification," Work performed under contract No DE-AC21-82MC19163 for US Department of Energy, Morgantown Energy Technology Centre.

Sarofim, A., and Hottel, H., 1978, "Radiative Transfer in Combustion Chambers: Influence of Alternative Fuels," in Proceedings of the Sixth International Heat Transfer Conference, Hemisphere, Washington, D.C., Vol.6, pp. 199-217.

Shao, Y., 2011, "Investigation of Ash Deposition During Co-firing Biomass/peat with Coal in a Pilot-scale Fluidized-bed Reactor," Ph.D thesis, University of Western Ontario London, Ontario,Canada.

Shi, S., Zitney, S., Shahnam, M., Syamlal, M., and Rogers, W., 2006, "Modelling Coal Gasification with CFD and Discrete Phase Method," *Journal of Energy Institute*, Vol. 79, pp. 217-221.

Salmi, T., and Hakkarainen, R., 1989, "Kinetic Study of the Low-Temperature Water-Gas-Shift Reaction over a Cu-ZnO Catalyst," *Applied Catalysis*, Vol. 49, pp. 285- 306.

Sato, T., Kurosawa, S., Smith Jr., R., Adschiri, T., and Arai, K., 2004, "Water Gas Shift Reaction Kinetics under Noncatalytic Conditions in Supercritical Water*," Journal of Supercritical Fluids*, Vol. 29, pp. 113-119.

Schlich, E., and Köhne H., 1977, "Mathematisches Modell für die Vergasung und Verbrennung von Steinkohle unter Druck," *Chemie Ingenieur Technik,* Vol. 55, pp 123-129.

Silaen, A., and Wang, T., 2005, "Simulation of Coal Gasification Process Inside a Two-Stage Gasifier," Paper 20-1, Proceedings of the 22nd International Pittsburgh Coal Conference, Pittsburgh, Pennsylvania, September 19-22.

Silaen, A. and Wang, T., 2006, "Effects of Fuel Injection Angles on Performance of A Two-Stage Coal Gasifier," Proceedings of the 23rd Pittsburgh Coal Conference, Pittsburgh, Pennsylvania, September 25-28,2006.

Silaen, A., and Wang, T., 2009, "Comparison of Instantaneous, Equilibrium and Finite Rate Gasification Models in an Entrained Flow Coal Gasifier," Paper 14-3, proceedings of the 26th International Pittsburgh Coal Conference, Pittsburgh, Pennsylvania, Sept. 21-24, 2009.

Silaen, A., and Wang, T., 2010, "Effect of Turbulence and Devolatilization Models on Gasification Simulation," International Journal of Heat and Mass Transfer, Vol. 53, pp. 2074-2091.

Silaen, A. and Wang, T., 2012, "Investigation of Coal Gasification Process under Various Operating Conditions Inside a Two-Stage Entrained Flow Gasifier," ASME Journal of Thermal Science and Engineering Applications, Vol. 4, 021006/1-11.

Spiro, C. L. and P. G. Kosky, 1982, "Space-filling Models for Coal. 2. Extension to Coals of Various Ranks," *Fuel,* Vol. 61, pp. 1080-1084.

Solomon, P. R., 1981, "Coal Structure and Thermal Decomposition," *In New Approaches in Coal Chemistry*, American Chemical Society, Washington, D.C., Vol. 169, pp 61-71.

Solomon, P., Hamblen, D., Caranglo, R., Sergio, M., and Deshpande, G., 1988, "General Model of Coal Devolatilization," *Energy and Fuels*, Vol. 2, pp. 405-412.

Solomon, P., Serio, M., Carangelo R., and Bassilakis, R., 1990, "Analysis of the Argonne Premium Coal Samples by Thermogravimetric Fourier Transform Infrared Spectroscopy," *Energy & Fuels*, Vol. 4, pp. 319-333.

Saffman, P., 1965, "The Lift on a Small Sphere in a Slow Shear Flow," *J. Fluid Mech.,* Vol. 22, pp. 385-400.

Schulze, K., Scharler, R., and Obernberger, I., 2011, "Development of an Advanced CFD Model for Ash Deposit and Aerosol Formation in Biomass Fired Boilers," 9th European Conference on Industrial Furnaces and Boilers, Estoril, Portugal, 2011.

Siegel, R., and Howell, J., 1980, *Thermal Radiation Heat Transfer,* Taylor & Francis.

Slezak, A., Kuhlman, J., Shadle, L., Spenik, J., and Shi, S., 2010, "CFD Simulation of Entrained-flow Coal Gasification: Coal Particle density/size Fraction Effects," *Powder Technology*, Vol. 203, pp. 98-108.

Smith, B., Loganathan, M., and Shanatha, M.S., 2010, "A Review of the Water Gas Shift Reaction Kinetics," *International Journal of Chemical Reactor Engineering*, Vol. 8, ISSN:1542-6580.

Smoot, L., and Smith, P., 1985, *Coal Combustion and Gasification*, Plenum Press, New York.

Smith, I., 1978, "The Intrinsic Reactivity of Carbons to Oxygen," *Fuel*, Vol. 57, pp. 409-421.

Smith, K., Smoot, L., Fletcher, T., and Pugmire, R., 1994, *The Structure and Reaction Processes of Coal*, Plenum Press, New York.

Sommerfeld, M., Kohnen, G., and Ruger, M., 1993, “Some Open Questions and Inconsistencies of Lagrangian Particle Dispersion Models,” Proceedings of the Ninth Symposium on Turbulent Shear Flows, Paper 5.1, Kyoto, Japan.

Sundararajan, A.T., and Shet, U., 2009, “Numerical Modeling of a Steam-Assisted Tubular Coal Gasifier,” *International Journal of Thermal Sciences*, Vol. 48, pp. 308-321.

Stegeman, Y., Chesters, A., Vosse, F., and Meijer, H., 1999, “Breakup of (non-) Newtonian Droplets in a Time-dependent Elongational Flow,” Proceedings PPS-15’s-Hertogenbosch, 1999.

Suuberg, E., Peters, W., and Howard, J., 1979, “Product Compositions and Formation Kinetics in Rapid Pyrolysis of PN Pulverized Coal—Implications for Combustion,” The Combustion Institute, Pittsburgh, PA, pp. 117-130.

Solomon, P., Hamblen, D., Carangelo, R., Serio, M., and Deshpande, G., 1988, “General model of coal devolatilization ,” *Energy and Fuels*, Vol. 2, pp. 405-422.

Talbot, L., Cheng, R., Schefer, R., and Willis, D., 1980, “Thermophoresis of Particles in a heated Boundary Layer,” *Journal of Fluid Mechanics*, Vol. 101, pp. 737-758.

Tampa Electric Polk Power Station Integrated Gasification Combined Cycle Project, Final Technical Report, August 2002.

Tanahashi, M., Yu, Y., and Miyauchi, T., 2000, “Effects of Turbulence Intensity on the Structure of Hydrogen-Air Turbulence Premixed Flames,” Proceedings of the Third International Symposium on Turbulence, Heat and Mass Transfer, Nagoya, Aichi Shuppan, pp. 823–830.

Thoesness, C., and Rosza, R., 1976, “Lawrence Livermore Laboratory in-situ Coal Gasification Program: Model Calculations and Laboratory Experiments,” Livermore, California, USA, Lawrence Livermore Laboratory.

Twigg, M.V., 1989, *Catalyst Handbook*, second edition, Wolfe Publishing Ltd.

Tunå, Per, 2008, “Substitute Natural Gas from Biomass Gasification,” Synopsis of Master Thesis, Department of Chemical Engineering, Lund University, P. O. Box 124, SE-221 00 Lund, Sweden.

Tyrkiel, E., and Cudnok, R., 1981, "Computer Modeling of Coal Combustion and/or Gasification in an Entrained-Bed System," Specialist Meeting on Coal Fired MHD Power Generation, Sydney.

Viskanta, R., Ungan, A., and Menguc, M., 1981, “Predictions of Radiative Properties of Pulverized Coal and Fly-ash Polydispersions,” ASME paper no. 81-HT-24.

Vannice, M. A, 1975, "The Catalytic Synthesis of Hydrocarbons from H2/CO Mixtures over the Group VIII Metals: II. The Kinetics of the Methanation Reaction over Supported Metals," *Journal of Catalysis*, Vol. 37, pp. 462-472.

Wabash River Coal Gasification Repowering Project, Final Technical Report, August 2000.

Waind, T., and Whitty, K., 2010, "Characterization of a Small Scale Slurry-Fed, Oxygen-Blown Entrained Flow Gasifier: How Injector Geometry Affects Flame Stability and Performance," 2010 International Pittsburgh Coal Conference, Istanbul, Turkey October 11 – 14, 2010.

Walker, P., Rusinko, F., Austin, L., 1959, "Gas reactions of carbon," *Advances in Catalysis,* vol. 11, pp. 133-221.

Wallace, S., Bartle, K., and Perry, D., 1989, "Quantification of Nitrogen Functional Groups in Coal and Coal Derived Products," *Fuel*, Vol. 68, pp.1450-1455.

Wang, T., Silaen, A., Hsu, H.W., and Lo, M.C., 2006, "Partial Load Simulation and Experiments of a Small Coal Gasifier," Paper 20-3, proceedings of the 23rd International Pittsburgh Coal-Gen Conference, Pittsburgh, Pennsylvania, Sept. 25-28, 2006.

Wang, T., Silaen, A., Hsu, H.W., and Shen, C.H., 2007, "Effect of Slag Tap Size on Gasification Performance and Heat Losses in a Quench-type Coal," Paper 37-4, proceedings of the 24th International Pittsburgh Coal-Gen Conference, Johannesburg, South Africa, Sept. 10-14, 2007.

Wang, T. and Silaen, A., 2009, "Numerical Investigation of Top Fuel Injection Design in a Coal Gasifier," Paper 26-2, Proceedings of the 26th International Pittsburgh Coal Conference, Pittsburgh, USA, September 20-23.

Wang, T., Silaen, A., Hsu, H.W., and Shen, C.H., 2010, "Investigation of Heat Transfer and Gasification of Two Different Fuel Injectors in an Entrained-Flow Gasifier," *ASME Journal of Thermal Science and Engineering Applications*, Vol.2, pp. 011001/1-10.

Wang, T., Silaen, A., Hsu, H.W., and Shen, C.H., 2011, "Top Fuel Injection Design in an Entrained-Flow Coal Gasifier Guided by Numerical Simulations," *ASME Journal of Thermal Science and Engineering Applications,* Vol. 3, pp. 011009/1-8.

Wang, T., Lu, X., Hsu, H.W., and Shen, C.H., 2011, "Investigation of the Performance of a Syngas Quench Cooling Design in a Downdraft Entrained-Flow Gasifier," Paper 45-2, proceedings of the 28rd International Pittsburgh Coal-Gen Conference, Pittsburgh, Pennsylvania, Sept. 15-18, 2011.

Wade J., Evar W, T., Bryan, L., Sunggyu, L., 2008, "Kinetics of Noncatalytic Water Gas Shift reaction in a supercritical Water Medium," American Institute of Chemical Engineers, AIChE Proceedings of the 2008 AIChE Spring National Meeting, April 2008: paper #139e.

Wolfstein, M., 1969, "The Velocity and Temperature Distribution of One-Dimensional Flow with Turbulence Augmentation and Pressure Gradient," *Int. J. Heat Mass Transfer*, Vol. 12, pp. 301-318.

Wojtowicz, M., Pels, J., and Moulijn, J., 1995, "The Fate of Nitrogen Functionalities in Coal during Pyrolysis and Combustion," *Fuel*, Vol. 74, pp. 507-515.

Watanabe, H., and Otaka, M., 2006, "Numerical Simulation of Coal Gasification in Entrained Flow Coal Gasifier," *Fuel*, Vol. 85, pp. 1935-1943.

Watanabe, M., Mochiduki, M., Sawamoto, S., Adschiri, T., and Arai, K., 2001, "Partial Oxidation of N-Hexadecane and Polyethylene in Supercritical Water," *J. Supercrit. Fluids,* Vol. 20, pp. 257-268.

Wen, C., Chen, H., and Onozaki, M., 1982, "User's Manual for Computer Simulation and Design of the Moving Bed Coal Gasifier," Work performed under contract No AT21-81MC16474 for Morgantown Energy Technology Centre by West Virginia University, Morgantown, W.VA.

Westbrook, C., and Dryer, F., 1981, "Simplified Reaction Mechanisms for the Oxidation of Hydrocarbon Fuels in Flames," *Combustion Science and Technology*, Vol. 27, pp.31-43.

Wheeler, C., Jhalani, A., Klein, E., Tummala, S., and Schmidt, L., 2004, "The Water-Gas-Shift Reaction at Short Contact Times," *Journal of Catalysis*, Vol. 223, pp. 191–199.

Wu, Y., Zhang, J., Smith, P., Zhang, H., Reid, C., Lv, J., and Yue, G., 2010, "Three-Dimensional Simulation for an Entrained Flow Coal Slurry Gasifier," *Energy Fuels*, Vol. 24, pp. 1156–1163.

WRI, 2008, "Substitute Natural Gas from Coal, Western Research Institute," Laramie, WY, USA. http://www.westernresearch.org/business.aspx?ekfrm=204.

Xu, L., Lee, J., and Kim, H., 2007, "Comparison of Low Temperature Ash Deposition Determined by Theoretical and Experimental Method in Coal Gasifier Condition," World of Coal Ash (WOCA), May 7-10, 2007, Northern Kentucky, USA.

Yong, S., Gazzino, M., and Ghoniem, A., 2012, "Modeling the Slag Layer in Solid Fuel Gasification and Combustion – Formulation and sensitivity analysis." *Fuel*, Vol. 92, pp.162-70.

Yong, S., and Ghoniem, A., 2012, "Modeling the slag layer in solid fuel gasification and combustion – Two-way coupling with CFD," *Fuel,* Vol. 97, pp. 457-466.

Yoon, H., Wei, J., and Denn, M., 1978, "A Model for Moving‐bed Coal Gasification Reactors," *AIChE Journal*, Vol. 24, pp. 885-903.

Zhang, H., and Modest, M., 2001, "Evaluation of the Planck-mean absorption coefficients from HITRAN and HITEMP databases," *Journal of Quantitative Spectroscopy and Radiative Transfer,* Vol. 73, pp. 649-653.

Zitney, S., 2010, "Process/equipment Co-simulation for Design and Analysis of Advanced Energy Systems," *Computers & Chemical Engineering*, Vol. 34, pp. 1532-1542.

Zhou, L., 1988, *Coal Combustion*, Hemisphere Publishing, New York.

Zwart, R., Boerrigter, H., Deurwaarder, E., Van der Meijden C., and Van Paasen. S., 2006, "Production of Synthetic Natural Gas (SNG) from Biomass," http://www.ecn.nl/docs/ library/report/2006/e06018.pdf.

APPENDIX
CALCULATING VOLATILESENTHALPY OF FORMAITON

The volatiles chemical composition in a coal is not usually provided, neither their enthalpy of formation. This appendix documents the method to determine the volatiles, overall hydrocarbon composition and the corresponding enthalpy formation. The Illinois No. 6 is used for an example. First, the proximate and ultimate analyses of Illinois No.6 bituminous coal are provided below.

Table A1. The proximate and ultimate analyses of Illinois No.6 bituminous coal

Coal	Illinois No.6
Proximate Analysis, wt %	
Moisture	11.12
VM	34.99
Ash	9.7
Fixed Carbon	44.19
Heating value (MJ/kg)	27.1

Ultimate Analysis, wt %	
Moisture	11.12
Ash	9.7
C	63.75
H	4.5
N	1.25
S	2.51
O	6.88
Cl	0.29

A.1 Volatile Composition

Calculate the weight percentage of each element in the volatiles using the moisture-free proximate and ultimate analyses (Table A.1),

$$\mathrm{wt\%_{C,volatile}} = \frac{\mathrm{wt\%_{C,ultimate}} - \mathrm{wt\%_{FC,proximate}}}{\mathrm{wt\%_{volatiles}}} = \frac{63.75\% - 44.19\%}{34.99\%} = 55.9017\%$$

$$\mathrm{wt\%_{H,volatile}} = \frac{\mathrm{wt\%_{H,ultimate}}}{\mathrm{wt\%_{volatiles}}} = \frac{4.5\%}{34.99\%} = 12.8608\%$$

$$\mathrm{wt\%_{O,volatile}} = \frac{\mathrm{wt\%_{O,ultimate}}}{\mathrm{wt\%_{volatiles}}} = \frac{6.88\%}{34.99\%} = 19.6628\%$$

$$wt\%_{N,volatile} = \frac{wt\%_{N,ultimate}}{wt\%_{volatiles}} = \frac{1.25\%}{34.99\%} = 3.5724\%$$

$$wt\%_{S,volatile} = \frac{wt\%_{S,ultimate}}{wt\%_{volatiles}} = \frac{2.51\%}{34.99\%} = 7.1735\%$$

$$wt\%_{Cl,volatile} = \frac{wt\%_{Cl,ultimate}}{wt\%_{volatiles}} = \frac{0.29\%}{34.99\%} = 0.8288\%$$

The overall composition of volatile matters is assumed to be $C_xH_yO_zN_aS_bCl_d$) Apply chemical element mass balance as:

x = 55.9017/12 = 4.658475

y =12.8606/1 = 12.8606

z =19.6628/16 = 1.228925

a = 3.5724/14 = 0.25517

b = 7.1735/32 = 0.22417

d = 0.8288/35.453 = 0.02338

Normalizethe coefficients by making x=1 then, we obtain:

y = 12.8608/4.658475 = 2.761

z = 0.264

a = 0.25517/4.658475 = 0.055

b = 0.22417/4.658475 = 0.048

c = 0.02338/4.658475 = 0.005

Thus, the overall Volatiles' composition is : $CH_{2.761}O_{0.264}N_{0.055}S_{0.048}Cl_{0.005}$

Undergoing thermal cracking, the volatile matters are assumed to be cracked to lighter gases, including CO, H_2, C_2H_2, CH_4, N_2, HCl, H_2S and COS as :

$CH_{2.761}O_{0.264}N_{0.055}S_{0.048}Cl_{0.005} \longrightarrow a\ H_2 + b\ CO + c\ CH_4 + d\ C_2H_2 + e\ N_2 + f\ HCl + g\ H_2S + i\ COS$

The coefficients of each reactant are determined by the mass balance of each chemical element:

e = 0.055/2 = 0.0275

f = 0.005

g = 0.04

i = 0.008

b = 0.264 - 0.008 = 0.256

c + 2d = 1 - 0.256 - 0.008 = 0.736

2a + 4c + 2d = 2.761 - 0.005 – 2 * 0.04 = 2.676

c = 0.336

d = 0.2

a = (2.676 – 4 * 0.336 – 2 * 0.2) / 2 = 0.466

The Volatile cracking model becomes:

$CH_{2.761}O_{0.264}N_{0.055}S_{0.048}Cl_{0.005} \longrightarrow$

$0.466H_2+0.256CO+0.336CH_4+0.2C_2H_2+0.0275H_2+0.005HCl+0.04H_2S+0.008COS$

The enthalpy formation of the volatile is not known and thus needs to be calculated. A correct enthalpy value of the volatile will ensure that energy is properly balanced and counted for during thema-cracking process.

A.2 Volatiles' Enthalpy of Formation

The steps taken to find the enthalpy of formation of the volatile, $CH_{2.761}O_{0.264}N_{0.055}S_{0.048}Cl_{0.005}$, are as follow.

The volatile's heating value is found by taking subtracting the carbon's heating value from the coal's heating value, as expressed below.

$$HV_{CH2.761O0.264N0.055S0.048Cl0.005} = HV_{coal} - HV_C$$

HV_{coal} = 27.1 MJ/kg

HV_{carbon} = 32.8 MJ/kg

wt fraction of volatile in coal = 30.94%

wt fraction of char in coal = 44.19%

⇨ $HV_{CH2.761O0.264N0.055S0.048Cl0.005}$ = 40.7423 MJ/kg = 773493.3 kJ/kmol

Calculate volatile's enthalpy based on the volatile's combustion reaction.

The chemical equation for the volatile combustion is (here, volatile is simplified as $CH_{2.761}O_{0.264}$):

$hf_{CH2.761O0.264}$
$= HV_{CH2.761O0.264} - (1.55825 * hf_{O2}) + (1 * hf_{CO2}) + (1.3805 * hf_{H2O})$
$= 773493.3 – (1.55825 \times 0) + [1 \times (-393860.5) + 1.3805 \times (-286096.8)]$
$= -1.53E+07$ J/kmol

A.3 Heat of Reaction for volatile cracking equation:

The heat reaction is calculated as follows:

$CH_{2.761}O_{0.264}N_{0.055}S_{0.048}Cl_{0.005} \longrightarrow$
$0.466H_2+0.256CO+0.336CH_4+0.2C_2H_2+0.0275H_2+0.005HCl+0.04H_2S+0.008COS$

The enthalpy formations of each species are listed below:

$h_{f\,H2}=0$,
$h_{f\,CO}=-110636.4$ KJ/Kmol,
$h_{f\,volatile} = -1.53*10^4$ KJ/Kmol
$h_{f\,CH4}=-74937.1$ KJ/Kmol
$h_{f\,C2H2}=226,748$ KJ/Kmol
$h_{f\,N2}=0$
$h_{f\,HCl}= -92300$KL/Kmol
$h_{f\,H2S}= -20630$ KJ/Kmol
$h_{f\,COS}= -139,000$ KL/Kmol

$H_r = 0.466 \times h_{f\,H2} + 0.256 \times h_{f\,CO} + 0.336\, h_{f\,CH4} + 0.2 \times h_{f\,C2H2} + 0.0275 \times h_{f\,N2} + 0.005 \times h_{f\,HCl} + 0.04 \times h_{f\,H2S} + 0.008 \times h_{f\,COS} - h_{f\,Volatile}$
$=0+0.256\times(-110636.4)+0.33\times(-74937.1)+0.2\times(226,748)+0+0.005\times(-92300)+0.04\times(-20630)+0.008\times(-139,000)-(-15300)$
$= 4749.25$ KJ/Kmol (It needs to be emphasized that reaction heat must be a positive value since volatile cracking is an exothermic reaction)

VITA

Xijia Lu was born in Hefei, Anhui, China, on October 15th, 1983. He obtained his Bachelor's degree in Mechanical Engineering from Hefei University of Technology in China in 2006. He obtained his Master's degree in Mechanical Engineering from University of Science and Technology of China in 2009. He has joined the University of New Orleans engineering graduate program to pursue a PhD in Mechanical Engineering since 2009. During this time, he has performed most of his research at the Energy Conversion and Conservation Center under the supervision of Dr. Ting Wang. He will receive his PhD's Degree in July, 2013.